Experimental and computational investigations of the flow within a scale model of a hydroelectric generator

by

Kevin Venne

Department of Mechanical Engineering

McGill University

Montréal, Québec, Canada

April 2022

A thesis submitted to McGill University in partial fulfillment of the requirements of the degree of Doctor of Philosophy.

DEDICATION

To my grandmother,

Francoise De Senneville

"When everything seems to be going

against you, remember that the

airplane takes off against the wind,

not with it."

Henry Ford

ACKNOWLEDGMENTS

First and foremost, the work presented in this thesis was a collaborative venture and without the help of the individuals and organizations mentioned herein, the work may have never been realized. This thesis was made possible by a joint venture between McGill University and Hydro-Québec.

I would like to start by thanking my advisers Professor Mydlarski (McGill), Professor Baliga (McGill), and Federico Torriano (IREQ) for their outstanding mentorship and support throughout this project. I am truly grateful to them for giving me the opportunity to pursue this project.

I would also like to thank Claude Hudon (IREQ) and Arezki Merkhouf (IREQ) for supporting all project endeavors and their mentorship. Their support in key moments played a major role in the success of this project.

Special thanks to Jean Philippe (J.P.) Charest-Fournier (IREQ), the technician I was lucky to have the chance to work with for more than five years. J.P. devoted countless hours to the research project and without his help, the work realized in this project would not have been possible. I will forever be grateful for his devotion to our research efforts.

I would like to thank my colleagues at McGill: Michael Hinton, Vincent Tremblay-Dionne, and Alais Hewes and at the IREQ: Mathieu Kirouac, Olivier Kokoko, and Luc Provencher for the fruitful conversations and friendship.

I would like to express my gratitude to the agencies that supported this project: McGill University, Mitacs, and the *Fonds de Recherche du Québec - Natures et Technologie*. Their support facilitated the success of this work.

I would also like to thank my family for their unwavering support throughout the ten years of my higher education.

ABSTRACT

Decarbonization of the Atlantic Northeast's electricity is achievable by utilizing Québec's power system, if the reliability of the latter can be ensured. However, a critical element is the thermal management of the power system's aging hydroelectric generators. To improve the thermal management, a 1:4 scale model of a hydroelectric generator was developed by Hydro-Québec. The research presented in this work utilized the scale model to refine a thermal mass flow meter and develop a numerical model to simulate the flow and heat transfer within hydroelectric generators. The new design of the flow meter enabled the first measurements of the flow rate within the rotor rim ducts of an in-service hydroelectric generator. Particle image velocimetry measurements demonstrated that the improved design had an accuracy of 8% and a 3.5% measurement repeatability, and allowed for the characterization of the flow in the rotor rim of the scale model. To further investigate the thermal management of hydroelectric generators, a numerical model capable of predicting the locations of hot-spots on the scale model's rotor pole was developed. The numerical model employed a meshing technique that reduced the mesh generation time for hydroelectric generators from months to hours, and predicted the net mass flow rate, windage losses, maximum and average pole temperatures to within 5%, 4%, 3°C, and 5°C of experimental results, respectively. Furthermore, the numerical model was utilized to investigate alternate ventilation configurations for the scale model, which showed that i) adding a deflector at the pit outlet reduced the windage losses by 8.8%, and ii) increasing the surface area of the spider arms reduced the pole's maximum surface temperature by 2.6°C.

RÉSUMÉ

La décarbonisation de l'électricité du Nord-Est de l'Atlantique est atteignable en utilisant le réseau du Québec, si sa fiabilité peut être assurée. Un des enjeux du réseau est la gestion thermique des alternateurs vieillissants. Pour gérer cet enjeu, une maquette tournante à l'échelle 1:4 d'un alternateur a été développée par Hydro-Québec. La présente recherche a utilisé la maquette tournante pour raffiner un débitmètre de type thermique et développer un modèle numérique pour simuler le comportement thermofluide des alternateurs. La nouvelle conception du débimètre a permis de réaliser les premières mesures de l'écoulement dans les canaux de jantes du rotor d'un alternateur en centrale. Des mesures PIV ont démontré que la conception améliorée avait une précision de 8% et une répétabilité de la mesure de 3,5%, et ont permis de caractériser l'écoulement dans le rotor de la maquette. Pour mieux investiguer la gestion thermique des alternateurs, un modèle numérique en mesure de prédire les localisations des points chauds sur le pôle du rotor de la maquette a été développé. Le modèle numérique a employé une méthode de maillage réduisant significativement (mois à heures) le temps de génération du domaine numérique pour les alternateurs, et a prédit le débit global, les pertes de ventilation, de même que les températures maximales et moyennes du pôle de 5%, 4%, 3°C, et 5°C des mesures expérimentales, respectivement. Le modèle numérique a aussi été utilisé pour investiguer différentes configurations de ventilation pour la maquette, lequel a démontré que i) l'ajout d'un déflecteur réduit les pertes de ventilation de 8,8%, et ii) l'augmentation de la surface des croisillons du rotor réduit la température maximale du pôle de 2,6°C.

CONTRIBUTIONS TO ORIGINAL KNOWLEDGE

The following aspects of the research presented in this thesis are considered as original scholarship and distinct contributions to knowledge:

1. The first flow measurements in the rotor rim of an in-service hydroelectric generator were undertaken.

2. A robust, improved prototype of a thermal mass flow meter (TMFM) for the measurement of the flow within a hydroelectric generator was designed, constructed, and tested.

3. The flow passing through the rotor rim of *l'Institut de recerche d'Hydro-Québec*'s (IREQ's) scale model was characterized using the developed TMFM.

4. A time-efficient meshing strategy for radially-cooled hydroelectric generators was developed and implemented.

5. Several numerical models for hot-spot detection on the scale model's rotor pole were formulated, implemented and tested, and related recommendations were made.

6. Three configurations were investigated to improve the ventilation of radially-cooled hydroelectric generators and their implications were presented and discussed.

LIST OF PUBLICATIONS

(A) Venne, K., Torriano, F., Mydlarski, L. and Baliga, B.R. 2022 Validation of a Numerical Model for Hot-Spot Detection on the Surface of a Rotor Pole Using a Scale Model of a Hydroelectric Generator. *Applied Thermal Engineering (Submitted).*

(B) Torriano, F., Venne, K., Provencher L., Kirouac, M. and Mydlarski, L., inventors; Hydro-Québec, assignee 2021 Débimètre électronique à bilan thermique. Canada Patent Application No. PCT/CA2021/051831.

(C) Venne, K., Torriano, F., Mydlarski, L. and Baliga, B.R. 2021 Validation of a Numerical Model for Hot-Spot Detection on the Surface of a Rotor Pole Using a Scale Model of a Hydroelectric Generator. *Proceedings of the 15^{th} International Conference on Heat Transfer, Fluid Mechanics and Thermodynamics (HEFAT)*, online.

(D) Torriano, F., Venne, K., Provencher, L., Kirouac, M., Levesque, J.-B. and Bissonnette, S. 2021 Développement d'un capteur anémométrique pour la mesure de débit d'air dans les events de jante d'un alternateur. *Rapport technique* IREQ-2021-0072, Institut de recherche d'Hydro-Quebec (IREQ), Varennes, Canada.

CONTRIBUTION OF AUTHORS

Publications A & C

K. Venne developed the meshing strategy for IREQ's scale model (Appendix A), performed the numerical simulations (Chapter 5), as well as wrote the conference and journal articles. All aforementioned tasks were supervised by F. Torriano, Prof. Mydlarski, and Prof. Baliga.

Publication B

K. Venne made all key decisions in the patented design (Chapter 4), designed the faceplate and heating element (section 4.3.1), performed all numerical simulations to determine the RTD placement (section 4.3.3) and the design's mechanical integrity (section 4.3.5), supervised all experiments performed by J.P. Charest-Fournier to validate the design's performance, and analyzed the results (section 4.4). All aforementioned tasks were supervised by F. Torriano and Prof. Mydlarski. F. Torriano wrote the patent application. L. Provencher designed the printed circuit boards (section 4.3.4) with guidance from M. Kirouac, K. Venne, and F. Torriano. L. Provencher also developed the data acquisition unit.

Publication D

K. Venne supervised and analyzed all experiments performed by J.P. Charest-Fournier to characterize the flow in the rotor-rim of an in-service generator (section 4.1) and the scale model (section 5.1), as well as those required to validate the TMFM (section 4.4). M. Kirouac developed a data acquisition (DAQ) unit that is powered using a direct current method. Jean Benoit Levesque analyzed all static structural test for the rapid prototyping plastics (section 4.3.2). S. Bissonnette developed a second DAQ unit that is powered using an alternating current method. All aspects were guided and supervised by F. Torriano and K. Venne.

TABLE OF CONTENTS

LIST OF TABLES

LIST OF FIGURES

NOMENCLATURE & ACRONYMS

NOMENCLATURE

A = area $[m^2]$

a = acceleration $[m \cdot s^{-2}]$

C_R = cross-correlation

CFL = Courant-Friedrichs-Lewy number

c_p = specific heat at constant pressure $[\mathrm{J} \cdot \mathrm{kg}^{-1} \cdot \mathrm{K}^{-1}]$

$C_{\dot{m}}$ = blockage factor

D_h = hydraulic diameter $[m]$

D = diameter $[m]$

D_a = aperture diameter $[m]$

d_e = particle diameter seen by camera $[m]$

d_p = particle size $[m]$

$\mathcal{D}$ = percentage difference

E = voltage $[V]$

e_i = sources of error

$\mathcal{E}$ = Young's modulus $[Pa]$

Er = error

F_Ω = centrifugal force $[N]$

$\mathcal{F}$ = average flux

f = frequency $[Hz]$

$f_\#$ = ratio between objective lens diameter and aperture diameter

F = Fourier transform

f_n = probability distribution function

g = gravity $[\mathrm{m} \cdot \mathrm{s}^{-2}]$

H = height of the rectangular duct $[m]$

h = convective heat transfer coefficient [$\mathrm{W \cdot m^{-2} \cdot K^{-1}}$]

I = current [A]

I_1 = image intensity of first image

I_2 = image intensity of second image

$\mathcal{K}$ = thermal conductivity [$\mathrm{W \cdot m^{-1} \cdot K^{-1}}$]

k = turbulent kinetic energy per unit mass [$\mathrm{m^2 \cdot s^{-2}}$]

$\mathcal{L}$ = energy losses [W]

M = million [$\times 10^6$]

M_{ag} = camera magnification

M_{win} = window length [$pixel$]

$\dot{m}_{empty}$ = mass flow rate without TMFM installed [$\mathrm{kg \cdot s^{-1}}$]

$\dot{m}_{TMFM}$ = mass flow rate with TMFM installed [$\mathrm{kg \cdot s^{-1}}$]

$\dot{m}$ = mass flow rate [$\mathrm{kg \cdot s^{-1}}$]

m = mass [kg]

N = cell count

N_{fine} = grid refinement ratio

N_{win} = window width [$pixel$]

N_L = mean number of particles seen by camera

n = normal vector

Nu = Nusselt number

P = pressure [$\mathrm{N \cdot m^{-2}}$]

$\mathcal{P}$ = power [W]

p = window width displacement [$pixel$]

Pe = Péclet number

Pr = Prandtl number

Q = rate of energy into the flow [W]

$\mathcal{Q}$ = general sensitivity index

q = window length shift $[pixel]$

$\mathcal{R}$ = result

r, R = radius/radial coordinate $[m]$

r_m = median of neighbors' residuals

r_0 = normalized vector residual

Ra = Rayleigh number

Re = Reynolds number

R_{inst} = instrument resolution

$\mathcal{S}$ = shape of the laser pulse

S = volumetric (per unit volume) rate of generation/source term

SD = particle density

s_0 = object distance $[m]$

T = temperature [℃]

$T_{universal}$ = temp. evaluated at a mean TCR and base resistance [℃]

$T_{\bar{R}_0,i}$ = temp. evaluated at a mean base resistance for an RTD, i [℃]

ΔT^* = temperature change between modified and baseline cases $[^\circ C]$

t = time $[s]$

$\mathcal{U}$ = uncertainty

$\mathcal{U}_0$ = zeroth-order uncertainty

u, U = velocity $[\mathrm{m \cdot s^{-1}}]$

W = width of the rectangular duct $[m]$

x_0 = displacement vector at point 0 $[m]$

x_m = median displacement $[m]$

$\mathcal{X}$ = given quantity of interest (floating variable)

X, Y, Z = cartesian coordinates $[m]$

Greek symbols

α = thermal diffusivity [$\mathrm{m}^2 \cdot \mathrm{s}^{-1}$]

α_{TCR} = temperature coefficient of resistance [$^{\circ}C^{-1}$]

Γ = diffusion coefficient [$\mathrm{kg} \cdot \mathrm{m}^{-1} \cdot \mathrm{s}^{-1}$]

δ = air-gap distance from rotor-to-stator [m]

ε = dissipation rate of turbulent kinetic energy per unit mass [$\mathrm{m}^2 \cdot \mathrm{s}^{-3}$]

ϵ = threshold

θ = angular position on the pole surface [$^{\circ}$]

Λ = orthogonality

λ = wavelength [m]

μ = dynamic viscosity [$\mathrm{kg} \cdot \mathrm{m}^{-1} \cdot \mathrm{s}^{-1}$]

μ_{stat} = mean

ν_{mech} = Poisson's ratio

ν = kinematic viscosity [$\mathrm{m}^2 \cdot \mathrm{s}^{-1}$]

ρ = density [$\mathrm{kg} \cdot \mathrm{m}^{-3}$]

σ = standard deviation

σ_m = constant normalization factor

σ_y = yield stress [Pa]

σ_U = ultimate stress [Pa]

σ_0 = orientation

σ_{proof} = proof stress [Pa]

σ_{sim} = numerically (simulated) predicted stress [Pa]

τ = torque [$\mathrm{N} \cdot \mathrm{m}$]

Φ = skewness

ϕ = general intensive dependent variable

Ω = rotor rotational speed [s^{-1}]

ω = specific dissipation rate [s^{-1}]

Subscripts

air = referring to the surrounding air

b = bulk

blt = belt

b_{in} = bulk at inlet

b_{out} = bulk at outlet

br = bearing

d = heating element wire diameter

exp = exposure

ext = extrapolated

inj = injected

i, j = indices

LF = lower fan blades

m = motor

max = maximum value

out = motor power output

$print$ = 3D printer

$pulse$ = laser pulse

R = rotor

RR = rotor-rim

rad = radiator

rel = relative position to center of heated pole

sim = simulated

$spot$ = laser's projection or spot

ss = steady-state

T = turbulent

U = velocity

UF = upper fan blade

w = windage

W = wire

$\bar{Z}$ = axially averaged

$\bar{\theta}$ = circumferentially averaged

ϕ = general intensive dependent variable

0 = base or reference

$0X$ = referring to a given TMFM label number X from 0 to 8

$1, 2, 3$ = referring to the first, second, or third instance

Superscripts

S = stationary frame

R = rotating frame

$0X$ = referring to a given TMFM label number X from 0 to 8

Accents

$\breve{}$ = per unit mass

$\hat{}$ = root-mean-squared quantity

$\tilde{}$ = instantaneous quantity

$\prime$ = fluctuating quantity

$\bar{}$ = average quantity

ACRONYMS

ABS = acrylonite butadiene styrene

ASA = acrylonitrile styrene acrylate

ASCII = American Standard Code of Information Interchange

AWT = governing equations

C = coupled, with constant properties of air at $46°C$

CAD = computer aided design

CFD = computational fluid dynamics

CFDHT = computational fluid dynamics and heat transfer

CHT = conjugate heat transfer

cRIO = compact re-configurable input/output modules

CV = control volume

DAQ = data acquisition

DC = decoupled, with constant properties of air at $46°C$

DIAAA = *Diagnostic Avancé des Alternateurs*

DFPO = deflector at the pit outlet case

DNS = direct numerical simulation

EDF = *Électricité de France*

EPFL = *École Polytechnique Fédérale de Lausanne*

FD = fluid domain

FDM = fused deposition modeling

FEM = finite element method

FLSA = full-length spider arm case

FFT = fast Fourier transform

FIS = fluid inside shell

FS = factor of safety

G = evaluation metric/grade

GE = General Electric

GEQ = governing equations

GGI = general-grid interfaces

GHG = greenhouse gasses

GUI = graphical user interface

HDT = heat deflection temperature

HE = heating element

HEG = hydroelectric generator

HEM = heating element matrix

HEX = *Numeca HEXPRESS/Hybrid*

HH = *Numeca HEXPRESS*

HPC = high performance computing

HRM = high Reynolds number modeling (with wall functions)

IO = input/output

IREQ = *Institut de recherche d'Hydro-Québec*

LES = large eddy simulations

LRM = low Reynolds number modeling (without wall functions)

LSA = laser sheet apparatus

MBD = model-based design

MIT = Massachusetts Institute of Technology

MP = mixing-plane

MRF = multiple reference frames

PCB = printed circuit board

PCRI = partially closed rotor inlet case

PHL = pole heat losses

PIV = particle image velocimetry

PLC = power line communication

RANS = Reynolds-averaged Navier-Stokes

RMSE = root-mean-square error

RPO = rounded pit outlet case

RSI = rotor-stator interface

RSM = Reynolds stress modeling

RTD = resistance temperature detector

SCDM = ANSYS Space Claim Design Modeler

SCM = scale model

SCWF = scalable wall functions

SD = solid domain

SM = sliding mesh

SST = shear-stress-transport

TCR = temperature coefficient of resistance

TDF = turbulent diffusive flux

TM = turbulence model

TMFM = thermal mass flow meter

TFP = thermofluid properties

TWR = ThermaWatch^{TM} Rotor

ULTEM = polyethermide

URANS = unsteady Reynolds-averaged Navier-Stokes

USB = universal serial bus

VP = coupled, with variable properties of air

2D = two-dimensional

3D = three-dimensional

CHAPTER 1
Introduction

Hydro-Québec is aiming to lead the fight against climate change, and a new study by the Massachusetts Institute of Technology (MIT) (Dimanchev *et al.*, 2020) showed that the company can do just that, as it has the ability to de-carbonize the entire Atlantic Northeast region. The viability of this goal is being tasked to IREQ: *Institut de recherche d'Hydro-Québec* (Hydro-Québec's research institute), which is using its experience extending over more than 50 years to increase our understanding, enforce better standards in the replacement, and retrofit the company's aging fleet of hydroelectric generators to meet this goal.

1.1 Motivation

Hydro-Québec outlined in its 2020-24 strategic plan (Hydro-Québec, 2019) its commitment to lead what it coined the "energy transition," which is the transformation in power generation, transmission, and distribution, as well as, energy consumption trends due to: an increased desire for power system efficiency, a greater access to technology, a customer base with evolving lifestyles, and a desire to lead the fight against climate change. The latter consists of four main objectives: contributing to the reduction of greenhouse gasses (GHG) in all their markets; driving Québec's economic development; improving the customer experience; and increasing earnings. Four main strategies were presented to achieve these objectives: electrifying Québec's energy sector; fighting climate change through the electrification of energy sectors beyond its border; developing a culture focused on customers and occupational health and safety;

and continuously improving its operating performance. Furthermore, the company highlights that it has not used the full potential of its hydroelectricity, because the electricity it generates only accounts for 35% of Québec's energy consumption. The plan also conveys that the utilization of hydroelectricity's full potential would see a future in which the province of Québec and the northeastern United States are decarbonized. This idea that was later shown to be viable by a study conducted at the MIT by Dimanchev *et al.* (2020). The study concluded that the creation of a two-way trade of electricity between the United States and Québec would help to reduce the overall power system costs between the regions and create a decarbonized electrical system for the Atlantic Northeast using Hydro-Québec's hydropower plants as a "backup battery" for variable wind and solar power generation in the United States. Furthermore, the study found that the existing hydropower resources of Hydro-Québec are sufficient to meet the demands. Although Hydro-Québec's plan and the MIT study both predict a future of decarbonized electricity for the Atlantic Northeast, ensuring the reliability of the power system is of utmost importance in making this a reality. For this reason, the research engineers and technicians at IREQ have been working to ensure the reliability of the power system using asset diagnostics and prognostics. However, one of the major concerns of the power system is the age of its hydroelectric generators.

A general rule of thumb given by manufacturers of hydroelectric generators is they have a lifespan of approximately 50 years, making the age of such machines a key indicator for their replacement. Publicly accessible data on Hydro-Québec's installed power over a sequence of multi-decade periods of construction is illustrated in figure 1.1. It shows that some of the company's hydroelectric generators are older than the company itself (1944). Furthermore, figure 1.1 illustrates two major points. Firstly, from 1910-1999, the

province of Québec doubled its hydroelectric power output about every two decades. Secondly, the period from 1960-1979 was the largest construction period, and is known as the power installation peak. The installation of 1.4 GW of hydroelectric power in approximately two decades is indeed an impressive engineering accomplishment. However, the installation peak will eventually result in a replacement peak in which the generators installed from 1960-1979 will need to be replaced. Calculating the age of a given machine is a rather elementary task, in practice, however, an effective age must be estimated because: i) many have undergone repairs since their service date, ii) repairs may have only been to sub-components of the machine, and iii) access to the records and details of such repairs is limited. To obtain a precise effective age of these machines requires diagnostic data – data that teams at IREQ are currently striving to obtain. In the meantime, a conservative estimate of the effective age of the 351 hydroelectric generators as of 2010, 2015, and 2020 was obtained by resetting their age to the date of the last major repair to demonstrate the evolution of the effective age over time, as illustrated in figure 1.2. Thus, figure 1.2 demonstrates that in the last decade (2010-2020), the number of hydroelectric generators over the age of 50 years has approximately doubled. Demonstrated in figure 1.3 is the forecast of the total amount of replacements that must be performed, and the yearly replacements required to achieve this in a given decade starting from 2020, if the manufacturers' replacement time frame of 50 years is followed. Thus, it would indicate that Hydro-Québec is currently in the replacement peak, requiring that approximately 10 hydroelectric generators per year be replaced over the next 9 years, as illustrated in figure 1.3. However, due to: i) the replacement cost, ii) replacement time, and iii) shortage of personnel, it is effectively impossible to replace 10 hydroelectric generators per year. Instead, difficult choices must be made to either replace or

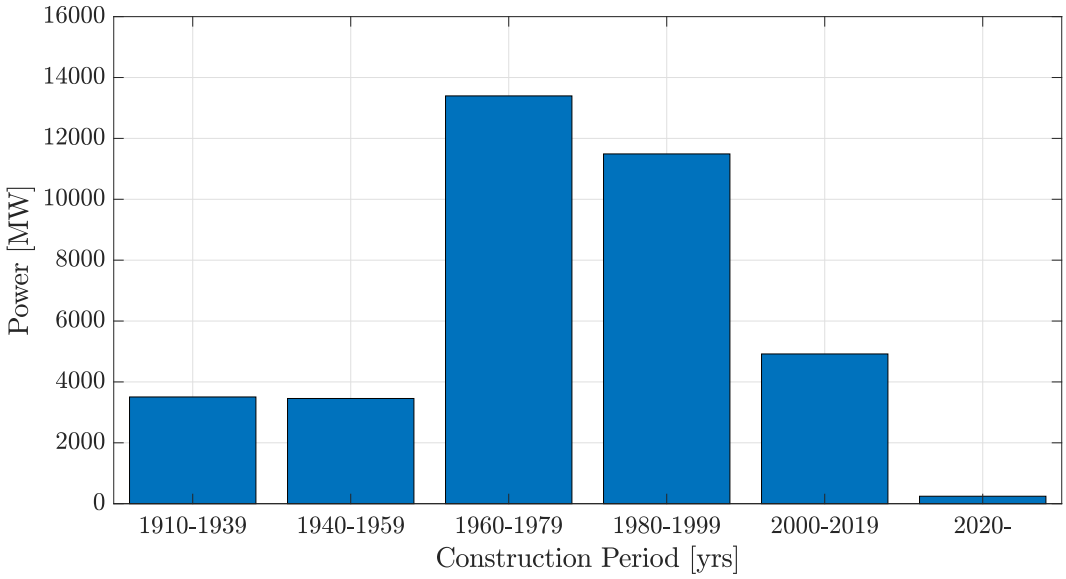

Figure 1.1: Hydro-Québec's installed power capacity over a sequence of multi-decade periods of construction (Hydro-Québec, 2021).

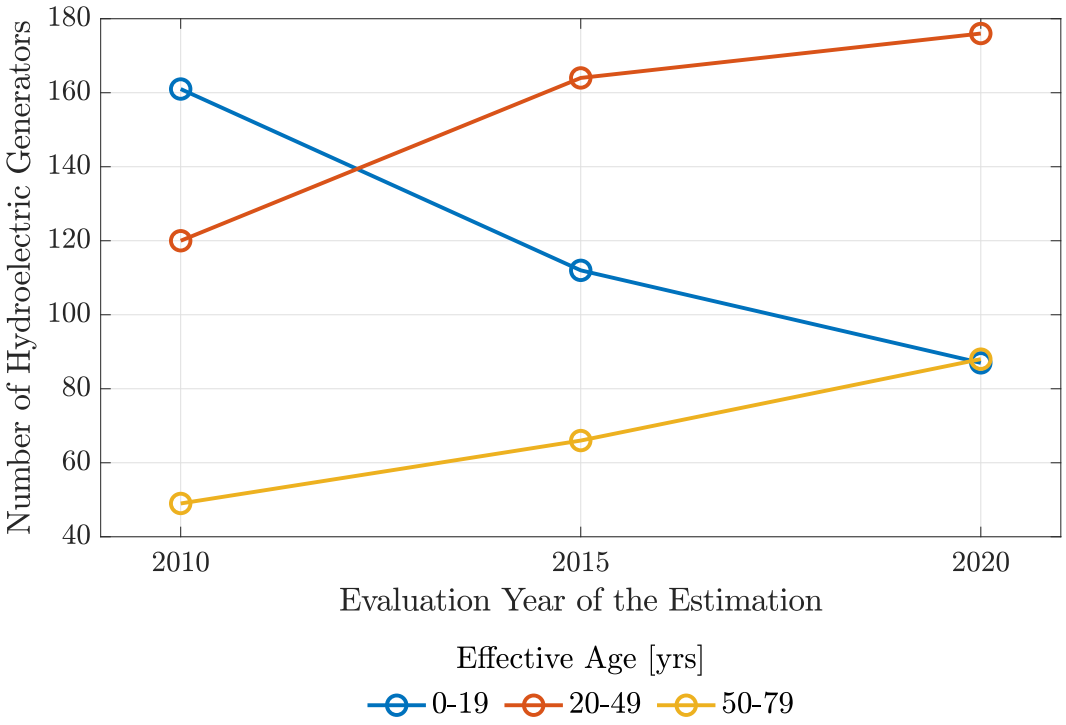

Figure 1.2: Evolution of the effective age of Hydro-Québec's hydroelectric generators from 2010-20 (private communication, A. Merkhouf).

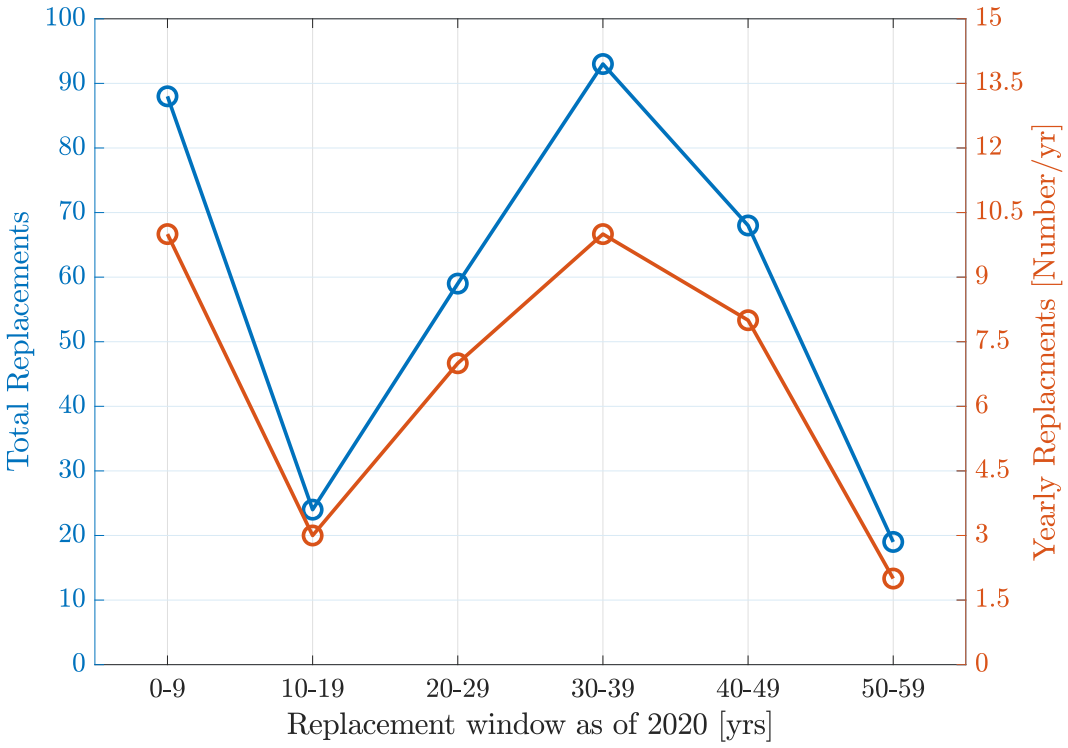

Figure 1.3: Forecast of the total and yearly replacement requirements for Hydro-Québec's hydroelectric generators in decade intervals as of 2020 (private communication, A. Merkhouf).

decommission a given hydropower plant. Additionally, when a decision is made to replace an older hydroelectric generator, Hydro-Québec must purchase the new generator from companies like General Electric (GE), Voith, or Andritz, because Hydro-Québec does not manufacture them. However, hydroelectric generators are not like standard products that are subject to competitive innovation. Thus, the purchasing company must demand that certain criteria be met. Therefore, to assist the company in establishing these criteria, IREQ initiated a project called DIAAA: *Diagnostic Avancé des Alternateurs* (Advanced Diagnostics of Hydroelectric Generators).

The main objective of the DIAAA project is to develop knowledge-based digital tools capable of monitoring the longevity of a given hydroelectric generator's rotor. Note that the word "advanced" in the project's acronym applies to rotor diagnostics, because existing rotor diagnostic methods are rather limited and complicated. The project has three phases: strategy development, longevity assessment, and rotor digitization, with each having three sub-phases as illustrated in figure 1.4.

The strategy development consists of reviewing all state-of-the-art diagnostic tools for the rotors of hydroelectric generators, conducting a failure mode analysis, and determining methods for which visual inspection is beneficial. The review of the state-of-the-art by Merkhouf *et al.* (2017) consulted over 250 documents and concluded that: i) many of the standardized tools in use are not utilizing the full potential of the data being collected, ii) some promising commercially available tools will require in-house laboratory testing to validate their effectiveness, and iii) emerging tools have shown promise, but more efforts are required to bring these tools to fruition. The failure mode analysis found over 150 modes requiring further investigation to fully characterize their symptoms. Lastly, once each failure mode was linked to a

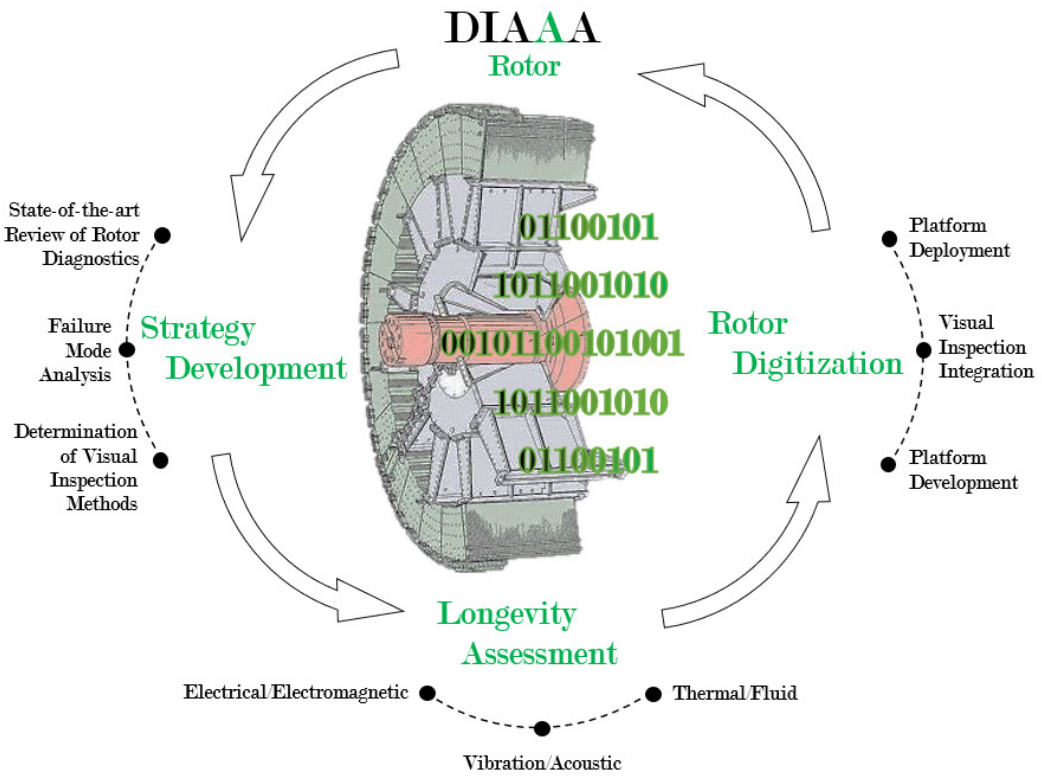

Figure 1.4: Overview of the main phases and sub-phases of the DIAAA project (Merkhouf *et al.*, 2017).

symptom, those capable of being detected via standard visual inspection will be tagged.

The longevity assessment phase of the project consists of obtaining valuable experimental data capable of measuring the rotor's characteristics in a laboratory setting, as well as on actual hydroelectric generators. This phase also consists of validating existing tools and developing new ones to obtain the required data. The experimental data deemed valuable can be grouped into three categories: i) electric/electromagnetic, ii) vibration/acoustic, and iii) thermal/fluid. The data to be collected in these categories span a wide range, from simple resistance measurements of sub components, to more complex air flow measurements in the rotor rim. The goal of such measurements is to determine whether they indeed can reveal the underlying "symptoms" that affect the overall "health" of a hydroelectric generator's rotor to determine the minimum number of tools or interventions required to asses its overall health.

The final phase is to "digitize the rotor," or develop software that, given the right inputs and visual inspection data, could provide a health report to the personnel responsible for the hydroelectric generator's maintenance. In the long-term, these tools could provide insight on the underlying issues of hydroelectric generators to the researchers at IREQ. Furthermore, this insight could potentially lead to new standards for hydroelectric generators, to which manufacturers of the new generation of machines would have to abide. Moreover, this would increase the durability and reliability of Hydro-Québec's future grid. However, this vision would not be achieved if the validation of existing diagnostic tools and development of new ones for hydroelectric generators is not performed.

In the context of the DIAAA project, the current research focuses on the development of novel diagnostic tools and numerical models (*i.e.* numerical solutions of mathematical models) capable of measuring and predicting the thermal/fluid behavior of hydroelectric generators. The need to develop the aforementioned tools/models and to fully understand the fluid flow and thermal behavior is due to the inadequate design of the thermal management arrangements within hydroelectric generators, which have led to accelerated thermal aging and the thermal failure of the rotor poles, as illustrated in figure 1.5, where the bottom image shows insulation oozing out of a rotor pool due to overheating. As mentioned in Hudon *et al.* (2010), most hydroelectric generators rely on convective cooling (using air) to avoid excessive temperatures in the main components (*e.g.* rotor poles). Furthermore, it is believed that the underlying causes leading to such failures are: i) insufficient air flow from the rotor rim ducts on either side of the poles, and ii) hot-spots (*i.e.* regions where the temperature limits of the insulation may be exceeded within hydroelectric generators). The latter cause has proven rather difficult to measure experimentally. Thus, two potential remedies were proposed to: i) measure the flow within the rotor rim ducts, and ii) develop a numerical model capable of predicting the location of hot-spots on the rotor poles.

Rotors of large radially-cooled hydroelectric generators are perforated with many small passages called rotor rim ducts that serve to cool the poles on the outer rim (shown in 1.5). In this context, Venne *et al.* (2018), developed a diagnostics tool capable of measuring the cooling flows within the rotor rim ducts by way of a thermal mass flow meter (TMFM). However, the device was considered a working prototype requiring further development at the time of the published paper.

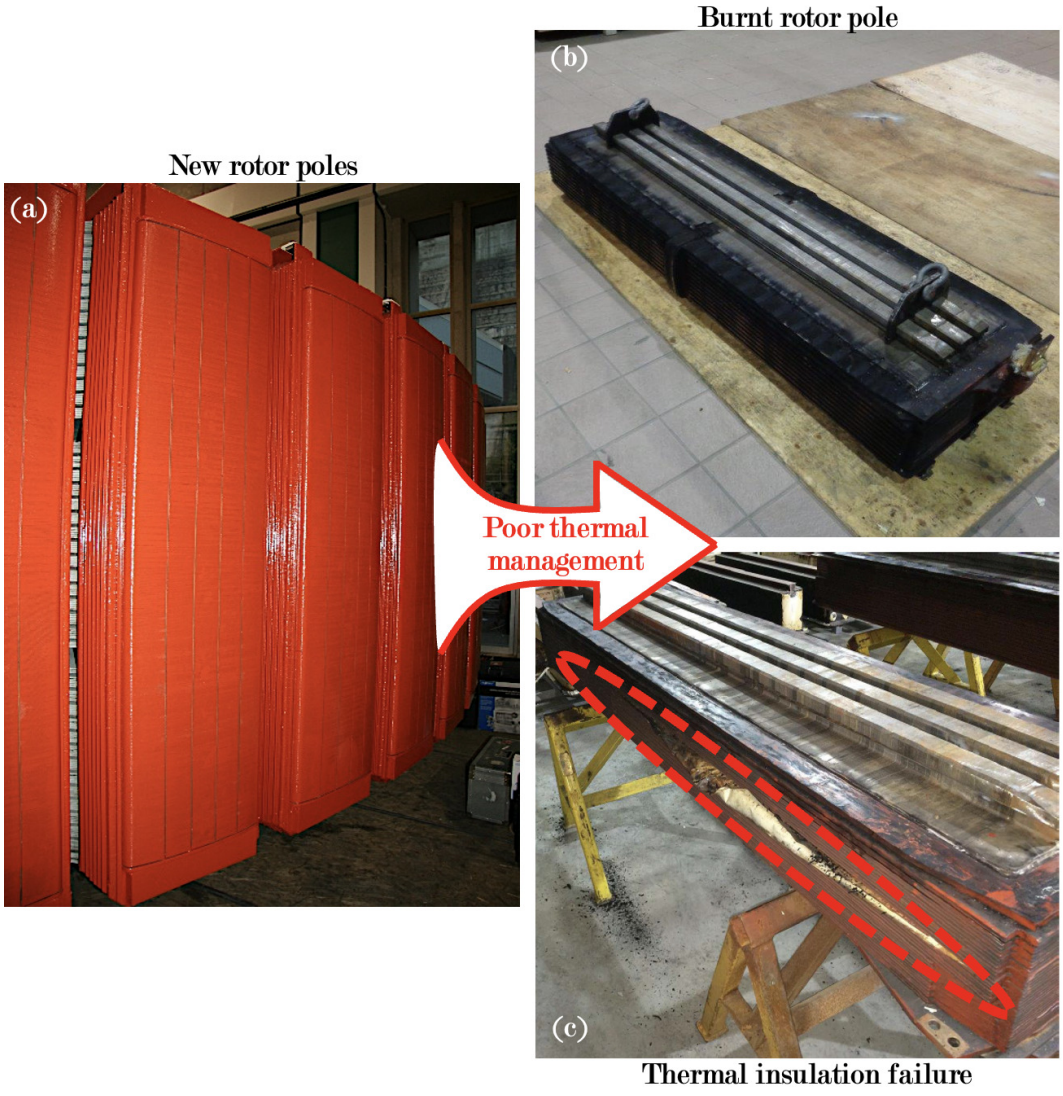

Figure 1.5: Damages to the rotor poles of a hydroelectric generator due to poor thermal management. (a) New set of rotor poles prior to their commissioning. (b) A burnt rotor pole. (c) A rotor pole with insulation oozing out due to overheating.

Hudon *et al.* (2010) explain that for numerical models to be able to predict the location of hot-spots reliably, they must account for both electromagnetic and ventilation losses. Electromagnetic losses generate heat in the stator core, rotor poles, damper bars, and end windings, due to induced eddy currents and the Joule effect. Ventilation or windage losses arising from the air flow passing through the generator increase the torque required to turn the rotor at the desired rotational speed. This method of cooling can account for up to 30% of the global losses in a hydroelectric generator. Thus, to increase the longevity and overall efficiency of hydroelectric generators, research engineers must find ways to eliminate hot-spots while simultaneously minimizing ventilation losses. When using validated numerical models, it is economically feasible to: i) minimize the pressure drop in the ventilation circuit for the required flow rate, and ii) optimize the flow path to appropriately cool (by convection) the components that are most susceptible to overheating.

Thus, to develop a diagnostic tool to measure the flow in the cooling passages and to develop models of the thermal behavior of hydroelectric generators, a review investigating the current state-of-the-art in numerical modeling, flow measurement, and fluid flow sensor development for such machines is in order. Since few papers were present in the published literature and the work outlined in this thesis either uses or directly expands upon the work performed at IREQ, the literature review was divided into two sections: research performed outside of IREQ (Section 1.2) and that performed at IREQ (Section 1.3).

1.2 Literature Review of Research Performed Outside IREQ

The review of the research conducted outside IREQ is divided into three subsections: i) convective heat transfer studies (fluid flow aspects only) of hydroelectric generators (HEGs), ii) conjugate heat transfer (CHT) studies

of HEGs, and iii) particle image velocimetry (PIV) measurements in a scale model of a HEG. Each subsection has direct relevance to the research herein.

1.2.1 Convective Heat Transfer Studies of HEGs

Gunabushanam & Suresh (2006) were among the first to develop a fluid-flow model for a hydroelectric generator. Their primary focus was on fluid flow through the stator components, as it can account for 30%-65% of the total pressure drop in the machine. To determine a method for reducing these pressure drops, the authors developed a numerical model of a section of the stator using PHOENICS CFD with 226K volume cells, and inlet velocity and no-slip wall boundary conditions. In a series of numerical experiments, the authors varied the inlet velocity in their model and found that the hydraulic loss factor (*i.e.* the ratio of the total head drop to the dynamic pressure difference across the stator) is greater at low flow speeds due to the formation of re-circulation zones, which can be minimized with simple modifications to the stator components. Their CFD results agreed with their experimental data to within 10%. However, they noticed that to improve the ventilation efficiency of the entire hydroelectric generator, it is necessary to also model the rotor, and thus, the rotor-stator interface (RSI).

The investigation of different RSI and turbulence models for a 3-D geometry was performed by Klomberg *et al.* (2014*a*,*b*). The authors found that the multiple reference frame (MRF) or frozen rotor approach (Luo *et al.*, 1994) with a $k-\omega$ shear-stress-transport (SST) turbulence model (Menter, 1994) was the most effective method.

Modeling of both the rotating and stationary components of generators was performed on axially-cooled synchronous machines with salient-pole rotors by Pickering *et al.* (2001). The authors modeled the fluid domain of a full-scale synchronous four-pole generator using FLUENT with 1.3M volume

cells, MRF, the standard $k-\varepsilon$ turbulence model (Pope, 2000; Launder & Sandham, 2002; Wilcox, 2006) and prescribed inlet velocity, outlet pressure, and constant-wall-heat-flux boundary conditions. When comparing both the air flow passing through the stator ducts and the convective heat transfer coefficients obtained on the poles in their simulations to the experimental data, Pickering *et al.* (2001) found both were underpredicted by 5% and 30%, respectively. Similar simulations were also undertaken by Lang *et al.* (2006), who modeled an axially-cooled synchronous generator with a slotted salient-pole rotor. The authors observed that the flow passing through all the cooling channels of the rotor was not evenly distributed, which can lead to overheating. Given the success of Pickering *et al.* (2001), Conner *et al.* (2013) modeled the entire generator's geometry in an effort to determine each component's effect on the windage losses. FLUENT was employed using 8M volume cells, MRF, a $k-\varepsilon$ turbulence model with enhanced wall functions (Kadar, 1981), and pressure boundary conditions for the inlet and outlet. The results of their simulation showed that the air flow and torque were under predicted by 4% and 30%, respectively, when compared to the experimental data. Moreover, they noted that the fan was responsible for 87% of the windage losses. Although these studies indicated differences between experimental and numerical results of up to 30%, the complexity of the models increased as the computational resources grew, and more valuable insight was obtained on the challenges associated with the development of numerical models of hydroelectric generators.

Moradnia *et al.* (2014*b*) state that early numerical models of the convective heat transfer in hydroelectric generators have shown 10%-30% errors in the heat transfer coefficients, as these models inaccurately captured multiple phenomena including the: i) windage losses, ii) wall shear stress, and iii) temperature gradient at the wall. Incorrect specification of the inlet boundary

conditions was one of the causes for the discrepancies between the experimental and numerical results. To remedy the latter, Moradnia *et al.* (2014*b*) proposed a fully predictive approach where no empirical boundary conditions were required and the flow quantities were solely determined by the rotation of the rotor. To prove the validity and effectiveness of the approach, Moradnia *et al.* (2014*b*) compared the numerical model employing a larger domain surrounding the hydroelectric generator where no inlet/outlet boundary conditions were applied, which the author called the fully predictive approach, to another numerical model using a smaller numerical domain with prescribed empirical boundary conditions at both the inlet and outlet. The latter utilized experimental data obtained using PIV and pitot-static tubes on a scale model to prescribe inlet boundary conditions of their numerical model to compare to the former (or fully predictive) approach. The numerical models used OpenFOAM with 18M elements, MRF, and the low-Reynolds number Launder-Sharma $k-\varepsilon$ turbulence model (Launder & Sharma, 1974). The authors found that both approaches yielded similar results, with the fully predictive approach yielding a 2%-7% under-prediction of the overall flow rate at the inlet when compared to experimental data. In a continuation of this work, Moradnia *et al.* (2014*a*) aimed to obtain the velocity profiles in various components of the generator by way of numerical simulations. However, when their results were compared to experimental pressure and PIV data, only qualitative agreements were obtained. They concluded that a fully predictive MRF approach is only capable of obtaining global quantities. However, from the numerical and experimental results of this study, the authors qualitatively observed unfavorable ventilation conditions, such as flow separation at the inlet baffles and fan-blade trailing edges, and a re-circulation zone near the inlet. In an effort to correct these inefficiencies, Jamshidi *et al.* (2015) numerically designed and experimentally

tested a new fan and intake system on a scale model that provided twice the flow rate to the rotor components in a more uniform fashion when compared to the same system without a fan. Similar work was performed by Kastner *et al.* (2010) using FLUENT and CFX. They were able to model the air flow rate through the stator ducts and the pressure rise for different fan configurations. Schrittwieser *et al.* (2014) undertook CFD simulations and found that the heat transfer rates in the stator ducts are not uniform due to flow separation caused by the rotation. They also observed that the flow at the leading edge was generally attached and provided better cooling, whereas the flow at the trailing edge was generally separated. Further studies in the stator ducts of a hydroelectric generator scale model were performed by Niebles Atencio *et al.* (2020), where the naphthalene sublimation technique was used to quantify the convective heat transfer coefficient in the upstream and downstream portions of the duct. The authors found that when a weighting method of measuring the sublimation rate was used, the experimental results were within 5% of the CFD results of Jamshidi *et al.* (2015).

1.2.2 Conjugate Heat Transfer Studies of HEGs

To improve the thermal performance of generators, it is not sufficient to only model the fluid-flow domain, as the surface temperatures of the solid components (and thus hot-spot locations) cannot be appropriately determined, because they are dependent upon the conduction of heat through the solid. Thus, to improve the model proposed by Pickering *et al.* (2001) of an axially-cooled synchronous machine with a salient-pole rotor, Shanel *et al.* (2003) modeled the conductive heat transfer in the solid components, but limited the numerical domain to a quarter of the salient-pole rotor. The numerical model used FLUENT with 2M volume cells, MRF, the standard $k - \varepsilon$ turbulence

model, and 90° periodicity. However, two main practical complications became apparent: i) meshing, and ii) modeling of contact resistances. Although automated meshing techniques have limited control and mainly use tetrahedral cells, they are preferred for the rather large and complex geometries of generators. However, hexahedral cells are preferred for the coils and poles, as they are composed of anisotropic materials, which require that the cell faces be aligned with the principal axis of the thermal conductivity tensor. The determination of the contact resistances between components in generators is key to obtaining accurate temperature distributions. However, it is extremely difficult to determine the contact resistance for the manufactured or assembled components. Even with these difficulties, Shanel *et al.* (2003) found that the numerical estimates of the coil peak temperature matched the experimental results quite well. Thus, using this model, the authors were able to quickly test numerous rotor ventilation configurations and asses their impact on the coil temperatures. Building upon this work, Vogt & Lahres (2013) modeled a large radially cooled hydroelectric generator using a hybrid CFD-CHT approach. Their numerical model used CFX with 125M volume cells, MRF, the standard $k - \varepsilon$ turbulence model, and 45° periodicity. The authors studied the impact of the covers (*i.e.* air guides) on the air flow distribution through the rotor, and the full temperature distribution in the stator core. The former quantified the economic benefit of the covers in terms of power savings caused by reducing the windage losses and thus torque, which was verified with experimental measurements and found to be within 3% of the CFD simulations. The hybrid CFD-CHT approach consisted of modeling a 3.75° sector of the fluid and anisotropic solid domains of the stator core using 15M volume cells with the boundary inputs (*i.e.* flow rate and surface temperatures) from the CFD results. This model allowed the authors to verify that the stator components

did not exceed the insulation temperature limits at different operating loads. The hybrid CFD-CHT simulation results were found to be within 5% of experimental resistance temperature detector (RTD) measurements in the stator core and windings. As part of a joint collaboration between *Électricité de France* (EDF), the *Université Lille Nord-de-France*, and IREQ, Lancial *et al.* (2017) numerically studied a scale model of an axially-cooled salient pole hydroelectric generator. The numerical model used CFX and EDF in-house codes with 4.4M and 5.4M volume cells in the fluid and solid domains, respectively, MRF, a low-Reynolds-number $k-\omega$ SST turbulence model with the first near-wall node in the fluid domain at $y^+ \approx 1$, and 36° periodicity with an experimentally obtained inlet velocity and a prescribed outlet pressure as the boundary conditions. The authors were able to determine the location of hot-spots and Nusselt number correlations for different flow regimes. The analysis showed that the leading edge of the pole is better cooled than its trailing edge, and that the heat transfer in the pole and inductive faces can be approximated using the classical Taylor-Couette-Poiseuille flow between two concentric and smooth cylinders, given that the Nusselt number dependence on the Reynolds number in these regions was found to be similar to the theoretical value of 1/7 in the turbulent regime (Aoki *et al.*, 1967; Viazzo & Poncet, 2014). Another study by Jichao *et al.* (2017) performed a CHT analysis of large radially-cooled hydroelectric generators. However, an oversimplified model was used with few points of validation.

1.2.3 PIV Measurements in the Chalmer's Scale Model

Scale models of hydroelectric generators designed to study the ventilation usually omit the electromagnetic and metallic components. The latter are often replaced by transparent elements that allow optical access and PIV measurements without disturbing the air flow. In only a few studies performed

outside of IREQ (Hartono *et al.*, 2012*b*,*a*; Moradnia *et al.*, 2014*a*; Jamshidi *et al.*, 2015) have PIV measurements been undertaken in a scale model of a hydroelectric generator. In the first study by Hartono *et al.* (2012*b*,*a*), PIV measurements were performed in the stator ducts and fan blades of a miniature (12.5 cm x 35.6 cm) axially-cooled scale model. The results of the flow within the stator ducts demonstrated large (*i.e.* half the channel width) recirculation zones within the stator ducts, which were believed to be caused by an insufficient flow rate resulting from the large inlet and fan pressure losses. The results pertaining to the air flow in the fan region demonstrated that large portions of the flow had a positive radial velocity component, rather than an expected predominately tangential velocity component with a small downward (negative) radial velocity component. In an extension of this work Moradnia *et al.* (2014*a*), made PIV measurements at the inlet of the scale model and concluded that the flow reversal in the region near the fan blades was be caused by flow separation at the inlet. Both inefficiencies were later resolved by Jamshidi *et al.* (2015) by fan and inlet modifications.

1.3 Literature Review of Research Performed at IREQ

The review of the research conducted at IREQ is divided into five subsections. The first outlines the CFD simulations of IREQ scale model of a hydroelectric generator. The next three sections are experimental studies performed using the scale model. These studies include the quantification of the windage losses, measurements of the rotor pole surface temperature, and measurements of the flows in various regions using PIV. The final section discusses the development of a fluid flow sensor for hydroelectric generators.

1.3.1 CFD Simulations of IREQ's Scale Model

The first CFD simulations undertaken at IREQ to investigate the ventilation circuit of a radially-cooled hydroelectric generator were performed in 2006.

Due to the complexity of such simulations and the lack of available validation data from in-service hydroelectric generators, a scale model of a hydroelectric generator was developed at IREQ (Bourdreault *et al.*, 2011). The goal of the scale model was to create an experimental facility that could provide the required access needed to obtain valuable data to validate numerical simulations of the ventilation circuit therein.

The first numerical simulations of IREQ's scale model's ventilation circuit were performed by Toussaint *et al.* (2011). In their study, the authors established some best practices for the numerical modeling of hydroelectric generators by investigating the sensitivity of different flow variables of interest to different mathematical models available in commercial CFD codes. Specifically, the authors performed a parametric study to determine the effects the rotor-stator interface (RSI) models, its location within the air gap (*i.e.* closer to stator or rotor), on key ventilation variables such as the windage losses, and the radial velocity profiles in the rotor rim and stator ducts. To establish this link, the authors first simplified the ventilation circuit of the scale model in 2D and then shifted to a 3D model.

The 2D model of Toussaint *et al.* (2011) consisted of a 10° sector, which included two halves of a rotor rim duct, one pole, two stator ducts, and two deflector plates. The numerical domain of this sector was generated using the ANSYS-ICEM code and consisted of 0.15M cells. With this 2D domain, the authors performed unsteady Reynolds-averaged Navier-Stokes (URANS) simulations invoking both a sliding mesh approach at the RSI and the standard $k-\varepsilon$ turbulence model employing a wall-function approach for the near-wall treatment to benchmark subsequent simulations. Ultimately, the model's simplicity allowed the authors to place 48 elements across the air gap and to perform a URANS simulation in a relatively short period of time (*e.g.* within

a day). By comparing different combinations of RSI models and air gap (δ) placements, the authors found that steady simulations using the mixing-plane model at $3\delta/4$ (measured from the rotor to the stator) were capable of accurately reproducing the radial velocity profiles and the windage losses of their benchmark case.

To provide more insight on the ventilation circuit itself, the authors shifted their attention to a 3D model by first invoking their findings from their 2D model. The 3D model consisted of a full 90° section of the scale model geometry and the numerical domain was generated using ANSYS-ICEM with over 65M cells (50M and 15M cells in the stationary and rotating components, respectively). The authors noted the many challenges imposed by the shift from 2D to 3D, which included an increase in meshing time (from days to several months) and computational time (from a day to months). Moreover, the numerical domain required several (6) subdivisions using general grid interfaces (GGIs) to ensure conservation of the dependent variables of interest. Using this 3D model, the authors investigated four different configurations using the frozen-rotor-RSI model and one configuration using the mixing-plane RSI model at a $3\delta/4$ placement. Ultimately, the authors found that the results from each case varied significantly and that an experimental validation was required to determine which approach was best.

Since Toussaint *et al.* (2011), only one other numerical study by Dang *et al.* (2017) was performed on IREQ's scale model. The authors studied the heat transfer on a small section of a heated rotor pole to reduce the required computational time and to avoid the complexities associated with generating the numerical domain of the full ventilation circuit of IREQ's scale model. Their model consisted of a 20° sector of the rotating domain (2 rotor rim

ducts and one pole) and a 5° sector of the stator (one stator duct). The numerical domain was generated using ANSYS-ICEM and consisted of 12M cells. In their study, the authors investigated the sensitivity of the three different turbulence models (standard $k-\varepsilon$ (Pope, 2000; Launder & Sandham, 2002; Wilcox, 2006), re-normalized group (RNG) $k-\varepsilon$ (Yakhot *et al.*, 1992), and the $k-\omega$ SST (Menter, 1994)) and the dependence of variable temperature fluid properties on the prediction of the convective heat transfer coefficient along one specific axial line of the rotor pole. Ultimately, the authors found good agreement with experimental results using the $k-\omega\ SST$ turbulence model, but found that a wall function approach provided similar results. Although these approaches yielded positive results, there were several drawbacks requiring further development, as the approach used could not be employed to study in-service hydroelectric generators.

1.3.2 Windage Loss Measurements in IREQ's Scale Model

In conjunction with work of Toussaint *et al.* (2011), Hudon *et al.* (2011) performed a series of measurements on IREQ's scale model to quantify the windage losses ($\mathcal{L}_w$) in the ventilation circuit, which are defined as:

$$\mathcal{L}_m = \Omega \tau_R, \tag{1.1}$$

and are solely a function of the rotor rotational speed (Ω) and torque (τ_R).

Unlike in-service hydroelectric generators, IREQ's scale model is driven by a 75 kW electric motor. Thus, the rotational energy provided by the electric motor is transmitted to the scale model rotor via a shaft supported by three (upper, mid, and lower) bearings that is connected to a belt-drive system. Since the rotational speed of the rotor is known (and measured), only the torque must be determined to estimate the windage losses. The torque can either be estimated using strain gauges, a torque meter, or by deducing the

system losses from the motor input power. Hudon *et al.* (2011) thought that the former would be very challenging because the strain on the outer edge of the rotor shaft may be too small to measure with a strain gauge. Moreover, since no torque meter was installed on the scale model, the authors deduced the windage losses by substracting all the losses from the motor power input ($\mathcal{P}_m$):

$$\mathcal{L}_w = \mathcal{P}_m - (\mathcal{L}_m + \mathcal{L}_{blt} + \mathcal{L}_{br}) = \mathcal{P}_{out} - (\mathcal{L}_{blt} + \mathcal{L}_{br}), \tag{1.2}$$

which includes losses arising from the motor ($\mathcal{L}_m$), belt ($\mathcal{L}_{blt}$,) and bearings ($\mathcal{L}_{br}$). All of the aforementioned losses are a function of the motor power output ($\mathcal{P}_{out}$). Ultimately, since the aforementioned quantities of interest are a function of the average air temperature in the scale model, Hudon *et al.* (2011) measured the motor power input over time and established a linear relationship between the motor input and the average air temperature at a fixed rotational speed. The authors determined that at a rotational speed of 300 rpm, the air enclosed in the scale model reached a steady state temperature of 46.2°C. Furthermore, the authors utilized the data to estimate the system losses (*e.g.* motor, belt, and bearing losses), which allowed for the evaluation the windage losses at 8.91 kW for a motor input power of 11.1 kW. The value for the windage losses was compared to the numerically estimated value of Toussaint *et al.* (2011) and the values were found to be within 3% of each other. Ultimately, the measurements of Hudon *et al.* (2011) provided support for the mathematical models and approaches chosen in the numerical simulations of IREQ's scale model's ventilation circuit.

1.3.3 Temperature Measurements in IREQ's Scale Model

Both Lévesque *et al.* (2013) and Torriano *et al.* (2014) performed a series of experiments on IREQ's scale model as part of the DIAAA project. These experiments employed an infrared pyrometer called the ThermaWatch$^{\text{TM}}$ Rotor

(TWR), which was specifically designed to measure the surface temperature on the rotor poles of hydroelectric generators. Ultimately, the authors performed a series of tests to gain the required level of confidence in the TWR's capabilities to measure the surface temperature of a rotor pole within an in-service hydroelectric generator. The work performed by the authors can be divided into two phases: i) laboratory benchmark tests, and ii) measurements on the scale model.

The first phase was completed by Lévesque *et al.* (2013) and consisted of three laboratory benchmark tests to quantify the TWR's: i) response time, ii) integration area, and iii) accuracy. In summary, the authors found that the TWR had a response time of less than 4 ms, an integration area of 33 mm for the scale model's air gap of 12.7 mm, and that errors in the manufacture's default calibration curve and the inconsistency in emissivity for different surfaces must be corrected by calibrating the TWR on the scale model's rotor pole directly. Thus, the authors deemed that the TWR could obtain 31 temperature measurements averaged over a 33 mm circular diameter across IREQ's scale model's rotor pole while rotating at 300 rpm to within one degree Celsius, once the calibration was applied to the data.

Upon completion of the benchmark experiment, Torriano *et al.* (2014) used the TWR as part of the second phase to obtain the temperature distribution on the surface of the scale model's heated pole, while under rotation and cooled by forced air convection. This was achieved by acquiring the temperature along the surface of the pole using the TWR and by tracking all the heat lost within the interior portion of the shell. Ultimately, the authors obtained the surface temperature on a heated pole at 26 different axial lines along the pole's height. These measurements provided the insight that the rotor poles are not uniformly cooled in either the axial or circumferential

directions, and demonstrated the presence of large hot spots. The authors claimed that the circumferential temperature imbalance was a result of both detached and recirculating flow along the surface of the pole, which resulted in a local temperature increase. Furthermore, the authors also claimed that the extra flow from the fan blades at the upper and lower regions of the rotor pole created an axial temperature imbalance, with lower temperatures located in these regions. Moreover, the lower portion of the pole was warmer than the upper portion due an asymmetry in the spider arms of the scale model.

To obtain the heat transfer coefficient on the surface of the heated pole using their experimental data, Torriano *et al.* (2014) developed a hybrid model (experimental-numerical) of the heated pole. Their model indicated that the convective heat transfer coefficient is approximately 25% higher near the center of the heated pole when compared to the upper/lower regions. The authors found this result to be surprising because of the presence of the fan blades near the upper/lower region, but concluded that flow generated by the fan blades predominately enters the interpole and is pushed outwards towards the air-gap and wraps around the center of the pole. Their model also portrayed the importance of the rotational effects on the convective cooling of the heated pole. The convective heat transfer coefficient was on average 10% higher on the the leading edge of the pole when compared to its trailing edge. Although, the simplified model provided insight on the convective cooling of the scale model's heated pole, the approach could not be extrapolated to in-service hydroelectric generators due to the lack of experimental data therein. However, the study identified where temperature sensors should be installed in the rotor poles of hydroelectric generators, which Hudon *et al.* (2016) later utilized to install fiber Bragg gratings in an in-service machine to demonstrate that the hot-spots can

be 24°C higher than the average temperature deduce from the measured from the field winding voltage and current.

Due to the limitations of the numerical model presented by Torriano *et al.* (2014), the authors recommended developing a numerical model employing a CHT approach for the scale model. The approach could then be validated using the experimental results presented in their study.

1.3.4 PIV Measurements in IREQ's scale model

Since the development of IREQ's scale model in 2011, the only experimental study using PIV was performed by Bach *et al.* (2015). This study, along with the study by Hartono *et al.* (2012*b*,*a*), are the only studies using PIV to quantify the flow in the ventilation circuit of a scale model of a hydroelectric generator. However, the scale models used in the two sets of experiments performed by Hartono *et al.* (2012*b*,*a*) and Bach *et al.* (2015) were different in many ways (axially vs. radially-cooled; and small (12.5 cm x 35.6 cm) versus large (1 m x 2 m), respectively; *etc.*). Ultimately, Bach *et al.* (2015) qualitatively and quantitatively described the flow in different regions within the scale model with spatial resolutions in the order of millimeters, while the scale model has dimensions in the order of meters. The authors provided insight on the performance of the ventilation circuit within the scale model by studying the flow in the following five regions: the pit opening, the region between the radiator exit and the enclosure, the radiator exit, the covers, and the interpole region.

One of the main flow passages of the scale model's ventilation circuit are the pit openings. The scale model has four pit openings, which are responsible for bringing large volumes of air to the bottom portion of the rotor. Therefore, due to the importance of flow in these regions, Bach *et al.* (2015) utilized PIV to obtain the mass flow rate passing through one of the pit openings.

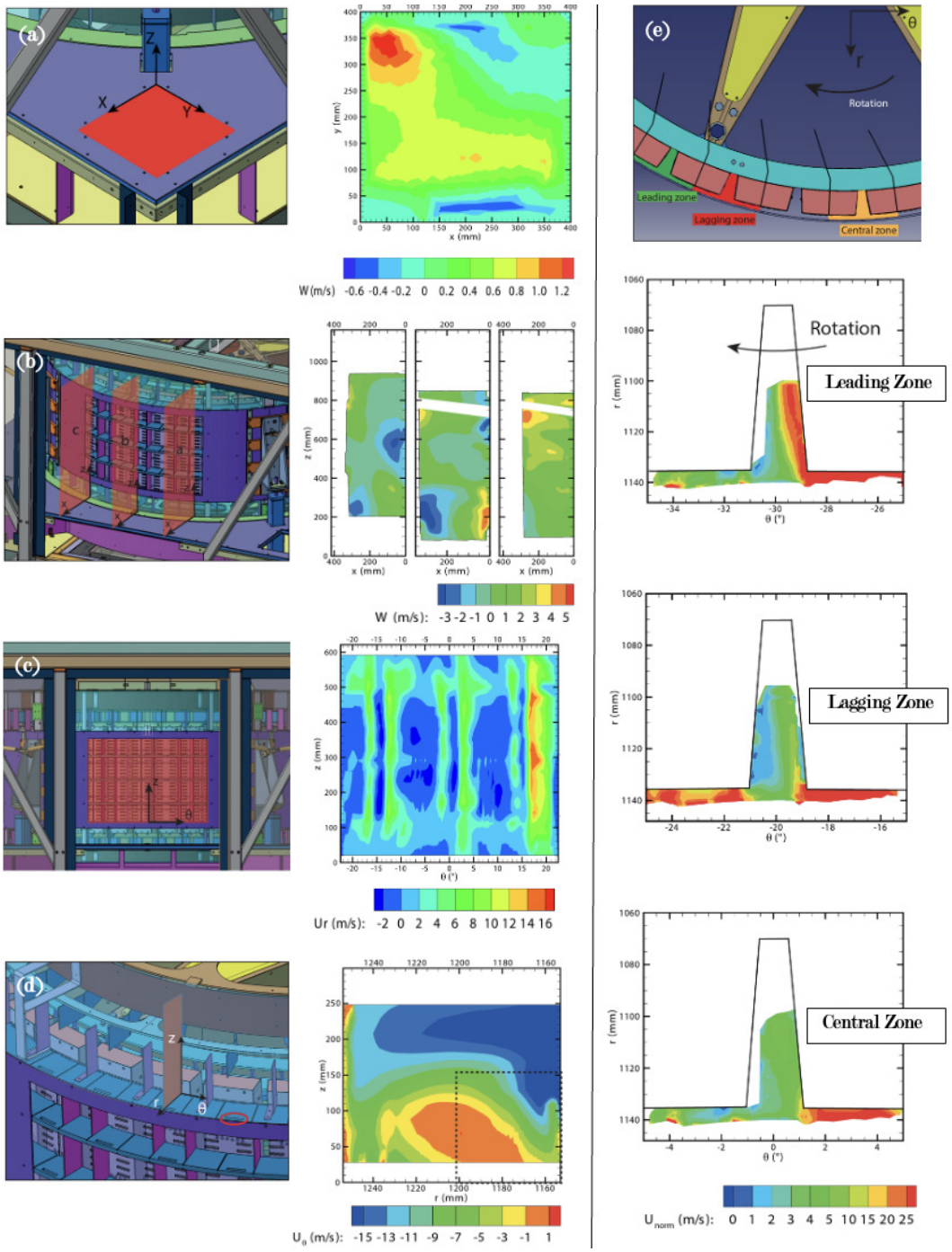

Figure 1.6: PIV measurements of Bach *et al.* (2015) made in the following key regions within the ventilation circuit of the scale model: (a) the pit opening, (b) the region between the radiator exit and the enclosure, (c) the radiator exit, (d) the covers, and (e) interpole region.

Ultimately, the authors constructed the velocity profile parallel to the pit inlet (*i.e.* in the XY plane as illustrated by the zone highlighted in red in figure 1.6(a)) using 10 XZ and YX planes to obtain the inlet velocity contour. Moreover, the authors took 2,000 frames of the flow along these planes and saw convergence of the mean velocity at 1,500 frames. The velocity contour at the pit inlet is illustrated in figure 1.6(a) and the integration of the resulting measurements resulted in an inlet mass flow rate of 0.056 kg/s. This result was particularly surprising for two reasons: i) the inflow is much lower than expected, and ii) prior numerical simulations of the scale model performed by Toussaint *et al.* (2011) indicated an inflow that was five times greater than the value obtained by PIV. The authors concluded that the discrepancies between the experimental and numerical results may be due to a modification made at the outlet of the pit opening in the numerical geometry. Moreover, in the actual model, a 3 cm radius of curvature is present at the outlet of the pit opening, which is a detail that was omitted in the numerical geometry to simplify the meshing process. Furthermore, the authors conducted some qualitative flow visualizations using smoke in this region and noticed that a large portion of flow swirling below the rotor is deflected by the curved outlet region back towards the inlet of the pit opening. Even with these discrepancies, it is clear that the flow in a region critical to the ventilation circuit is not behaving as designed, resulting in a decreased flow rate towards the lower portion of the rotor. The authors indicated that the geometry used for numerical simulations could be altered to determine if this phenomenon is also observed numerically. Furthermore, this region could be altered altogether to improve the ventilation circuit of the scale model.

An additional region of interest in the ventilation circuit of the scale model is the region between the radiator exit and the enclosure. Its characterization

provided insight on the directional tendencies of the flow once it exits the radiator opening. To determine the former, Bach *et al.* (2015) considered the flow in three XZ planes as illustrated in figure 1.6(b). To obtain the average flow along these planes and to remove the influence of the passage of the spider arms, 100 images at 20 different locations relative to the spider arms for a total of 2,000 images were taken. The velocity contours along the three planes are shown in figure 1.6(b) and indicate an upward and downward motion split above and below the midplane, respectively, corresponding to the expected ventilation behavior. Furthermore, the velocities in the middle (b) plane were found to be more prominent due to the circumferential component of the flow, which is better explained when analyzing other regions of the flow within the scale model. Due to limited optical access, the authors only made qualitative comparisons with the results of the numerical simulations of Toussaint *et al.* (2011), but the comparisons were promising.

Another region of interest was the radiator exit, as it is: i) the location within the ventilation circuit where the flow from the upper and lower regions meet, and ii) where the flow is measured in in-service hydroelectric generators to provide estimates for the total air flow rate. Therefore, due to the importance of flow in this region, Bach *et al.* (2015) utilized PIV to obtain the mass flow rate passing through the radiator. Ultimately, the authors constructed the velocity profile parallel to the radiator exit (*i.e.* in the $R\theta$ plane as illustrated by the zone highlighted in red in figure 1.6(c)) using 20 planes over a distance of 570 mm in increments along the z-axis of 30 mm. Using the same averaging technique as before, 60 $R\theta$ planes were used to construct the velocity contour shown in figure 1.6(c). The results indicate that a larger portion of the flow exits the upstream location due to the rotation of the rotor and flow impingement along the vertical plates at the radiator exit. Moreover,

there are larger portions of flow in the upper and lower axial regions due to the flow coming from the covers in these regions. Integrating the velocity contour resulted in a mass flow rate of 1.40 kg/s, which matched the results of the numerical simulations of Toussaint *et al.* (2011) to within ±2%.

The flow within the covers of hydroelectric generators are of particular interest as they house the end windings, which are a key component of the stationary magnetic circuit that is often susceptible to overheating. Although the scale model end windings are simply represented by vertical plates, the flow passing in the region surrounding them, and encapsulated by the covers, are still of interest due to its influence on the end winding temperature. Therefore, in an effort to obtain the mass flow rate in this region, Bach *et al.* (2015) carried out 11 different PIV measurements along 12 $R\theta$ planes, in steps of 20 mm using the same averaging technique as before to construct the velocity contour. The result of this exercise is illustrated in figure 1.6(d) and the integration of the measurements resulted in an average mass flow rate of 0.227 kg/s, which was within 15% of the numerical simulation of Toussaint *et al.* (2011), which was deemed acceptable by the authors.

The final of the five PIV measurements performed was the only one taken in the rotating frame. This measurement was performed in the interpole region because the flow in this region is directly responsible for cooling the rotor poles, which is the major rotating component of the magnetic circuit that is susceptible to overheating. Thus, to quantify the flow in this region, Bach *et al.* (2015) performed PIV measurements along 12 $R\theta$ planes along different axial position along the height of the rotor. Due to the limited optical access, axial positioning of the PIV measurements were confined to the locations of the stator duct openings. Moreover, the angular positions of the measurements were chosen relative to the spider arms in three different zones: leading, lagging

and central zones, as illustrated in figure 1.6(e). The authors were only able to make a qualitative assessment of the flow within these regions due to the limited optical access. Their conclusions were the following: i) the air flow generated by the upper and lower fan blades penetrates axially inwards to the center of the rotor poles, but over an unknown distance, ii) a vortex is present at the end of each interpole, which convects the flow exiting the rotor rim ducts towards the lagging side of the pole, and iii) recirculating zones that are present within the interpole are closer to the pole trailing edge in the leading and lagging zones, whereas the recirculating zone is closer to the pole leading edge in the central zone. Furthermore, when comparing their results to the numerical simulations, the authors found that the latter is closely associated with the flow entering the rotor rim ducts at a large tangential angle, which is not an ideal ventilation design. However, the effect these flow phenomena have on the overall air flow distribution through the rotor rim requires further investigation.

To date, this was the last study at IREQ that provided experimental measurements with which the numerical simulations of Toussaint *et al.* (2011) could be compared.

1.3.5 Fluid Flow Sensors for Hydroelectric Generators

During the development of IREQ's scale model (Bourdreault *et al.*, 2011) researchers at IREQ were also developing fluid flow sensors for in-service hydroelectric generators. Although access to in-service hydroelectric generators is limited, instrumentation campaigns to gain valuable data can occur. However, very few sensors were developed for hydroelectric generators, let alone fluid flow sensors for the ventilation circuit of such machines.

To acquire much needed ventilation data for in-service hydroelectric generators, Hudon *et al.* (2010) began the development of a sensor that could

measure the air flow distribution at the exit of the stator cooling ducts. This goal was achieved with the development of a Venturi-type flow meter called the "converging cone." Using this device, the axial flow distribution exiting the stator of an in-service hydroelectric generator could be obtained. Since its development, the device has been used in many hydroelectric generators throughout the province of Québec and Europe.

Building on the success of direct measurements in the stator, an attempt to develop an anemometer to measure the flow rate in the rotor rim ducts was undertaken by Saleban *et al.* (2013), in a collaboration between IREQ and the *École Polytechnique Fédérale de Lausanne* (EPFL). Ultimately, Saleban *et al.* (2013) developed a mini-turbine flow meter that could convert the turbine's rotational speed (induced by the flowing fluid) into a velocity, by measuring the voltage generated by a DC motor attached to the turbine shaft. This method, however, did not meet expectations as the device could not sustain the centrifugal forces in IREQ's rotating scale model. Although this project did not achieve all of its objectives, the challenges involved in developing an anemometer for the rotor rim ducts were better understood.

In 2015, a new project was launched by Venne *et al.* (2018) to develop a flow sensor that would overcome the obstacles encountered by Saleban *et al.* (2013). The authors designed a thermal mass flow meter (TMFM) capable of measuring the flow rate in the rotor rim ducts of a hydroelectric generator. The prototype developed was capable of measuring the flow in static short rectangular ducts with an accuracy around $\pm 10\%$. In unison with Venne *et al.* (2018), Kirouac (2017) developed a data acquisition (DAQ) unit for the TMFM to undertake measurements in either the rotating scale model or in an in-service hydroelectric generator. After the conclusion of both studies, the authors determined that further work was required to test both systems in the

scale model. In 2018, the authors successfully tested both systems in IREQ's scale model (unpublished work). Furthermore, an effort was made to improve the design process of the prototype, by developing a numerical model to determine the optimal placement of the outlet temperature sensors, which would circumvent the numerous experimental measurements required to do so. The results of the numerical model used to streamline the design were unpublished. However, it was clear that prototype required further development to enable its widespread use within Hydro-Québec's in-service hydroelectric generators.

1.4 Objectives of the Research

The literature review demonstrates a need for further research on radially-cooled hydroelectric generators, as most of the previous research in the field had focused on axially-cooled ones. To fill this void, five objectives were proposed for the research presented herein: i) to make improvements to the design of the TMFM developed by Venne *et al.* (2018) to enable its deployment as a standardized tool for Hydro-Québec in the assessment of the ventilation circuit of in-service hydroelectric generators, by allowing the collection of previously unavailable ventilation data, ii) to make flow measurements in the rotating components of a scale model of a hydroelectric generator, iii) to develop a meshing strategies to enable more efficient numerical simulations of hydroelectric generators, iv) modeling of hot-spots using conjugate heat transfer simulations, and v) providing some recommendations for improving the cooling efficiency of hydroelectric generators using a model based design (MBD) approach – a technique that uses experimentally-validated numerical models to perform simulations with the aim of improving the design of a system.

Firstly, a new TMFM design, which improved upon many aspects of the previous design proposed by Venne *et al.* (2018), was achieved. The implemented improvements stemmed from the experiences gained developing, manufacturing, and utilizing the previous design. Ultimately, the improved design has fewer parts, takes advantage of modular parts/materials, and utilizes innovative manufacturing techniques, all of which, lead to a more usable and refined product. To achieve the latter, several tasks were required including: material characterization tests, CHT simulations, a printed circuit board redesign, and mechanical simulations. The information obtained from these tasks was implemented within the new design and then validated in a laboratory environment.

Secondly, increasing our understanding of the flows within the rotating components of hydroelectric generators was feasible because of the availability of IREQ's scale model, which allowed for the installation of the newly designed TMFM within the rotor rim ducts. This allowed for the confirmation of the aforementioned non-uniform flow distribution exiting the rotor observed earlier in the CFD simulations of Toussaint *et al.* (2011).

Thirdly, although a functioning numerical model of a hydroelectric generator had already been developed by IREQ before this research, there still existed a need to improve the modeling process because the computational grid (or mesh) was generated using a manual meshing software called *ANSYS ICEM CFD*, which required over 128 working hours to complete. Given that IREQ could not quickly mesh a given hydroelectric generator using this approach, it had invested in new automatic structured meshing tools by *Numeca* (*HEXPRESS* and *HEXPRESS/Hybrid*) to develop a new approach in this work, that would accelerate the meshing (and therefore modeling) process without compromising on the quality of the simulation results.

Fourthly, a numerical model employing CHT of a 90° section of IREQ's scale model that is capable of accurately predicting the location of hot-spots was developed in this work. However, such a model required a large amount of computational resources. The complete CHT analysis for the scale model required approximately 200M volume elements; 120M in the fluid domain and 80M in the solid domain. Ultimately, numerical simulations of such complexity and detail required over 512 processing cores per simulations; a feat that was only achievable using CASIR – IREQ's high performance computing (HPC) cluster.

Lastly, once the numerical model proposed in this work was capable of predicting the measured temperature distribution on a heated pole in IREQ's scale model (Torriano *et al.*, 2014), modifications were proposed using a MBD approach to improve the ventilation efficiency/cooling of IREQ's scale model. The proposed modifications to the ventilation circuit can then be implemented and validated experimentally using IREQ's scale model, prior to their on-site application.

1.5 Thesis Structure

The remainder of the thesis is organized into five chapters: i) Experimental Facilities, Instrumentation, and Techniques (Chapter 2), ii) Numerical Models (Chapter 3), iii) Thermal Mass Flow Meter: Measurements and Innovations (Chapter 4), iv) Results (Chapter 5), and v) Conclusions and Future Work (Chapter 6). The second chapter provides an overview of the experimental facilities utilized at Hydro-Québec and the associated instrumentation and techniques employed within those facilities to obtain the valuable diagnostic data for the rotor of hydroelectric generators. The third chapter discusses the mathematical models, modeling strategy, and the meshing strategy employed in the numerical simulation of IREQ's scale model of a hydroelectric generator.

The fourth chapter exposes the shortcomings of the initial TMFM prototype, details the development of an improved design, and demonstrates the validation approach used to evaluate the performance of the newly designed TMFM used to measure the air flow passing through the rotor rim ducts of a hydroelectric generator. The fifth chapter delineates the main results of both the experimental and computational investigations. The final chapter outlines the main contributions of the present research and proposes recommendations for future work.

CHAPTER 2
Experimental Facilities, Instrumentation, and Techniques

This chapter provides detailed descriptions of the experimental facilities, instrumentation, and techniques that were used in this work. This chapter is divided into two main sections: experimental facilities; and the instrumentation. The former section is subdivided into three subsections describing: i) hydroelectric generators, ii) the scale model, and iii) the static model. The latter is subdivided into the two subsections, thermal mass flow meters, and particle image velocimetry.

2.1 Experimental Facilities

One of the main objectives of the DIAAA project (discussed in Section 1.1) is to collect data on in-service hydroelectric generators as part of the longevity assessment phase. As mentioned in section 1.1, validating and developing emerging tools for the diagnosis of hydroelectric generators is necessary to obtain the data required for the evaluation of the overall health of such machines. However, the validation and development processes often require detailed and time consuming testing. Such tests cannot be readily performed on in-service machines because they require shutdowns that cause significant disruption of normal operations and monetary losses for the company. Only when the emerging tools are sufficiently mature, can they be installed on in-service hydroelectric generators to collect the necessary data during shutdowns associated with regularly scheduled maintenance. Thus, the strategy illustrated in figure 2.1 was adopted and used by IREQ. The scale model shown is figure 2.1 was designed and built by IREQ is a scaled-down version of a hydroelectric generator in the Beauharnois hydropower plant. Although use of the scale

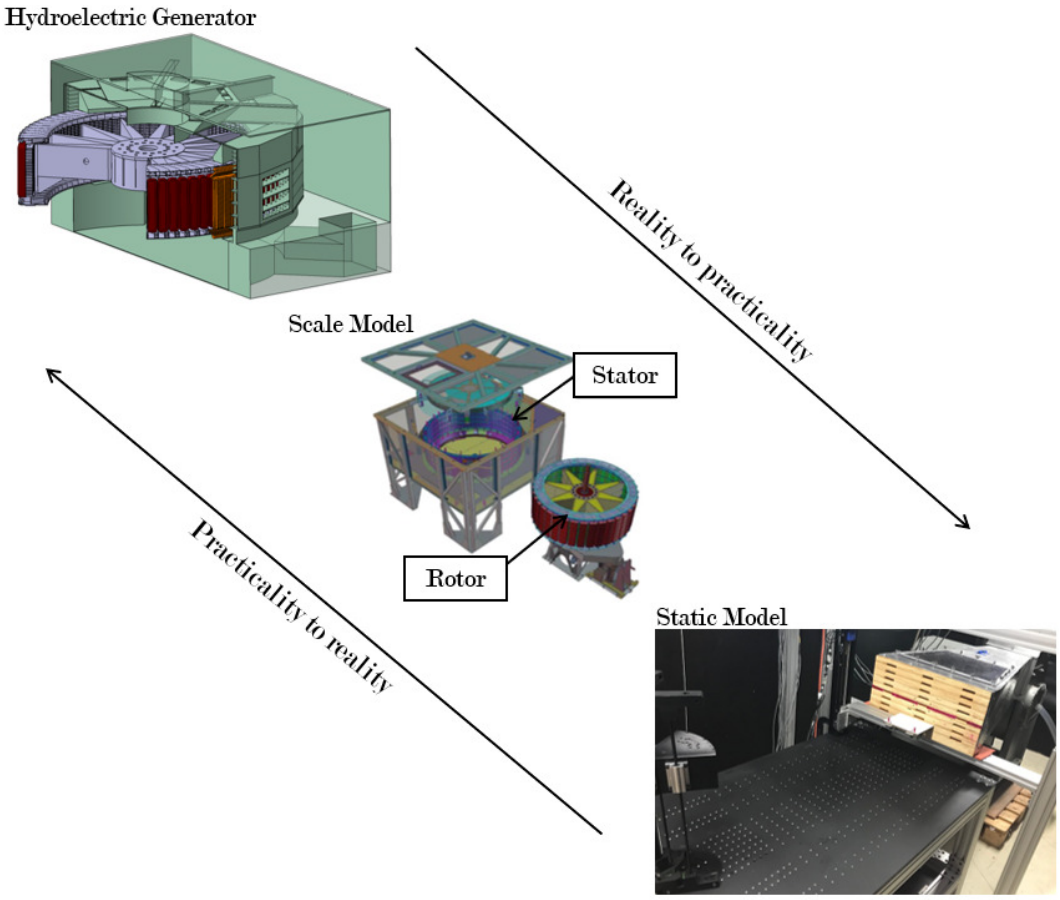

Figure 2.1: Illustration of the experimental methodology used to develop emerging diagnostics technology and acquire the necessary data to evaluate the overall health of a hydroelectric generator.

model avoids shutdowns and provides the necessary access for testing, it still has some challenging aspects. For example, experimental measurements in rotating machinery are rather complex and may slow down the overall design process. To resolve these issues, a static model of the rotor rim of the scale model was also designed and built by IREQ.

2.1.1 Hydroelectric Generators

The focal points of a hydropower plant are the generating units, for which one example is illustrated in figure 2.2. A generating unit is comprised of a hydroelectric generator and turbine assembly. At the heart of the latter is a turbine comprised of a runner and a set of runner blades that extract the kinetic energy of flowing water, which is directed towards the blades via the spiral case and guide vanes. The hydroelectric generator, which is connected to the turbine by a shaft, then transforms this kinetic energy into electrical energy. Generating units typically have a high operating efficiency (approaching 98%), but the small fraction of kinetic energy not converted to electrical energy is lost as heat. Given the large amounts of total kinetic energy involved, the heat lost can amount to 2-3 MW which can result in a significant temperature rise of the machine. Moreover, this rise can create hot spots in the machine resulting in the degradation of the insulation, which can lead to mechanical or electrical failures. Thus, the operating temperature of the machinery needs to be well controlled to increase its longevity.

Most hydroelectric generators cool themselves by drawing in air (like a fan) and pushing it through the rotor and stator (shown in figure 2.3). The air passes through the rotor via small rectangular openings called rotor rim ducts. The flow passing through these ducts cools the poles on the outer rim of the rotor and the stator. Thus, the rotor acts as a fan, and an optimal equilibrium is required between the air flow rate needed to efficiently cool the equipment

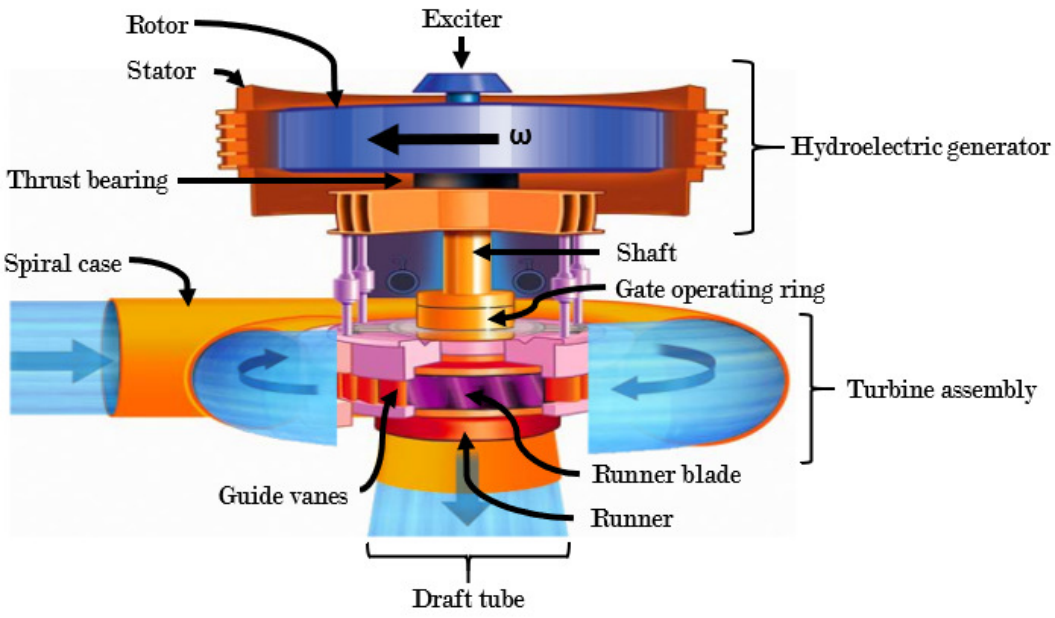

Figure 2.2: A generating unit highlighting its main components: the hydroelectric generator rotating at a rotational speed (Ω) to supply a 60-Hz alternating current in North America along with the turbine assembly. From Hydro-Québec (2020).

and the associated windage losses. ("Windage losses" is a term typically used in electric machines that refers to the resistance experienced by the rotating shaft resulting from forces required for the air to pass through the machine.) Between 20% and 30% of the total energy lost in a hydroelectric generator is attributed to windage losses. Therefore, cooling is an important factor to consider when aiming to improve both the efficiency and the longevity of a generating unit.

The pattern of the air flow within a hydroelectric generator is depicted in figure 2.3. As the rotor (1-5) spins, the rotor spider arms (1) act like a fan drawing in the flow through the rotor rim (2) and the fan blades (3). The flow can pass through the rotor via the rotor rim ducts, which allow the flow to cool the poles (5) on the outer rim. The portion of the flow that passes through the fan blades is primarily directed toward the end windings (7) and covers (8), but a portion of it is also deflected in the air gap. Once the flow passes the rotor, it goes through the stator (6), and exits through the water-cooled radiators (9). Finally, the air returns to the rotor through the ceiling and pit openings (10). The geometry is not only complex and characterized by a broad range of length scales, but it also involves both stationary and rotating parts making the flow exceptionally difficult to model numerically. Thus, experimental measurements are necessary to increase our understanding of the air flow in hydroelectric generators, to improve the cooling efficiency of this machinery and validate numerical simulations of such phenomena. However, as mentioned earlier, measurements on operational hydroelectric generators are rare as shutdowns for the required tests are disruptive and the related costs are overly high. For these reasons, IREQ designed and built a scale model of a hydroelectric generator.

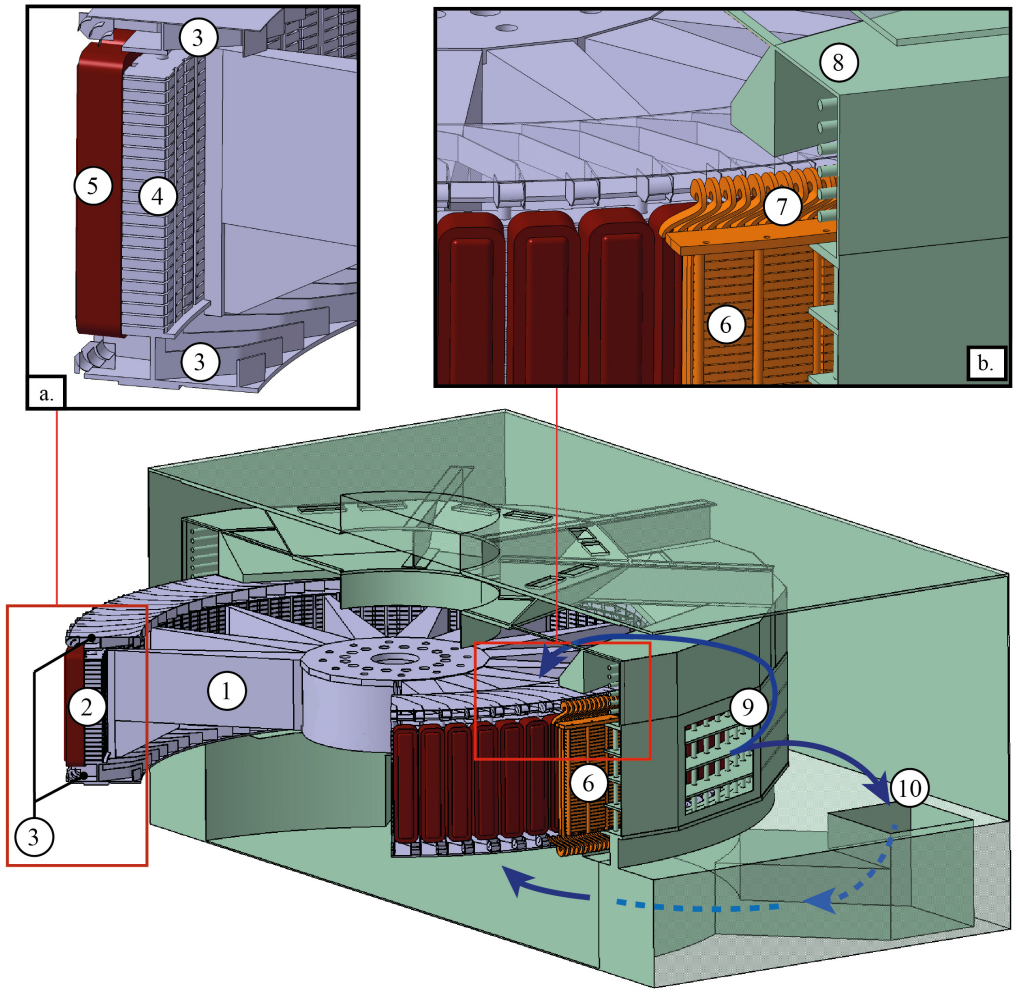

Figure 2.3: Schematic of a radially-cooled hydroelectric generator illustrating the main rotating (1-5) and stationary (6-10) components, and the air flow in it.

2.1.2 The Scale Model

Laboratory models are. commonly used to study the flow physics in real-life equipment using the principles of dimensionless similarity. This approach is particularly useful when the real-life equipment is too large/expensive to study in detail, and a smaller/less-expensive model is more practical. The measurements obtained on the model can then be scaled up to estimate the performance of the actual system. This strategy was adopted in the design and construction of IREQ's scale model of a hydroelectric generator, which was a two-year collaboration with its robotic division (Bourdreault *et al.*, 2011).

As illustrated in table 2.1, dimensionless similarity in the scale model can be maintained by adjusting the rotational speed to compensate for the reduction in size in the radial direction. One of most relevant dimensionless parameters to maintain similarity between the hydroelectric generator (HEG) and the scale model (SCM) is the air gap Reynolds number (Re_δ), which is defined as (Hudon *et al.*, 2011):

$$Re_\delta = \left[\frac{\rho(\Omega_{HEG} r_{HEG})\delta}{\mu}\right]_{HEG} = \left[\frac{\rho(\Omega_{SCM} r_{SCM})\delta}{\mu}\right]_{SCM}, \qquad (2.1)$$

which is a function of the rotational speed of the rotor (Ω), the rotor radius (r), the air gap (*i.e.* the distance between the rotor and stator, δ), and the properties of the working fluid (*i.e* the dynamic viscosity, μ, and density, ρ).

The dimensions of the critical components of the scale model and their counterparts in an in-service hydroelectric generator are given in table 2.1. The rotor is scaled down by a factor of 4 in the radial direction and by a factor of 2 in the axial direction when compared to the in-service machine. Smaller scaling was applied in the axial direction to facilitate access to its interior for maintenance and instrumentation purposes. Several dimensions were not scaled, including the cooling ducts in the rotor rim and stator, and the air

gap. This was done for two reasons: i) to allow for direct modeling of the air flow within these regions, and ii) to facilitate the transfer of developed emerging diagnostics technology to in-service hydroelectric generators. Assuming that the temperatures of the working fluid are approximately the same in the laboratory as they are in an in-service hydroelectric generator, the dynamic similarity simplifies to:

$$\left[\frac{\Omega_{SCM}}{\Omega_{HEG}}\right] = \left[\frac{r_{HEG}}{r_{SCM}}\right] = 4. \tag{2.2}$$

Therefore, to maintain the same tangential velocity at the rotor tip, the speed of the scale model must be 379 rpm, because the hydroelectric generator on which it is modeled rotates at 94.7 rpm. Thus, by maintaining this rotational speed, it can be assumed that the air flow within the rotor rim and stator ducts are of the same order of magnitude as the air flow in an in-service hydroelectric generator, because as detailed in table 2.1, the dimensions of the ducts are almost identical and the local Re_δ is conserved at these locations.

Although, dimensionless similarity was used to guide the design, its strict application was not the priority, because the principle interest was not to scale up experimental measurements to an in-service hydroelectric generator, but rather to develop numerical models of such machines and obtain data for the validation of such models with ease-of-access to perform the experimental studies. Given that the primary interest was the fluid dynamics and convective heat transfer, some components of an in-service hydroelectric generators were either omitted from the scale model (e.g. electromagnetic components) or dramatically simplified (e.g. the stator core), as they had a minimal impact on the physics of the air flow. Furthermore, the materials of the scale model differ from an in-service hydroelectric generator, as transparent materials such as polycarbonate were favored to give optical access for PIV measurements. From

Table 2.1: Hydroelectric generator (HEG) and scale model (SCM) dimensions.

Part	**Component Dimension**	**HEG** $[mm]$	**SCM** $[mm]$
Rotor	Diameter/Height	9081/1604	2270/802
	Duct Height/Width	12.2/50.8	12.7/47.7
	Air Gap (δ)	12.7	12.7
Stator	Thickness	282	4.76
	Duct Height/Width	6.0/48.7	6.0/42.5

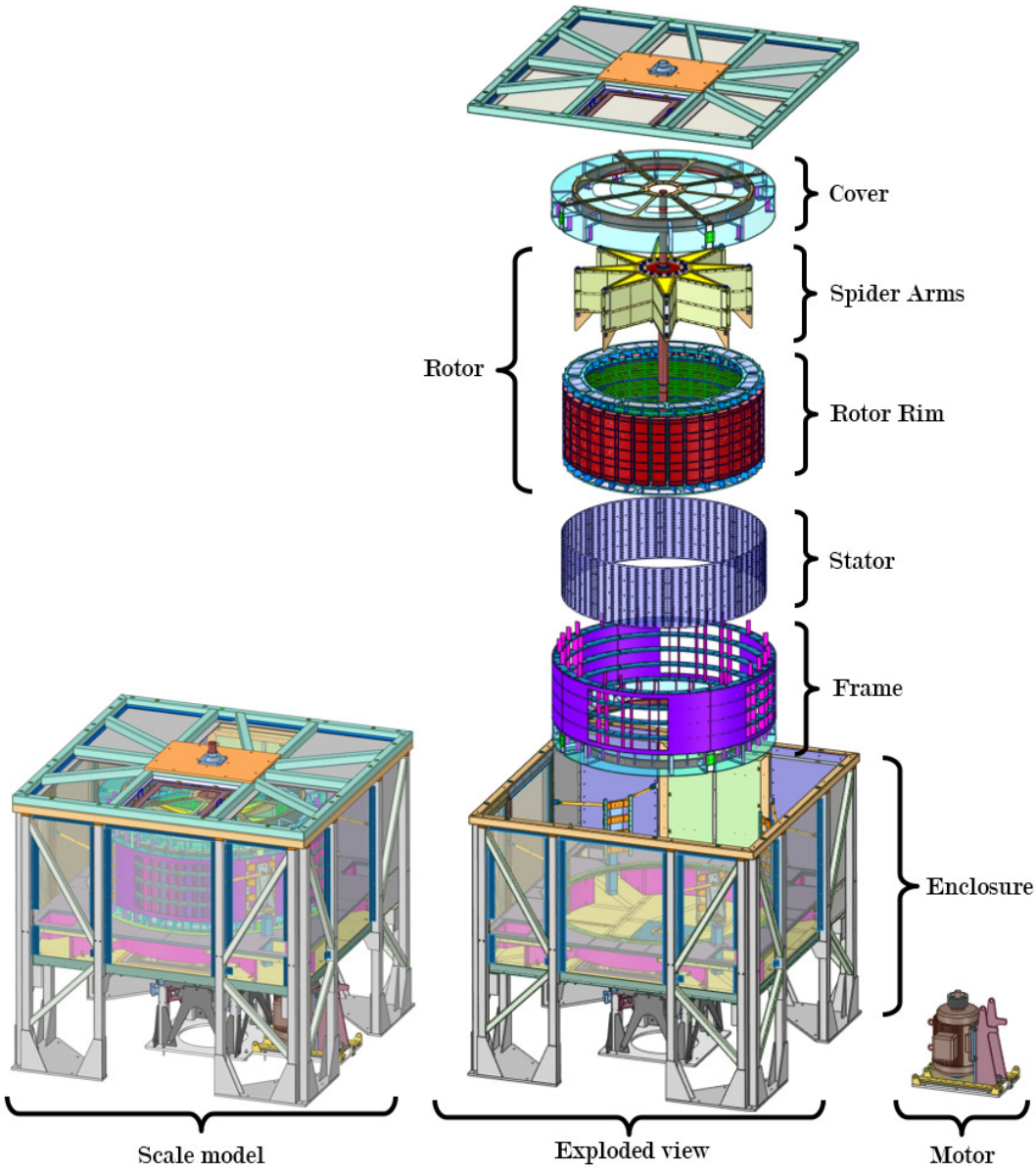

Figure 2.4: Overview of the scale model and its main components.

a numerical modeling point-of-view, some of the most challenging aspects to model, namely, the overall complexity of the geometry, were maintained (*e.g.* large differences of length scales: small channels, thin gaps, large diameter; stationary and rotating components, *etc.*).

The final configuration of the scale model illustrated in figure 2.4 has following seven major components: i) rotor, ii) stator, iii) frame, iv) enclosure, v) security shelter, vi) electric motor, and vii) heated pole. Each component has several sub-components that play a major role in the overall air flow within the scale model.

The Scale Model Rotor

As illustrated in figure 2.5 and table 2.2, the key features of the rotor of the scale model are similar to those in the in-service hydroelectric generator on which it is based (Beauharnois-35) and has four main components: i) spider arms, ii) fan blades (upper/lower), iii) rotor rim ducts, and iv) poles, of which there are fewer than these in an in-service machine. Furthermore, the scale model mimics the main ventilation features (*e.g.* an open rotor and radially-positioned spider arms) that are common to radially-cooled hydroelectric generators. From an aerodynamics point-of-view, the rotor resembles a dual inlet centrifugal fan having two different mechanisms to move air radially: i) upper/lower fan blades resembling a dual-inlet forward curved (DIFC) fan, and ii) spider arms resembling a large dual inlet radial fan. Approximately 87% of the fan outlet is restricted by the rotor rim, which is perforated by 828 rectangular ducts called rotor rim ducts. Under clock-wise rotation (when viewed from the top), the rotor draws the air axially-inwards from both inlets (*i.e.* bottom and top openings) into the intra-spider-arm region and pushes it radially outwards, either through the rotor rim, via the rotor rim ducts (see figure 2.5), or through the fan blades at the outer axial edges of the rotor. The

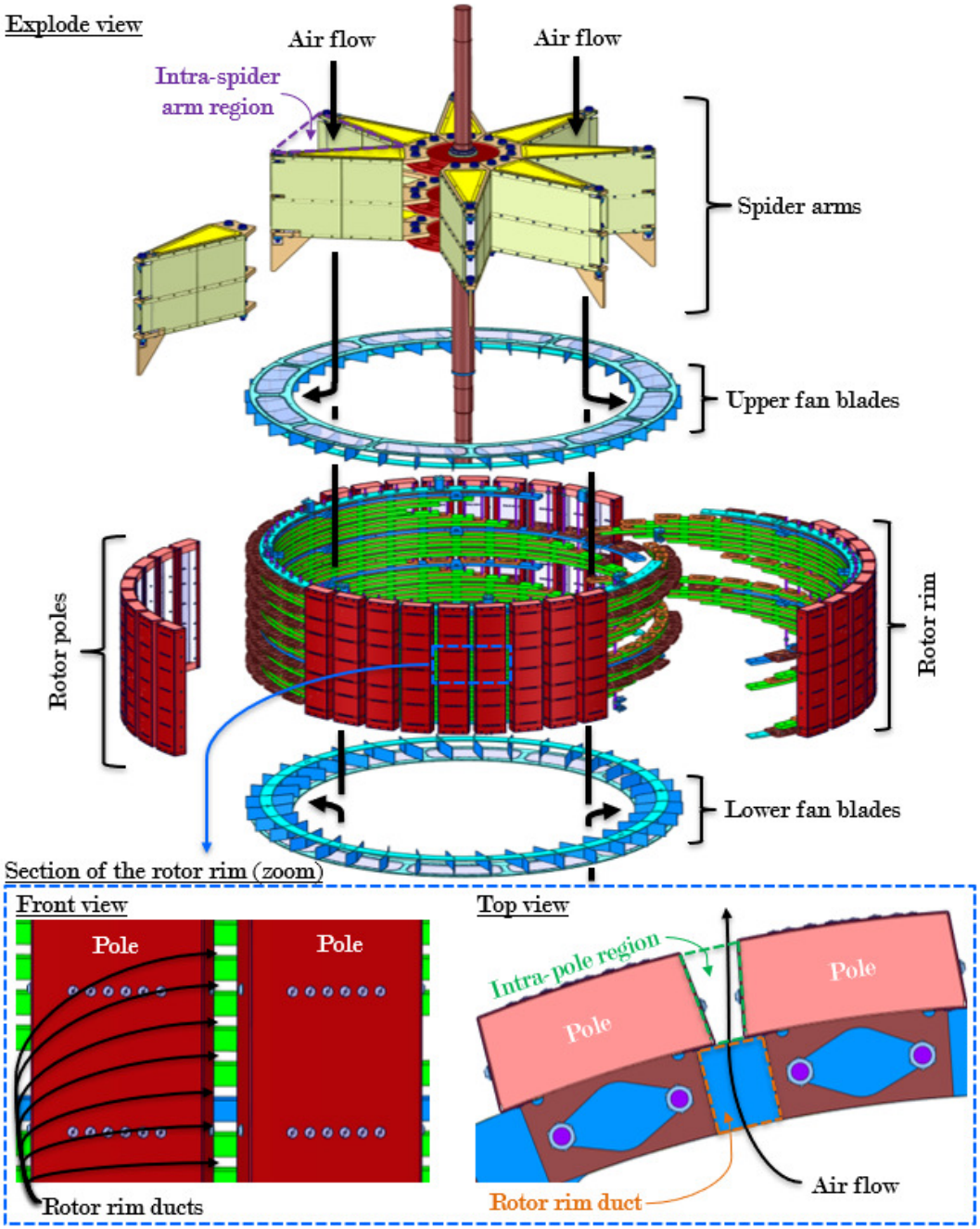

Figure 2.5: Overview of the scale model rotor and its main components.

Table 2.2: Main components of the scale model rotor

Component	**Quantity** [#]	**Circumferential Periodicity** [°]
Spider arms	8	45
Fan blades	36 (θ) by 2 (Z)	10
Rotor rim ducts	36 (θ) by 23 (Z)	10
Poles	36	10

air passing through the rotor rim ducts then passes through the intra-pole region to cool the poles at the outer radial edges.

The Scale Model Stator

The portion of the air leaving the rotor travels through a thin (12.7 mm) air gap and then through the stator via another array of rectangular ducts called the stator ducts. As illustrated in table 2.3 and figure 2.6, the stator is the most simplified component of the scale model as it only consists of an array of polycarbonate sheets with a thickness of 4.76 mm with 2,088 rectangular openings that represent the stator ducts, whereas the in-service hydroelectric generator upon which it is based has a steel stator with a thickness of 282 mm. This simplification was made to allow for the optical access required to perform PIV measurements in and around the rotor.

The Scale Model Frame

The air passing through the fan blades and stator goes into the scale model's frame. The air then passes through the frame's five major components: i) covers, ii) end winding plates, iii) flow deflectors, iv) radiator openings, and v) ceiling openings, which are illustrated in figure 2.7. The air passing through the fan blades goes directly into the covers. Typically, radially-cooled hydroelectric generators require the fan blades to direct sufficient air flow to the end windings. However, since the scale model lacks electromagnetic components, vertical plates (called winding plates) are placed in the polycarbonate covers to emulate the end windings and typical air flow in the covers. The second portion of the air that passes through the stator ducts is directed towards the radiator openings. In-service hydroelectric generators typically place radiators in these locations, which take advantage of the cold water from the river beneath the generator to cool the air convecting through the machine by passing it through its coils. However, the radiator was omitted to simplify the scale

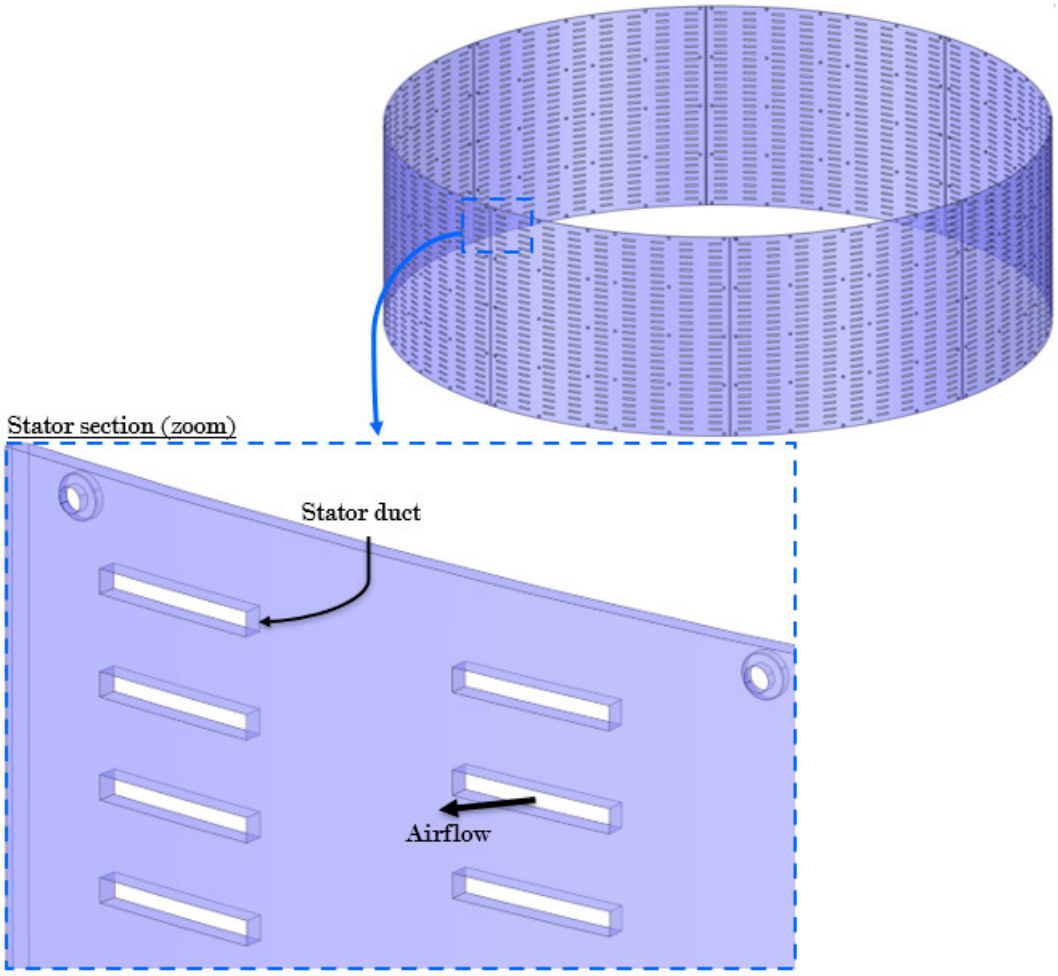

Figure 2.6: Overview of the scale model stator and its main components.

Table 2.3: Main components of the scale model stator, frame and enclosure

Component	**Quantity** [#]	**Circumferential Periodicity** [°]
Stator Ducts	72 (θ) by 29 (Z)	5
End winding plates	36 (θ) by 2 (Z)	10
Radiator Openings	4	90
Flow Deflectors	4 series of 24	90
Ceiling Openings	8	45
Pit Openings	4	90

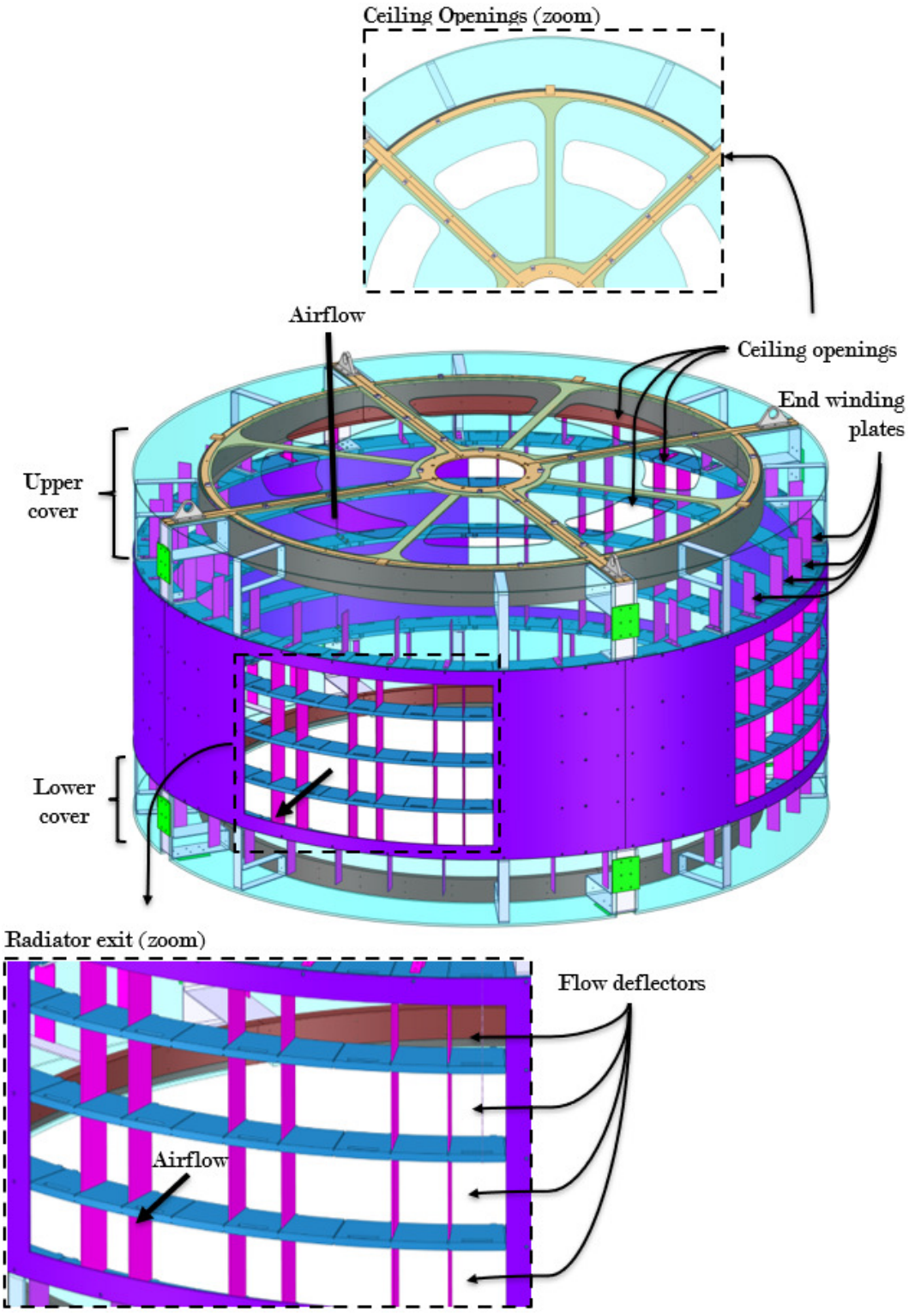

Figure 2.7: Overview of the scale model frame and its main components.

model and to directly link the temperature increase within it to the viscous dissipation in the circulating air flow. Furthermore, in-service hydroelectric generators have sufficiently long stator ducts that force the air to enter the radiators in a purely radial fashion. However, due to the thickness of the scale model rotor, a tangential component of the flow at the exit of the stator ducts exists, thus flow deflectors were placed in the radiator exit to direct the flow in a more usual fashion. Once the air passes through the radiator openings, it either goes up to the polycarbonate ceiling to restart the flow's cycle or goes down to the enclosure.

The Scale Model Enclosure

The enclosure is an artifact and serves to contain the air flow, hold the components together, and allow for optical/physical access for instrumentation purposes. The only portion of the enclosure that is authentic are the pit openings. Thus, as illustrated in figure 2.8, the recirculating air flow is contained within the enclosure and a portion of the flow radially exiting the frame's radiator openings is drawn downwards into the pit openings to be eventually redrawn into the rotor. Similarly, the air flow directed upwards to the frame's ceiling openings are redrawn into the rotor to recommence the air flow cycle shown in figure 2.8. The enclosure has three main openings that allow physical access to the scale model's main components: the upper/lower hatch and the main entrance. These entrances provide the access required for the installation of various instrumentation (thermocouples, resistance temperature detectors (RTDs), accelerometers, *etc.*) and to position the PIV camera. Prior to an incident during the summer of 2010, the enclosure was thought to be satisfactory protection of those in the vicinity of the scale model preceding start-up.

The Scale Model Security Shelter

An incident in the summer of 2010 exposed critical safety flaws with the scale model's design and demonstrated that the scale model enclosure was not sufficient protection from potentially unintended projectiles. Specifically, the initial fan blade and cover designs were made entirely of polycarbonate, to maximize optical access in this region. However, the potential thermal/structural effects that this material had to endure in a closed air circuit under rotation were neglected. This became evident during a thermal stabilization test on a hot (28°C) summer day in August of that year. The incident report found that within two hours of the test, the air temperature within the covers rose to 65°C, thus both the (stationary) covers and (rotating) fan blades experienced slight thermal expansion and made contact. The contact resulted in a piece of the fan blade detaching and piercing the covers and the outer polycarbonate sheets of the enclosure. The projectile was only stopped by a cement wall located 15 m away. Luckily, the research engineers and technicians monitoring the test were not in the path of the projectile and were able to activate the emergency stop, thus no one was harmed. The incident left the scale model inoperable and requiring modifications before its safe operation could resume.

Using mechanical simulations, Dastous & Lanteigne (2010) made three modifications to the scale model resulting in an improved and much safer design: i) the addition of metallic structural supports in the covers, ii) the addition of metallic structures in the fan blade assembly, and iii) the addition of a security shelter. The covers were solidified with the aluminum L-shaped supports shown in figure 2.7 to limit the thermal expansion. Similarly, the polycarbonate fan blades were replaced by aluminum ones and their polycarbonate support structure was reinforced by aluminum, as depicted in figure 2.5. Lastly, the security shelter, shown in figure 2.9, which surrounds the enclosure,

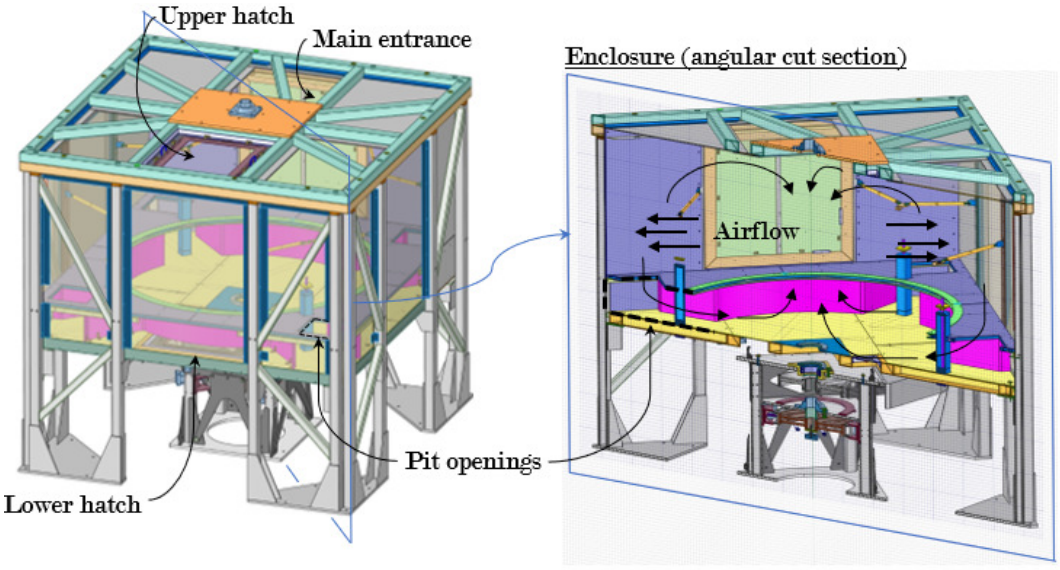

Figure 2.8: View of the scale model enclosure highlighting the main entrance, upper/lower hatch and pit opening, as well as, a cross-section of the enclosure showing the general air flow within.

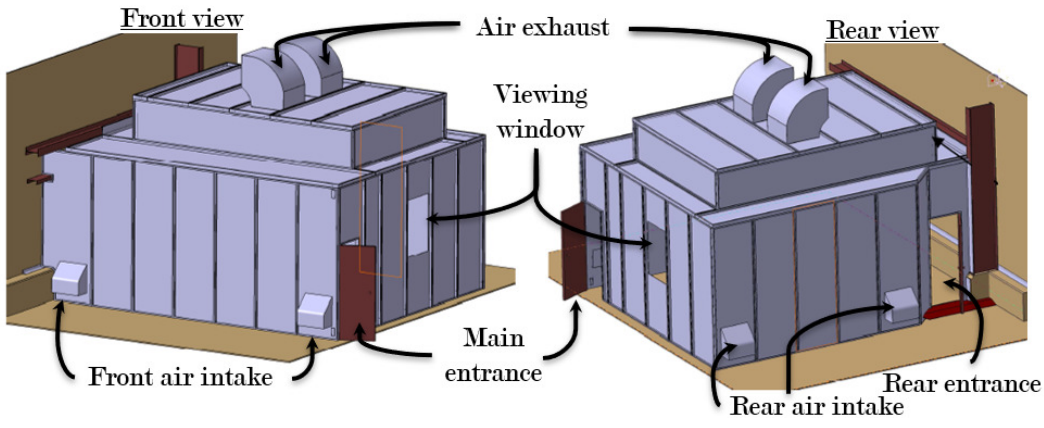

Figure 2.9: Views of the scale model security shelter highlighting the major points of interest.

was made of 4.8 mm thick structural steel capable of stopping a projectile of 60 m/s with a mass of 1 kg corresponding to the mass of the largest bolt found in the scale model. Furthermore, it was found that when the scale model is rotating at 50 rpm, the polycarbonate sheets found at the exterior of the enclosure are capable of stopping a projectile of 0.5 kg. Thus, individuals may enter the security shelter via the main and rear entrances while the scale model is rotating at rotational speed of 50 rpm or below. Furthermore, the air flow around the scale model was increased using large industrial fans, placed at the back wall of the security shelter and within the ceiling of the security shelter to decrease its operating temperature. Since the modifications and the inclusion of the security shelter, the scale model has been operating safely.

The Scale Model Electric Motor

Hydroelectric generators are typically driven by hydraulic turbines. But, for the scale model, the energy required to spin the rotor at the desired rotational speed is provided by a 7.5 kW electric motor. The rotational energy is then transmitted to the shaft of the scale model rotor, which is fixed by three (upper, mid, and lower) bearings via a belt system, as illustrated in figure 2.10. Since no torque meter was installed around the scale model shaft, the windage losses were calculated by deducing the motor, belt, and bearing losses from the motor power input.

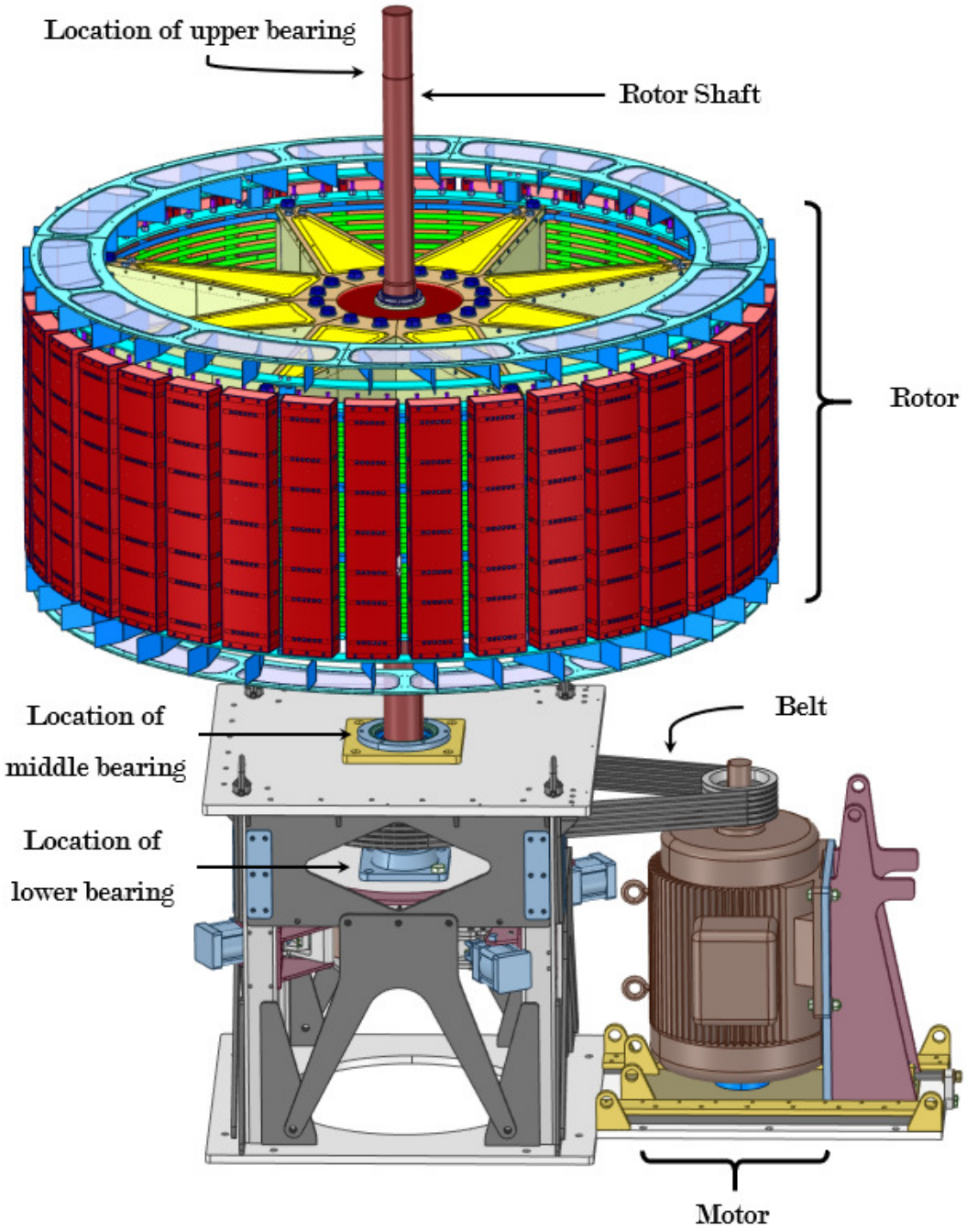

Figure 2.10: View of the motor assembly and the scale model rotor highlighting the main components (transmission belt and three bearings) that transfer the rotational mechanical energy of the electrical motor to the scale model's rotor shaft.

The Scale Model Heated Pole

The final component of interest for the present research is the heated pole, which permitted the study of the impact of the flow over and around a rotor pole of the scale model on its cooling by convection. Since all electromagnetic components were omitted from the scale mode design, a rotor pole was modified to emulate the heat generated within a pole of a hydroelectric generator arising from the Joule and electromagnetic losses. The details of the modifications are illustrated in figure 2.11, which highlight the heated pole (colored in black), the method of fixation used to link the poles to the rotor rim, and the heating pad assembly installed within the inner portion of the shell. The scale model rotor poles are made of thin (0.912 mm) 304 stainless steel shells riveted to seven aluminum supports that are wedged within the rotor rim. The empty nature of the shell allowed for the installation of heating pads or heating element matrices (HEMs) comprised of a serpentine copper resistance wire embedded within a 1.27 mm thick orange silicone matrix. Ultimately, 18 HEMs were installed, to cover all the unequally sized free surfaces (*i.e.* those not covered by the aluminum supports), and the power input to the HEMs was varied to obtain an equivalent desired heat flux, as illustrated in figure 2.12(a). Although maintaining a constant heat flux aided in the isolation of the physical interaction between the heat dissipated from the HEMs and the extraction of that heat by the air flowing over the outer surface of the shell, minimizing and tracking the heat dissipated/lost within the shell was equally important. Figure 2.11 illustrates the two methods used to minimize the heat losses, which included: i) insulating the HEMs, and ii) applying a thin silicone layer between the shell and the HEM. The insulating layer used was a 6.35 mm thick foam layer with a thermal conductivity of 0.1 W/m·K. Furthermore, a thin (1 mm) layer of silicon with a thermal conductivity of 0.88 W/m·K (illustrated in the

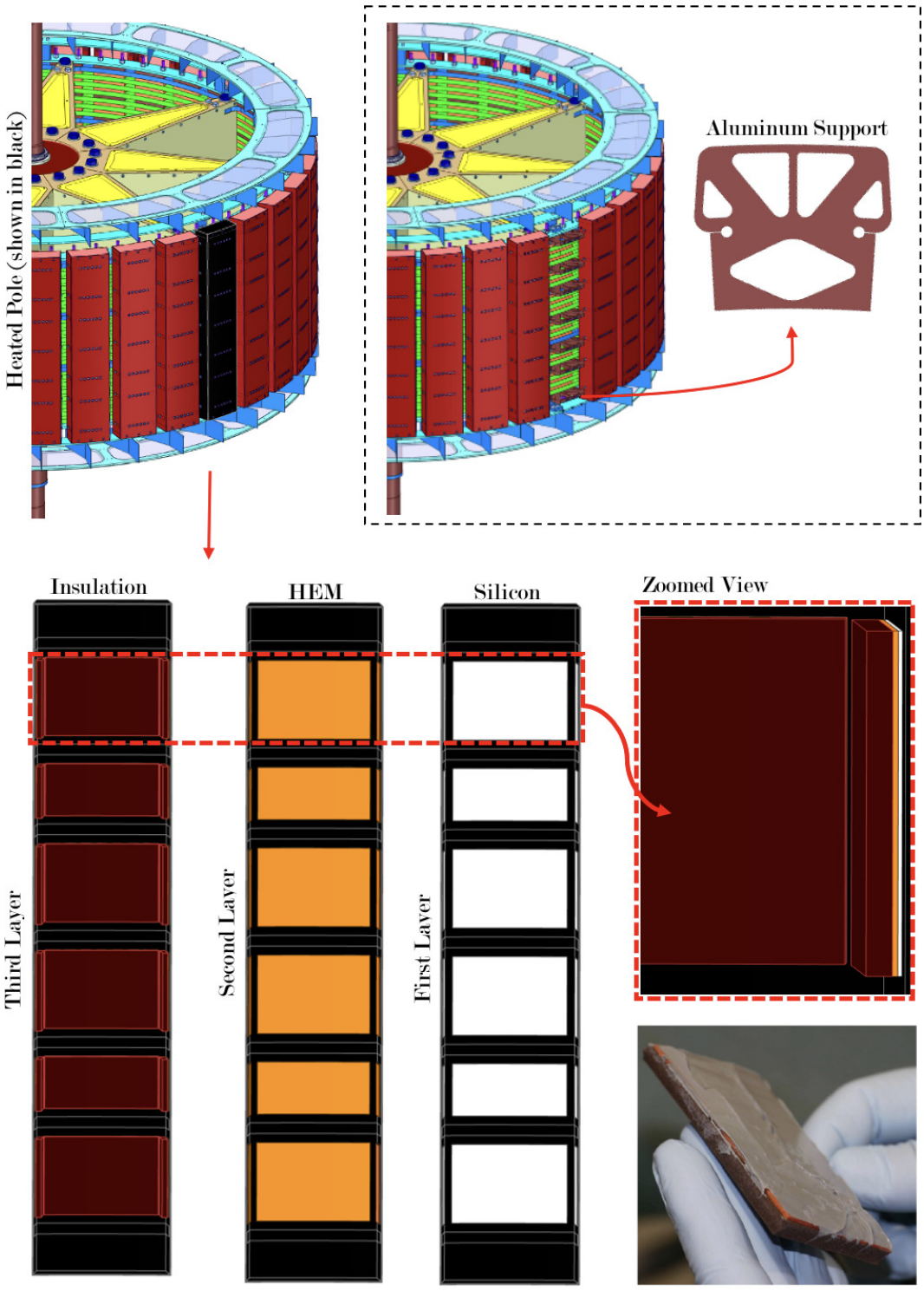

Figure 2.11: Views of the heated pole (shown in black) highlighting the aluminum support fixtures. Vertical arrow pointing to views of the back side of the heated pole showing the three different layers of pads: i) (white) silicon, ii) (orange) heating element matrix (HEM), and iii) (brown) insulation. S-shaped arrow pointing to a magnified view of the assembled pads showing their placement relative one-another, and an image prior to their installation.

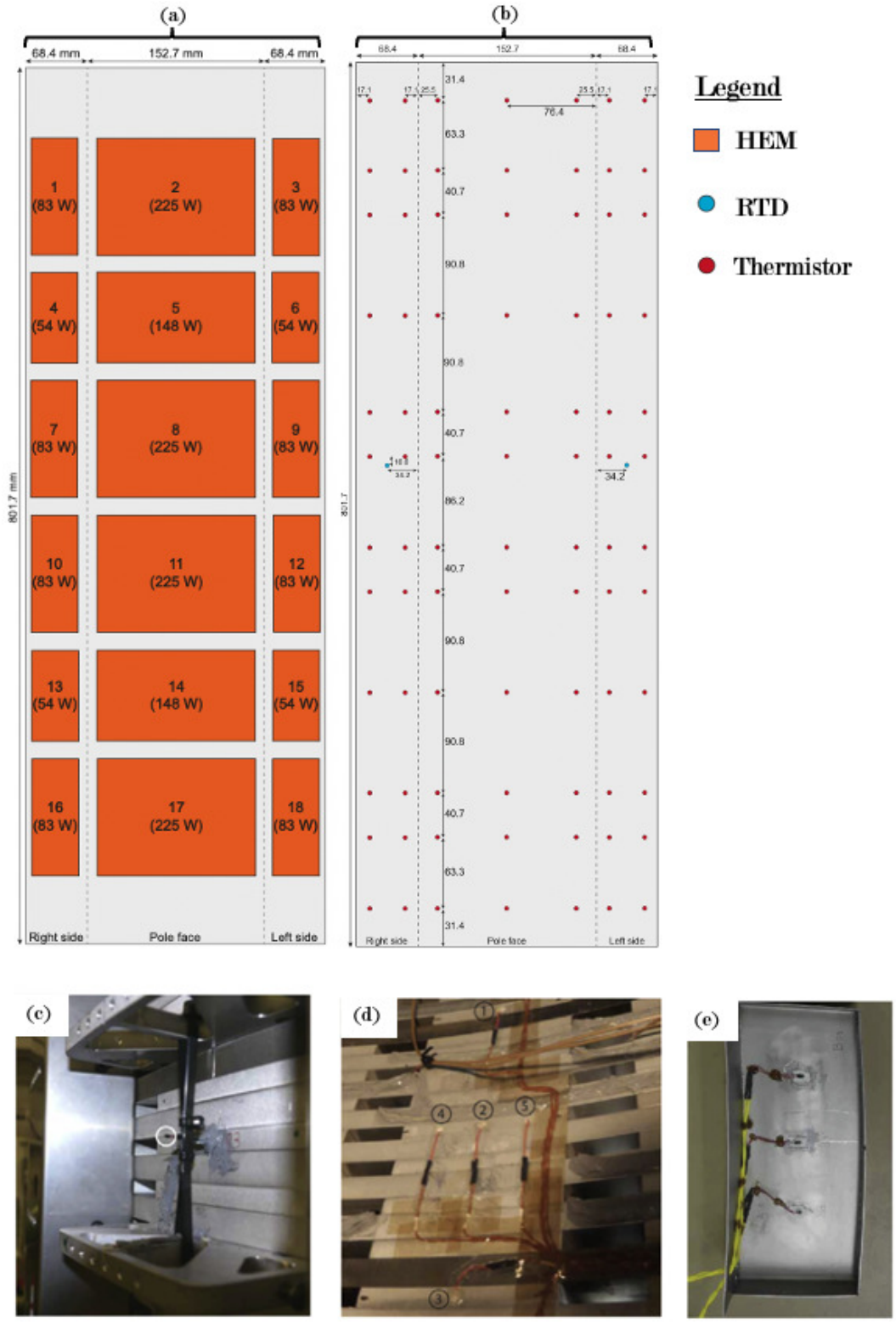

Figure 2.12: (a) Power ratings of the HEMs installed, and (b) location of the installed sensors within the shell's interior. Images of the temperature sensors used to track the heated pole's interior heat losses installed at: (c) the outer and (d) inner radii of the rotor rim, and (e) in the inner surfaces of the caps.

bottom right image of figure 2.11), was applied to the HEM (surrounded by an orange padding with a thermal conductivity of 0.19 W/m·K) to bond it to the shell. However, these efforts were incapable of eliminating all unwanted heat losses. Thus, various temperature sensors (*i.e.* thermistors and RTDs) were installed within the silicone layer, on the outer and inner portion of the rotor rim, and within the caps, as illustrated in figures 2.12(b-e) to measure the temperature and allow for the estimation of the heat lost to the surrounding components. Lastly, to improve the mechanical integrity and enhance the surface emissivity of the heated pole, several modifications were made to the shell including: i) changing the material, ii) increasing the thickness, and iii) oxidizing the outer surface of the shell. The installation of the HEMs, insulating layers, and various sensors, required improvements to the mechanical integrity of the shell. This was achieved by replacing the original material (304 stainless steel) with 4130 grade steel and increasing the shell thickness to 1.27 mm. A coating of black oxide was later applied to the outer surface of the shell to increase its surface emissivity. This facilitated the use of optical temperature sensors for the measurement of the heated pole's surface temperature. Ultimately, these modifications increased the weight of the heated pole when compared to the initial design of the rotor poles of the scale model by approximately 1 kg. Therefore, weights were positioned at the opposite end of the rotor to balance it.

2.1.3 The Static Model

One objective of the research presented in this thesis was to improve an earlier design of a thermal mass flow meter (TMFM) for the measurement of the flow within the rotor rim ducts of a hydroelectric generator (Venne, 2017; Venne *et al.*, 2018). The improvements to the diagnostic tool were initially experimentally validated using a static model. The static model, as the name

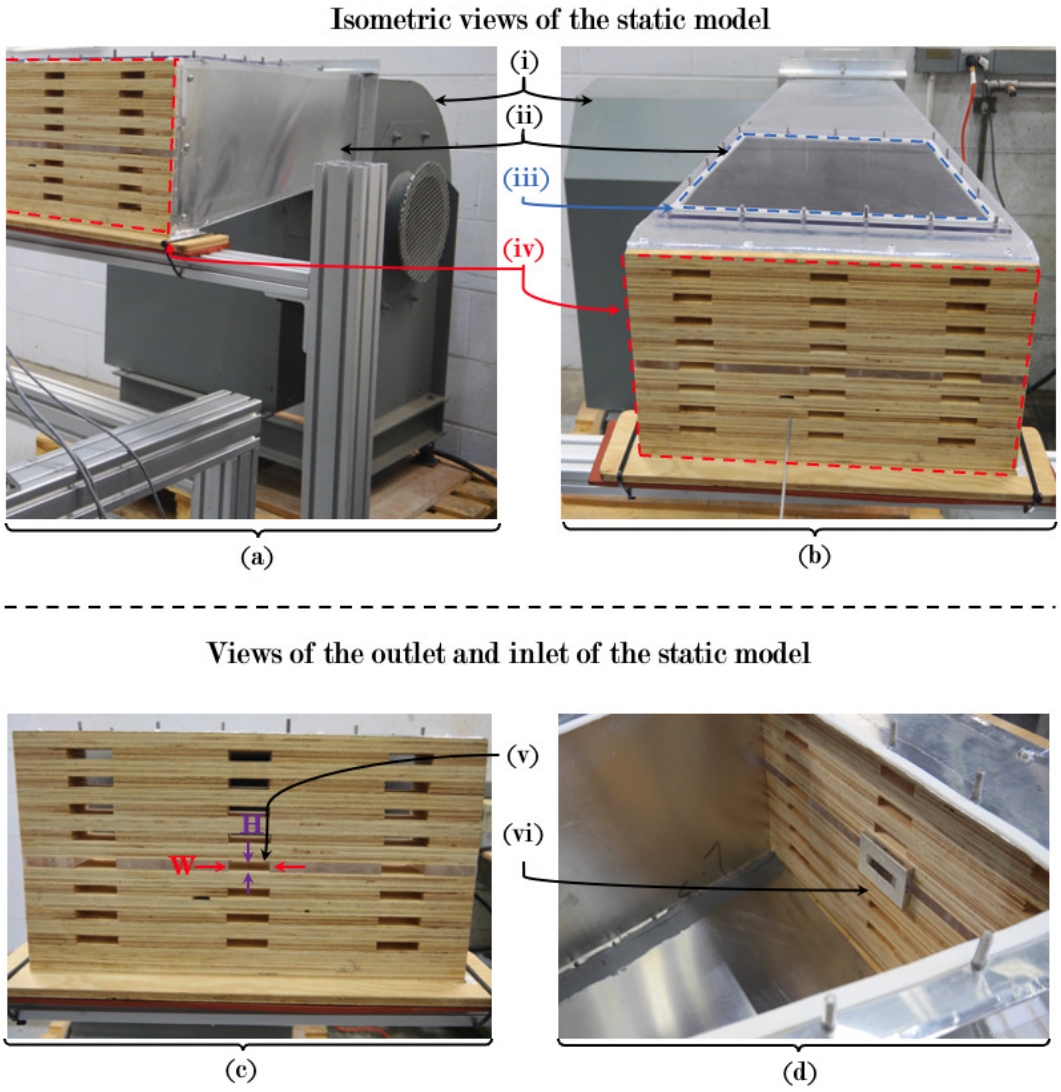

Figure 2.13: (a) Side and (b) front views highlighting the main components of the static model: the centrifugal blower (i), the ventilation duct (ii) with an inlet opening (iii), and (iv) the wood insert. (c) Front view of the wood insert and the 24 static model ducts highlighting the center duct (v) with a height (H) and width (W) of 12.2 mm and 51 mm, respectively. (d) View of the inlet of the static model showing where an (vi) original TMFM prototype installed at the center duct.

implies, is a stationary system. Thus, the complexities associated with rotating machinery (such as data collection via slip rings or wireless systems, large g-forces, high temperatures, and stringent safety measures) were initially avoided to facilitate the performance validation of the new diagnostic tool. The static model could not be used to validate the TMFM's ability to survive the harsh environments found in rotating machinery and conduct accurate measurements in them, but it allowed for the validation of its ability to accurately measure the mass flow rate in a small stationary rectangular duct. Ultimately, the experiments validated the measurement accuracy and repeatability of the improved TMFM (discussed in Chapter 4), which demonstrated its viability for installation in the scale model's rotor rim ducts and to measure the air flow in them. The latter subsequently provided confidence for its installation within the rotating scale model to validate its ability to survive the harsher environment and ultimately allow for its implementation within an in-service hydroelectric generator during a regularly scheduled maintenance. Thus, this methodology enabled the proper development of this new and improved emerging diagnostic tool, which would have been unavailable and impracticable using only in-service hydroelectric generators and the rotating scale model.

The static model has three main components: a perforated wood insert, a ventilation duct made of thin sheet metal, and a large industrial centrifugal blower, which are illustrated in figures 2.13(a,b). The wood insert (shown in figure 2.13(c)) replicated a section of the scale model's rotor rim and has 24 ducts with a height (H) and width (W) of 12.2 mm and 51 mm, respectively, which ensured that the geometric constraints are met for any diagnostics tool. An industrial blower connected to a diverging ventilation duct was used to generate the air flow passing through the static model's wood insert. The diverging duct connects the blower to the wood insert and provided the access

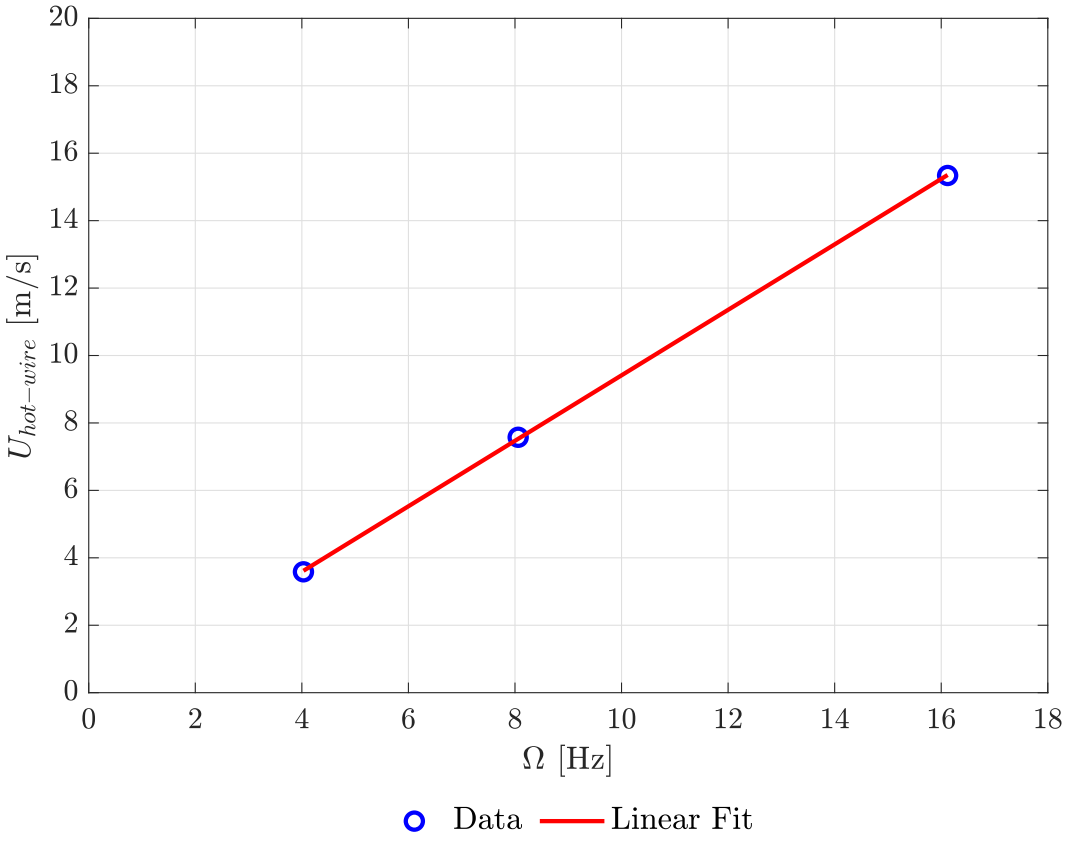

Figure 2.14: The inferred average velocity ($U_{hot-wire}$) exiting the static model duct as a function of the blower motor rotational speed (Ω) obtained using hot-wire anemometry (Venne, 2017).

required to install sensors at the inlet of the ducts within the wood insert, as illustrated in figure 2.13(d). The flow passing through the center duct of the static model was first characterized by Venne (2017). The author used a hot-wire anemometer to obtain the relationship between the centrifugal impeller's rotational speed (input) and the average velocity exiting the center duct of the static model (output), as shown in figure 2.14. Although this method was able to characterize the flow exiting the static model, it had many shortcomings, including the need for a large number of point measurements to obtain the flow field and the inability to use it within the rotating scale model. Thus, the static model was retrofitted and placed within in an enclosure, such that the flow exiting the static model could be characterized using PIV.

2.2 Instrumentation of IREQ's Experimental Facilities

The experimental investigations in this project consisted of acquiring the data necessary to validate the performance of both the new TMFM design and the numerical simulations of the scale model using two different techniques. Each technique was capable of acquiring different information pertaining to the flow in the experimental facilities mentioned above. Thus, each technique is discussed in a separate subsection. The first subsection discusses the TMFM, and in particular: i) its working principle, ii) a prototype developed for hydroelectric generators, and its instrumentation in iii) the static and iv) scale models. The second subsection discusses particle image velocimetry (PIV), including: i) its working principle, ii) its implementation for measurements within the static model, and iii) the post-processing procedure used in the current study.

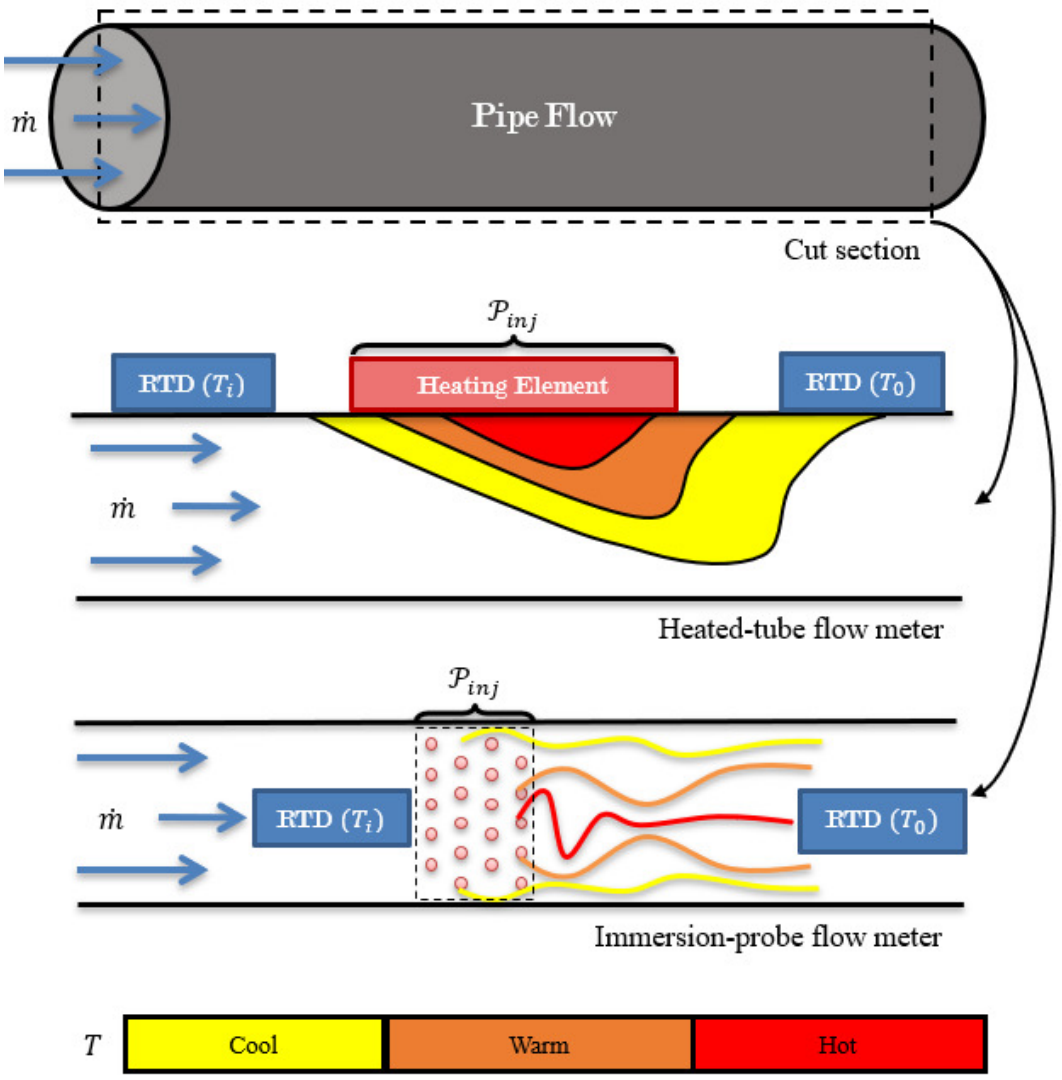

Figure 2.15: Sketch of a heated-tube and immersion-type thermal mass flow meter for pipe flow measurements.

2.2.1 Thermal Mass Flow Meters

The first two objectives of the proposed research were met by improving the original thermal mass flow meter (TMFM) of Venne *et al.* (2018) by measuring the flow passing through the center duct of the static model; and then measuring the flow passing through the rotor rim ducts of the scale model using the improved TMFM design. Ultimately, the experiments consisted of: i) employing the working principle of a TMFM, ii) instrumenting the static model, and iii) instrumenting the scale model.

TMFMs are devices that rely on the principle of conservation of energy applied to a fluid flowing over or through a heating element to infer the mass flow rate of the fluid. Illustrated in figure 2.15 are the two main types of TMFMs that exist for the measurement of pipe flows (Tavoularis, 2009): heated-tube flow meters and immersion-probe flow meters. The latter was shown by Venne (2017) to be a more viable option for measurement of the flows within hydroelectric generators. The working principle of such a device can be derived by applying the first law of thermodynamics for an open system, as illustrated in figure 2.15. Using several assumptions (adiabatic walls being the most difficult to achieve in practice), this exercise ultimately yields the following:

$$\mathcal{P}_{inj} = EI = \dot{m}c_p(T_{b_{out}} - T_{b_{in}}) = \dot{m}c_p\Delta T_b, \tag{2.3}$$

where the rate of energy injected into the flow ($\mathcal{P}_{inj}$) by way of a heating element is a function of the voltage (E) and current (I) across the heating element, and the specific heat at constant pressure of the fluid (c_p), the bulk temperature difference (ΔT_b) between the outlet ($T_{b_{out}}$) and inlet ($T_{b_{in}}$), and the mass flow rate of the fluid ($\dot{m}$). Thus, a TMFM initially i) measures the bulk temperature of the flow ($T_{b_{in}}$) passing through a duct at an initial upstream location, and ii) injects energy into the flow using a heating element at

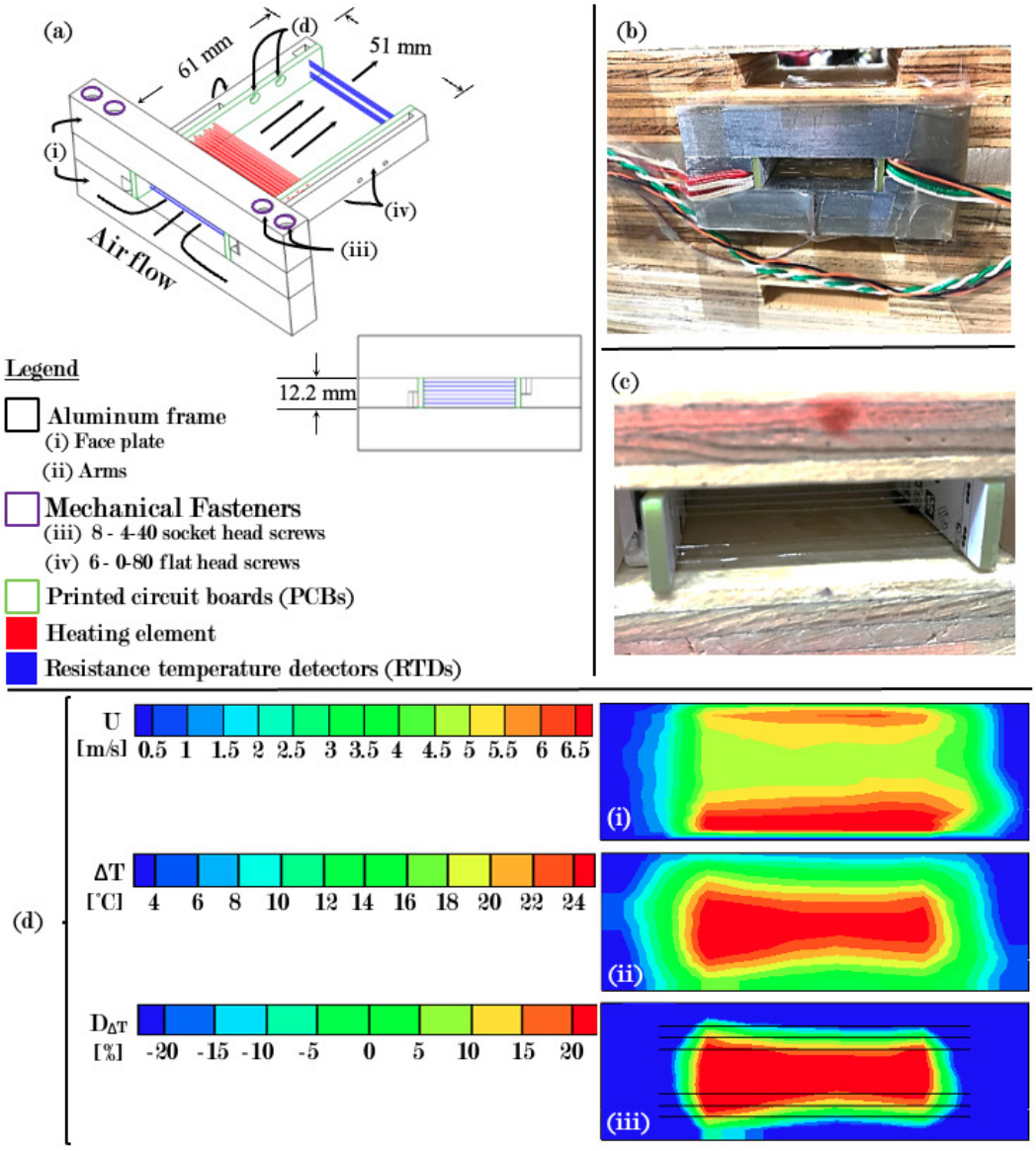

Figure 2.16: (a) Original TMFM design showing both isometric and front projections and its major components. Installation of the prototype at the inlet (b) and outlet (c) of the center duct of the static model. (d) Duct outlet contours of the velocity (i), temperature difference (ii), and the percentage difference in the bulk temperature (iii) from Venne *et al.* (2018) and obtained using a hot-wire anemometer/thermocouple setup.

a downstream location. Typically, the energy is injected via resistance heating, where a voltage (E) is imposed and a current (I) is measured. From this information, the rate of energy injection ($\mathcal{P}_{inj}$) can be deduced. Further downstream of the heating element, the outlet bulk temperature of the flow ($T_{b_{out}}$) is measured. Thus, by calculating the: i) bulk temperature difference (ΔT_b), ii) rate of energy injection into the flow, and iii) knowing the specific heat at constant pressure of air (c_p) at the bulk temperature, the mass flow rate ($\dot{m}$) of the flow can be inferred. However, Venne *et al.* (2018) discuss that the main challenge for such devices is making an accurate measurement of the outlet temperature that correctly represents the outlet bulk temperature. Although it is well known that flow passing through a heat source will achieve a fully-mixed state (*i.e.* where the temperature profile would uniformly asymptote to the bulk temperature) sufficiently far downstream, this phenomena is not attained at the outlet of the relatively short (rotor) rim ducts of the static and scale models.

Due to the limited availability of ventilation data and challenges (limited optical access and complexity) associated with performing PIV measurements in the rotating components of the scale model, Venne *et al.* (2018) developed a TMFM to measure the flow passing through the rotor rim ducts of a hydroelectric generator. The prototype developed by the authors was an immersion type TMFM, uniquely developed for the rotor rim ducts of a hydroelectric generator, because the small rotating rectangular ducts are not the large stationary pipes for which such devices are typically designed. The authors' prototype is depicted in figure 2.16(a) and consisted of: an aluminum frame with nichrome wires as heating elements (shown in red), RTDs to measure the upstream and downstream temperatures (shown in blue), and printed circuit boards (PCBs) to ensure electrical continuity between the wires of the heating element and the

RTDs. The heating element consists of a compact bank of 30 wires placed in a staggered fashion to enhance thermal mixing and is powered by a 0-5 A, 48 V power supply. The design has an operating power range of 20-170 W, which is capable of generating a temperature differential of 20°C across a duct with an average velocity varying between 1.4 and 12 m/s. To overcome the challenges associated with the measurement of the bulk outlet temperature in a region of non-uniform temperature, the prototype uses 6-resistance wires (RTDs) precisely placed at the outlet to make the appropriate measurement. Both the placement of the outlet RTDs and the performance of the prototype were experimentally validated in the static model. The validation process consisted of installing the TMFM at the inlet of the static model as shown in figure 2.16(b) and measuring the flow at the outlet, which is shown in figure 2.16(c) using a hot-wire anemometer attached to a small (30 AWG) type-T thermocouple to simultaneously obtain the velocity and temperature of the flow exiting the static model. The results of those measurements are shown in figure 2.16(d), which includes the velocity (U) contour, a contour of the difference between the outlet and inlet temperatures (ΔT), and a contour of the percentage difference in the bulk temperature ($\mathcal{D}_{\Delta T_b}$). The measurement technique, which is explained in greater detail in Venne (2017), used the method of Lienhard & Helland (1989) to account for the large temperature variations in the flow at the outlet generated by the heating element of the TMFM by compensating the hot-wire output voltage for the effects of variable temperature. From the velocity (i) and temperature (ii) contours illustrated in 2.16(d), the $\mathcal{D}_{\Delta T_b}$ contour (iii) is obtained to pinpoint the ideal RTD placement. For this instance, the post-processed value of the arithmetic mean of the temperature across the black lines (representing the RTD wire placement) of 2.16(d) is within $\pm 1\%$ of the bulk mean temperature. Furthermore, the difference in the mass flow

rate between the deduced TMFM value and the hot-wire/thermocouple value was ±11.5%. Thus, the measurements of the former were compensated (by use of a "blockage factor") to account for the fact that its presence alters and restricts the flow. This was done using a calibration curve formulated using measurements of the flow exiting the static model ducts with and without the TMFM installed therein. Although this prototype proved to be effective, further improvements were required to measure the flow in the scale model, the detailed explanation of such improvements are discussed in the fourth chapter of this thesis.

Once a new TMFM was designed (Chapter 4), several were manufactured and installed within the static model to experimentally validate the i) repeatability of the mass flow rate measurements from one prototype to the next, and ii) the accuracy of the measurement. Both validation experiments consisted of measuring the mass flow rate passing through the center duct of the static model at various flow rates. The experimental setup for the validation experiments is shown in figure 2.17(a-d). Figure 2.17(a) highlights the inlet (ii) and outlet (iii) of the center duct, and the reference RTD (iv) inserted below the centermost duct to measure the temperature of the flow at the inlet. Each prototype was installed in the center duct as shown in figures 2.17(b,c). The eight RTD wires (4 inlet and 4 outlet), two power, and two board voltage measurements were passed to the bottom of the optics table where the data acquisition (DAQ) unit was located, as shown in figure 2.17(d). Since the TMFM was originally designed to be installed within the rotor of a hydroelectric generator, the DAQ was fastened to a structural support (iv), with a design that depended upon the hydroelectric generator. The DAQ unit is comprised of power management (v), communication (vi), and acquisition (vii) subsystems, as highlighted in figure 2.17(d).

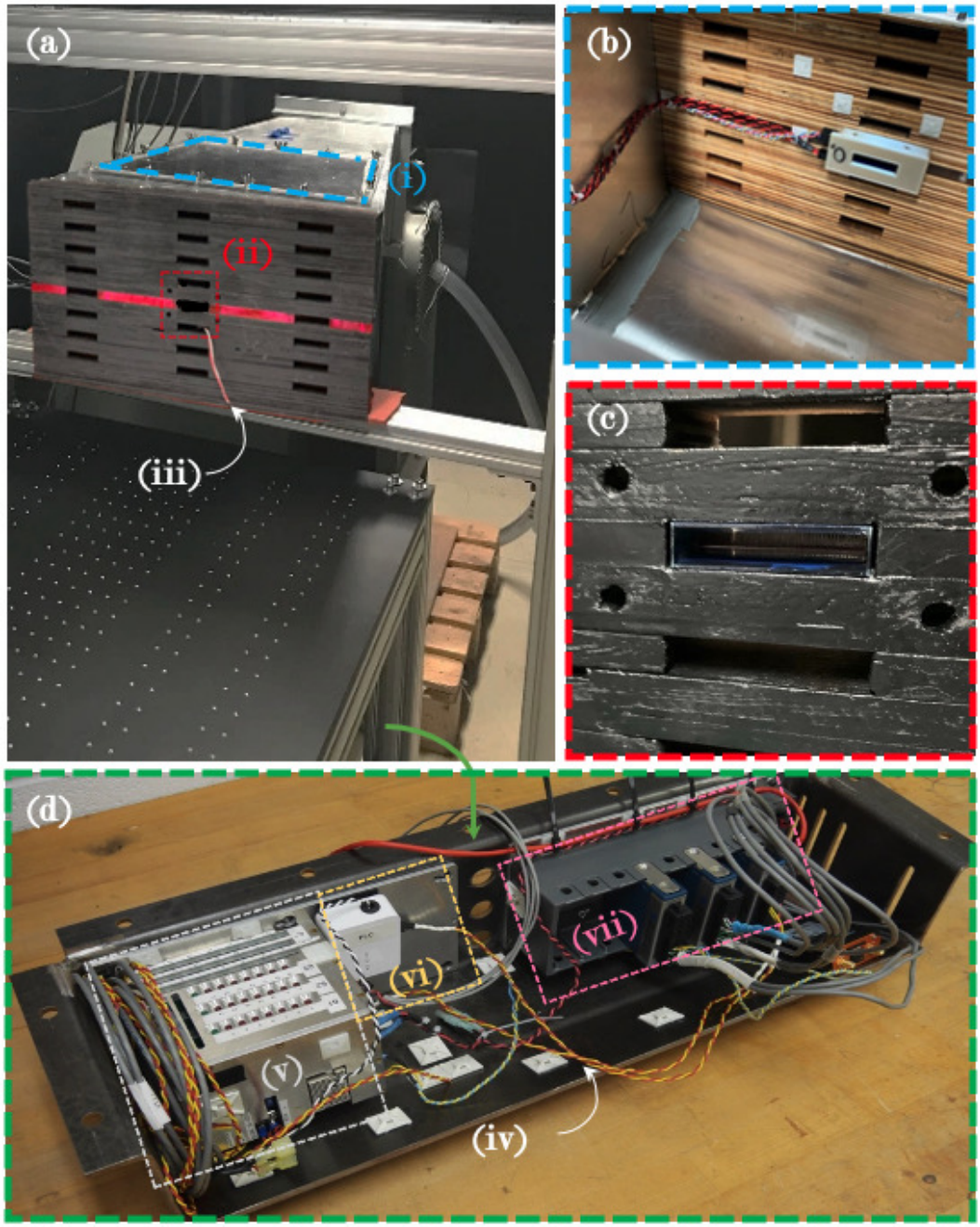

Figure 2.17: (a) The static model within the isolated room at IREQ's experimental laboratory highlighting the static model inlet (i), the center duct outlet (ii), and the reference RTD (iii). (b) View of the static model inlet with the TMFM installed in the center duct. (c) Magnified view of the center duct outlet showing the improved TMFM design installed within. (d) The DAQ unit for the TMFM located beneath the optics table highlighting its structural support (iv), as wells as its acquisition (v), communication (vi), and power management (vii) subsystems.

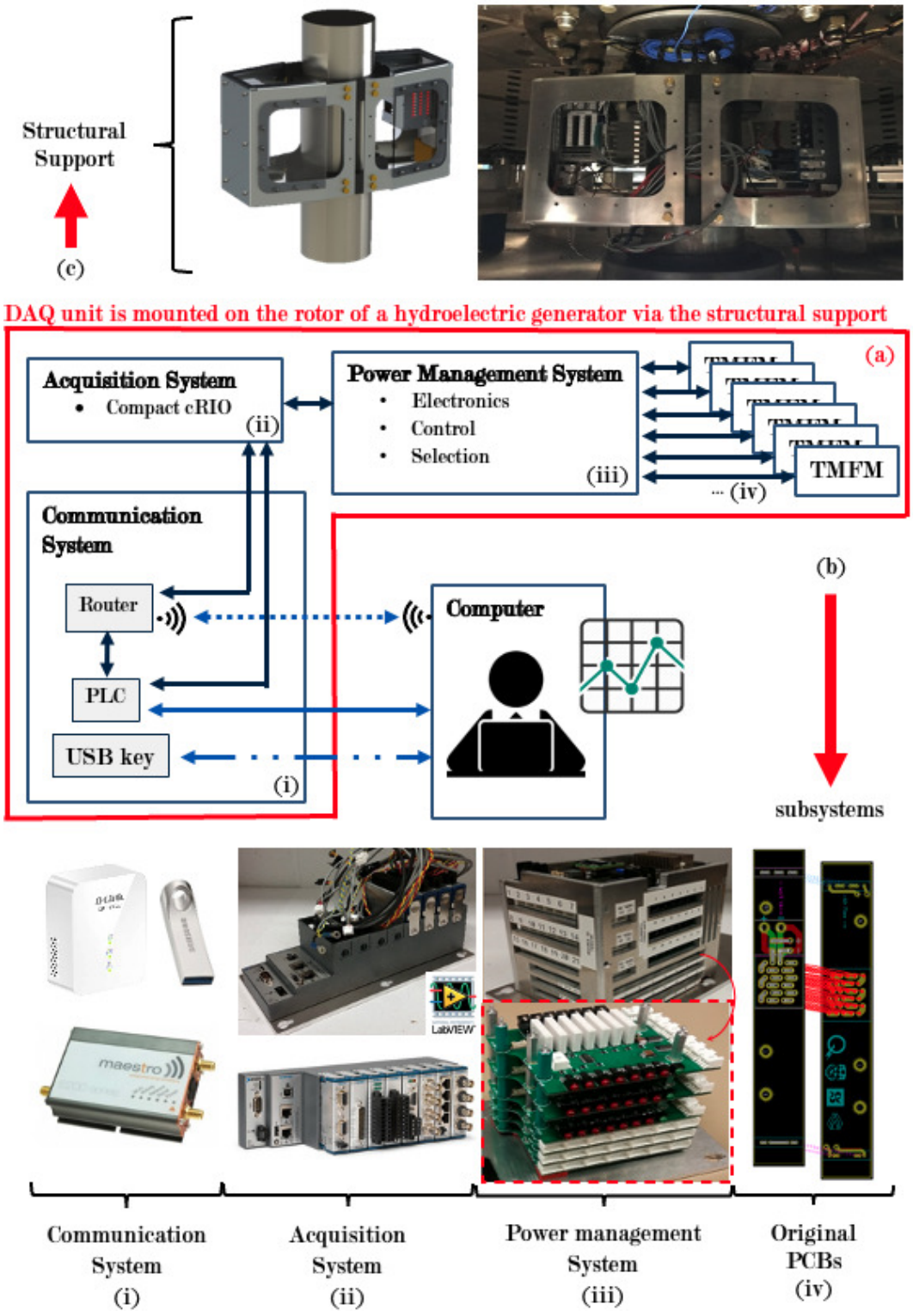

Figure 2.18: (a) Interconnection schematic between each subsystem of the DAQ unit developed by Kirouac (2017), the communication (i), acquisition (ii), and power management (iii) subsystems, as well as, the PCBs (iv) of the TMFM. (b) Components of the aforementioned subsystems. (c) Structural support and its installation on the scale model shaft.

The PCBs of the TMFMs and the subsystems of the DAQ unit were developed in close collaboration with Kirouac (2017) and were all designed to be mounted to the rotor of a hydroelectric generator. The interconnections between each subsystem and their components are presented in greater detail in figures 2.18(a-c). Figure 2.18(a) illustrates the overall system-level schematic and the interaction between the user/computer and the three subsystems (i-iii) of the DAQ unit and PCBs (iv) of the TMFMs. Furthermore, images of the communication (i), acquisition (ii), power management (iii) systems, and PCBs (iv) of the original TMFM design are illustrated in figure 2.18(b). The heart of the overall system is the compact re-configurable input/output (IO) modules (cRIO), which allows for the acquisition of pertinent data and the control of the sensors via an intermediate power management system, which are both regulated via the DAQ system and the dedicated software of the cRIO (LabVIEW). The power management system is comprised of a series of PCBs with relays that adequately distribute a 48 V input to the other subsystems and switch between three groups of seven simultaneously powered TMFMs. Lastly, the communication system uses two redundant methods with a backup to provide a fail-safe system to protect against electrical noise present in hydroelectric generators. If the conditions permit, the data is communicated to the operator of the software via a WiFi system. Otherwise the data is communicated through power line communication (PLC). In either case, the data is saved on a universal serial bus (USB) drive connected to the cRIO to prevent inadvertent loss of data if the communication with the cRIO is momentarily lost. To mount the entirety of the DAQ unit to the scale model shaft, the structural support illustrated in figure 2.18(c) was developed and its structural integrity was numerically and experimentally verified (see Appendix B.2 and B.3).

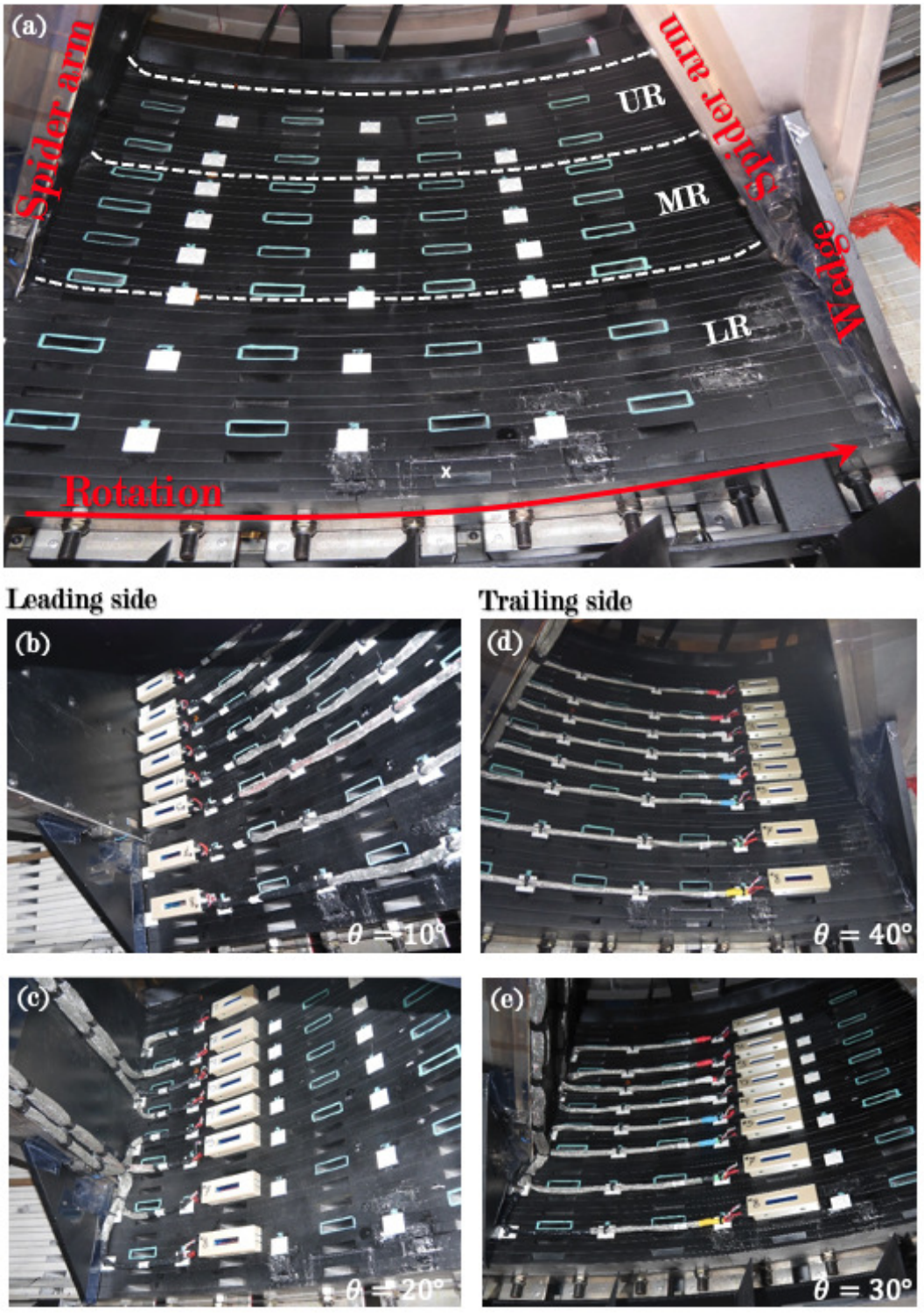

Figure 2.19: (a) Intra-spider arm region highlighting the upper (U), middle (M), and lower (L) regions. Installation of the TMFM in the following columns: leading (b), mid-leading (c), trailing (d), and mid-trailing (e).

The second objective of the present research was achieved by installing eight prototypes of the new TMFM design in the rotor of the scale model, to characterize the flow rates passing through the rotor rim ducts therein. The scale model has eight intra-spider arm regions, each consisting of four circumferential columns of 23 axially positioned rotor rim ducts. The 23 positioned ducts can be separated into 3 regions as illustrated in figure 2.19(a): upper, middle and lower regions defined by the three flanges that fasten the spider arms to the rotor rim. Since the rotor rim is slightly taller than the spider arms, there is one duct above the upper flange, seven ducts in the upper region, seven ducts in the middle region, and eight in the lower region. Moreover, the upper region is located between the top and middle flanges of the spider arm, the middle region is located between the middle and lower flanges, and the lower region is below the lower flange corresponding to the region of the spider arm wedge, as shown in 2.19(a). Thus, to characterize the flow passing through the rotor rim, eight prototypes were installed in each column of ducts in an evenly distributed manner: two in the upper region, four in the middle region, and two in the lower region. Moreover, their axial position is highlighted in teal in figure 2.19(a). To dynamically balance the rotor due to the added mass of the wiring and the TMFMs shown in figures 2.19(b-e), a counter weight was placed following the ISO-1940 standard in the intra-spider arm region located 180° from the region painted in black in figure 2.19(a). To obtain both the axial and circumferential distribution of the mass flow rate passing through the rotor rim, the TMFMs were moved from one column to the next, as illustrated in figures 2.19(b-e). Each column in figures 2.19(b-e) are labeled with respect to the clockwise rotation and relative to the nearest spider-arms as: leading, mid-leading, trailing, and mid-trailing locations, respectively.

2.2.2 Particle Image Velocimetry System

As previously mentioned, the first objective of the proposed research was met by improving the original TMFM design of Venne *et al.* (2018). The improvements were experimentally validated via measurements of the flow passing through center duct of the static model. This consisted of obtaining nine objective measurements (corresponding to each prototype) of the mass flow rate passing through the center duct of the static model at three different flow speeds. Of interest were the repeatability in the mass flow rate measurement from one prototype to the next and the accuracy of the prototype in obtaining the mass flow rate. The former simply required a comparative analysis of the nine individual objective measurements, whereas the latter required a baseline measurement of the flow exiting the static model duct using an established and non-intrusive measurement technique, such as PIV. Obtaining the baseline measurement required: i) employing the working principles of PIV, ii) instrumenting the static model with the equipment necessary to perform PIV measurements, and iii) applying a post-processing procedure to remove spurious vectors from the data and obtain the average flow rate.

PIV is an optical velocimetry method in which visible tracers (or seeding particles) are tracked to deduce the velocity of the flow in which they are transported. This is quantitatively performed by illuminating the flow with a pulsed laser, and recording two images of the particles at a known time interval (the time between the pulses). The velocity can then be deduced from the displacement of the particles in the images and the time interval.

Once acquired, the images are subdivided into interrogation windows. The windows must be small enough to assume that all the particles inside a window travel at the same speed, but large enough such that a sufficient amount of particles occupy a window to allow for a meaningful statistical description of

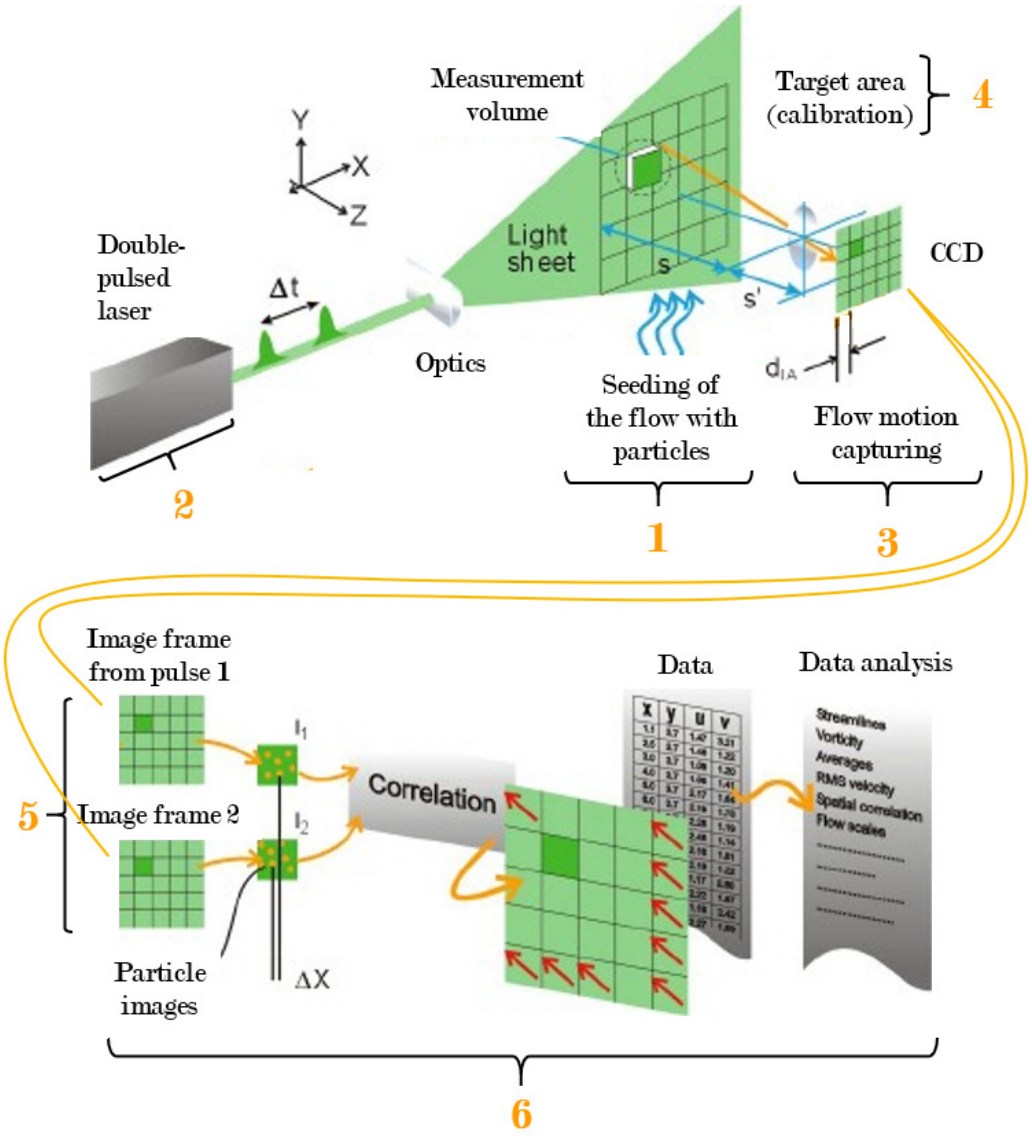

Figure 2.20: Illustration of the six main steps in performing a PIV measurement: i) seeding of the flow, ii) illumination of the seeding particles, iii) capturing the motion of the illuminated particles, iv) calibration, v) synchronization of the illumination and imaging process, and vi) post-processing of the data. (Modified image from Dantec Dynamics (2018).)

the particles' velocity. The particles within these windows appear as bright spots as they are selected for their capacity to scatter the light from the laser pulses. The mean displacement of the particles is obtained via cross-correlation of the illuminated particles within an interrogation window common to both images. Knowing the time between pulses, the velocity of the particles within the window is then determined. Since the time between pulses is small, it is assumed to be the instantaneous velocity at the time of the first pulse. Therefore, the process of obtaining the velocity of a given flow field using PIV can be divided into six steps as illustrated in figure 2.20: seeding of the flow, illumination of the seeding particles, capturing the motion of the illuminated particles, calibration, synchronization of the illumination and imaging process, and post-processing of the data. Each step is explained in greater detail in Appendix C.1 and was applied to obtain the baseline measurement of the flow exiting the scale model, with a summary of the procedure given below.

The static model was instrumented with the following equipment illustrated in figures 2.21(a-c) to obtain a baseline measurement of the flow exiting the ducts using PIV: laser, camera, fluid atomizer, optics table, light sheet apparatus (LSA), and a set of linear ball screw actuators. Figure 2.21(a) shows a FlowSense 4M Mk2 camera (i) mounted on three different Velmex linear ball screw actuators allowing the camera to move in three directions (X, Y, Z) over the static model. Also shown is a large plastic tube (v) attached to the inlet of the centrifugal blower, which feeds the oil particles generated by the fluid atomizer. Furthermore, an optics table (iv) coated in black oxide is positioned underneath the wood insert to align the laser light sheet that is generated using the LSA (vii). The LSA is an apparatus designed to generate and move a laser light sheet over several vertical positions in the static and scale models. The apparatus is comprised entirely of aluminum fixtures, rods, linear bearings,

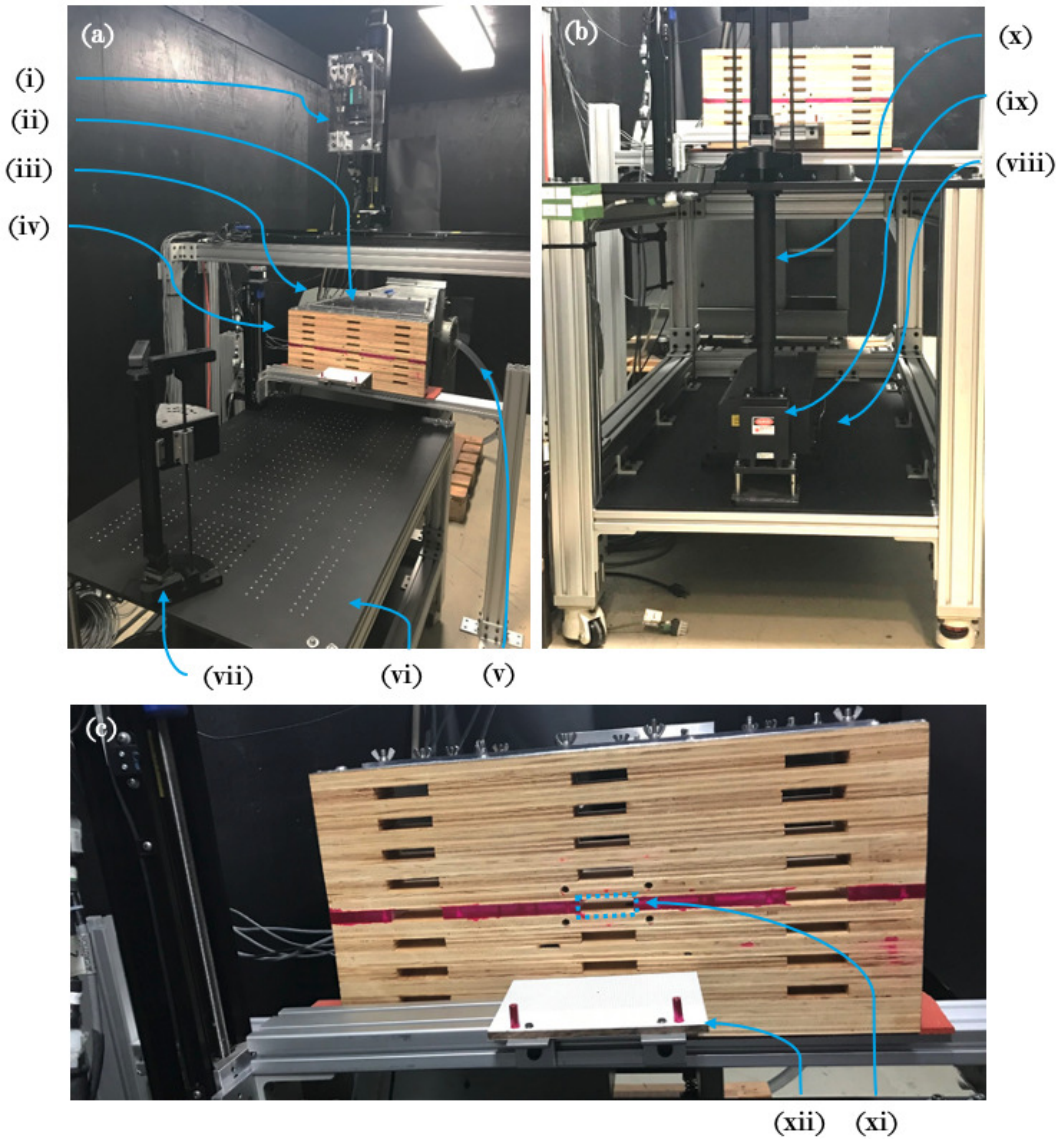

Figure 2.21: (a) Isometric view of the static model highlighting: the camera (i) fixed on three motorized axes, the ventilation duct (ii), the blower (iii), the wood insert (iv), the seeding tube (v) installed at the blower inlet, the optics table (vi), and the laser sheet apparatus (LSA) (vii). (b) View underneath the optics table highlighting: the laser (viii), a mirror box (ix), and the laser tube (x). (c) Magnified view of the of the wood insert highlighting: the outlet of the center static model duct (xi), and the calibration target (xii).

and a vertically mounted linear ball screw actuator, which vertically displaces a pie shaped enclosure containing a 45° mirror and a 80×63 light sheet thickness adjuster made by Dantec Dynamics. The latter component is a metal tube containing cylindrical and spherical optics, which extend and contract to control the light sheet thickness. As illustrated in figure 2.21(b), the laser is directed to the LSA using a Solo PIV 200XT laser (viii) and mirrors (ix), which are all located below the optics table and enclosed in a metal tube (x). Once the laser passes through the LSA's 80×63 optics, the cylindrical shaped laser is converted into a light sheet and projected to the outlet of the center most duct (xi) of the static model, as illustrated in figure 2.21(c). The velocity profile exiting the static model duct is obtained by vertically displacing the laser light sheet along the height of the duct outlet. Also shown in the figure is a linear actuator used to position the calibration target (xii) required to convert the camera's pixel positions to physical displacements in meters.

A post-processing procedure was required to obtain a vectorial representation of the flow at the outlet of the static model once a sufficient number of particle images in a given axial location of the laser light sheet was obtained. The procedure employed in the *Dynamic Studios* software used in the present work is illustrated in figures 2.22(a-f) and included the following four steps: adaptive correlation, range and N-Sigma validation, universal outlier detection, and vector dewarping and statistics. The essential mechanics of PIV post-processing entails subdividing the field-of-view into small interrogation windows and calculating the cross-correlation of the particle displacement between two frames in a given window to obtain the vectorial displacement in that window. This process is represented in figure 2.22(a), where the particles in the window associated with the first image are drawn in white, and those in the same window but associated with the second image are in black. Once the

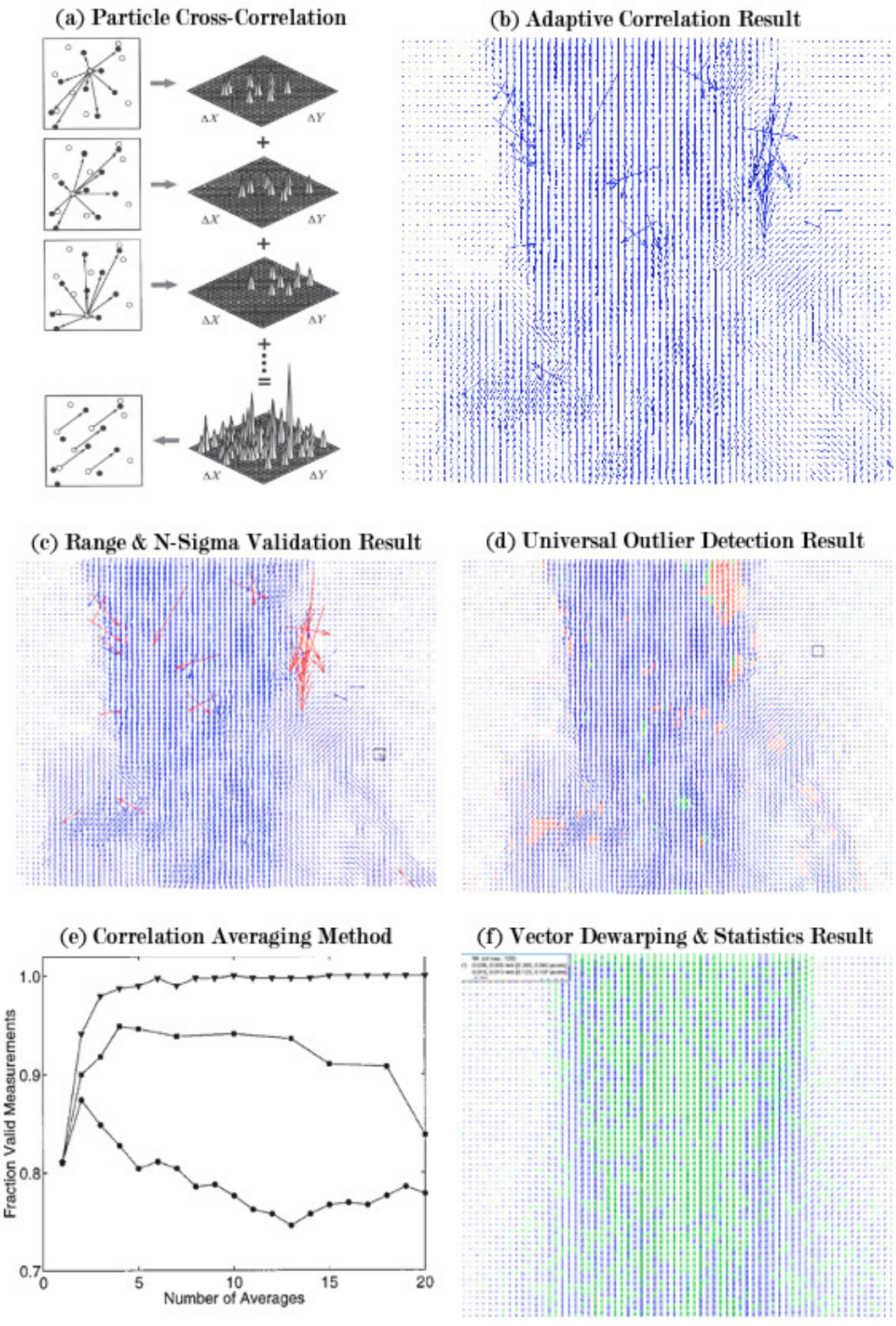

Figure 2.22: (a) Cross-correlation sketch (Adrian & Westerweel, 2011). (b) adaptive correlation. (c) Range/N-Sigma validation. (d) Universal outlier detection. (e) Correlation (triangle), displacement (circle), and image (square) averaging methods (Meinhart *et al.*, 2000). (f) Vector dewarping/average.

particles within the window for each frame have been identified, the displacements between a given particle in the first frame and the particles in the second frame are computed and represented by peaks. This process is repeated for all the particles. Then the collection of peaks for each particle is summed and represented in a cross-correlation histogram where the tallest peak corresponds to the most likely displacement. In the current study, a modified version of this technique, called adaptive correlation, was employed using *Dynamics Studios*, which increases the resolution by adapting the interrogation window to capture more particles per window. Window adaptation is a technique that offsets the interrogation window around a given point between the two images by first calculating a rough displacement with a larger window and then reducing its size and translating it by the calculated rough displacement to obtain a more precise displacement. This technique therefore captures more particles per window and reduces the size of the interrogation window, which increases the spatial resolution. In the current study, this technique was applied with two successive window size reductions and two iteration for each size, and resulted in the vectorial representation of the flow shown in figure 2.22(b). To remove the spurious vectors shown in figure 2.22(b) other statistical methods, such as, range validation, N-Sigma validation, and universal outlier detection were employed to reject the vectors shown in red in figures 2.22(c-d). Once all spurious vectors were removed, the vector field was converted into physical units using a dewarping method and the statistical quantities of interest to the flow field were extracted. Illustrated in figure 2.22(e) are three averaging methods which can be employed. Correlation averaging was used over 2,700 frames resulting in the average flow field shown in figure 2.22(f). The details of the methods employed in the post-processing procedure are explained in greater detail in Appendix C.2.

CHAPTER 3
Numerical Models

This chapter provides an overview of the numerical models developed as part of the current research, which focused on the investigation of different turbulence models, effects of the thermofluid properties of the working fluid, methods for modeling the pole heat losses, and subsequent model-based design (numerical) experiments to assess the impact of modifications to the scale model geometry on the performance of the ventilation circuit. In addition, efficient domain discretization (or meshing) technique were implemented. The aforementioned topics are described in two sections in this chapter: i) modeling methodology; and ii) model-based design experiments. The first section discusses the mathematical models and boundary/initial conditions utilized. The second section describes the modifications made to the ventilation circuit as part of model-based design experiments. The meshing strategy for hydroelectric generators that was designed and implemented in this work is described in Appendix A

3.1 Modeling Methodology

To meet the objectives of the present research, a numerical model (*i.e.* a numerical solution of a mathematical model) was developed to predict the global flow quantities (such as the windage losses, and the mass flow rate through the radiator), local flow quantities (such as the distribution of the mass flow rate through the rotor rim), global heat transfer quantities (such as the average operating temperature of the heated pole), and the local heat transfer quantities (such as the maximum operating temperature and temperature distribution of the heated pole) of IREQ's scale model. The validation of

the numerical predictions of this model are presented in Chapter 5.2 by comparisons with the experimental measurements of Hudon *et al.* (2011) and Bach *et al.* (2015) for the global flow quantities, the data presented in Chapter 5.1 for the local flow quantities, and the measurements of Torriano *et al.* (2014) for the global and local heat transfer quantities. The proposed numerical models was developed as follows. First, the mathematical models of the underlying fluid flow and heat transfer phenomena of the air flowing around and through the solid components of a hydroelectric generator were formulated. The necessary boundary and initial conditions required by the mathematical models were then specified. Due to the complexity of these models, and the level of geometric and related details, commercial computational fluid dynamics and heat transfer (CFDHT) software (*ANSYS CFX*) and modern meshing techniques were used herein.

3.1.1 Mathematical Models

The governing equations of the underlying fluid flow and heat transfer for the proposed CHT analysis of the scale model of a hydroelectric generator can be expressed as follows:

$$\frac{\partial(\rho\tilde{\phi})}{\partial t} + \frac{\partial(\rho\tilde{u}_i\tilde{\phi})}{\partial x_i} = \frac{\partial}{\partial x_i}\Big(\Gamma_\phi \frac{\partial\tilde{\phi}}{\partial x_i}\Big) + S_\phi, \tag{3.1}$$

where ρ is the density, $\tilde{\phi}$ is the general intensive dependent variable, $\tilde{u}_i$ is the instantaneous velocity, and Γ_ϕ and S_ϕ are the corresponding diffusion coefficient and volumetric rate of generation (or source) term, respectively. To appropriately detect the hot-spots on the surface of the scale model's heated rotor pole, the conduction of heat within all its isotropic solid components was modeled, as well as, the surrounding air flow. Furthermore, since only the predictions of steady-state conditions were of interest, the governing equations modeled steady heat conduction in the solid components and steady flows of

air, neglecting viscous dissipation. It was assumed that Fourier's Law and Stokes' Law for a fluid apply. Thus, the general governing equations were the familiar equations for the conservation of mass, momentum, and energy, with the scalar dependent variables, diffusion coefficients, and source terms for the solid and fluid domains given in table 3.1. It should be noted, however, that the governing equations in the fluid domain were modified to suitably account for the effect of turbulence on the mean properties of the flow.

The air flow through the many passages of the rotating scale model was turbulent. To model the turbulent flow, Reynolds-averaged formulations of the governing equations for the fluid were employed (introduced by Osborne Reynolds, see Jackson & Launder (2007)). The instantaneous dependent variables ($\tilde{\phi}$) were decomposed into their mean (ϕ) and fluctuating quantities (ϕ'):

$$\tilde{\phi} = \phi + \phi'. \tag{3.2}$$

Subsequent time-averaging of the governing equations results in:

$$\frac{\partial(\rho\phi)}{\partial t} + \frac{\partial(\rho u_i \phi)}{\partial x_i} = \frac{\partial}{\partial x_i}\Big(\Gamma_\phi \frac{\partial \phi}{\partial x_i} \underbrace{-\rho\overline{u_i'\phi'}}_{TDF}\Big) + S_\phi, \tag{3.3}$$

where a new term referred to as the turbulent diffusive flux (TDF), is introduced by the averaging process. It should be noted that for the statistically steady turbulent fluid flow and heat transfer considered in this work, the time-derivate term in equation 3.3 is zero. The TDFs in the Reynolds average governing equations create a closure problem that must be resolved by the introduction of turbulence models. In this work, eddy-viscosity-based turbulence models were used (Pope, 2000; Wilcox, 2006). The TDFs and their modeled approximations are given in table 3.2. A relatively simple approach for the calculation of the eddy viscosities is the use of two-equation turbulence models,

Table 3.1: Dependent variable, diffusion coefficient, and source term in the governing equations (GEQ) in the solid and fluid domains.

Domain	**GEQ**	ϕ	$\partial(\rho u_i \phi)/\partial x_i$	Γ_ϕ	S_ϕ
Solid	Energy	T	0	$\mathcal{K}/c_p$	S_T/c_p
Fluid	Mass	1	$\partial(\rho u_i)/\partial x_i$	0	0
	Momentum	u_i	$\partial(\rho u_i u_j)/\partial x_i$	μ	$-\partial P/\partial x_i$
	Energy	T	$\partial(\rho u_i T)/\partial x_i$	$\mathcal{K}/c_p$	S_T/c_p

Variable	**Description**
u_i	Velocity
T	Temperature
$\mathcal{K}$	Thermal conductivity
c_p	Specific heat at constant pressure
P	Pressure

Table 3.2: The turbulent diffusive fluxes in the Reynolds-averaged governing equations (GEQ) and their modeled approximations.

GEQ	ϕ	**TDF**	**Name**	**Modeled flux**
Momentum	u_i	$-\rho\overline{u_i' u_j'}$	Reynolds Stress	$\rho\nu_T\left(\frac{\partial u_i}{\partial x_j}+\frac{\partial u_j}{\partial x_i}\right)$
Energy	T	$-\rho\overline{u_i' T'}$	Turbulent Heat Flux	$\frac{\rho\nu_T}{Pr_T}\left(\frac{\partial T}{\partial x_i}\right)$

which are commonly employed in industrial practice due to their broad applicability and reasonable computational resource/time requirements, when compared to other approaches such as direct numerical simulations (DNS), large eddy simulations (LES), and Reynolds stress models (RSM). In the present study, predictions obtained with the $k-\varepsilon$ and $k-\omega$ SST turbulence models (Launder & Spalding, 1972; Menter, 1994) were assessed by comparing them with corresponding experimental results. The $k-\varepsilon$ model used was based on a high Reynolds number modeling (HRM) approach with scalable wall functions (SCWF) (Esch & Menter, 2001); and the $k-\omega$ SST model was based on a hybrid low/high Reynolds modeling (LRM/HRM) approach with an automatic wall treatment (AWT) wall function method (Vieser *et al.*, 2002). Both the SCWF and AWT methods were employed to meet the challenges associated with i) respecting the minimum y^+ criteria on the many faces of the complex computational domain, and ii) accurately capturing important geometrical features.

To resolve the closure problem associated with the Reynolds-averaged energy equation, a constant turbulent Prandtl number (Pr_T) was invoked (Kays, 1994):

$$Pr_T = \frac{\nu_T}{\alpha_T} = 0.85, \tag{3.4}$$

which relates the turbulent thermal diffusivity (α_T) to the turbulent viscosity (ν_T). It has been shown that at high turbulent Péclet numbers (Pe_T):

$$Pe_T = \left(\frac{\nu_T}{\nu}\right) Pr, \tag{3.5}$$

the turbulent Prandtl number approaches a constant value of 0.85 (Kays, 1994), which corresponds to the default value employed in the CFDHT codes used in this work (ANSYS-Inc., 2011). (ν is the kinematic viscosity of the fluid and Pr is the Prandtl number).

The experiments of Hudon *et al.* (2011) demonstrated that although the scale model (described in Section 2.1.2) has no electromagnetic components, the air temperature within it increased 24°C after six hours of operation at 300 rpm, mainly due to viscous dissipation in the recirculating flow of air. Three approaches for modeling the thermofluid properties (TFP) were investigated, and their effect on the predictions of the global and local quantities of interest were assessed. The first TFP model consisted of solving the equations of conservation of mass, momentum and energy in a coupled manner, but evaluating the fluid properties at the experimentally measured steady-state temperature of Hudon *et al.* (2011) (labeled as case-C hereafter). This approach assumes that the change in fluid properties in regions of higher temperatures (*e.g.* near the heated pole) have a minor effect on the heat transfer. To assess the applicability of the aforementioned, a second TFP model employing the ideal gas law to calculate the density, the Sutherland correlation for the dynamic viscosity, and an empirical correlation for the thermal conductivity of the air (referred to as the variable-property (VP) model and labeled as case-VP hereafter). This method would permit the model to appropriately calculate the thermofluid properties of the air near the pole. Lastly, the final TFP model considered here, investigated potential reductions in the required computational resources and time, by decoupling (DC) the solution of the mass and momentum equations from the solution of the energy equation (*i.e.* imposing the "frozen" or independently converged flow solution on the surfaces of the heated pole), and evaluating the thermofluid properties at the same experimentally measured steady-state temperature of case C (labeled as case-DC hereafter).

Another key aspect investigated in this work was the approach employed to model the pole heat losses (PHL) within the interior (or backside) of the

heated pole. Although the heating element matrices (HEMs) of the heated pole were insulated with thick foam pads (see figure 2.11), some heat is invariably lost to the adjacent stagnant air due to natural convection. The latter phenomenon is important, as it can directly impact the temperature distribution or hot-spots on the exterior face of the heated pole. To model this heat loss, the temperature measurements taken on the backside of the heat pole by Torriano *et al.* (2014) were utilized, and two different approaches of modeling the PHL were investigated in the present research. The first approach modeled the PHL arising from natural convection by prescribing convective heat transfer coefficients deduced from empirical relations for the Nusselt number proposed by Churchill & Chu (1975) for the vertical surfaces and by Goldstein *et al.* (1973) and Lloyd & Moran (1974) for the horizontal surfaces of the heated pole. The surface temperature values used in the empirical relations were obtained from the experiments, and the calculated convective heat transfer coefficients (in W/m^2K) were in the following range:

$$2.3 \leq h \leq 22.4. \tag{3.6}$$

This approach was utilized in unison with the other TFP models considered (*e.g.* case-C, case-VP, and case-DC) by default, and thus, no additional indicator was prescribed in the naming convention. Given the uncertainty associated with modeling the PHL within the interior of the heated pole using empirical Nusselt number relations, the second PHL model incorporated all aspects of case-VP, including the modeling of the natural convection of fluid within the heated pole (or fluid inside the shell (FIS)) to approximate the energy losses therein (labeled as case-FIS hereafter).

In summary, the investigations of different i) turbulence models, ii) TFP of the working fluid, and iii) PHL models, were grouped in seven different categories, as given in table 3.3. For each of these categories, table 3.3 also provides the number of cells used in the solid (SD) and fluid (FD) computational domains in millions (M) of cells. The cell count for the solid computational domain remained constant, whereas the cell count in the fluid domain was increased by 52% when using the $k-\omega\,SST$ turbulence model to adhere to its stricter near-wall cell size requirement.

Since the rotor of the scale model is rotating (and the other portions of the scale model are stationary), the governing equations for the fluid flow in the rotor passages are solved in the rotating frame of reference, and fictitious (Coriolis and centrifugal) forces are therefore introduced in the source term of the general transport equations (details are given in Appendix D). Moreover, special care is required at the boundary between the rotating and stationary computational domains, which is commonly referred to as the rotor-stator interface (RSI). Several RSI modeling approaches are readily available in commercial codes and are discussed in Appendix D. Ultimately, the recommendations of Toussaint *et al.* (2011) were followed in the present study, in which the mixing-plane model at the RSI was employed. Following the same authors' recommendations, the location of the RSI was placed three quarters of the way within the air gap (*i.e.* distance between rotor and stator, and closer to the stator).

The approach taken to define the fluid and solid computational domains is shown in figures 3.1(a-c). This approach consisted of simplifying the scale

Table 3.3: Summary of the seven cases considered and their associated turbulence model (TM), thermofluid properties (TFP), pole heat losses (PHL), and cell count in millions (M) for the solid (SD) and fluid (FD) computational domains.

Case Label	**TM**	**TFP**	**PHL**	**SD** [M]	**FD** [M]
C-$k-\varepsilon$	$k-\varepsilon$	Constant	Empirical	19.4	125.0
VP-$k-\varepsilon$	$k-\varepsilon$	Variable	Empirical	19.4	125.0
DC-$k-\varepsilon$	$k-\varepsilon$	Decoupled	Empirical	19.4	125.0
C-$k-\omega\ SST$	$k-\omega\ SST$	Constant	Empirical	19.4	190.6
VP-$k-\omega\ SST$	$k-\omega\ SST$	Variable	Empirical	19.4	190.6
FIS-$k-\varepsilon$	$k-\varepsilon$	Variable	Direct	19.4	125.0
FIS-$k-\omega\ SST$	$k-\omega\ SST$	Variable	Direct	19.4	190.6

model geometry (figure 3.1(a)), reducing the computational domain to a subsection with 90° periodicity (figure 3.1(b)), then further dividing it into the following six sub-components as shown in figure 3.1(c): i) the spider arms (fluid-rotating), ii) heated pole (solid-rotating), iii) rotor rim (fluid-rotating), iv) stator (fluid-stationary), v) frame (fluid-stationary), and vi) enclosure (fluid-stationary). All of the solid components of the heated pole were also included in the computational domain. The six subcomponents of the heated pole are shown in figures 3.1(d-e): i) the shell, ii) caps, iii) supports, iv) insulation, v) HEM, and vi) silicone. The subdivisions of both the fluid and solid domains of the computational domain required the use of special general grid interfaces (GGIs) to guarantee conservation of the intensive dependent variable between components with mismatching nodes.

The commercial code employed in this work numerically solved the integral form of the Reynolds-averaged governing transport equations:

$$\frac{\partial}{\partial t}\left(\int_{CV}\rho\phi dV\right)+\int_{A}\underline{\mathrm{n}}\cdot(\rho u_i\phi)dA=\int_{A}\underline{\mathrm{n}}\cdot\left(\Gamma_\phi\frac{\partial\phi}{\partial x_i}-\rho\overline{u_i'\phi'}\right)dA+\int_{CV}S_\phi dV, \tag{3.7}$$

using finite-volume methods (FVMs) to discretize the mathematical models. The discretized algebraic approximations to the models were solved use iterative algebraic multi-grid methods. The convergence of all quantities of interest was deemed satisfactory when their relative change over ten-thousand iterations was less than ±1%.

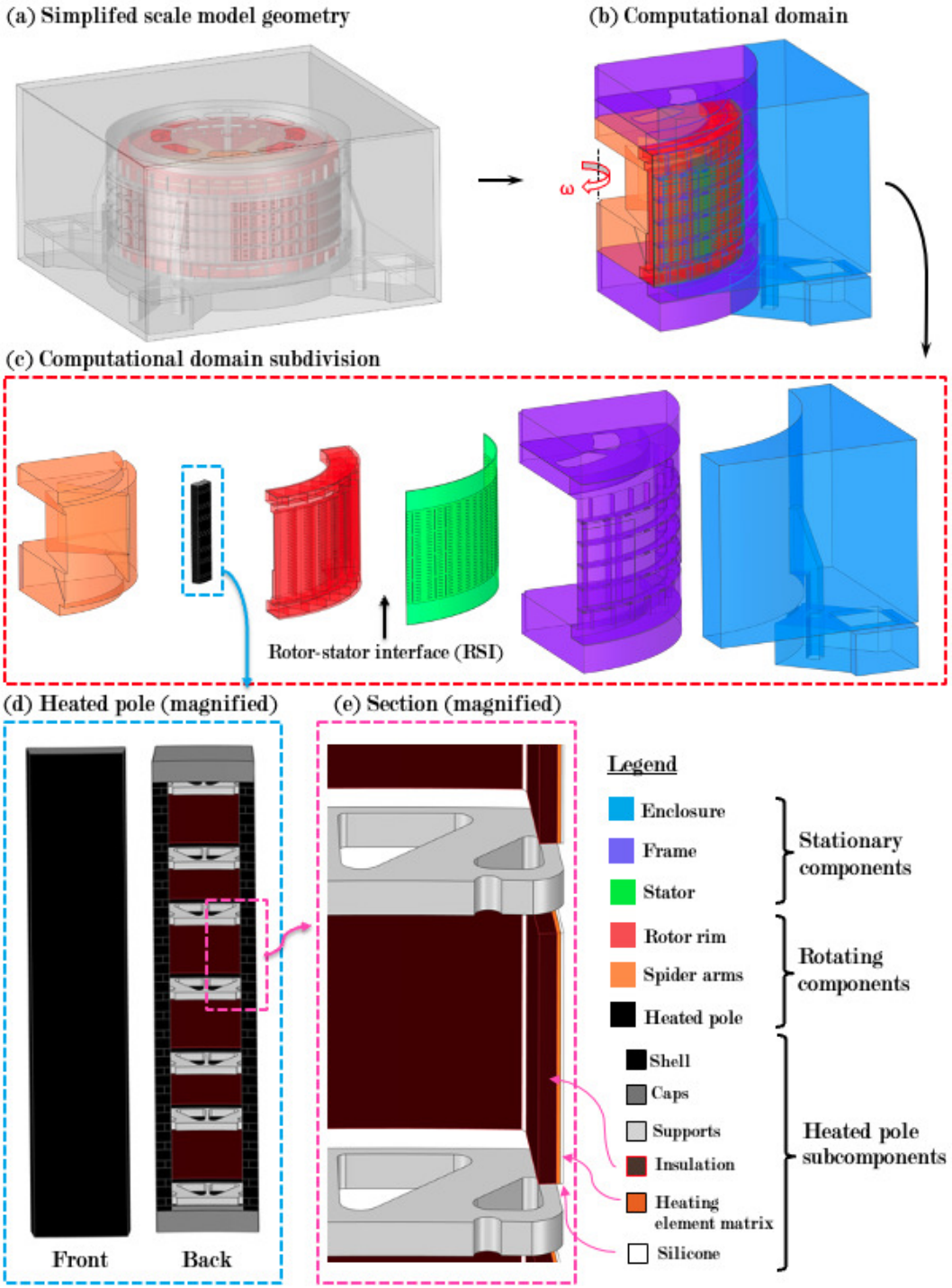

Figure 3.1: (a) Simplified scale model geometry. (b) Computational domain showing the clockwise rotation (ω). (c) Subdivisions of the computational domain showing rotating and stationary domains and the rotor-stator interface. (d) Magnified view of the front and back sides of the heated pole. (e) Magnified section view of the heated pole showing its six subcomponents.

3.1.2 Boundary and Initial Conditions

Since the air flow within the computational domain was modeled as a closed circuit (*i.e.* no inlet nor outlet boundary conditions were required as in Moradnia *et al.* (2014*b*)), only four boundary conditions were imposed on the fluid domain. First, the no-slip condition was imposed along the surfaces of every wall within the computational domain. The second and third boundary conditions, illustrated in figure 3.2(a), consisted of imposing the scale model's steady-state rate of rotation of 300 rpm, and applying the periodicity condition along the 90° section cuts. The final boundary condition on the fluid domain, illustrated in figure 3.2(b), consisted of uniformly dissipating the energy transported from the heated pole to the flow by convection at all outer vertical and horizontal boundaries of the fluid domain.

The computational domain of the solid pole (see figure 3.1) consisted of a thin (1.27 mm) stainless steel shell equipped with an array of insulated heating elements connected to the rotor rim via seven aluminum supports. To emulate the numerical approach and experiments of Torriano *et al.* (2014), and to predict the heat transfer distribution through the subcomponents of the heated pole, four different types of boundary conditions were used. First, to simulate a pole heated by the Joule effect, uniform volumetric heat sources within the array of HEMs in the front facing interior surfaces of the heated pole (corresponding to powers ranging from 54 W to 225 W and illustrated in figure 2.12(a)) were prescribed. Second, as shown in figure 3.2(c), the contact resistances on the 45 surfaces between the pole and its supports/caps were specified according to the recommendations of Torriano *et al.* (2014). Third, constant-temperature boundary conditions were specified based on the measurements of Torriano *et al.* (2014) at the interface between the seven aluminum supports and the rotor-rim (see figure 3.2(d)). Lastly, as shown in figure 3.2(d), the PHL

resulting from natural convection within the 315 interior surfaces of the shell were modeled using two approaches. The first approach (employed in cases-C, VP, and DC) consisted of directly modeling the losses using imposed empirical natural convection heat transfer coefficients (h) prescribed on all interior surfaces, based on average Nusselt number ($\overline{Nu}_L$) correlations that are proportional to the Rayleigh number to some power (Ra^n). Using this approach, the natural convective heat transfer coefficient varied from 2.3-22.4 $W/(m^2 \cdot K)$. The second approach (employed in case-FIS), consisted of directly modeling the fluid within the shell and applying the same constant-temperature boundary condition imposed at the support and rotor-rim boundary.

Because only steady-state conditions were of interest, the initial (or guess) conditions were prescribed using the experimental results of Hudon *et al.* (2011). Thus, the temperature of the fluid was specified to be equal to its measured steady-state value, as was that of the solid components. The rotational rate was also set to the steady-state value of 300 rpm. Lastly, the velocity field was initialized using the average values from the simulations of Toussaint *et al.* (2011).

3.2 Model-Based Design Experiments

Model-based design (MBD) is a technique that alters selected features in the computational domain in experimentally validated numerical models, with the aim of improving its performance using numerical tools (rather than experimental ones). Validation of the numerical model proposed in the previous section provided the required confidence to subsequently perform a series of MBD experiments in which the ventilation circuit of IREQ's scale model was modified with the aim of improving the performance of the model with respect to the original (*i.e.* current) design. In the present research, MBD experiments investigated increasing the surface area of the spider arms, restricting

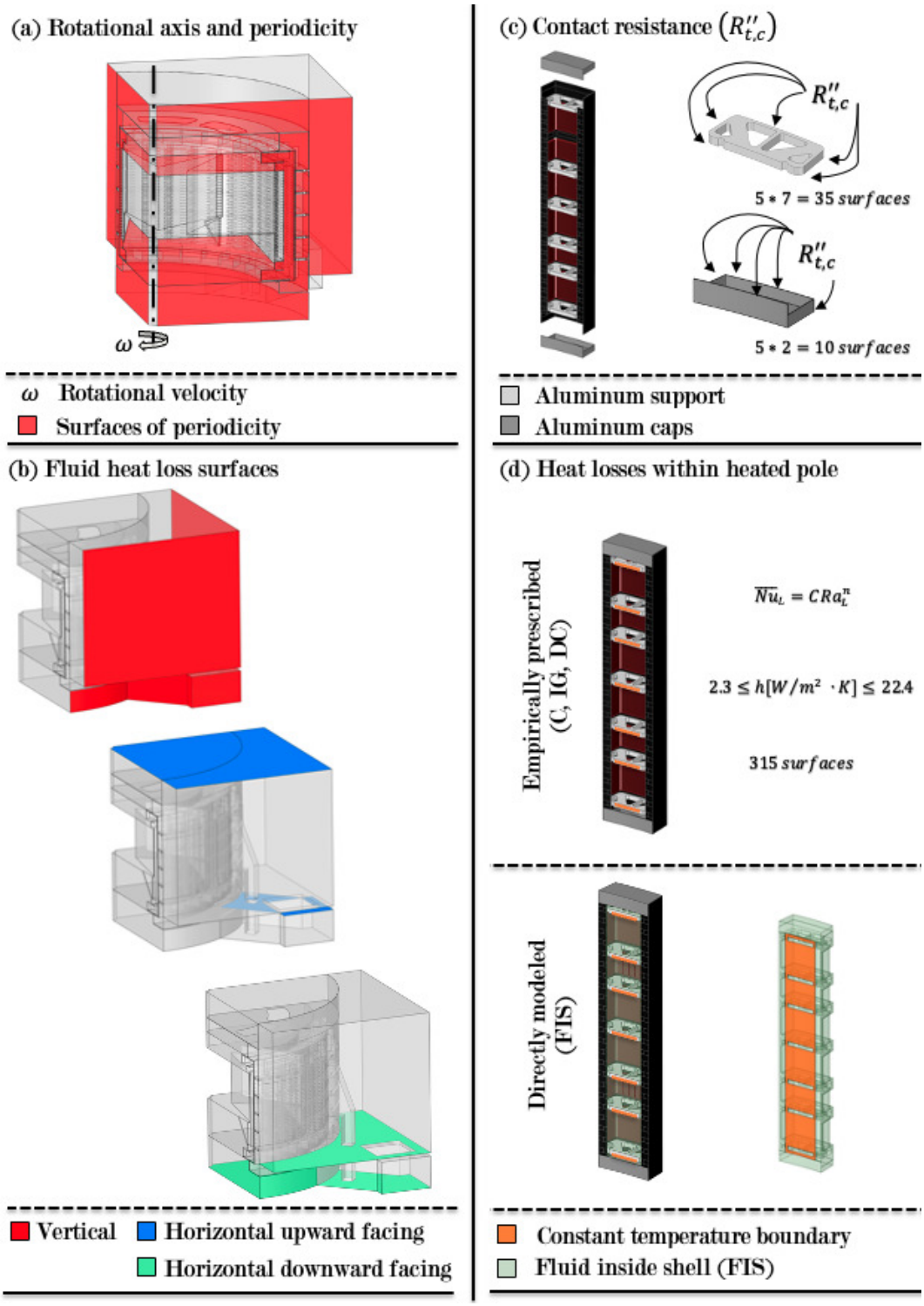

Figure 3.2: Boundary conditions of the fluid (a-b) and solid (c-d) computational domains. (a) The rotational axis and periodic surfaces. (b) The surfaces upon which the heat transfer rate is prescribed. (c) The contact resistance between the metal components. (d) The approaches used to model the pole heat losses (PHL) from the interior surfaces of the heated pole: empirical Nusselt number relations (C, VP, DC) and direct modeling (FIS).

the rotor inlet, and modifying the pit openings, all while monitoring the effects of the modifications on the (global and local) flow and (global and local) heat transfer quantities of interest.

Both the numerical simulations of the ventilation circuit of IREQ's scale model by Toussaint *et al.* (2011) and the experimental measurements of the temperature distribution of the scale model's heated pole by Torriano *et al.* (2014) exhibited non-uniform axial distributions of the flow and temperature within the scale model, which may be attributed to the axial asymmetry in the spider arms. As shown in figure 2.5 and highlighted in figure 2.19, the eight spider arms of the scale model start with a considerable length and thickness and reduce to a small wedge near the bottom of the rotor. The axial height of the wedge zone covers 30% of the rotor rim ducts. The large frontal area of the spider arms is responsible for pushing the flow through the rotor rim. However, imposing a uniform axial configuration of the spider arms would increase the frontal area by 35%, which could potentially increase the mass flow rate passing through the lower position of the rotor.

Investigation of several proprietary ventilation configurations of hydroelectric generators demonstrated that those with open rotor inlet configurations were more susceptible to overheating than those with partially closed rotor inlets. However, the sample size was small and the size of the hydroelectric generators and the rotor inlet openings varied. Even with this limited information, it was deemed worthwhile to reduce the inlet area by 25%, to determine the impact of doing so on the mass flow rate passing through the rotor rim, as well as on the average/maximum temperatures of the scale model's heated pole.

The numerical simulations of Toussaint *et al.* (2011) and the experimental measurements of Bach *et al.* (2015) both demonstrated that the flow passing

through the pit opening was predominately exiting (rather than entering). The authors of the latter study claimed that the differences in the results between the two studies might be attributed to differences in the computational domain and the actual geometry at the pit outlet in the rotating scale model. Thus, in this work, the computational domain was modified to more accurately reflect the geometry, to quantify its effect on the mass flow rate passing through the pit openings. Moreover, the results of the numerical simulation of the flow within the ventilation circuit exhibited a large tangential component of the velocity at the bottom and outer edge of the scale model's enclosure. The flow in this region impinges on the outlet of the pit opening, resulting in a net outflow. Therefore, in an attempt to prevent the flow from exiting the pit outlet, a flow deflector was added to the computational domain to investigate its effect.

CHAPTER 4
Thermal Mass Flow Meter: Measurements and Innovations

The present chapter is divided into four sections. The first reviews the measurement campaign performed at Paugan (a hydropower plant owned and operated by Hydro-Québec) to provide the necessary context in which the improvements to the thermal mass flow meter (TMFM) were undertaken as part of the present research. This review includes a discussion of the original TMFM developed by Venne *et al.* (2018) for use within in-service hydroelectric generators, and the results of the measurements undertaken at Paugan with this device. The second section discusses the imperfections in the design of the original TMFM; and the third section presents the improvements made to the TMFM as a part of the present research. The final section discusses the validation of the improved TMFM, which includes the characterization of the RTD boards and PIV measurements in the static model.

4.1 Measurement Campaign at Paugan

In the summer of 2019, an opportunity emerged in which IREQ researchers involved in the DIAAA project were able to undertake a measurement campaign at one of Hydro-Québec's hydropower plants, named Paugan, to gain valuable diagnostics data (such as temperature, vibration, air flow, and electrical/electromagnetic). This particular power plant is of the run-over-river type, with an installed capacity of 226 MW. Moreover, Paugan is one of Hydro-Quebéc's oldest power plants, as it was commissioned in the late 1920s. It is located in the lower Outaouais region of Quebéc, and is approximately 300 km from IREQ. The access gained for the installation of diagnostics tools allowed IREQ researchers to assess the utility of the TMFM prototype developed by

Venne *et al.* (2018) with the goal of obtaining valuable ventilation data from an in-service hydroelectric generator. To demonstrate the TMFM's capabilities, several prototypes and a DAQ unit were installed within the rotor of the hydroelectric generator, and measurements of the flow within the rotor rim ducts were undertaken.

4.1.1 Instrumentation of Several TMFMs

Prior to the installation of any device on an in-service hydroelectric generator, the equipment must be deemed capable of sustaining the significant centrifugal forces imposed by the rotor's rotation at both nominal and runaway speeds. This was achieved by performing both numeral simulations and experimental testing that had to be approved by engineers licensed by the *Ordre des ingénieurs du Québec* (OIQ) and not by the author of this thesis. Both the numerical simulations and the experimental tests performed by the author had to demonstrate to the licensed engineers that all equipment to be installed at Paugan was capable of withstanding centrifugal accelerations of 51 g at a nominal speed of 128.5 rpm, and 199 g at a runaway speed of 260 rpm for a rim radius of 5.6 m (219 in).

The necessary experimental tests and numerical simulations were undertaken using IREQ's scale model, which can apply 114 g at a nominal speed of 300 rpm, and 318 g at a maximum speed of 500 rpm. The numerical simulations, which were done using the finite element method (FEM), consisted of modeling both the TMFM and the structural support holding the DAQ unit at their required radial installation positions, applying the associated boundary conditions (at the runaway speed), and analyzing the stresses within the system (explained in greater detail in Appendix B). In summary, the mechanical simulations showed that all the components for both the TMFM and the structural support had factors of safety of 1.3 and 1 when exposed to an

acceleration of 318 g, which exceed the threshold required for installation at Paugan.

The experimental tests complemented the numerical simulations by installing both the TMFM and the structural support within the scale model and exposing them to increasingly large forces by rotating the scale model from 50 to 300 rpm for different lengths of time (also explained in greater detail in Appendix B). Ultimately, after several hours of operation, the equipment was inspected by licensed engineers and no features or abnormalities were observed, demonstrating its capability for withstanding the induced g-forces. Thus, all the required equipment was certified for installation on the rotor of an in-service hydroelectric generator at Paugan.

The installation of several TMFM prototypes and related subsystems within an in-service hydroelectric generator (G7) at the Paugan hydropower plant is illustrated in figure 4.1. Figure 4.1(a) demonstrates the first challenge associated with such an installation, which is providing the necessary electrical current that powers the heating elements of the TMFMs from a stationary power source to the (rotating) rotor. This was achieved by installing an electrical slip ring at the end of the generator's exciter. After connecting all the external stationary equipment to the slip ring, the transmission wires were then connected to the DAQ unit and the TMFMs. The former was achieved by passing the transmission wires through the generator's hollow shaft, as illustrated in figure 4.1(b), and connecting them to structural support fastened to the undercarriage of the rotor, as illustrated in figure 4.1(c). The support was installed as close to the rotor shaft as possible to limit the centrifugal forces applied to the sensitive electronic components within the DAQ unit. Lastly, three large wire shields (containing 12 wires per shield) were passed to the three TMFMs installed within the rotor rim ducts of the generator, as

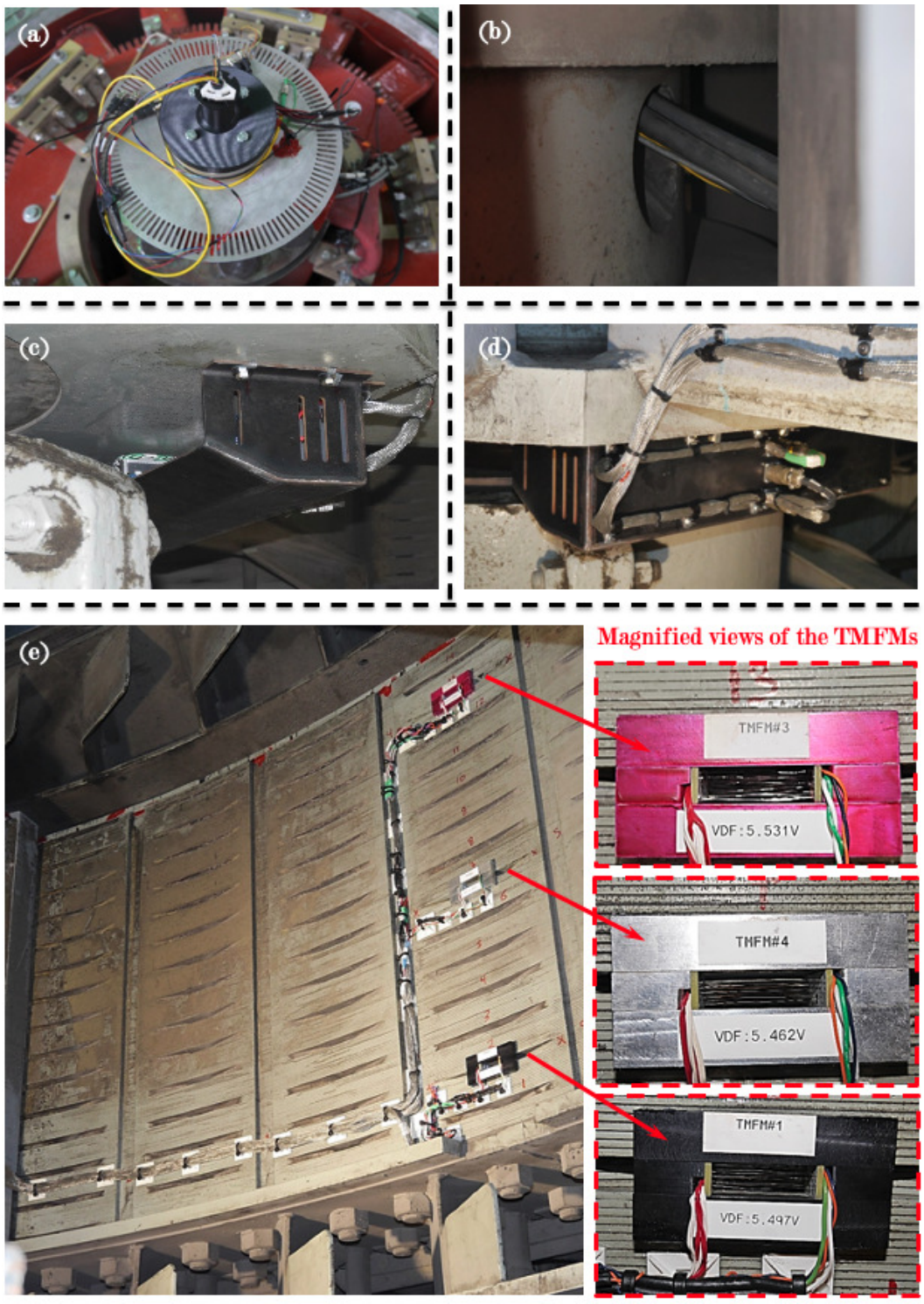

Figure 4.1: Instrumentation of the TMFMs at the Paugan hydropower plant. (a) Miniature slip ring. (b) Wires passing through the hollow shaft. (c) Structural support fastened to the undercarriage of the rotor. (d) Shielded wiring passing along the spider arm. (e) Three TMFMs installed at the inlet of different rotor rim ducts, highlighting their magnified views.

illustrated in figures 4.1(d) and 4.1(e). All the wires leading to the TMFMs were fastened at 15 cm (6 in) intervals to minimize any displacement while under rotation. To verify the TMFMs' functionality and to measure the mass flow rate in the upper, mid, and lower regions of the rotor rim ducts, three TMFMs (labeled 1, 3, and 4, and color coded black, silver, and pink) were installed in the third, seventh, and thirteenth rows of the middle column of rotor rim ducts (as shown in figure 4.1(e)). This arrangement enabled three measurements of the mass flow rate along the middle column, which would permit the detection of related variations within the rotor rim ducts in the axial direction.

4.1.2 Flow Measurement Within the Rotor Rim Ducts

The flow measurements within the rotor rim consisted of verifying that the deduced mean velocity obtained by the TMFMs was not affected by the hydroelectric generator's magnetic field nor by the thermal conduction from the TMFM's heating element, which could negatively impact the temperature reading of the (metallic) RTD wires. Other tests were planned, but not undertaken on account of two blown fuses in the power management system, which left only TMFM #1 (in the lower region) operational during the tests. This issue could not be resolved prior to start-up because of the strict time frame allocated to these experiments, given the tight scheduling of the "down-time" of hydroelectric generators imposed by Hydro-Québec. (There are high costs associated with offline generators.)

To verify that the generator's magnetic field did not influence the mean velocity obtained using the TMFM, the opening of the wicket gates (or inlet guide vanes) of the hydraulic turbine were adjusted to obtain a given generator power output, and once achieved, the TMFM's injected (or supplied) power was fixed during an acquisition period of 120 s. For this experiment, three

TMFM injected power inputs were utilized (41, 55, and 75 W) for each of the four generator power outputs considered (0, 24.7, 25.4, and 30.5 MW). The results of the experiment for a TMFM injected power of 55 W are given in figure 4.2(a), and in table 4.1. Table 4.1 depicts the mean values of the deduced velocity and their standard deviations for each experiment. The results indicated that the measured values of velocity were within ±5% of the average value for the experiments undertaken at the four generator power outputs. To verify that the power injected to TMFM's heating element did not influence the measured mean velocity, the former was varied at each generator power, and the mean velocity was measured over the same acquisition period of 120 s. The injected (TMFM) powers tested (41, 55, and 73 W) resulted in temperature differences between the inlet and outlet of the TMFM of 15°C, 20°C, and 25 °C, respectively. For a given generator power output of 25.4 MW, the deduced mean velocity for each injected power was very similar, as observed in figure 4.2(b). Specifically, the variation in the mean velocity for each case was less than ±2% from its average value. The different combinations of the measured velocity summarized in table 4.1, demonstrate that the variation in the measured mean velocities in the rotor rim duct about the average value was within 9% with a maximum standard deviation of 8% (both within acceptable margin of error (10%) of the device). This unique measurement campaign demonstrated that the developed TMFM was still a prototype that would benefit from further improvements to be undertaken at Hydro-Québec. Moreover, it is also worth noting that this measurement campaign at Paugan was historic for Hydro-Québec given that this was the first time in the history of the company that the flow within the rotor of a hydroelectric generator was measured.

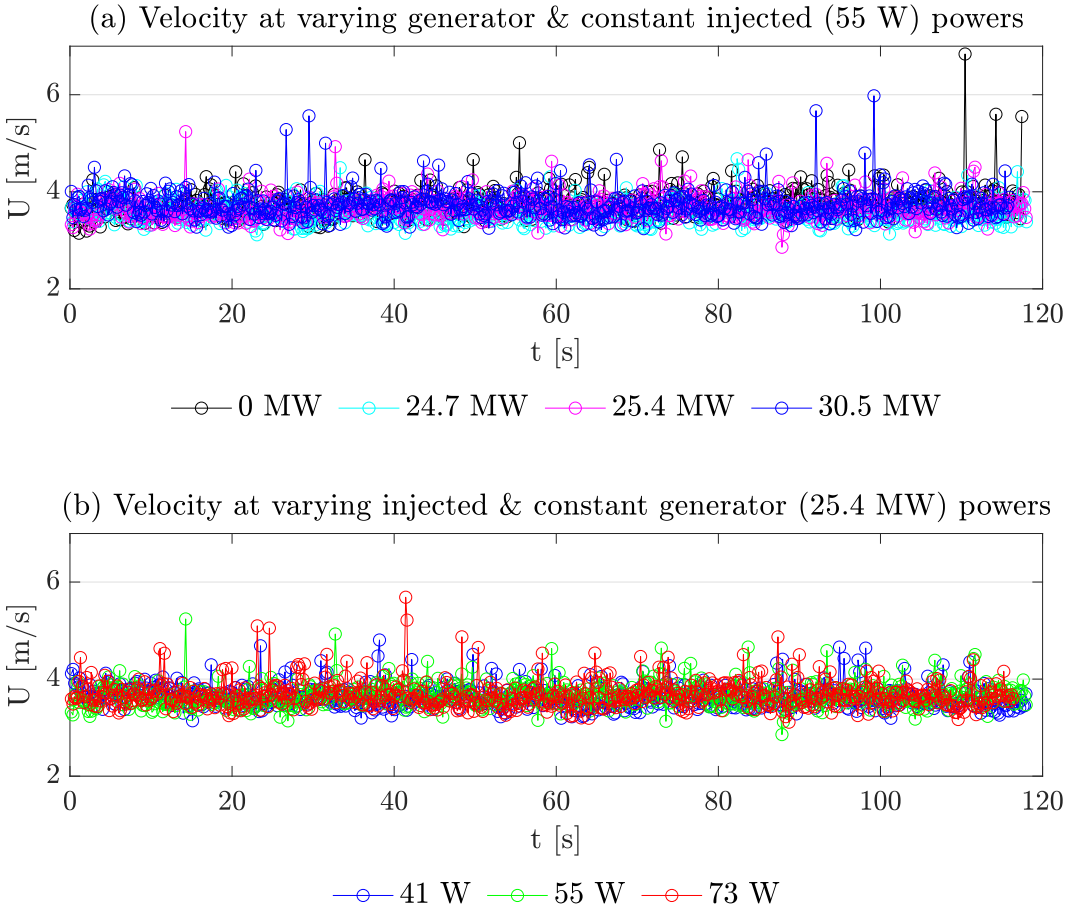

Figure 4.2: Time (t) series of the mean velocity (U) measured by a TMFM at Paugan. (a) The effect of varying the generator output power (0, 24.7, 25.4, and 30.5 MW) for a constant TMFM injected power of 55 W on the measured mean velocity. (b) The effect of varying the TMFM injected power (41, 55, and 73 W) for a constant generator output power of 25.4 MW on the measured mean velocity.

Table 4.1: Effect of varying the TMFM injected ($\mathcal{P}_{inj}$) and generator output ($\mathcal{P}_{HEG}$) powers on the mean velocity (U) and its standard deviation (σ_U).

$\mathcal{P}_{HEG}$ **[MW]**	0	24.7	25.4	30.5
$\mathcal{P}_{inj}$ **[W]**	**U [m/s]** $\pm$ σ_U **[m/s]**			
41	3.89 $\pm$ 0.26	3.55 $\pm$ 0.21	3.64 $\pm$ 0.23	3.74 $\pm$ 0.23
55	3.75 $\pm$ 0.29	3.57 $\pm$ 0.21	3.67 $\pm$ 0.24	3.74 $\pm$ 0.29
73	3.79 $\pm$ 0.32	3.58 $\pm$ 0.27	3.69 $\pm$ 0.28	3.72 $\pm$ 0.26

4.2 Improvements Required to the Original TMFM Design

The goal of the original TMFM designed by Venne *et al.* (2018) was to collect *in situ* data of the mean velocity passing through the rotor rim ducts of a hydroelectric generator. Although, this goal was attained, the prototype had many imperfections, with the most notable being the inability to conveniently replace blown fuses (described section 4.1.1). Other imperfections were also noted throughout different stages of the prototype's design cycle. For example, flaws in the RTDs were found during experiments undertaken in the lab as part of the work of this thesis. However, other more subtle, unfavorable design features were only observed during the fabrication process, and later during the on-site installation.

The RTDs developed as part of the original TMFM design of Venne *et al.* (2018) were found to have four main flaws: i) variability of the base resistance (R_0) between different prototypes; ii) a resistance-temperature behavior requiring prior heat treatment to stabilize; iii) a nonlinear resistance-temperature behavior in the range of 20-80°C, which is dependent on the manufacturing processes; and iv) the lack of repeatability in the temperature measurements, and thus, deduced mass flow rate measurement from one prototype to the next.

The variability of the base resistance between different prototypes was determined by manufacturing several prototypes and measuring the resistance of each respective prototype. The original prototype had two RTDs (inlet and outlet) comprised of six 50 μm diameter Balco (a nickel alloy comprised of 70% nickel and 30% iron) wires of 37 mm in length (totaling 22 cm when connected in series), with a base resistance of 23 Ω at 22.7 °C. However, the base resistance for the six RTDs manufactured for the three prototypes (utilized at Paugan) varied between 22.3-26.2 Ω, with an average value of 23.5 Ω and relative standard deviation of 6%. This variability was attributed to the

artisanal fabrication process, where many factors (such as weaving procedure, wire tension, and distance between the PCBs) led to differences in the wire length and diameter from one prototype to the next.

Once the fabrication process of the prototypes was completed, both the inlet and outlet RTDs were calibrated to quantify their resistance-temperature behavior. The latter was quantified by placing the prototypes in forced air convection ovens, installing reference RTDs near the inlet/outlet RTDs of each prototype, and recording: i) the resistance of the prototypes' RTDs, and ii) the reference RTD temperature when the surrounding air temperature reached steady-state (occurring approximately after one hour). This process was repeated at different temperature settings (from 20-80°C in 10°C increments), such that a sufficient temperature range was covered. However, when the prototypes were utilized to measure the air flow in the static model, the initial base resistance at the ambient temperature was never recovered at the conclusion of the test. It was concluded that the RTD wires required a low-temperature annealing process so that the heat from the TMFM prototype's heating element did not alter the resistance of the RTDs. Ultimately, this required two sets of heat treatment and calibration.

In the temperature range of interest (20-80°C), it was found that the resistance-temperature behavior of the Balco RTDs were nonlinear, and varied from one prototype to the next. To circumvent the time required to calibrate the RTDs of each prototype, a set of universal resistance-temperature calibration coefficients were preferred. However, due to the artisanal fabrication process, the use of common calibration coefficients could incur errors up to 14% in the inferred temperature values.

Lastly, the artisanal nature of the fabrication process also affected the measurement repeatability from one prototype to the next. The measurement

accuracy in the mass flow rate yielded by the original prototype was highly dependent on the location of the RTD wires at the outlet, over which the manufacturing process offered little control. Furthermore, differences in the wire location (caused by wire sagging after being heated) was found from one prototype to the next. To quantify the prototypes' measurement repeatability and accuracy, a validation experiment was performed, which consisted of installing three different TMFMs in the center duct of the static model and deducing the mass flow rate at six estimated flow speeds (1, 2, 3, 5, 7.5, and 10 m/s). For a given velocity, the differences mass flow rate yielded by the prototypes were found to be as high as 9%. Therefore, if these prototypes were to be used to compare the mass flow rate exiting the rotor rim ducts of the scale model (from row-to-row and column-to-column) it would be difficult to conclude that the different values obtained from each prototype would be due to flow variations within the rotor rim and not the variability in the measurement from one prototype to the next.

Although there was much emphasis on the uniformity and repeatability of the RTD measurements, there were also other characteristics of the prototype that could benefit from improvements. These characteristics were grouped into two categories: i) aspects complicating the fabrication process, and ii) those hindering on-site installation.

Improvements to the TMFM, which fell under the first category included the: i) cost/lead-time for the fabrication of the aluminum body; ii) assembly method; and iii) robustness/consistency of the design. The aluminum frame of the original prototype cost about $1,000 CAD and had a fabrication lead-time of two weeks, which was the component with the highest cost and lead-time. Replacing the aluminum frame with rapid-prototyping plastics available at IREQ would decrease the lead-time to a few hours at a fraction of the cost.

The assembly method of the original design was rather intricate and required weaving of a heating element wire through PCBs, which took several hours. Simplifying the connection between the mechanical and electronic components, and welding the heating element wires to the PCBs could drastically reduce the assembly time. Lastly, the original design was lacking robustness/consistency due to the fragility of the RTD wires and their manual assembly. Embedding the RTD wires within PCBs would make them less fragile and less susceptible to being knocked out of position, which would improve the precision of the outlet temperature measurement.

Improvements to the TMFM, which fell under the second category included: i) alternatives to soldered wire connections, and ii) better location of or avoiding blown fuses within the DAQ unit. In the original design, the wires connecting the DAQ unit to the prototype were directly soldered during an on-site installation, which increased the installation time. This issue could be resolved by embedding connectors within the faceplate. Although a fuse is helpful in protecting the electrical system, they were irreplaceable once the DAQ unit was fastened to the undercarriage of the hydroelectric generator's rotor. There were two ways that the issue could have been resolved: i) placing the fuse in a location that was accessible once the DAQ unit was fastened to the rotor, or ii) eliminating them by making it impossible for excess currents to pass in areas that would damage the system.

4.3 Improved TMFM Design

To address the design aspects of the original design that required improvements (highlighted in section 4.2), a new and improved TMFM was developed herein as a part of this research. The new design included: i) a frame made from a high-temperature rapid-prototyping thermoplastic; ii) an alternate orientation and fixation method for the heating element; and iii) a structure made

entirely of PCBs. To achieve the aforementioned changes, the new design required: i) material testing; ii) CHT simulations; iii) a new electronic structure; and iv) mechanical simulations, respectively allowing: i) the characterization of the mechanical properties of the plastic used in the rapid-prototyping process; ii) the determination of the ideal RTD placement to deduce the outlet bulk temperature; iii) a purely electronic interface; and iv) the verification of the mechanical integrity of the system. Ultimately, the design mentioned in the subsequent sections of this Chapter was patented by Torriano *et al.* (2021*a*) and its description was published internally at IREQ by Torriano *et al.* (2021*b*).

4.3.1 Overview of the new TMFM Design

The differences between the design of Venne *et al.* (2018) and the new design are illustrated in figure 4.3; and a detailed list of the changes in key parameters is given in table 4.2. Both figure 4.3 and table 4.2 demonstrate the many changes implemented in the new design, the two major ones being: i) a structure made entirely of rapid-prototyping plastics and PCBs, and ii) vertically-oriented and welded heating element wires.

As was noted earlier, the aluminum components of the mechanical structure were replaced by rapid-prototyping materials and PCBs to reduce the amount of fasteners/parts, and to simplify the assembly process, which consequently reduced the lead-time. Ultimately, the design improvements led to a reduction in parts by a factor of two (from 32 to 16).

The structural components serve as an anchor to position and hold the electronic components within the rotor rim duct and prevents them from becoming a projectile within the rotating generator. In the original design, several fasteners were used to link four pieces of aluminum together, which were then fastened to the electronic components. Using rapid prototyping,

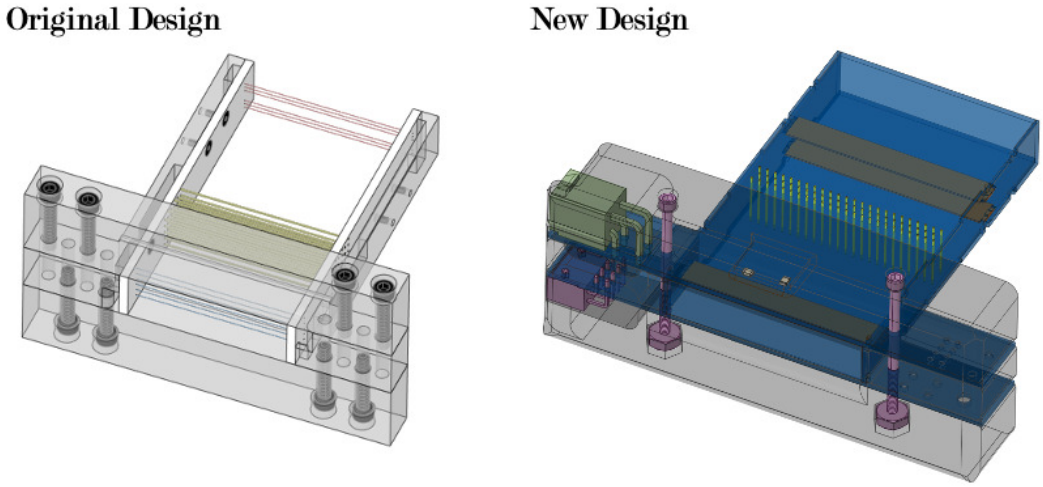

Figure 4.3: Original and new TMFM designs.

Table 4.2: Parameters of the original and new designs.

Group	Name	Original	New
Quantities	Inlet/Outlet RTD wires [#]	6/6	1/2
	Heating element (HE) wires [#]	30	71
	Fasteners [#]	12	2
	Parts (omitting HE) [#]	32	16
Geometric	HE wire diameter [μm]	406	330
	RTD wire diameter [μm]	50	76 x 17
	RTD wire length [mm]	37	4,700
	Inlet height/width [mm]	37.0/11.2	45.1/9.3
	Hydraulic diameter [mm]	17	16
Material	RTD	Balco	Copper
	HE	Nichrome	Nichrome
	Frame	Aluminum	ULTEM
Electrical	Current [A]	0-5	0-4
	Voltage[V]	0-50	0-31
	HE Resistance	10	12
	Inlet/Outlet RTD Resistance	23/30	23/60
Thermal	$\Delta T[^{\circ}C]$	20	20
	$T_w[^{\circ}C]$	<250	90-120
	$\mathcal{P}_{inj}$ [W]	30-170	0-81
Cost	Structural components [$CAD]	1000	37
	Electronic components [$CAD]	10	63

the mechanical components were simplified to one solid face-plate, with three openings: one to provide a smooth entrance for the air to enter the duct, and the remaining two to hold the fasteners needed to anchor the electronic components to the face-plate. Furthermore, the latter was made of polyethermide (ULTEM) 9085 resin, a flame-retardant, lightweight, high-performance thermoplastic with a high (153°C) heat deflection temperature (HDT). This feature dictated the choice of ULTEM over other materials, such as acrylonitrile styrene acrylate (ASA), having an HDT of 98°C and acrylonite butadiene styrene (ABS), having an HDT of 96°C, because the face-plate gad to be capable of withstanding higher operating temperatures. However, there were also other advantages of fabricating the face-plate by way of rapid prototyping rather than conventional methods, which included reducing the lead times from several weeks to a few hours using a Stratasys Fortus 450mc fused deposition modeling (FDM) printer, and reducing the production cost from about $1,000 CAD to $37 CAD.

The electronic components of the new design connect to one another forming an electronic structure which creates the electrical path required to pass the current to the heating element and RTDs. In the previous design, this was achieved using two parallel PCBs, assembled with the heating elements and (fragile) RTD wires using a jig. Additionally, the improved electronic structure included an enclosed duct made of two T-shaped boards and two side boards, which decreased the hydraulic diameter by 6%, but provided better thermal insulation. To facilitate on-site installation, two Molex connectors, one for the RTDs and the other for the power/voltage supply were added. The only disadvantage of this new feature is that it leads to a 15 mm protrusion of the PCBs outside of the rotor rim duct. To resolve the fragility and non-linearity of the RTDs, very thin copper wires were embedded into the PCBs to protect

them from the environment. All the PCBs were manufactured in China and had a lead time of less than two weeks. The assembly of the aforementioned electronic components consisted of: i) soldering the three RTD boards to the side PCB boards; ii) soldering the Molex connectors to opposing sides of the two T-shaped boards; iii) soldering the T-shaped boards to the side boards to form the electronic structure; iv) fastening the electronic structure to the face-plate; v) passing 71 wires (bent in an L-shape) through the 71 holes of the T-shaped PCBs; and vi) performing 142 welds to bond the heating element wires to the PCBs. Although, soldering four PCBs together and two connectors together, passing 71 small wires through two PCBs, and performing 142 welding operations may seem daunting, each task required 30, 60, and 90 min, respectively, which combined was less than the time required to weave the heating element wire through the PCBs of the previous design.

The wires of the heating element in the new design were placed vertically to: i) align the principal axis of the thermal expansion stresses at an angle of 90° to the axis of the RTDs; ii) provide a more uniform heating; iii) shorten the wire length to make a more reproducible heating element; and iv) facilitate the welding of the wires to the PCBs. One of the imperfections in the original design was that the principal axis of the thermal stress was inline with the RTD wires; by making this axis perpendicular to the wires of the RTDs, the thermal expansion of the heating element no longer influenced the resistance of the RTDs. The original design's heating element wires were also parallel to the longest side of the rectangular rotor rim duct; thus, large portions of the flow above and below the heating element were unheated. Positioning the wires vertically (parallel to the short side of the rectangular duct), left smaller portions of unheated air, and, consequently provided more uniform heating. Placing the wires vertically also reduced the wire length by a factor of three,

making it easier to place a straight wire through the PCBs. However, changing the wire orientation also affected the required quantity and diameter of the heating element wires. To obtain the same resistance and maintain the staggered transverse and longitudinal positioning of the wires suggested by Venne (2017), 71 wires (3 rows of 24, 23, and 24 wires, respectively) with a diameter of 330 μm were used. Lastly, a vertical orientation of the heating element provided a larger and more accessible surface, and thus, facilitated the welding process. Laser welding was chosen because it is capable of reaching temperatures between 300-3,000°C (Dagel *et al.*, 2016), which was well within the required range for nichrome (1,400°C). For the required application, a 6V-laser welder by Z-Tech Advanced Technologies (figure 4.4(a)) was used to weld the wires of the heating element to the PCBs. Furthermore, the input parameters illustrated in table 4.3(a) were utilized, which led to a successful weld, as can be observed in figures 4.4(b-e). Nevertheless, figures 4.4(b-e) also demonstrate that over the 142 welds, variations in the weld quality were present. For example, some welds lacked the proper fusion (figure 4.4(b)), whereas some did not have a sufficient amount of material (figure 4.4(d)), and only a few had the correct amount of fusion (figure 4.4(e)). Ultimately, the purpose of the weld is to create an electrical contact, thus even a cold weld would provide this. However, a cold weld could momentarily disconnect when overheated or when installed in a rotating hydroelectric generator. Therefore, all parameters that could influence the weld quality should ideally be controlled. Preliminary qualitative tests showed that the parameters/processes critical to a successful weld could be classified into four groups: i) the laser welder inputs illustrated in table 4.3 (including: the spot diameter (D_{spot}), pulse power ($\mathcal{P}_{pulse}$), laser exposure time (t_{exp}), pulse frequency (f_{pulse}), and pulse shape ($\mathcal{S}_{pulse}$)); ii) manufacturing tolerances (the hole clearance between the PCB and nichrome

Table 4.3: 6V-laser welder input parameters.

$D_{spot}\,[mm]$	$\mathcal{P}_{pulse}\,[kW]$	$t_{exp}\,[ms]$	$f_{pulse}\,[Hz]$	$\mathcal{S}_{pulse}$
0.8	1.4	3.0	1.0	Square

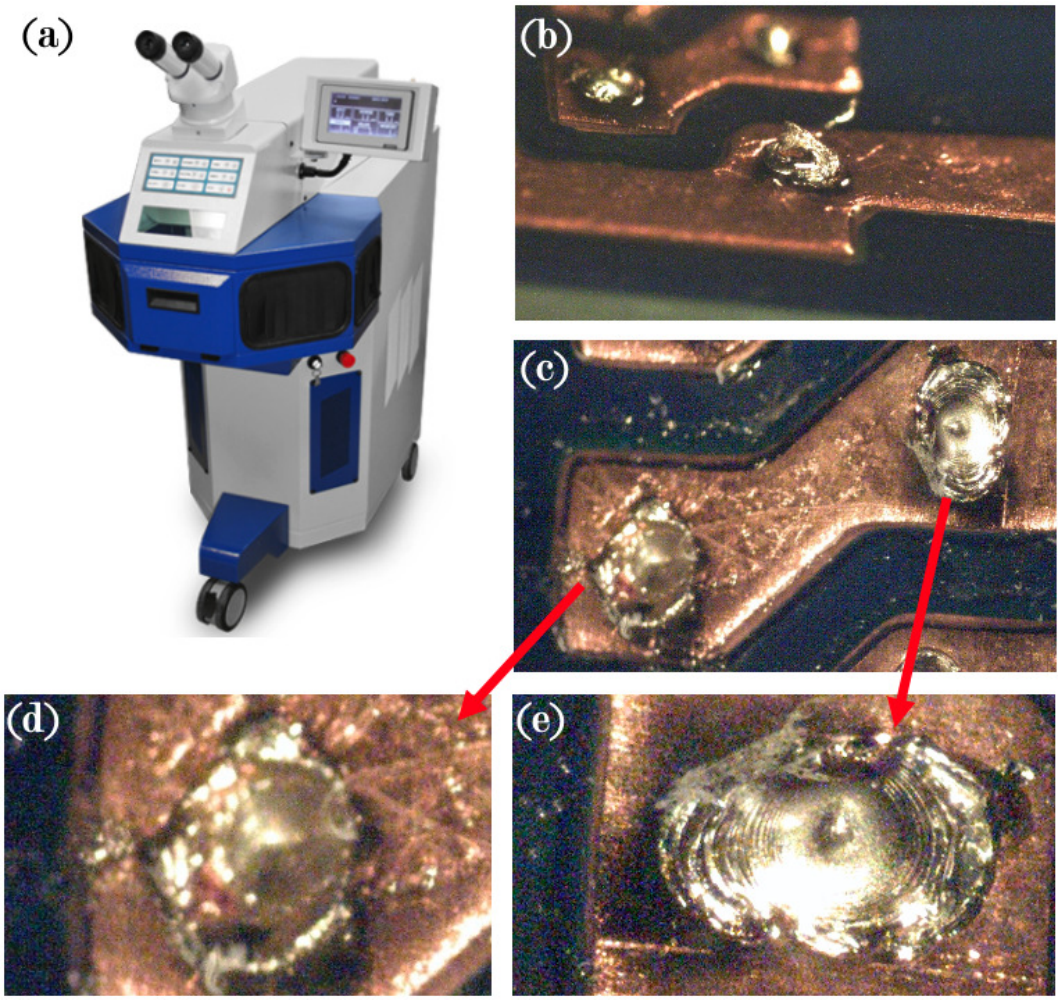

Figure 4.4: Laser welder utilized to weld the nichrome wires of the improved TMFM design. (a) 6V-laser welder by Z-Tech Advanced Technologies used to weld the nichrome wires to the PCBs. (b) Side view of a cold weld. (c) View of two welds showing a weld missing material (d) and an optimal weld (e).

wire); iii) assembly procedure (excess wire length passing the PCB); and iv) operator skill (ability to effectively align the laser target perfectly inline with nichrome wire). To obtain 142 perfect welds, these parameters/process would have to be tuned/automated. Although the process could be further improved, it showed sufficient promise to commence the design process for an improved TMFM.

4.3.2 Material Testing

Among the required improvements to the original design, was the aluminum frame, which affected the fabrication/assembly process. As previously described, the remedy to this issue was to use in-house rapid-prototyping to fabricate the mechanical structure in a single component. However, the mechanical properties of the plastics used for rapid prototyping are seldom quantified. The values of such properties are necessary inputs to FEM models that are required to demonstrate that a given prototype is capable of withstanding the centrifugal forces to which it is subjected when installed in a hydroelectric generator. Thus, in collaboration with Lévesque & Pichette (2020), three mechanical traction tests under a controlled environment were performed to validate the mechanical properties of the plastics used: i) an ambient temperature test; ii) a heated (70°C) test; and iii) a 100 hour thermal-aging test. The material test samples were printed in two out of the three possible configurations illustrated in figure 4.5(a) (XZ and XY), and followed the ASTM D-638-14 standard with the specimen dimensions depicted in figure 4.5(b). The Fortus 450mc rapid prototyping machine uses a FDM technology, which is a material extrusion process that builds components by depositing a hot plastic filament in a layer-by-layer fashion, which thus have inherently anisotropic mechanical properties. For example, parts created using FDM are more likely to delaminate or fracture when pulled in the Z-axis or perpendicular to the

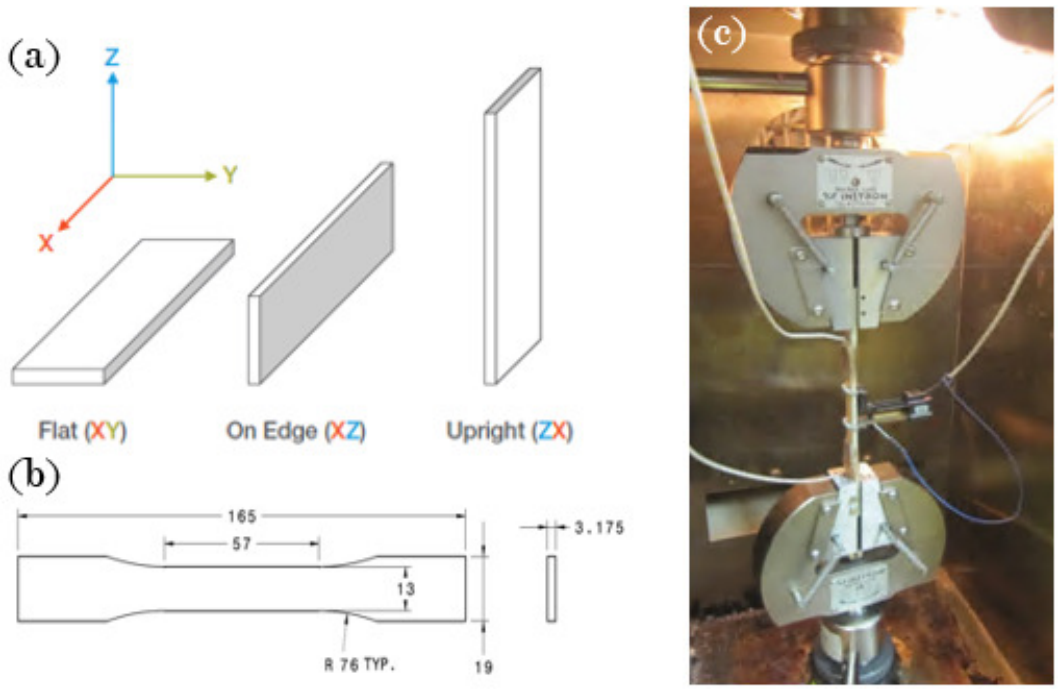

Figure 4.5: Characteristics of the test specimen and the experimental setup of the material characterization tests. (a) The three possible FDM printing orientations. (b) Dimensions of an ASTM D-638-14 specimen. (c) The temperature-controlled servo-hydraulic traction machine.

Table 4.4: Mechanical properties of ULTEM 9085 at different test temperatures (T_{test}) and FDM printing orientations ($\mathcal{O}_{print}$).

T_{test} [°C]	$\mathcal{O}_{print}$	σ_y [MPa]	σ_U [MPa]	$\mathcal{E}$ [GPa]	ν_{mech}
20	XZ	45.15	75.30	2.52	0.4
	XY	41.96	65.45	2.42	0.4
70	XZ	41.15	60.95	2.40	-
	XY	38.38	52.37	2.22	-
70*	XZ	40.32	59.00	2.41	-
	XY	39.02	54.17	2.37	-

*Tests conducted after 100 hours of thermal aging

axis of deposition (XY-axes). However, since the printing orientation depends on many factors (*e.g.* hole orientations, part size, *etc.*), both configurations were tested. The three tests used an enclosed temperature-controlled servo-hydraulic traction machine with a 10 kN load cell, for which the test setup is shown in figure 4.5(c), which depicts a material specimen between the jaws of the traction machine equipped with an extensometer to measure both the longitudinal and transverse deformations to obtain the material's Poisson's ratio (ν_{mech}). Thus, the ambient temperature test consisted of pulling several samples apart until failure to obtain the mechanical properties (*e.g.* yield stress (σ_y), ultimate stress (σ_U), Young's modulus ($\mathcal{E}$), and Poisson's ratio) at a temperature of 20°C. The second and third tests were similar to the first except only the longitudinal deformation was obtained and the temperature was increased to a temperature of 70°C. This temperature was chosen as it corresponded to the highest temperature that the plastic face-plate would experience when the heating element is powered during an on-site installation. The third test exposed the samples to 100 hours of thermal aging at the same temperature to quantify the material's mechanical integrity after prolonged exposure at the operating temperature. The results for all the tests are given in table 4.4 and demonstrated that a 50°C temperature increase reduced the yield stress (σ_y) by 9% and the ultimate stress (σ_U) by 20%. Furthermore, the thermal aging test had little to no effect on the mechanical properties. Thus, a minimum yield stress of 30 MPa and a Poisson's ratio of 0.40 were used for the FEM simulations as conservative estimates.

4.3.3 Conjugate Heat Transfer Simulations

To deduce the mass flow rate using a TMFM, it is necessary to accurately measure the bulk temperature downstream of the heating element. Furthermore, since the length of the scale model's rotor rim ducts (for which the

TMFM was designed) are only 61 mm, the flow passing through the heating element is not thermally fully developed when it reaches the outlet RTDs; thus, the RTDs must be strategically placed to measure the bulk temperature of the flow. In the original design by Venne *et al.* (2018), the strategic placement of the RTDs was determined experimentally using hot-wire anemometry. However, it was demonstrated that CHT simulations could be employed to determine the RTD placement within $\pm 1\%$ of the hot-wire experiments. Therefore, CHT simulations were performed to determine the optimal location of the outlet RTDs in the new design of the TMFM. Formulation of the mathematical model for the numerical simulations consisted of specifying the governing equations and boundary/initial conditions that underlie the physics of the flow passing through the TMFM.

Specifying the governing equations of the fluid (air) flow required the estimation of the Reynolds number (or the flow speed and hydraulic diameter). The hydraulic diameter of the rotor rim ducts of the scale model in which the new design was installed was 20 mm, but reduced to 16 mm when the improved TMFM was inserted within the duct (as compared to 17 mm with the original design of Venne *et al.* (2018)). The flow speed is difficult to estimate, because the insertion of the TMFM within a given rotor rim duct restricts the flow passing through it, and the flow velocity within the rotor rim ducts of the scale model have been shown to vary from row-to-row and also from column-to-column, as demonstrated by the numerical simulations of Toussaint *et al.* (2011), which are illustrated in figure 4.6(a). Since the hydraulic diameters of the original and new design are similar, it was assumed for the initial design process that the blockage factor (*i.e.* $C_{\dot{m}} \equiv \dot{m}_{empty}/\dot{m}_{TMFM} \approx 2$) would be approximately the same as in the original design. To determine the flow speeds of interest, a histogram of the simulated radial flow velocities from the

(a) Radial velocity contrours exiting the rotor rim ducts

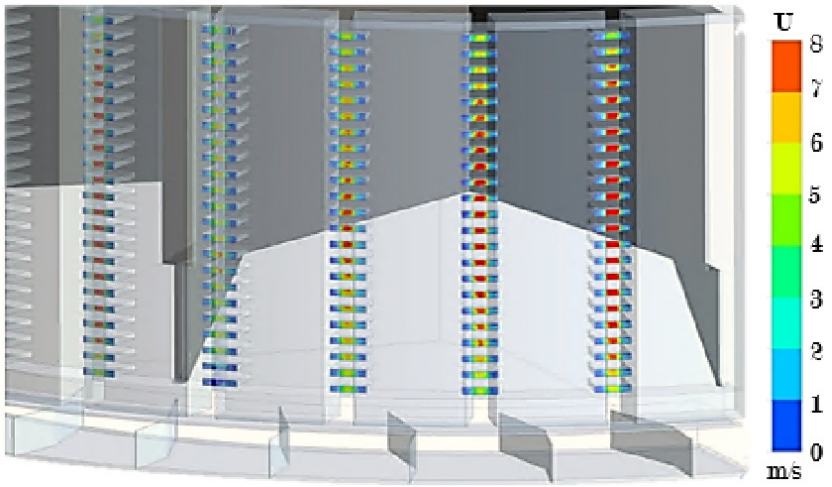

(b) Histogram of the radial velocity through the rotor rim ducts

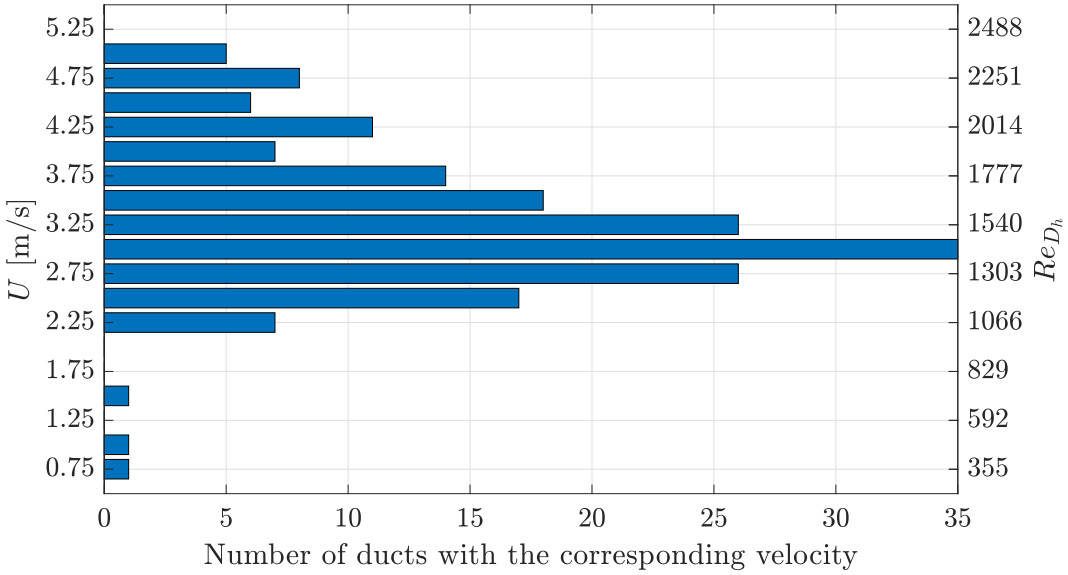

Figure 4.6: Numerical Predictions of the radial velocities exiting the 184 rotor rim ducts of the scale model. (a) Distribution of radial velocities exiting the rotor rim ducts from the numerical simulations of Toussaint *et al.* (2011). (b) Histogram of the average radial velocity exiting the 184 rotor rim ducts with corresponding Reynolds number (Re_{D_h}), based on the reduced hydraulic diameter due to the insertion of the TMFM.

184 rotor rim ducts were obtained from the data of Toussaint *et al.* (2011), and the Reynolds numbers based on the reduced hydraulic diameter (Re_{D_h}) were calculated using the flow speeds reduced by a factor of two (due to the assumed aforementioned blockage factor), as illustrated in 4.6(b). The estimated Reynolds numbers were always less than 2,400, indicating that the flow passing through the TMFM would be effectively be laminar. To determine the effect of different flow speeds on the placement of the RTDs, three nominal flow speeds (2.5, 3.25, and 4.25 m/s) spanning a range of the expected flow speeds in the rotor rim ducts were considered. For these three flow speeds, the Reynolds numbers based on the wire diameter (Re_d) of the heating element were all less than 40, implying that the flow in the wake of the heating element would be within the regime of symmetric Föppl vortices (according to Blevins (2001)), where no vortex shedding is present, simplifying the numerical simulations by permitting the simulations of steady laminar flow (in contrast with the original design, due to the reduced wire diameters employed in the new design's heating element). Therefore, the equations for the conservation of mass, momentum, and energy were specified for steady, incompressible, and laminar flow.

Once the governing equations were established, the boundary/initial conditions were specified for the fluid flow and heat transfer. Due to the symmetry in the XY plane in the new design illustrated in figure 4.7(a), only the upper portion of the flow was taken into account in the numerical (or calculation) domain. Thus, the inlet boundary conditions for the mass flow rate ($\dot{m}$) were 0.3, 0.4, and 0.5 g/s or half of the estimated restricted flow rates (*i.e.* 0.6, 0.8, and 1.0 g/s), which correspond to the aforementioned rotor rim duct flow speeds of 2.5, 3.25, and 4.25 m/s (when taking into account the blockage factor and symmetry condition). The remaining boundary conditions for the

flow consisted of an ambient pressure outlet and the no-slip condition on all the walls of the computational domain. Moreover, the inlet mass flow and outlet-pressure boundary conditions were both placed at the extremities of artificially constructed extensions of $4D_h$ and $5D_h$ in length, respectively, to reduce the influence of these boundary conditions from the regions of interest, as illustrated in figure 4.7(a). The boundary conditions for the heat transfer, consisted of an imposed heat flux (Neumann) boundary condition on the surfaces of the wires and specified temperature (isothermal) on the exterior walls of the computational domain. The value of the imposed heat flux was chosen to ensure that the difference between the bulk temperature at the duct outlet and inlet YZ planes remained at 20°C (which corresponds to the operating condition of the new design). The latter boundary condition was imposed due to the low thermal conductivity ($0.25\ W/m \cdot K$) of the glass-reinforced laminate material (FR-4) of PCBs, which is the material for the external walls. Lastly, the prescribed guess/initial conditions consisted of prescribing the flow speed in the axial (X) direction corresponding to the inlet mass flow rate, and the initial/guess air temperature was set equal to the ambient temperature of 20°C.

To determine the effect of the flow speed on the placement of the RTDs, three numerical simulations were performed corresponding to the three aforementioned flow speeds of interest, and for each simulation, the temperature along different configurations (locations and number of RTDs) of artificial post-processing (XY) planes (corresponding to the shape of RTDs) were analyzed and compared to the bulk temperature of the flow. The configurations considered variations in both the cross-stream (Z) and downstream (X) directions in the wake of the heating element wires, as illustrated by the different planes

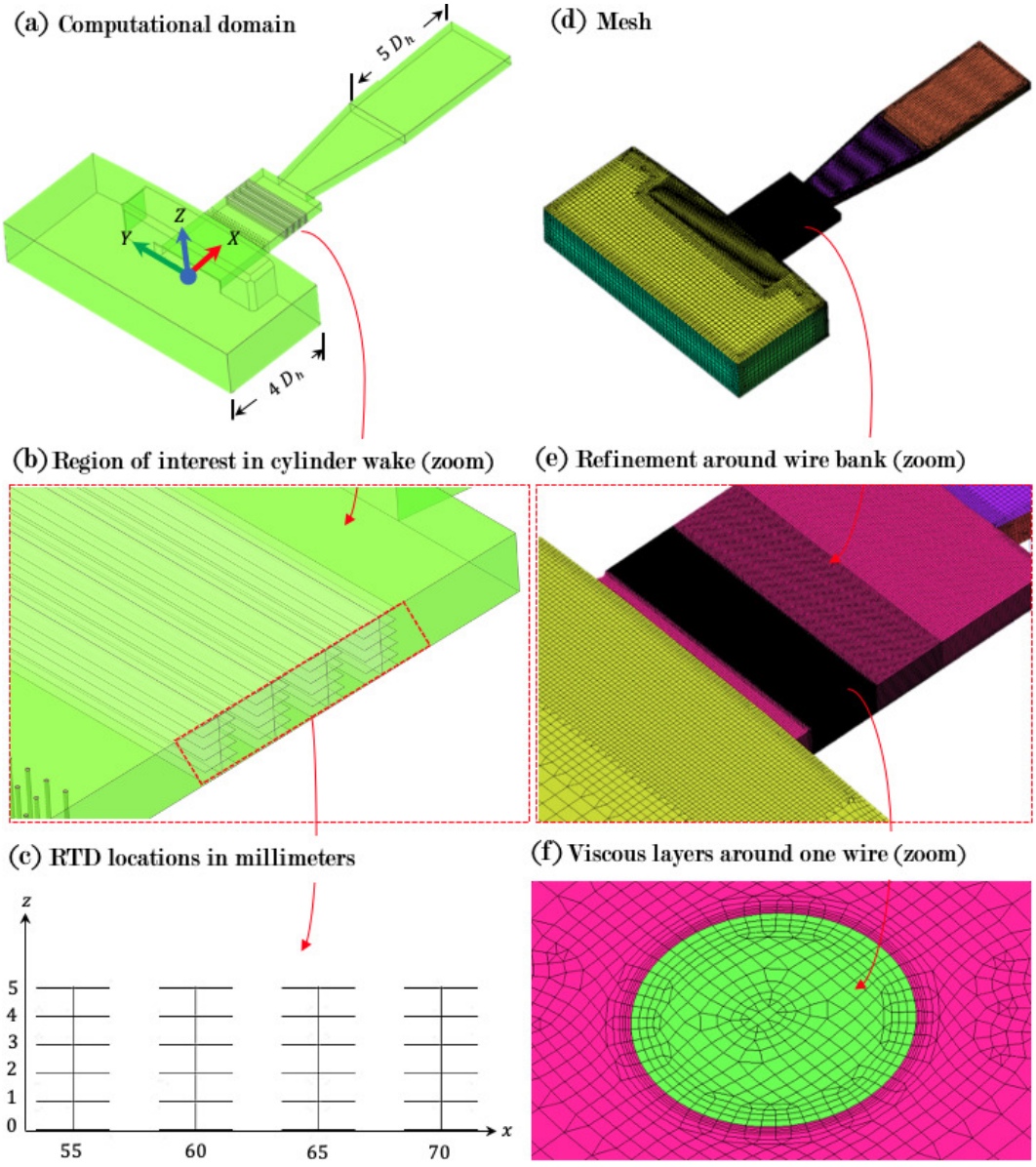

Figure 4.7: Details of the computational domain of the improved TMFM design. (a) Fluid computational domain. (b) Regions of interest in the wake of the heating element wires. (c) Post-Processing planes where the RTD locations (horizontal lines) were considered. (d) Mesh of the computational domain. (e) Mesh refinement around the wire bank. (f) Viscous layer around one of the wires.

shown in figure 4.7(b). Moreover, each plane's specific cross-stream and downstream locations from the center of the duct ($Z = 0$ mm), and inlet of the TMFM ($X = 0$ mm) are illustrated by the black lines in figure 4.7(c). The different configurations were determined based on the following practical considerations: i) an RTD too close to the heating element wires could measure temperature values greater than the bulk temperature; ii) an RTD too close to the restricted outlet; where zones of high velocity are present could measure temperature values less than the bulk temperature; and iii) any configuration over 3 RTDs would add unnecessary flow restriction and cost. Thus, three cross-stream configurations were considered: i) one RTD in the center-plane of the duct ($Z = 0$ mm); ii) two RTDs at mirrored locations from the center-plane of the duct in vertical (Z) increments of 1 mm, from 1-5 mm; and iii) three RTDs combining configurations of scenarios (i) and (ii). Furthermore, the variation in the downstream direction was also considered for each of the previous three scenarios (i-iii) at distances (X) of 55-70 mm in increments of 5 mm. Ultimately, the different configurations at each aforementioned cross-stream and downstream locations resulted in 44 different possibilities.

For each of the 44 potential RTD configurations, only one mesh was employed, because its effect on the flow was assumed to be negligible. The design of the RTDs for the new TMFM design consisted of plates which spanned the width (Z) of the duct, with a 6 mm length (X) and a thickness (Y) of 0.4 mm. Although these small plates would inevitably affect the flow field, this effect was judged to be minimal compared to the costs that would be required to generate 44 independent meshes. Thus, only the mesh illustrated in figure 4.7(d) was employed, and the average temperature along the surface of artificial post-processing planes (shown in figures 4.7(b) and 4.7(c)) where the RTDs would be placed was calculated. Furthermore, the mesh illustrated

in figure 4.7(d) consisted of 46 M and 6 M cells in the fluid and solid computational domains, respectively. The large quantity of cells was required to i) account for the different length scales between the duct and wires of the heating element, as illustrated in figure 4.7(e), and ii) capture the wall-effects of the flow around each wire, as illustrated in figure 4.7(f).

The computed velocity and temperature contours at the midplane (XY plane) are illustrated in figures 4.8(a) and 4.8(b), respectively. In the figures, the four black lines spanning the duct represent the downstream (X) locations of the RTDs. Note that the contours in figure 4.8 include the zone before the inlet of the TMFM (top), the zone within the TMFM (middle), and the zone at the outlet (bottom), which is restricted by the backside of the poles. The latter creates: i) small re-circulation zones in the corners along the sidewalls, and ii) a large zone of high velocity that increases in size as the speed increases, suggesting that the RTDs positioned at the downstream locations of 65 and 70 mm may not accurately capture the bulk temperature of the flow. The temperature contours are very similar in each case, as the heat flux imposed on the outer surface of the wires was increased to the level required to increase the bulk temperature by 20°C from inlet to outlet. To meet the aforementioned criterion, the injected power was found to be 12, 16, and 21 W, resulting in average wire temperatures of 96, 107, and 121°C, for the three respective flow speeds. At the downstream location of 55 mm, the temperature contours demonstrate that the flow has not yet sufficiently mixed to uniformly attain the bulk temperature at all positions in the cross-section. Although the analysis of the mid-plane velocity and temperature contours provided a good indication of the optimal downstream location, it did not consider any variations of the flow in the cross-stream direction.

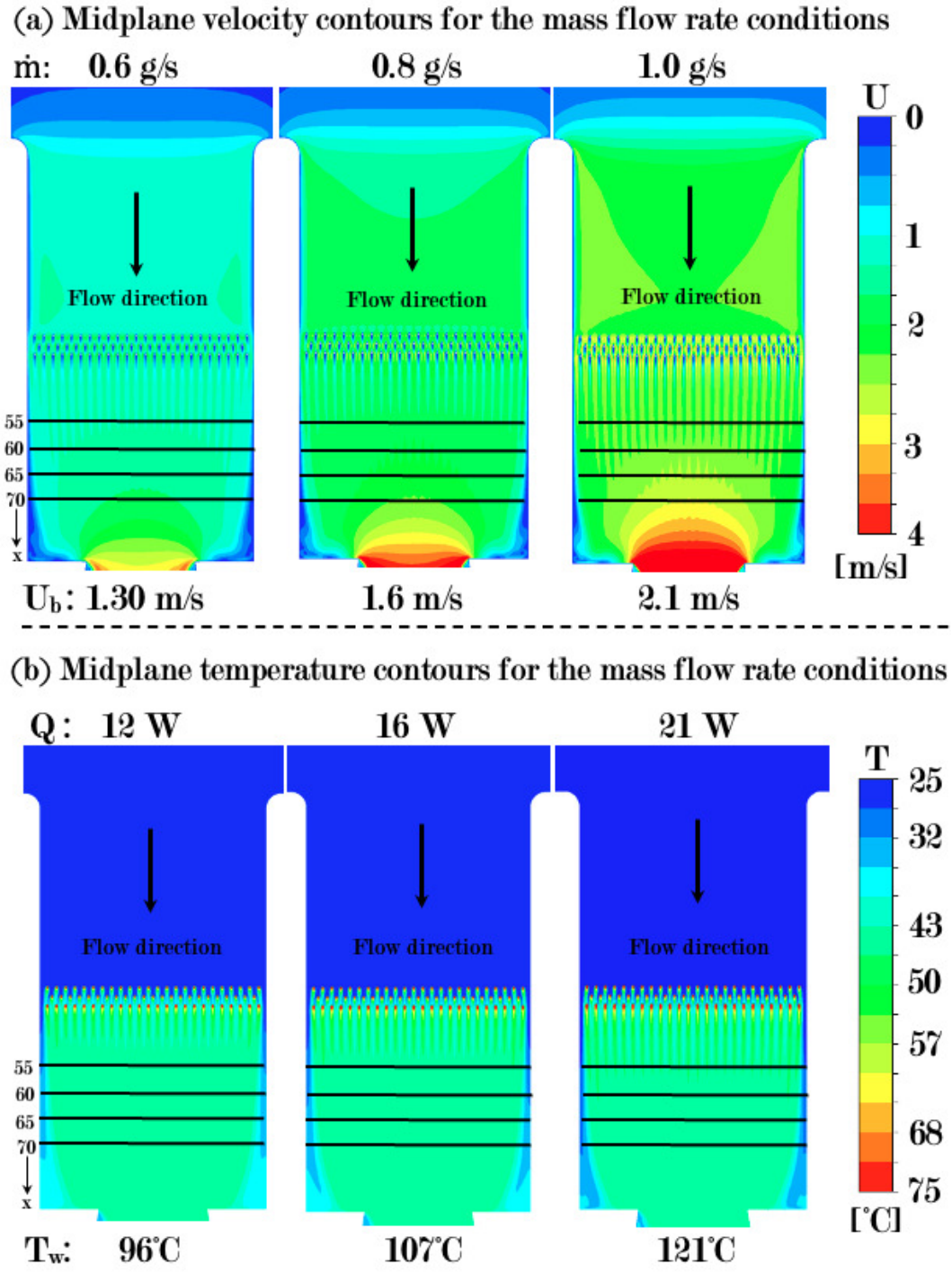

Figure 4.8: Results of the numerical simulations of the improved TMFM. (a) Velocity contours at the midplane indicating the mass flow rate ($\dot{m}$) and the bulk velocity (U_b) of the flow. (b) Temperature contours at the midplane indicating the energy injected into the flow (Q) and the wire temperature (T_W).

For each RTD configuration, the bulk temperature deviations ($|\Delta T_b|$), defined as the absolute value of the percentage difference between the predicted bulk temperature (T_b) and the estimated temperature on the artificial RTD surfaces (T_{RTD}) were calculated for each flow speed and are shown in figures 4.9(a-c). These results demonstrate that the flow speed and downstream/cross-stream configurations of the RTDs have an effect on how well the average temperature along the surface of artificial post-processing planes (representing the RTDs) approximates the bulk temperature of the flow. These results also indicated that the bulk temperature of the flow is more accurately approximated using the two-RTD configuration (placed at symmetric locations above and below the centerline) at the cross-stream location of ± 3 mm for any downstream location. To determine the best downstream location for the aforementioned configuration, the cross-stream location of ± 3 mm was isolated for the three flow speeds considered, as illustrated in figure 4.9(d). The results demonstrate that the two-RTD configuration positioned at this cross-stream location for each of the four downstream locations predicted the bulk temperature of the flow to within $\pm 2\%$. Thus, by combining the information highlighted in figures 4.8 and 4.9, it was concluded that the two RTD configuration at $Z = \pm 3$ mm and $X = 60$ mm, which can estimate the bulk temperature within $\pm 1\%$, was therefore the best choice.

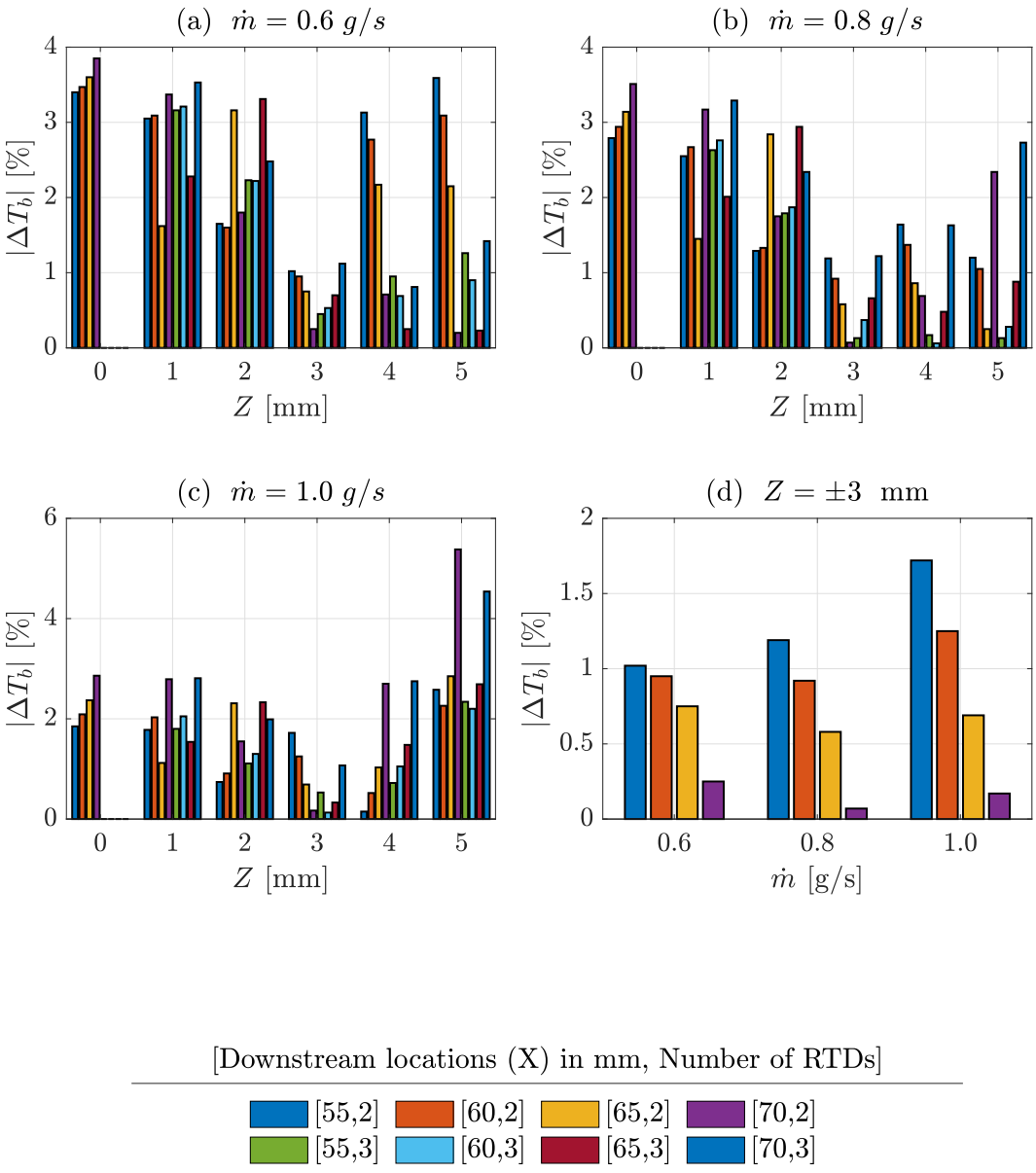

Figure 4.9: Simulated bulk temperature deviations ($|\Delta T_b| = |T_b - T_{RTD}|$) for the different RTD configurations and locations considered for the improved TMFM design. (a,b,c) Simulated Bulk temperature deviations at different cross-stream (Z) and downstream (X) locations, and for different RTD configurations: (1) one in the center ($Z = 0$ mm), (2) two symmetrically ($Z = \pm 1$, 2, 3, 4, 5 mm) placed RTDs, and (3) three RTDs, one in the center and two symmetrically placed above and below the centerline at the three different mass flow rates 0.6 (a), 0.8 (b), and 1.0 g/s (c). (d) The optimal cross-stream location ($Z = \pm 3$ mm)/configuration of two symmetric RTDs at different downstream locations (X).

4.3.4 Electronic Structure

Although in the new TMFM design, the aluminum face-plate of the original design was replaced with a rapid-prototyping plastic frame, the remaining components of the metallic frame were replaced with a newly designed electronic structure. The latter reduced the overall weight of the TMFM and created a thermally insulating barrier between the heated flow on the inside and the metallic rotor rim duct on the outside. Furthermore, the manufacturing of the electronic structure was outsourced to one sole provider and delivered within a week. This ultimately reduced the lead time required to develop a TMFM for a measurement campaign.

The electronic structure is illustrated in figure 4.10(a). An internal view is also shown in figure 4.10(b), demonstrating the final RTD arrangement. Both figures 4.10(a) and 4.10(b) depict the three main components of the electronic structure, which are made entirely of PCBs: the heater board (shown in figure 4.10(c)), the support board (shown in figure 4.10(d)), and the RTD board (shown in figure 4.10(e)). Each of these boards has a specific function allowing the TMFM to operate as designed.

The first major component of the electronic structure is the heater board (T-shaped PCB) depicted in figure 4.10(c). This board is the main component of the system and directs the current required to power the heating element and the RTDs to each of the respective components by way of two (white) Molex connectors. The connector on the right-hand-side of figure 4.10(c) has four pins for the voltage measurement on the board and directs the current required to power the heating element. The voltage (sense) measurement is made using a resistance divider near the heating element to compensate for the power losses in the connector leads. The current passing through the other two pins is directed through a unique series interconnection of 71 heating

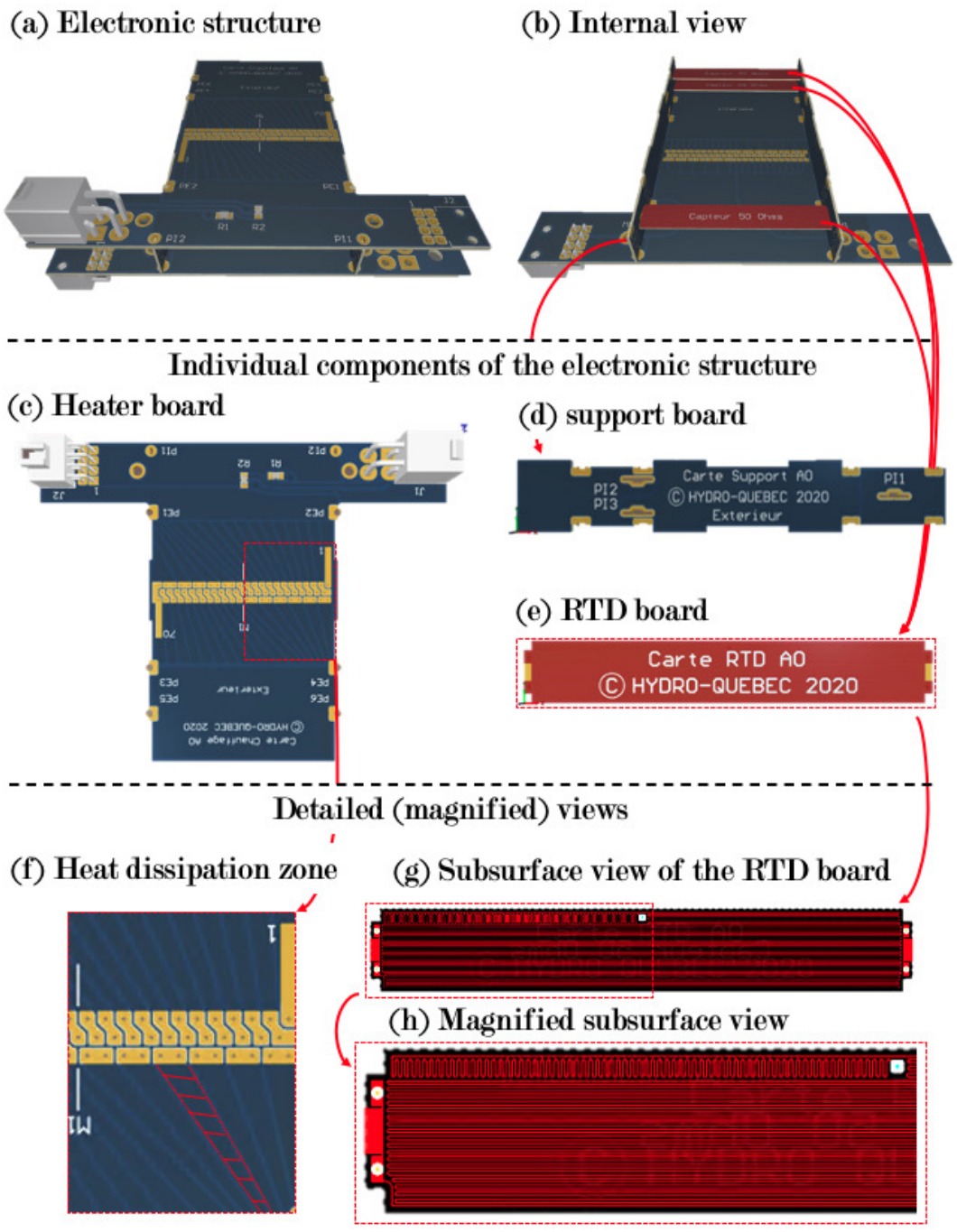

Figure 4.10: Views of the improved TMFM's electronic structure and its components. (a) Isometric view of the electronic structure. (b) Isometric view showing the internal components. (c-e) The three main components of the electronic structure: the T-shaped heater board (c), the support or side board (d), and the RTD board (e). (f-h) Detailed (magnified) views of: the heater board highlighting the heat dissipation zone (f), and an internal view of the RTD board (g) showing the copper track in the subsurface (h).

element wires embedded into the heater board. This allowed a symmetric heater board design that reduced the manufacturing costs, given that two are required on opposite ends of the electronic structure. Furthermore, each pad for the heating element wires were connected to a large zone of copper (illustrated in figure 4.10(f)), to dissipate the heat from the laser welding process. The quantity of copper utilized was chosen to improve the welding process, and the details are highlighted in the work of Torriano *et al.* (2021*b*). The other connector on the left-hand-side of figure 4.10(c) has eight pins for the two RTDs using the four-wire technique, which eliminates the error resulting from the resistance of the leads. The current passing through this connector on the heater board is passed through support boards to reach the RTD boards.

As was mentioned in section 4.3.1, the change in orientation of the heating element with respect to the RTDs improved the new design. This was accomplished using the symmetric support boards shown in figure 4.10(d), which provided both a mechanical support and an electrical connection between the other boards. The former fastened all the components together, which created an artificial duct that prevent the air flow downstream of the heating element from escaping to the metallic rotor rim duct at the exterior. The latter directed the current from the heater board to the RTD boards.

The final components of interest in the electronic structure are the RTD boards, illustrated in figure 4.10(e). They were 0.4 mm thick with a copper track embedded within them, as illustrated in figures 4.10(g) and 4.10(h). The copper wire was approximately 4 m in length, 76 μm in width, and 17.5 μm in height, to achieve a maximum resistance of 50 Ω per RTD board at an ambient temperature of 20°C. Two RTD boards were placed at the outlet, as illustrated in figure 4.10(b), following the results of the analysis in section 4.3.3. These two boards were connected in series creating one outlet RTD measuring 100

Ω, to improve the signal-to-noise ratio. Since the air entering the TMFM is at a uniform temperature, only one RTD board was needed.

Ultimately, the new electronic structure eliminated the need for fasteners used in the original design, which also reduced the manufacturing costs. The electronic structure consisted of only 5 components, since most of the boards were symmetric and cost $53 CAD. Therefore, the total cost of the new design was approximately $100 CAD, which is about ten times lower than that of the original design.

4.3.5 Mechanical Simulations

As part of the last phase of the design process, FEM simulations using ANSYS Mechanical were performed to verify the mechanical integrity of the new components. The approach used is illustrated in figure 4.11(a), and consisted of simulating the TMFM placed at a distance (R) of 1.135 m from the center of rotation, and imposing the maximum rotational speed of the scale model (500 rpm). The computational domain, shown in figure 4.11(b), was generated using tetrahedral elements for the frame and hexahedral elements for the fasteners and the PCBs. Rather than modeling a section of the rotor rim, the following boundary conditions (shown in figures 4.11(c) and 4.11(d)) were used: i) zero-displacement boundaries along the symmetry planes of the calculation domain (*i.e.* perpendicular to the XY and XZ planes) to prevent the TMFM from moving vertically and circumferentially, and ii) a zero-displacement condition on the back of the frame, where it makes contact with the rim to prevent radial motion. Furthermore, a (5 N) pretension force was applied to the fasteners to artificially assist their positioning in space and simulate their actual function. The results of the mechanical simulations shown in figures 4.11(e-g) demonstrated that the (von Mises) stresses (σ_{sim}) are much lower than the yield stress (σ_y) for the three major components. Moreover,

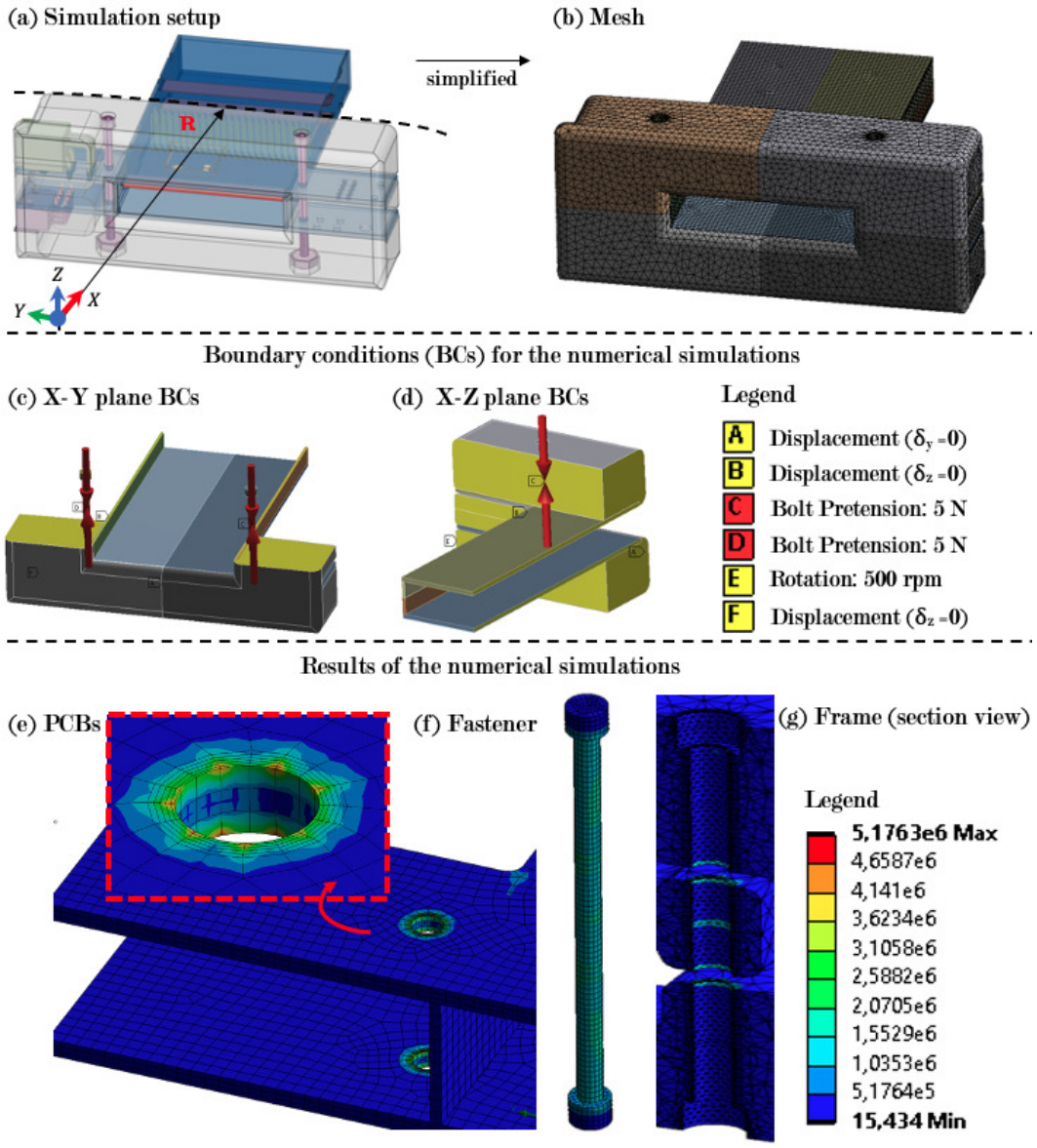

Figure 4.11: Mechanical simulation setup and results for the improved TMFM. (a) Simulation setup and placement of face-plate from the origin (R). (b) Mesh of the simplified domain. (c,d) Boundary conditions. (e-g) Contours of the von Misses stresses in Pascals for the PCBs (e), fastener (f), and frame (g).

Table 4.5: Factor of safety (FS) of the TMFM's components.

Component	**Material**	σ_y **[MPa]**	σ_{sim} **[MPa]**	**FS**
Frame	ULTEM 9085	38.38	2.84	13.5
PCBs	FR-4	241	5.18	46.5
Fasteners	ASTM A574	1055	3.21	328

table 4.5 highlights that all the components were well within the acceptable safety margins, as the factor of safety (FS) for each component was greater than ten. Thus, the mechanical integrity of the new design was deemed satisfactory given its capability to withstand accelerations greater than 318 g, which is more than two times the acceleration induced under normal operation (114 g) of the scale model, which was utilized for the initial validation tests.

4.4 TMFM Design Validation

After completing the design and subsequent manufacturing of the improved TMFM, its design was experimentally validated. The validation process was divided into two parts: i) those relating to the RTD calibration process, and ii) those related to the measurements in the static model. The former quantified the resistance-temperature relationship and variability in the base resistance (resistance measured at ambient conditions), and determined if the resistance-temperature calibration coefficients were universal. The latter quantified the TMFMs' ability to accurately measure the mass flow rate passing through a rectangular duct and the repeatability of the measurements from one prototype to the next. This was undertaken by characterizing the flow exiting a static model duct using PIV, with and without the TMFM installed.

4.4.1 Results of the RTD Characterization

Eighteen RTDs for nine different prototypes were calibrated to: i) quantify their resistance-temperature relationship; ii) determine the variability of their base resistance; and iii) check if their calibration coefficients were universal. To quantify the resistance-temperature relationship, a calibration process similar to one discussed in section 4.2 was employed, with the only differences being: i) the RTDs for each TMFM were immersed in a beaker of oil and then placed in a forced-convection oven (rather than simply being placed in the ambient

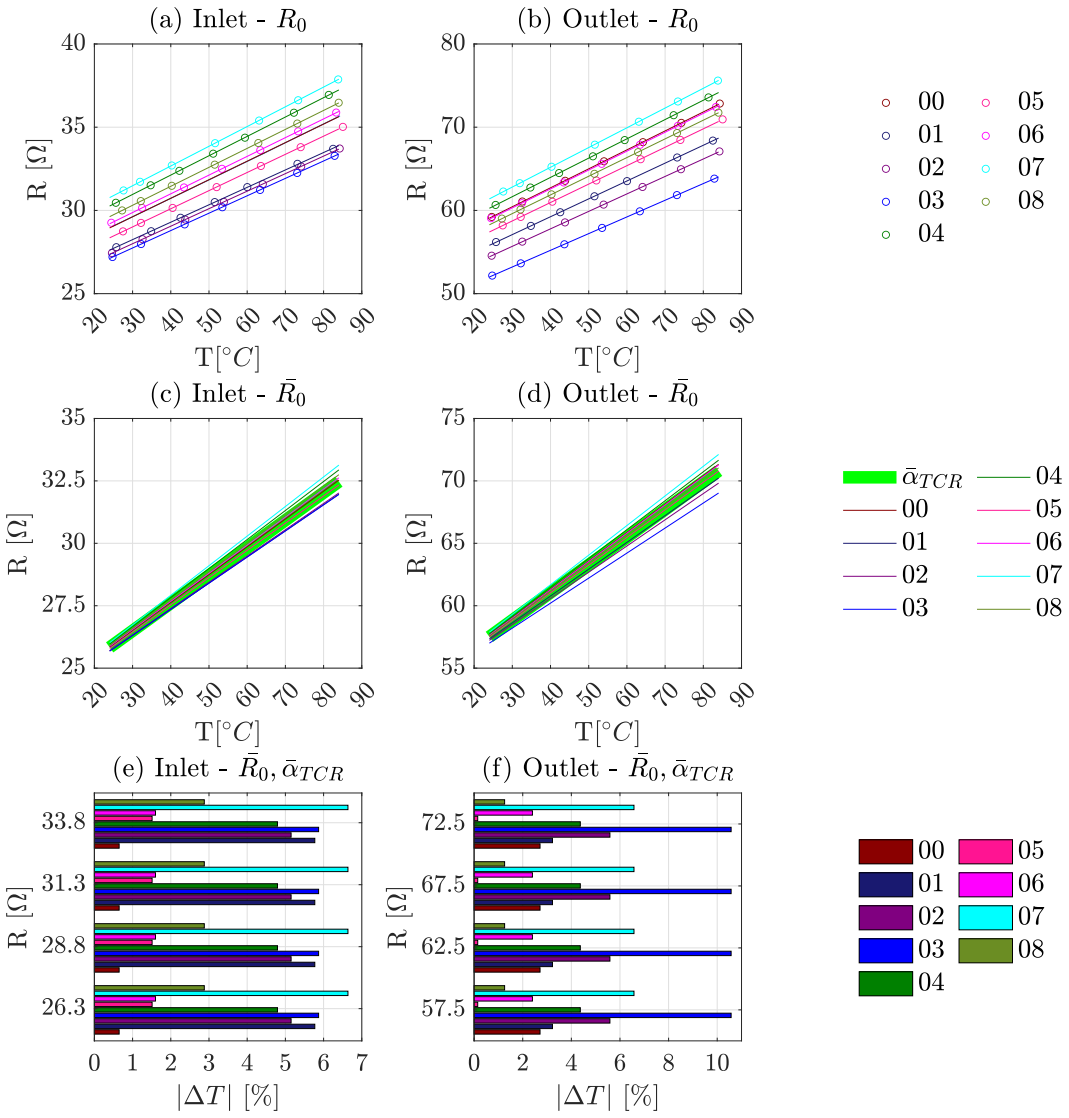

Figure 4.12: Resistance-temperature calibration curves for improved TMFM. (a,b) Calibration curves for the inlet (a) and outlet (b) RTDs for each the nine prototypes (00-08). (c,d) The resistance-temperature calibration curves with an averaged base resistance ($\bar{R}_0$) and one universal calibration curve using both an average TCR and base resistance ($\bar{\alpha}_{TCR}$, $\bar{R}_0$) for the inlet (c) and outlet (d) RTDs. (e,f) Percentage difference in temperature ($|\Delta T|$) for each prototype using the average base resistance ($\bar{R}_0$) compared to the average calibration curve ($\bar{\alpha}_{TCR}$, $\bar{R}_0$) for the inlet (e) and outlet (f) RTDs.

air, because the components of the new design could now be cleaned), and ii) only one reference RTD was needed per beaker, since all the RTD boards were immersed in the same beaker of oil. Thus, the resistance of each board was monitored simultaneously and measurements were taken when the oil in the beaker reached (thermal) steady-state (which took approximately one hour) at temperatures from 20-80°C in increments of 10°C. The resulting resistance-temperature curves for the nine inlet and outlet RTDs are illustrated in figures 4.12 (a) and 4.12(b).

From the results, it can be concluded that changing the material of the RTDs from Balco (original design) to copper (new design) resulted in an improvement, because it was characterized by a linear fit to the resistance-temperature curves:

$$R = \alpha_{TCR} T + R_0, \tag{4.1}$$

where R is the board resistance, T is the temperature of the surrounding medium (oil bath), α_{TCR} is the temperature coefficient of resistance (TCR), and R_0 is the base resistance. Using two PCBs connected in series for the outlet RTDs doubled the outlet RTD resistance when compared to that of the inlet RTD. However, both figures 4.12(a) and 4.12(b) also revealed larger variability in the base resistance than excepted. The inlet and outlet resistances were between 27-31 Ω and 52-62 Ω, respectively, which were: i) different from the expected values of 50 Ω and 100 Ω, and ii) varied between 15-20% from one board to another at ambient conditions. Lastly, no universal calibration curve was found. Even if an average base resistance ($\bar{R}_0$) were taken for each of the calibration curves, as illustrated in figures 4.12(c) and 4.12(d), considerable differences in the measured values of the TCR values were observed. Moreover,

the percentage difference ($|\Delta T|_i$) between i) the estimated average temperature ($T_{\bar{R}_0,i}$) approximated using the calibration curves with an average base resistance for each prototype and ii) the estimated universal temperature values ($T_{universal}$) approximated using a universal calibration curve (employing an average TCR ($\bar{\alpha}_{TCR}$) and base resistance($\bar{R}_0$)) for a given resistance (R):

$$|\Delta T|_i = \left|T_{\bar{R}_0,i} - T_{universal}\right| = \left|\frac{R - \bar{R}_0}{\alpha_{TCR,i}} - \frac{R - \bar{R}_0}{\bar{\alpha}_{TCR}}\right|, \tag{4.2}$$

were calculated. These values were found to be as high as 7% for the inlet RTDs and 10% for the outlet RTDs, as shown in figures 4.12(e) and 4.12(f). Thus, it was concluded that each RTD board must be calibrated prior to use and no universal calibration curve exists for the newly designed RTDs. However, upon further investigation of the PCB manufacturer's inspection sheets, supplemented by discussions with the PCB manufacturer led to the conclusion that the tolerances regarding the track width and height (which are parameters that affect the resistance of the RTD boards) were not satisfactory and imposing more stringent criteria in their manufacturing may resolve this problem in the future. However, the dimensional specifications of the copper tracks within the RTD boards were near the limits of current PCB manufacturing processes. Nevertheless, as technology progresses, an improved ability to achieve the necessary specifications may become more routine.

4.4.2 Results of the Static Model Measurements

The experimental methodology employed to validate the performance of the TMFM using the static model consisted of comparing an objective measurement to a baseline measurement. The objective measurement was defined as the measurement of the flow exiting the center duct of the static model using the TMFM itself (installed therein). The baseline measurement was defined as the measurement of the mass flow rate exiting the same static model

duct (with and without the TMFM installed) using PIV. Furthermore, a non-intrusive baseline measurement of the flow exiting the static model with and without the TMFM installed permitted the quantification of the blockage effect of the TMFM. The validation was undertaken at three different flow speeds, to determine whether the blockage effect was dependent on the flow rate.

To quantify the baseline flow rate exiting the center duct of the static model, the following parameters were specified: i) the nominal flow speed; ii) the number of vertical scans required to obtain the velocity contours at the duct outlet; and iii) all pertinent PIV parameters (interrogation area, time between pulse, and total number frames).

Three nominal flow speeds were chosen for the baseline and objective measurements such that comparative evaluations could be made to validate the performance of the TMFM. The chosen flow speeds approximately corresponded to: the lowest flow speed (2.15 m/s), the average between the minimum and maximum flow speeds (4.91 m/s) used in the numerical simulations for the TMFM (previously discussed in section 4.3.3), and the average flow speed exiting the scale model ducts (6.88 m/s) from the numerical simulations of Toussaint *et al.* (2011). However, these values were only approximately matched because the static model only provided control over the blower impeller rotational speed, which is only one of several factors that controlled the flow speed in this instance.

Having selected the flow speeds, the number of vertical scans was specified to obtain the velocity contours, and thus, baseline measurement for the mass flow rate at the duct outlet using PIV. Since the PIV system discussed in section 2.2.2 consisted of only one camera, only two velocity components in a plane perpendicular to the camera could be simultaneously obtained (referred

to as two-dimensional two-component (2D2C) PIV). Moreover, since the camera was positioned directly above the outlet of the static model's center duct (see section 2.2.2), only the velocity in thin sheets (or planes) perpendicular to the duct outlet plane and parallel to its width (long side of the rectangular outlet) of the duct could be obtained. Thus, to obtain the mass flow rate exiting the duct outlet, 15 vertical lines were used to assemble the two-dimensional velocity distribution parallel to the duct outlet plane. The lines were unequally spaced from the wall to the center of the duct, such that a higher density of line measurements were taken near the wall than at the center of the duct. Analogous measurements using a hot-wire anemometer were performed by Venne (2017), at 15 axial lines of 10 points each at the duct outlet plane to obtain the same velocity distribution. Venne (2017) found that for a flow speed of 6.88 m/s (corresponding to the highest flow speed of the baseline measurement), the integration error was approximately 1.5% for 15 axial lines spaced in the aforementioned manner when compared to numerical simulations of the rectangular duct. Thus, the same vertical line spacing were also used in the present validation. However, the number of points per line was determined by the PIV parameters

The three main parameters in the PIV measurements were the interrogation area, time between pulses, and total number frames. Using a 2048×2048 pixel Flow Sense 4M II camera positioned at a distance of one meter from a calibration target placed at the center of the duct outlet plane resulted in a field of view that was approximately 128×128 mm with a resolution of 16 pixels per millimeter. Given this field of view, the span of the duct outlet plane could either be divided into 25 or 50 windows, resulting in 25 or 50 velocity vectors across this span if 32×32 or 16×16 pixel interrogation windows were respectively used, since the outlet plane of the static mode duct

was approximately 50 mm wide. However, as was discussed in section 2.2.2, post-processing techniques typically employ interrogation windows that overlap by 50%, such that, a 32×32 and 16×16 pixel interrogation window would provide 50 and 100 velocity vectors, respectively. Although a larger number of points spanning the measurement is generally desirable, a constraining parameter is typically the quantity of seeding particles found within an interrogation window. In practice, it is best to have between six to ten particles within the interrogation window (Keane & Adrian, 1990). Thus, a 16×16 pixel interrogation window (corresponding to 1×1 mm) was chosen for the proposed experiments as approximately ten particles were found within windows of such size. In conjunction with this constraint, the time between pulses was varied for each of the three flow speeds and each of the 15 lines. The time between pulses was selected such that the particles travel a quarter of the length of the interrogation window in the selected time interval (Adrian & Westerweel, 2011). Since the quarter-length of the interrogation window was 0.25 mm, the time between pulses were of the order of 115, 50, and 40 μs for the three respective flow speeds of 2.15, 4.91, and 6.88 m/s. However, the precise values for each of the 15 lines varied, as the average velocity of a given line was not the same as the average velocity at the duct outlet plane. Lastly, the method for determining the number of frames required for converged statistics was determined by verifying the convergence of the average velocity as the number of frames increased, and it was impossible to determine *a priori*. Finally, 2,700 frames (the maximum number of frames allowed by the camera) were used for the experiments. Furthermore, the optimal acquisition frequency (between two pairs of pulses) required to maximize the laser output energy was 4 Hz, and thus, the maximum data acquisition time was 675 s, corresponding to an acquisition interval of 0.25 s between frames. Since the time scales of the

flows of interest were much greater than the acquisition rate, averaging the flow speed over 675 s was more than sufficient.

Utilizing the aforementioned parameters, the baseline measurements illustrated in figures 4.13(a-f) were obtained and their corresponding uncertainties are provided in Appendix E.2. Comparing the velocity contours without (figures 4.13(a-c)) and with (figures 4.13(d-f)), the TMFM installed within the static model duct demonstrated the reduction in flow due to the intrusive nature of the device. To quantify this effect, a numerical integration of the velocity contours (shown in figures 4.13(a-f)) was performed and the resulting values were compared to evaluate the blockage factor ($C_{\dot{m}}$), which is defined as the ratio of the mass flow rate without the TMFM inserted into the duct ($\dot{m}_{empty}$) to that with the TMFM installed within the duct ($\dot{m}_{TMFM}$):

$$C_{\dot{m}} \equiv \frac{\dot{m}_{empty}}{\dot{m}_{TMFM}} = 1.92\dot{m}_{TMFM}^{-0.16}. \tag{4.3}$$

According to the data illustrated in 4.13(g), the dependence of the blockage factor on the flow rate in the duct followed a power law in the range of 1-3 g/s in the experiments conducted. Thus, using the power law fit for the blockage factor, the value of the mass flow rate deduced using the TMFM can be converted to the actual value of the mass flow rate exiting the duct in its absence. However, it bears noting that the applicability of the blockage factor measured in the static model to the rotating scale model is unclear as any potential effects of the rotation on the blockage factor are not accounted for. Nevertheless, the analysis of the baseline measurements established a comparative measure for the objective measurements.

Having determined the blockage factor induced by the presence of the TMFM and the baseline measurement, the objective measurements were performed to verify: i) the performance of the TMFM in measuring the mass

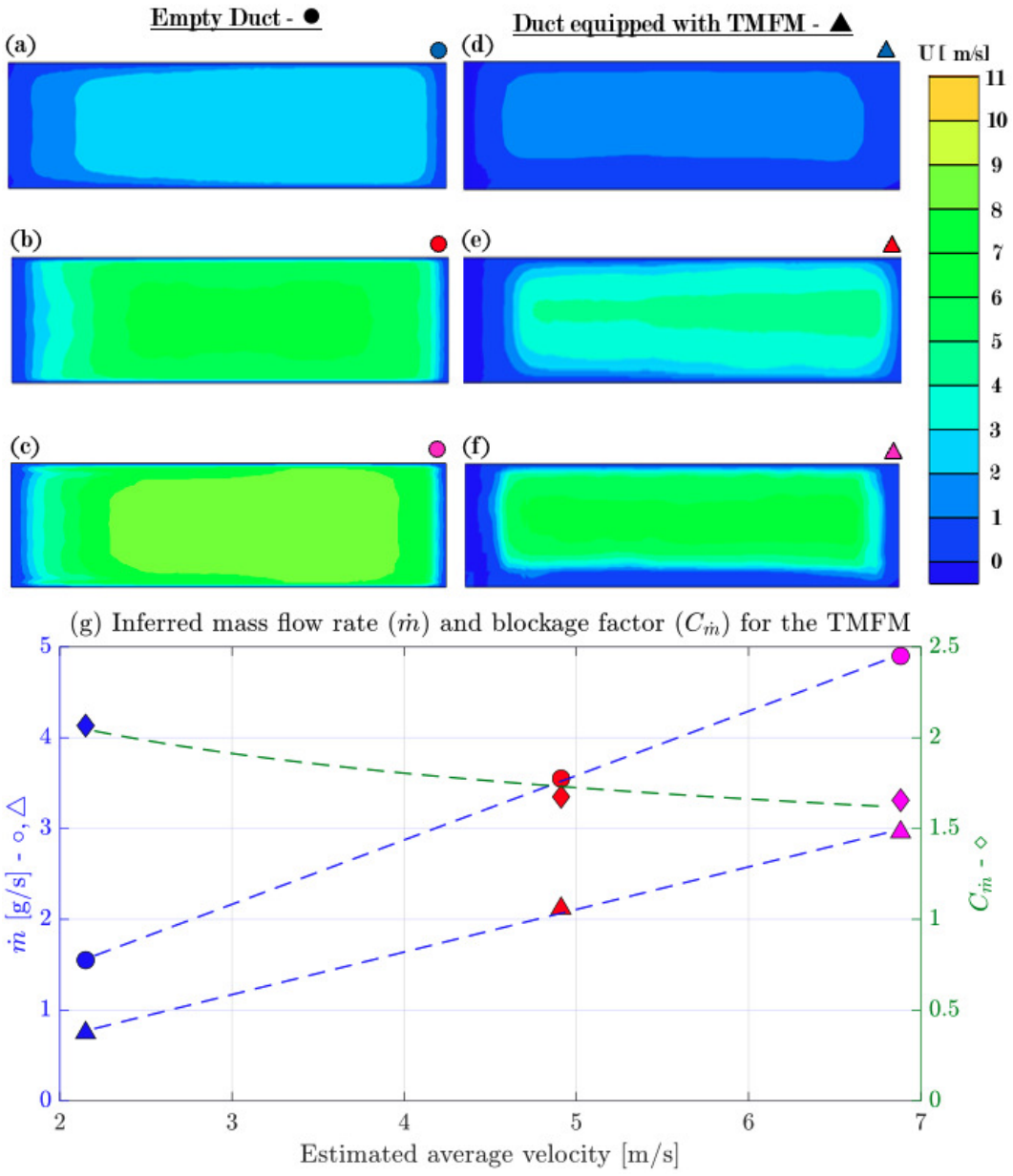

Figure 4.13: Results of the PIV static model measurements for the improved TMFM. (a-f) Velocity contours of the flow exiting the static model for an empty duct (a-c) and a duct equipped with a TMFM (d-f) at three different flow speeds (2.15 m/s in blue (a,d), 4.91 m/s in red (b,e), and 6.88 m/s in magenta (c,f)). (g) The deduced mass flow rates ($\dot{m}$) and blockage factor ($C_{\dot{m}}$) for the new TMFM design as a function of the estimated average velocity.

flow rate exiting the static model duct, and ii) the repeatability of these measurements from one prototype to the next. Eight prototypes were sequentially installed in the static model to deduce the mass flow rate passing through the center duct at the same three flow speeds as prescribed in the baseline measurement. The comparison of the objective and baseline measurements is illustrated in figure 4.14(a) and the corresponding uncertainties are provided in Appendix E.3. It was observed that the differences between the mass flow rates using the TMFM and by PIV were within 8% for each of the three respective flow speeds, which was within the desired threshold of 10% established by Venne (2017). The results obtained were also utilized to calculate the percentage difference in the deduced mass flow rate ($\Delta\dot{m}_{0X}$) at a given velocity from one prototype to the next. As illustrated in figure 4.14(b), it was observed that the deduced mass flow rate for a given prototype was always within 3.5% of the average value of all the prototypes, at each velocity. Thus, the repeatability of the measurement from one prototype to the next, was indeed improved by the changes in its design.

In summary, the results presented in this section demonstrate that the measurements obtained using the TMFM are both sufficiently accurate and repeatable to warrant its installation in the scale model. Installing all the developed prototypes within the scale model will provide insight into the mass flow rates passing through the rotor rim ducts and their overall spatial distribution. Furthermore, the completion of the validation discussed in this section also justifies the installation of the improved TMFM in an in-service hydroelectric generator.

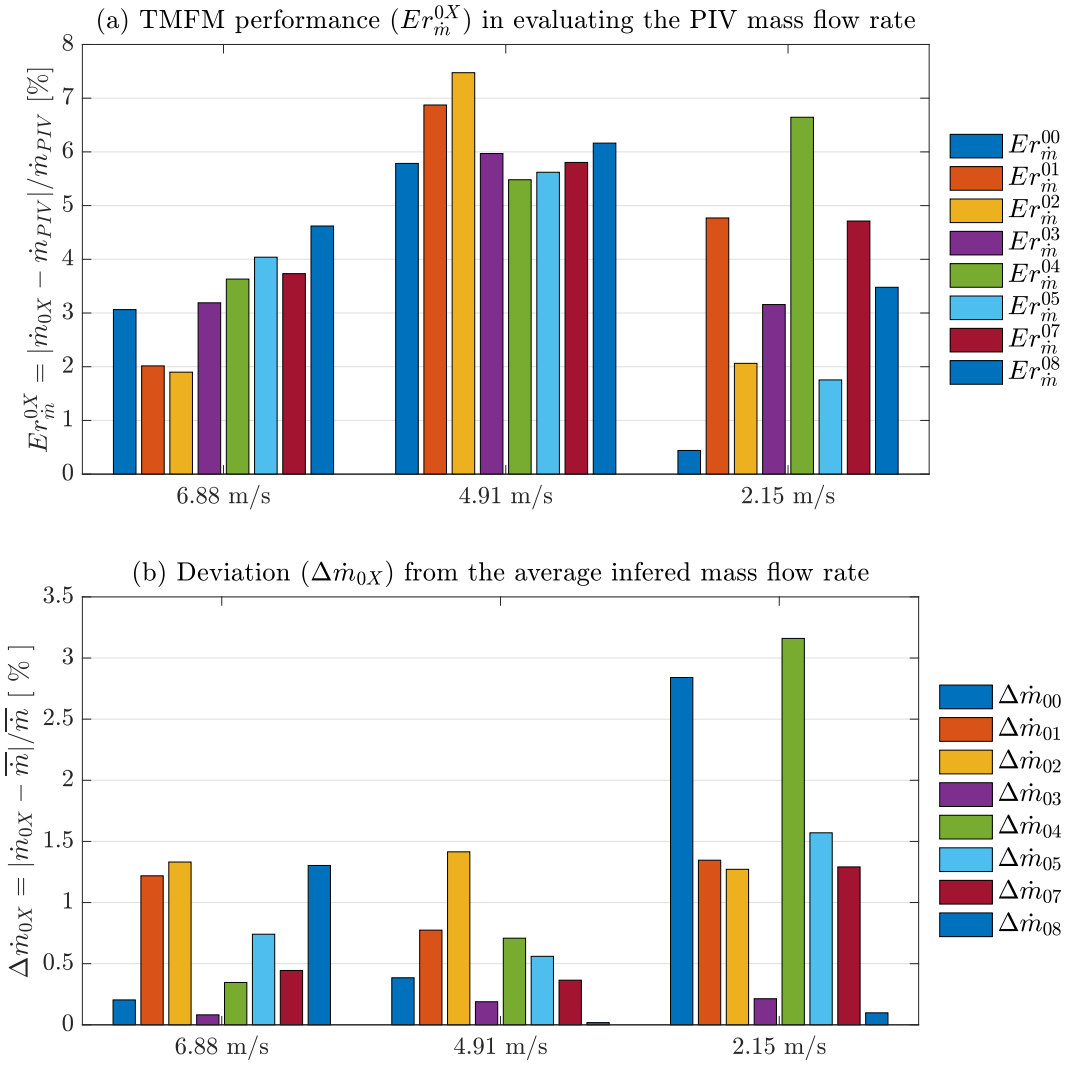

Figure 4.14: Validation of the measurement accuracy and repeatability of the improved TMFM with respect to the baseline (PIV) measurements. (a) Comparison of each prototype's deduced mass flow rate to the value obtained by the baseline (PIV) measurement at a given static model flow velocity. (b) Percentage difference in the deduced mass flow rate ($\Delta\dot{m}_{0X}$) between each prototype at a given velocity.

CHAPTER 5
Results

This chapter is devoted to a presentation of the results (other than those already presented in Chapter 4) of this research and is divided into three sections. The first section presents the results of the TMFM experiments that measured the mass flow rate of the air passing through the rotor rim of the scale model. The second section discusses the results of the numerical simulations of the fluid flow and heat transfer within the scale model, and compares them to experimental measurements. The final section presents assessments of the three main modifications made to the scale model in an attempt to improve the ventilation circuit using model-based design.

5.1 Experimental Measurements

The objective of the experimental measurements undertaken in IREQ's scale model was to increase our understanding of the flow within the rotor of hydroelectric generators. This was achieved by first confirming the steady-state operating temperature of the scale model, as well as the steadiness of the mass flow rates inferred by the TMFMs, then proceeding to measure the mass flow rates within 32 different rotor rim ducts using the improved TMFM. Since the TMFMs are intrusive measurement devices, the raw, measured mass flow rates presented in this section were corrected for the blockage effect of the TMFM.

Having validated the performance of the TMFMs (see section 4.4.2), eight prototypes were installed on the rotor of the scale model to characterize the flow within the rotor rim ducts. The measurements were performed once the

air temperature within the scale model's ventilation circuit reached its steady-state value, so that they could be compared with the steady-state predictions of the numerical simulations (presented in subsequent sections). The establishment of steady-state conditions was verified using a thermocouple installed inside the enclosure, directly below the rotor, and taken to prevail once the air temperature variations in the scale model were less than 0.5°C over a period of one-hour. The evolution of the air temperature in the scale model rotor with time for one set of measurements is illustrated in figure 5.1(a); and in this case, the steady-state temperature (T_{ss}) was estimated to be 46.2°C after 6.5 hours of operation at 300 rpm. Once the steady-state air temperature of the scale model was achieved, the steady-state mass flow rates were deduced from TMFM measurements.

After the steady-state conditions described above were achieved, the heating element of the TMFM was powered on to deduce the mass flow rate passing through a given rotor rim duct. However, several minutes were required for the heating element (itself) to reach its steady-state operating temperature, and the approximately prescribed 20°C temperature increase between the TMFM's inlet and outlet RTDs was attained (for a given flow rate). The time-averaged mass flow rates ($\dot{m}_{ss}$) passing through each duct were obtained by averaging over the final 300 revolutions of the 1,500 revolution acquisition period, which corresponds to the last minute of a five minutes of this period, as shown in figure 5.1(b).

Once both steady-state conditions were attained, the mass flow rates through the rotor rim ducts of the scale model were measured at 32 different locations over four sets of experiments in a sequential manner from the upper to lower axial regions using eight TMFMs initially installed in an axial

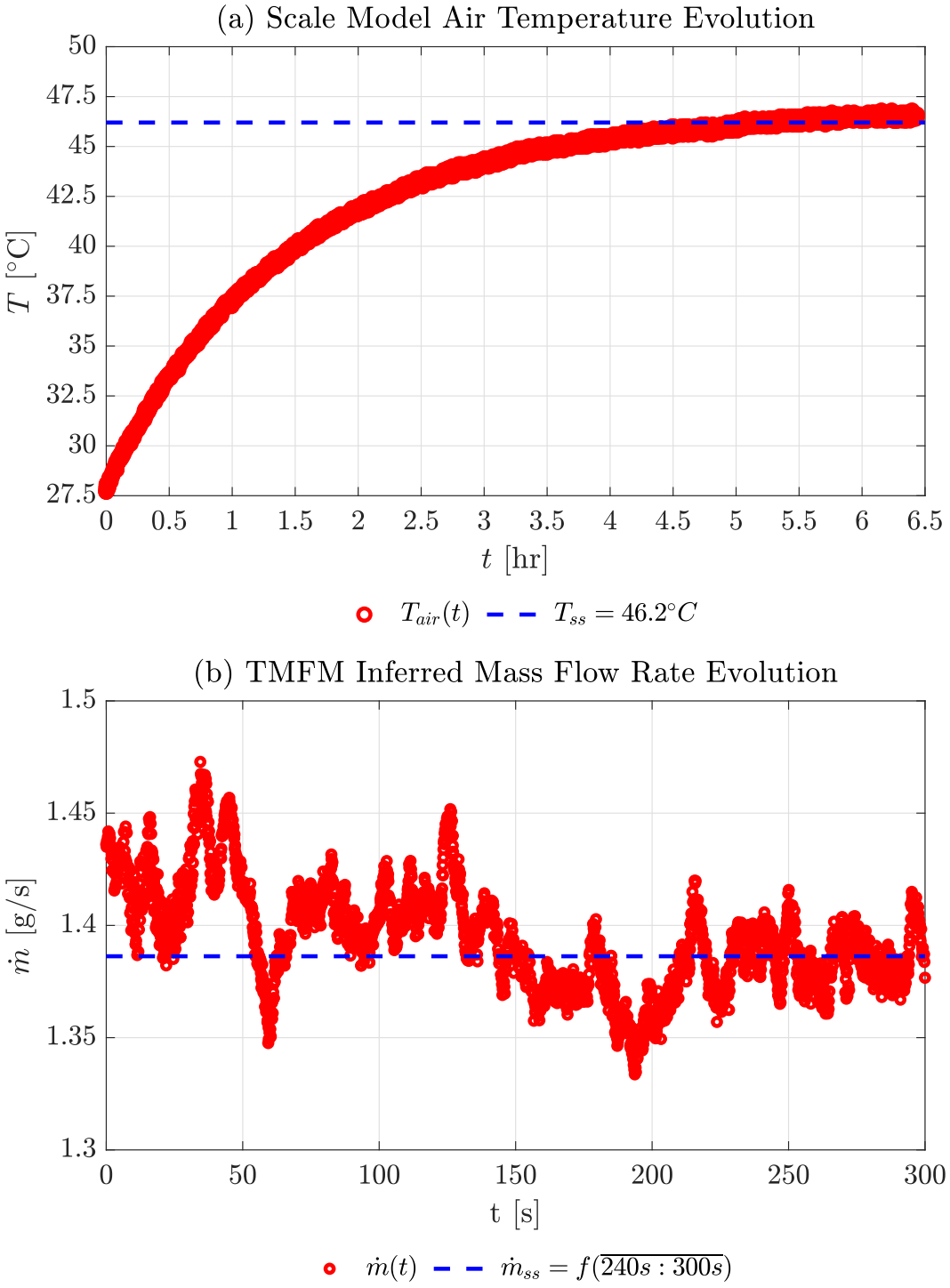

Figure 5.1: Evolution of the air temperature and deduced mass flow rate in a rotor rim duct of the rotating scale model. (a) Evolution of the air temperature (T_{air}) in the scale model indicating the resulting steady-state temperature (T_{ss}). (b) Evolution of the deduced mass flow rate ($\dot{m}$) passing through one rotor rim duct, and the resulting steady-state mass flow rate ($\dot{m}_{ss}$) obtained by averaging over the final minute of acquired data.

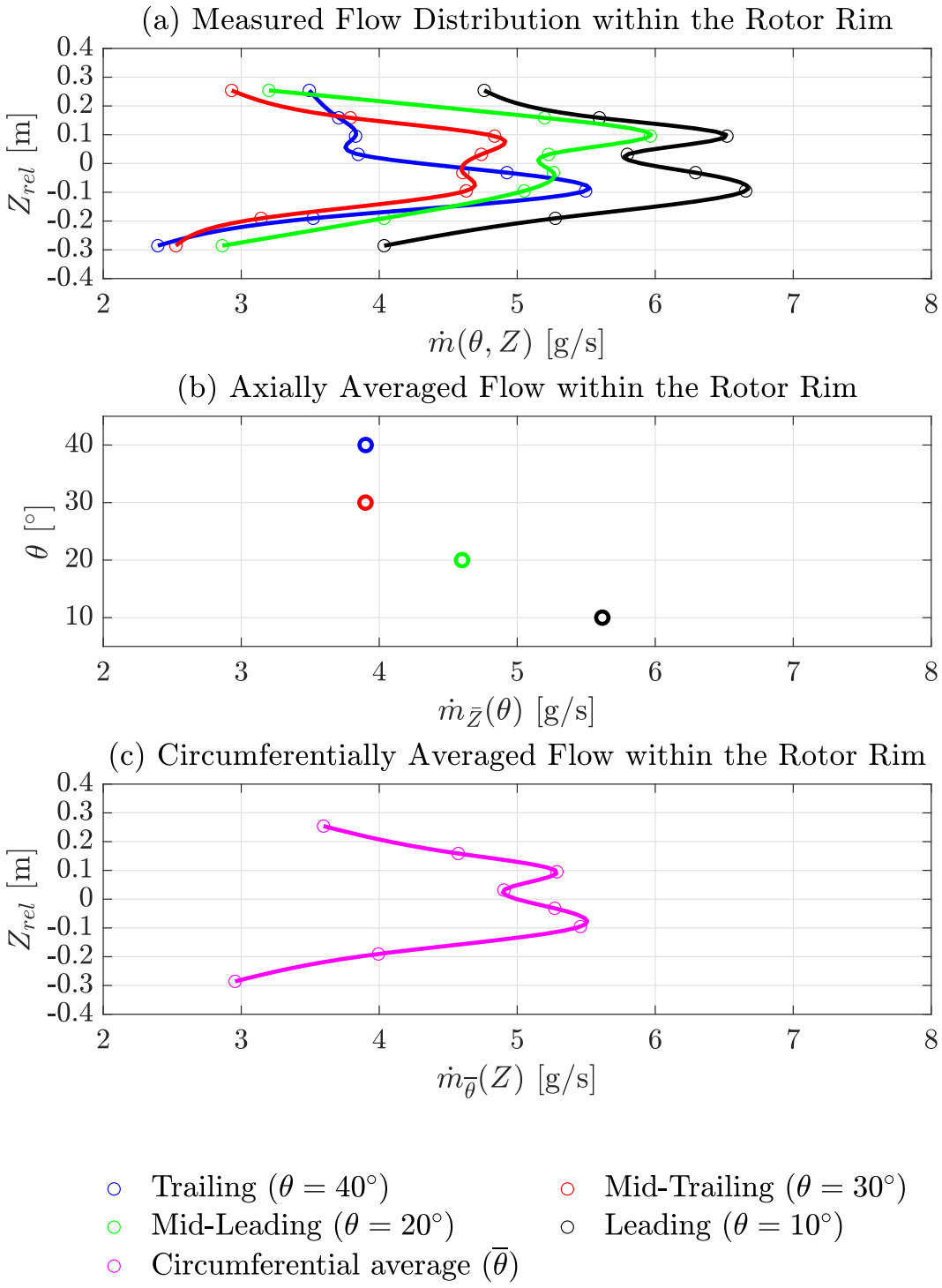

Figure 5.2: Measured mass flow rate distribution at steady-state through the rotor rim ducts using eight TMFMs. (a) The measured mass flow rate ($\dot{m}$) through the rotor rim using TMFMs installed at eight different axial heights and four circumferential (θ) locations. (b) The axially averaged mass flow rates ($\dot{m}_{\bar{Z}}(\theta)$) at each circumferential location within the rotor rim. (c) The circumferentially averaged mass flow rates ($\dot{m}_{\bar{\theta}}(Z)$) at each axial location within the rotor rim.

column of ducts, and then moved circumferentially from the trailing to leading edge (columns of ducts) at the conclusion of all axial measurements in a given column (which required a shutdown of the scale model). The mass flow rates for the 32 rotor rim ducts of interest (8 ducts in four different circumferential columns) are plotted in figure 5.2(a) as a function of the axial height (Z_{rel}) relative to the center of the rotor pole. The measured values highlight four important features of the flow passing through the rotor rim. First, the measurements confirmed that the mass flow rate passing through the columns is neither axially nor circumferentially uniform. Second, the mass flow rate increases from the trailing to leading edge in the circumferential direction, as observed in figure 5.2(b). This is attributed to a "Coandă-like effect" on the spider-arms, where a high pressure side is formed near the leading edge and a suction (or low pressure) side is formed near the trailing edge. Third, the mass flow rate is much larger in the middle of the rotor than in the upper/lower regions, as inferred from the circumferentially averaged values plotted in figure 5.2(c). This is presumably due to the presence of the fan blades near the extremities, which draw large portions of the flow and prevent it from passing through the extremities of the rotor rim. Fourth, there is a larger reduction in the mass flow rate between the middle and lower regions of the rotor rim when compared to its middle and upper regions. This maybe due to the reduction in surface area of the spider arm at the wedge location (located at the end of the lower region of the rotor rim, as shown in figure 2.19). As the TMFM's blockage factor was quantified using the static model, it is not inconceivable that the blockage factor could be different when employed in the rotating scale model. Nevertheless, the results presented herein will be used to qualitatively assess the numerical predictions of flow passing through the rotor rim in subsequent sections.

5.2 Numerical Simulations of the Scale Model

The goal of these simulations was to develop and validate a numerical model that was capable of detecting hot-spots on the surface of a rotor pole of IREQ's scale model, and thus provide confidence in future simulations of a full-scale hydroelectric generator. The development of such a model was divided into three phases, which are delineated in the three subsequent subsections. In the first phase, the numerical model of the fluid flow within the ventilation circuit of IREQ's scale model was used to mimic the simulations of Toussaint *et al.* (2011), with the aim of validating the results obtained with the improved meshing approach discussed in section A. The second phase builds upon the first by incorporating the heat transfer from the solid components to investigate the influence of different turbulence models, thermofluid property (TFP) models, and pole heat loss (PHL) models on the predicted locations of the hot-spots on the surface of a rotor pole. The predictions obtained as part of the second phase are then validated against the experimental temperature measurements of Torriano *et al.* (2014), who measured the surface temperature of the scale model's rotating heated pole using a high frequency pyrometer called the ThermaWatch^{TM} Rotor (TWR). The final phase investigated the mesh independence of the predictions obtained with one models proposed in the previous phase.

5.2.1 Results/Validation of the New Meshing Approach

A preliminary validation of the meshing strategy discussed in section A was performed, which consisted of comparing the global and local flow quantities obtained from simulations undertaken using the improved meshing strategy relative to a benchmark. Such a confirmation was necessary given the challenges associated with controlling the minimum value of y^+ at the grid points adjacent to the more than ten-thousand surfaces of the computational

domain, to respect the requirements of the turbulence models invoked in the numerical models.

To evaluate the applicability of the new meshing strategy in the proposed numerical models, the simulations of Toussaint *et al.* (2011), who developed a numerical model of the ventilation circuit of IREQ's scale model, were chosen as the benchmark case. The results of Toussaint *et al.* (2011) were selected because i) the numerical model's computational domain was generated using ICEM, which is a non-automated meshing software that permits control over all aspects of the mesh, and ii) their numerical predictions were in good agreement with experimental results of Bach *et al.* (2015) and Hudon *et al.* (2011). Therefore, the present validation consisted of comparing the windage losses ($\mathcal{L}_w$), the radiator (net) mass flow rate ($\dot{m}_{rad}$), their associated errors with respect to experiments ($Er_{\mathcal{L}_w}$ and $Er_{\dot{m}_{rad}}$), and the distribution of the mass flow rate through the rotor rim when employing different meshing strategies, but identical mathematical models.

The numerical model employing the new meshing strategy (labeled as HH-$k-\varepsilon$ herein) was capable of predicting the global flow quantities of interest within the ventilation circuit of IREQ's scale model, as demonstrated in table 5.1. The errors with respect to the experimental results of Hudon *et al.* (2011) for the windage losses ($Er_{\mathcal{L}_w}$) and of Bach *et al.* (2015) for the radiator mass flow rate, were 4% and 2.1%, respectively. Furthermore, for the same turbulence model (TM), the prediction of the windage losses and the radiator mass flow rate were within 2% of the results of Toussaint *et al.* (2011) (labeled as ICEM-$k-\varepsilon$ herein). To further evaluate the new meshing strategy, the distribution of the mass flow rate through the main components of the ventilation circuit obtained with the two models were also compared.

Table 5.1: Comparison of the numerical predictions for the windage losses ($\mathcal{L}_w$), mass flow rate ($\dot{m}_{rad}$), and their associated errors with respect to experiments (Er) obtained with different meshing approaches and identical turbulence models (TM).

Mesh	**TM**	$\mathcal{L}_w$ **[kW]**	$Er_{\mathcal{L}_w}$ **[%]**	$\dot{m}_{rad}$ **[kg/s]**	$Er_{\dot{m}_{rad}}$ **[%]**
ICEM*	$k-\varepsilon$	9.18	+3.0	5.54	-1.0
HH	$k-\varepsilon$	9.27	+4.0	5.48	-2.1

*ICEM-$k-\varepsilon$ data corresponds to the result of Toussaint *et al.* (2011)

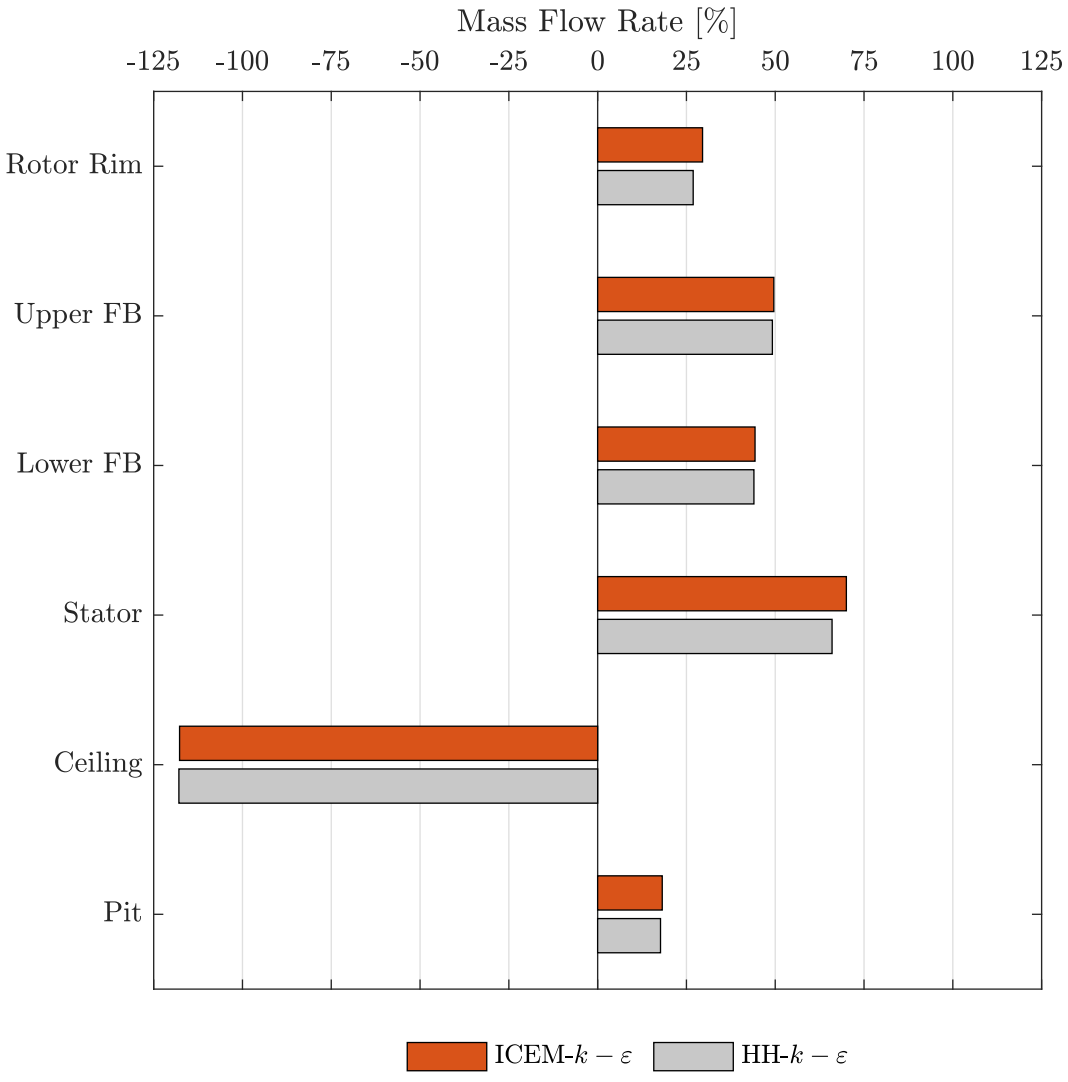

Figure 5.3: Flow distribution through the main components of the ventilation circuit normalized by the radiator mass flow rate for the two cases considered.

The flow distribution through the various components of the scale model's ventilation circuit (normalized by the total mass flow through the radiator) is presented in figure 5.3. The flow within the scale model was designed to enter both the ceiling and pit inlet axially downwards, and exit radially through the radiator. Following the usual convention for cylindrical coordinates, flow exiting radially outwards was denoted as positive for the radially positioned ventilation components (*viz.* the rotor rim, upper/lower fan blades (FB), and the stator), whereas downward or entering flow was denoted as negative for the axially positioned ventilation components (*viz.* the ceiling and pit openings). Note that the percentages do not sum to zero in figure 5.3, (and all subsequent figures of the same type) for two reasons. Firstly, the mass flow rate entering the ceiling is greater than 100%, because it also includes the flow from the pit, as the flow in this region is exiting and redirected towards the ceiling (hence the positive value), and is thus double counted. Secondly, the flow entering the rotor (rotor rim, and upper/lower fan blades) sums to the value of the flow entering the ceiling (thus conserving mass), but 65-70% of this value exits through the stator, because the remaining portion of the flow is passed to the covers and leaked through the gaps and into the radiator or redirected towards the pit outlet. In this context, the principal conclusion drawn from the results given in figure 5.3 is that the simulations of Toussaint *et al.* (2011) and those undertaken in this work give nearly identical results, confirming that use of the new meshing approach does not significantly alter the predictions of the global distribution of the flow. To further evaluate the new meshing strategy, the distributions of the flow through the rotor obtained from the simulations employing the different meshing strategies were also compared.

Figure 5.4 plots the predicted radial mass flow rate distributions through the rotor rim obtained with the ICEM-$k-\varepsilon$ and HH-$k-\varepsilon$ simulations. The

figure illustrates the flow passing through the rotor rim at the four angular positions (leading [10°] to trailing [40°]) with respect to the axial height (Z_{rel}) relative to the center of the rotor pole. These results span four "columns" of 23 rotor rim ducts that lie between two spider arms. The predictions of the flow distribution in the rotor are similar, but the new approach predicts a slightly lower outflows at each angular position. This may be attributed to the presence of more flow separation in the new approach, which resulted in less flow passing through the rotor rim, when compared to the approach employed by Toussaint *et al.* (2011). The ability of the HH-$k-\varepsilon$ simulations to capture more flow separation could be attributed to the higher cell count and lower expansion ratio from one cell to the next in the new meshing strategy.

Given that the present validation exercise indicated that similar results were obtained when using the two approaches compared herein, and since the setup/mesh generation time was reduced from several weeks to less than one day, the new automated meshing approach was adopted. Although the purpose of the numerical simulations was to benchmark the new meshing strategy, the close agreement of the HH-$k-\varepsilon$ simulations model's predictions with experimental data provided further confidence that useful conclusions would be drawn from the simulations.

However, the predictions of the global and local flow quantities shown in figures 5.3 and 5.4, respectively, also highlight several deficiencies. Figure 5.3 demonstrates that only a quarter of the flow passes through the rotor rim, and the flow at the pit inlet is predominately exiting rather than entering. Figure 5.4 demonstrates that the flow passing through the rotor rim is non-uniform (in both the axial and circumferential directions), which contradicts what manufacturers of hydroelectric generators assume when designing such machines. These fluid-flow predictions could have a major impact on the

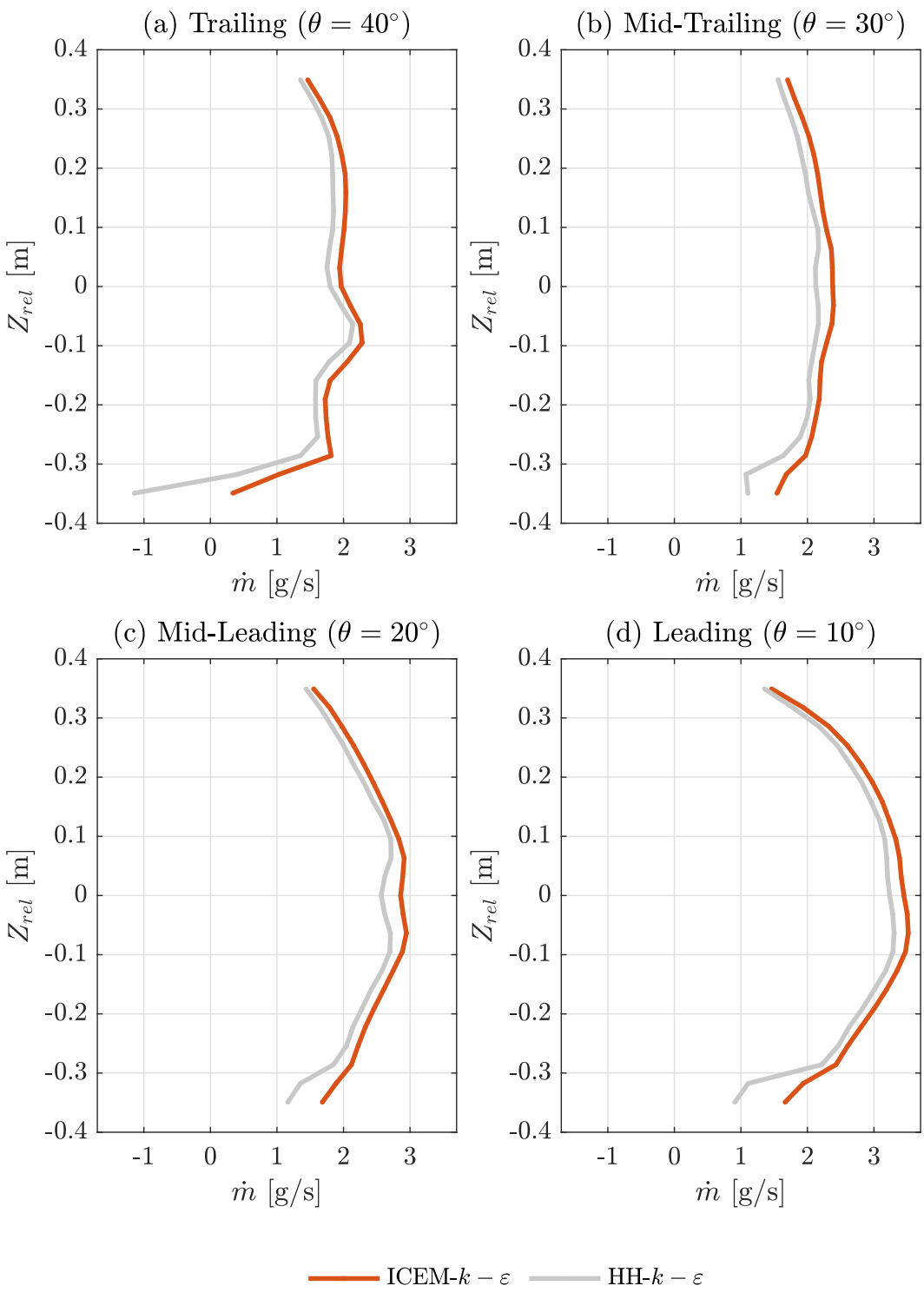

Figure 5.4: Axial distribution of the radial mass flow rates passing through the rotor rim ducts of the scale model at four circumferential positions for the two cases considered. Each position corresponds to the trailing (a), mid-trailing (b), mid-leading (c), and leading (d) locations of the rotor rim ducts.

cooling of the critical components within the machine, which justify the need for additional studies such as those undertaken in the present research.

5.2.2 Results of the Conjugate Heat Transfer Simulations

The second phase of the development of the numerical model consisted of investigating the effects of the choice of the turbulence model, TFP model, and PHL model on the predictions of the global and local surface temperatures of the heated pole, by incorporating the solid-component heat transfer in the numerical model discussed in the previous section. Including the solid-component heat transfer entailed modifications to the numerical model, depending on the three different mathematical models employed (as detailed in section 3.1), which resulted in the seven different cases studied herein and summarized in table 5.2 (which is a reproduction of table 3.3 for the reader's convenience). Firstly, predictions obtained with the $k-\varepsilon$ and $k-\omega$ SST turbulence models in simulations of the fluid flow and heat transfer were investigated. Secondly, predictions obtained with the following thermofluid property (TFP) models were studied: i) constant or fixed properties at the experimental measured value of 46.2 °C (case-C), ii) variable properties (case-VP), and iii) the use of constant properties while solving the continuity and momentum equations in a decoupled manner from the energy equation (case-DC). Thirdly, the following pole heat loss (PHL) models were investigated: i) imposing natural convective heat transfer coefficients derived from empirical Nusselt number correlations on all interior surfaces of the heated pole, and ii) directly modeling the fluid inside the heated pole's shell (case-FIS) and imposing an experimentally measured constant temperature boundary condition at the interface between the fluid boundary and the rotor rim. In all cases, the cell count in the solid computation domain (SD) was 19.4M elements, whereas the cell count for the fluid computational domain (FD) was 125M for the $k-\varepsilon$ model and 190.6M for the

Table 5.2: Summary of the seven cases considered and the associated differences in turbulence model (TM), thermofluid properties (TFP), pole heat losses (PHL), solid computational domain (SD) cell count, and fluid computational domain (FD) cell count.*

Case Label	**TM**	**TFP**	**PHL**	**SD** [M]	**FD** [M]
C-$k-\varepsilon$	$k-\varepsilon$	Constant	Empirical	19.4	125.0
VP-$k-\varepsilon$	$k-\varepsilon$	Variable	Empirical	19.4	125.0
DC-$k-\varepsilon$	$k-\varepsilon$	Decoupled	Empirical	19.4	125.0
C-$k-\omega\ SST$	$k-\omega\ SST$	Constant	Empirical	19.4	190.6
VP-$k-\omega\ SST$	$k-\omega\ SST$	Variable	Empirical	19.4	190.6
FIS-$k-\varepsilon$	$k-\varepsilon$	Variable	Direct	19.4	125.0
FIS-$k-\omega\ SST$	$k-\omega\ SST$	Variable	Direct	19.4	190.6

*This is a reproduction of table 3.3 for the reader's convenience.

$k-\omega$ SST model, to respect the minimum y^+ requirements at nodes adjacent to the solid surfaces. The new meshing strategy was adopted for all cases, such that the abbreviation of HH was omitted from the notation presented in this section and is thus implied from this point forward. Furthermore, the addition of the solid components necessitated modifications to the computational domain of the previous section. Thus, the simulation results for each case were again validated against experimental measurements of the windage losses, net mass flow rate, distribution of the mass flow rate through the rotor, as well as the temperature distribution along the surface of the heated pole.

The effects of the turbulence, TFP, and PHL models on the global flow quantities are depicted in table 5.3. The predictions of the windage losses ($\mathcal{L}_w$) yielded by each model and their comparison with the experimental measurements ($Er_{\mathcal{L}_w}$) of Hudon *et al.* (2011) demonstrated that: i) the $k-\varepsilon$ model overestimates, and the $k-\omega$ SST model underestimates, the windage losses, with very similar relative errors, ii) the effects of the TFP models on these quantities were minimal (for a given turbulence model), and iii) there were minor differences in the predictions with respect to the PHL models (for a given turbulence model). A possible hypothesis for the first observation is that the $k-\varepsilon$ model is known to inaccurately predict and delay flow separation (Wilcox, 2006); and the $k-\omega$ SST may be estimating more flow separation than what occurs, such that the wall shear stress, and thus, windage losses are incorrectly approximated when compared to the experimental values. The last observations indicate that the energy transported to the flow from the heated pole is not sufficient to alter the average temperature of the fluid. However, in a real hydroelectric generator with 36 active poles, the conclusion could be different.

Predictions of the radiator mass flow ($\dot{m}_{rad}$) for each model and their respective errors when compared to the experimental measurements ($Er_{\dot{m}_{rad}}$) of Bach *et al.* (2015) demonstrate that changes in all the models considered here gave similar results. This is consistent with the lower levels of flow separation present in this region. In summary, all simulations predicted the windage losses within 7%, and the net mass flow rate through the radiator within 5% of the experimental values.

Having demonstrated that the global flow quantities compared favorably with the experimental measurements, the distributions of the mass flow rate of the air passing through the main ventilation components of the generator were analyzed, as shown in figure 5.5. All quantities presented therein are normalized relative to the air flow passing through the radiator (given in table 5.3). Furthermore, the meaning of the sign of the values in figure 5.5 is dependent upon the orientation (*i.e* radially/axially) of the ventilation components and are defined in the same manner as in figure 5.3. Figure 5.5 demonstrates a slight dependence of the global flow rates through the main ventilation components on the turbulence models, but a minimal dependence on the TFP for each model. Note that there is only a small difference between case-C and case-VP, which indicates that the zones of temperature deviations from the assumed uniform temperature used in case-C (46.2°C) do not sufficiently change the fluid properties to change the global flow rates within the ventilation circuit. In some regions of the ventilation circuit (rotor rim, ceiling, and pit opening), the $k-\omega$ SST turbulence model predicts lower overall flow rates when compared to the $k-\varepsilon$ turbulence model. Since the $k-\varepsilon$ turbulence model is known to delay/not accurately predict flow separation (Wilcox, 2006), it is plausible that, in regions where more flow separation is present (*e.g.* rotor rim, ceiling, and pit openings), the model would predict higher overall flow rates

Table 5.3: Validation of the windage losses and mass flow rates for different turbulence (TM), thermofluid property (TFP), and pole heat loss (PHL) models.

Case Label	$\mathcal{L}_w$ **[kW]**	$Er_{\mathcal{L}_w}$ [%]	$\dot{m}_{rad}$ **[kg/s]**	$Er_{\dot{m}_{rad}}$ [%]
C-$k-\varepsilon$	9.36	+5.0	5.42	-3.3
VP-$k-\varepsilon$	9.49	+6.6	5.33	-4.8
DC-$k-\varepsilon$	9.51	+6.8	5.33	-4.9
C-$k-\omega\ SST$	8.41	-5.6	5.57	-0.5
VP-$k-\omega\ SST$	8.32	-6.7	5.54	-1.1
FIS-$k-\varepsilon$	9.33	+4.7	5.45	-3.0
FIS-$k-\omega\ SST$	8.47	-4.9	5.59	-0.2

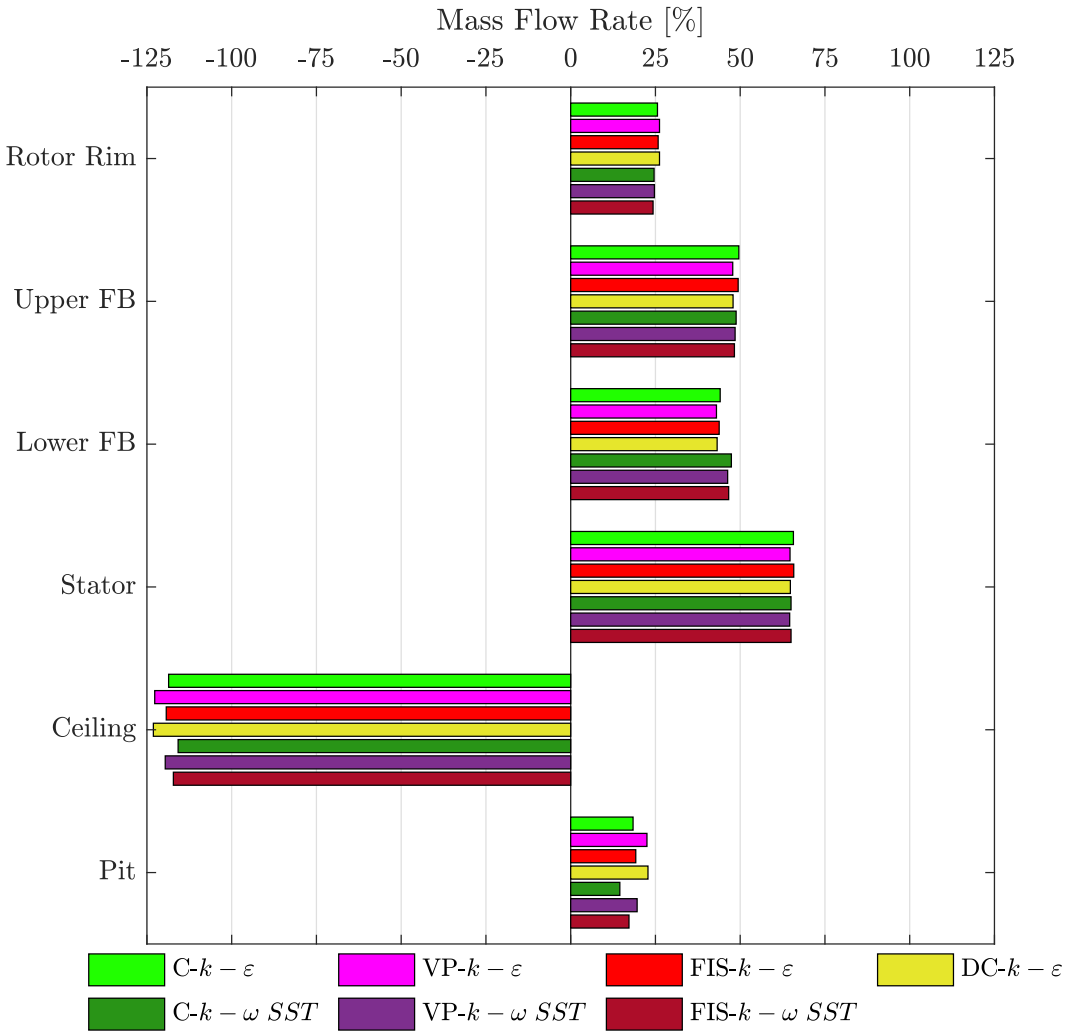

Figure 5.5: Flow distribution through the main components of the ventilation circuit normalized by the radiator mass flow rate for the seven cases considered.

when compared to the $k-\omega\ SST$ model. Nevertheless, the small differences between these two models does not warrant the extra computational cost of using the $k-\omega\ SST$ turbulence model. Although both the choice of turbulence and TFP models had only a minor influence on the global ventilation quantities, larger discrepancies were found in the local flow quantities, which are therefore described in more detail below.

The predicted mass flow rates through the rotor rim for the seven cases considered are illustrated in figure 5.6 along with a qualitative comparison with the experimental results presented in section 5.1. Four columns of rotor rim ducts at different circumferential positions between two spider arms were considered (see figure 2.19). The columns are labeled trailing, mid-trailing, mid-leading, and leading based on their position relative to location of the spider arm and the direction of rotation. Furthermore, it is important to note that the heated pole is located between the mid-trailing and mid-leading columns of rotor rim ducts. For the three columns of ducts that would experience more flow separation (trailing, mid-trailing, mid-leading), the $k-\omega\ SST$ predicts lower flow rates and a different flow distribution when compared to the $k-\varepsilon$ model. To investigate the influences of the turbulence models, the experimental results presented in section 5.1 were compared to the simulation results, as shown in figure 5.6. It is important to note that there exists a substantial discrepancy between the experimentally measured values of the mass flow rates through the rotor rim ducts and the values predicted by the simulations. The former values are approximately *twice* the latter ones. Therefore, the experimental values were plotted using a different scale (multiplied by a factor of two) to facilitate a *qualitative* comparison of the distributions on a single plot given the discrepancy in the magnitudes of the rotor rim duct mass flow rates.

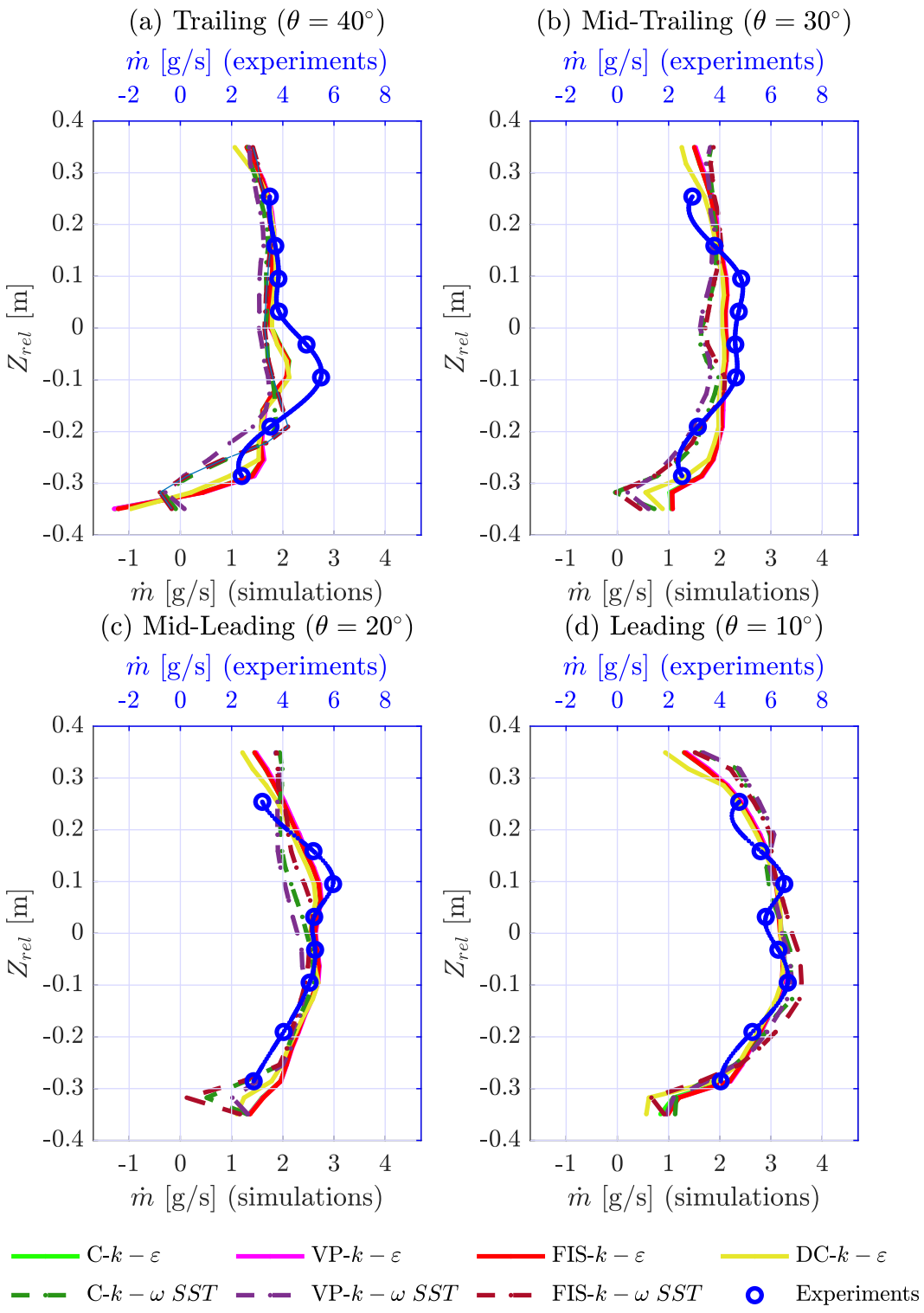

Figure 5.6: Axial distribution of the radial mass flow rates passing through the rotor rim ducts of the scale model at four circumferential positions (trailing (a), mid-trailing (b), mid-leading (c), and leading (d)) for the seven cases investigated (lower axis), along with experimental measurements (upper axis; note the different scales of the lower and upper axes). The lines shown are for clarity, as the results are discrete points for each duct.

Such a *qualitative* comparison between the numerical predictions and experimental data indicate that the numerical predictions obtained using the $k-\varepsilon$ model may more closely follow the trends of the experimental data, than those obtained using the $k-\omega\ SST$ model. Only small differences were observed in the flow distributions shown in figure 5.6 obtained with the three TFP and two PHL cases considered. This is attributed to the fact that the difference in heat transfer from the heated pole are insufficiently large to impact the flow distribution through the rotor rim ducts. Nevertheless, the inconsistency in the magnitude of the mass flow rates in the rotor rim ducts measured using the TMFM and those obtained by way of numerical simulations must be resolved in the future, possibly by way of independent PIV measurements in the rotating scale model, which were beyond the scope of the present research.

To investigate the thermal aspects, the predicted temperature profiles at three (relative) axial positions ($Z_{rel} = -0.2916$, 0.0243, and 0.2916 m) are plotted as a function of the (relative) angular position from the center of the pole for the seven cases considered, along with the corresponding experimental data of Torriano *et al.* (2014) in figure 5.7. Note that negative angular positions denote the leading edge of the pole and *vice versa*. In all cases, the predicted angular location of the maximum temperature on the pole, and the asymmetry between the leading and trailing edges, are reasonable, although the magnitudes of the temperature distribution in the upper/lower regions of the pole are generally more accurately predicted than in the middle regions.

Comparing figures 5.7 and 5.6, it can be observed that there is a correlation between the higher mass flow rates measured by the TMFM and the lower temperatures measured by the TWR. Although the applicability of the blockage factor (quantified in the static model) to the rotating scale model has not been confirmed, an underprediction of the simulated flow rates passing

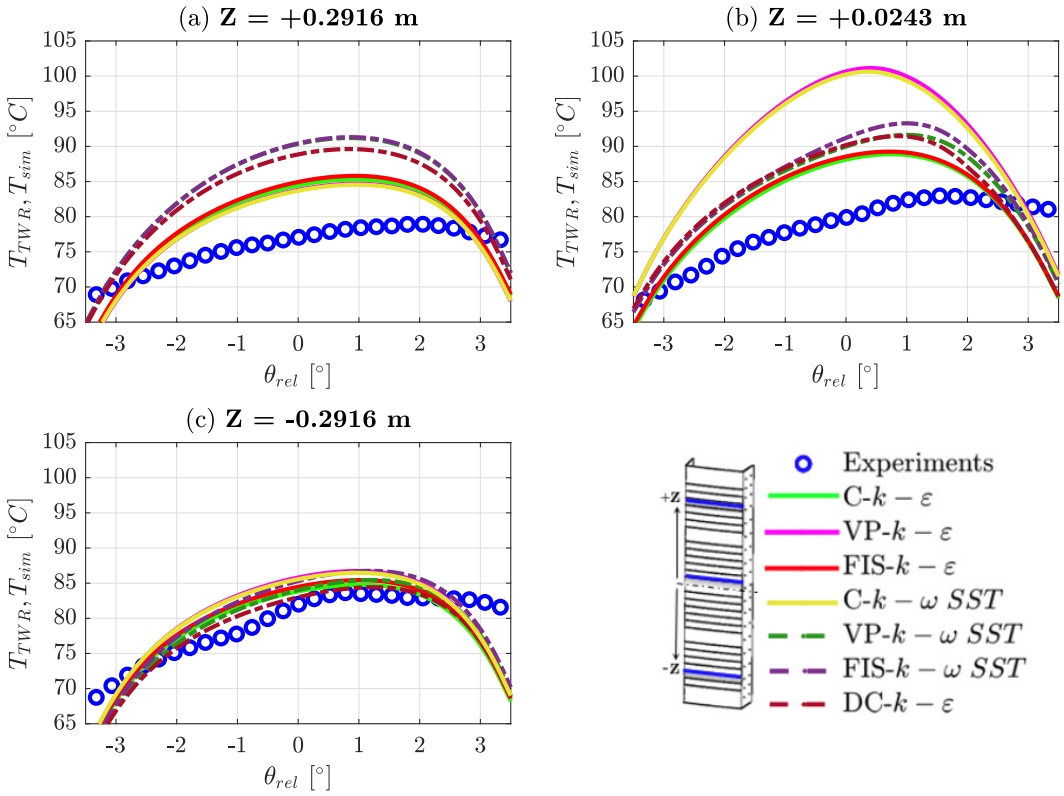

Figure 5.7: Experimental (T_{TWR}) and predicted (T_{sim}) temperature profiles at three of the twenty-six relative axial positions along the height of the heated pole. Each height corresponds to the upper (a), middle (b), and lower (c) regions of the pole.

Table 5.4: Validation of the numerical predictions for the average ($\bar{T}_{sim}$) and maximum ($max(T_{sim})$) pole surface temperatures for the cases considered.

Case Label	$\bar{T}_{sim}$	$\hat{Er}_{\bar{\theta},\bar{Z}}$	$\hat{Er}_{\bar{\theta},U}$	$\hat{Er}_{\bar{\theta},M}$	$\hat{Er}_{\bar{\theta},L}$	$max(T_{sim})$	Er_{max}
C-$k-\varepsilon$	60.6	4.8	3.3	3.7	3.1	108.0	+2.7
VP-$k-\varepsilon$	62.4	8.2	5.0	9.5	3.3	123.9	+18.6
DC-$k-\varepsilon$	62.4	8.0	4.9	9.3	3.2	113.9	+8.6
C-$k-\omega$ SST	61.9	6.7	3.4	5.5	5.0	114.8	+9.5
VP-$k-\omega$ SST	62.0	6.9	3.9	5.5	5.0	115.9	+10.6
FIS-$k-\varepsilon$	60.8	4.9	3.5	3.8	3.2	108.6	+3.3
FIS-$k-\omega$ SST	61.5	6.1	3.0	5.2	4.5	113.9	+8.6

through the rotor rim ducts is consistent with the model's overprediction of the temperatures along the surface of the pole. A possible hypothesis supporting this claim is that the chosen turbulence models are overpredicting the turbulent viscosities in the rotor rim ducts, which would decrease the flow passing through them.

To objectively quantify each numerical model's ability to predict the average and maximum pole temperatures, the root-mean-square error (RMSE) and the difference in maximum temperatures obtained in the simulations and measured in the experiments were respectively evaluated. Both metrics were not evaluated on a percentage basis nor normalized, contrary to all other similar comparison made herein for three reasons. First, the percent difference between two temperatures is not useful, because a temperature difference is a relative measure, and thus, the values must be normalized by a reference temperature. Second, no obvious (imposed of otherwise) reference temperature could be used to normalize temperature differences. Third, the comparison between the numerically predicted temperatures and the maximum allowable temperature defined by the class of insulation used within the rotor poles of a particular generator is of interest. Thus, the RMSE (denoted by a circumflex) averaged over the circumference (θ) of the pole at each axial (Z) position ($\hat{Er}_{\bar{\theta}}(Z_j)$) was evaluated as:

$$\hat{Er}_{\bar{\theta}}(Z_j) = \sqrt{\frac{1}{I}\sum_{i}^{I}[T_{TWR}(\theta_i, Z_j) - T_{sim}(\theta_i, Z_j)]^2}, \tag{5.1}$$

where I is the number of circumferential points at a given height j, T_{TWR} are the temperature measurements of Torriano *et al.* (2014), and T_{sim} are the numerical predictions of the temperature along the surface of the pole. To obtain a metric of the overall temperature deviation from the experiments,

the above equation can be averaged over the height of the pole as follows:

$$\hat{Er}_{\bar{\theta},\bar{Z}} = \frac{1}{J}\sum_{j}^{J} \hat{Er}_{\bar{\theta}}(Z_j), \tag{5.2}$$

where J is the number of axial points. To better evaluate the numerical predictions in different axial zones, the RMSE averaged over the upper (U), middle (M), and lower (L) regions of the pole at each circumferential position ($\hat{Er}_U$, $\hat{Er}_M$, and $\hat{Er}_L$) was also evaluated as:

$$\sqrt{\frac{1}{J}\sum_{j}^{J}[T_{TWR}(\theta_i, Z_j) - T_{sim}(\theta_i, Z_j)]^2} = \begin{cases} \hat{Er}_U(\theta_i), \text{ if } 0.2 \leq Z_{rel} \leq 0.3 \\ \hat{Er}_M(\theta_i), \text{ if } -0.1 \leq Z_{rel} \leq 0.1 \\ \hat{Er}_L(\theta_i), \text{ if } -0.3 \leq Z_{rel} \leq -0.2, \end{cases} \tag{5.3}$$

where each of the three zones are defined as given above. In a similar fashion, the overall circumferential averaged temperature deviation from the experiments at each zone ($\hat{Er}_{\bar{\theta},U}$, $\hat{Er}_{\bar{\theta},M}$, and $\hat{Er}_{\bar{\theta},L}$) was obtained as follows:

$$\frac{1}{I}\sum_{i}^{I} \hat{Er}_X(\theta_i) = \begin{cases} \hat{Er}_{\bar{\theta},U}, \text{ if } 0.2 \leq Z_{rel} \leq 0.3 \\ \hat{Er}_{\bar{\theta},M}, \text{ if } -0.1 \leq Z_{rel} \leq 0.1 \\ \hat{Er}_{\bar{\theta},L}, \text{ if } -0.3 \leq Z_{rel} \leq -0.2. \end{cases} \tag{5.4}$$

Lastly, the error in the numerical predictions of the maximum temperature ($max(T_{sim})$) compared to the maximum measured temperature ($max(T_{TWR})$) is defined as:

$$Er_{max} = max(T_{sim}) - max(T_{TWR}), \tag{5.5}$$

where a positive value indicates an overprediction and *vice versa*.

The numerical predictions of the average and maximum temperatures, as well as the five aforementioned metrics are given in table 5.4 and figures 5.8(a-d) for the seven cases considered. The RSME and maximum temperatures were

predicted within 9°C and 10°C, respectively, for all models (excluding both VP cases), as depicted in table 5.4. Furthermore, the zonally averaged RMSE values in table 5.4 generally agreed with the prior observation that the numerical models more accurately predicted the average temperature in the upper/lower regions than the middle region. It can also be observed in figure 5.8(a) that all cases considered failed to predict the average surface temperature in the upper/middle portion of the pole. A plausible cause is the inability of the turbulence models to capture the correct flow distribution and location of separation along the surface of the pole. It is expected that the flow will separate near the trailing edge of the pole, but it is difficult to predict that numerically. This is confirmed by considering the circumferential profiles of the axially zone averaged RMSE shown in figures 5.8(b-d), where in the upper (figures 5.8(b)) and middle (figures 5.8(c)) regions, large differences are found with respect to the experimental vales near the trailing edge ($\theta \geq 2.5°$). Figure 5.8(a), also highlights the axial location of the aluminum supports and the maximum temperature measured in the experiments ($max(T_{TWR})$). The former highlights the lack of correlation between the imposed contact resistance (where the aluminum supports are located) and the prediction of the surface temperature. The latter demonstrates the importance of accurately predicting the flow in the middle region, where the maximum measured temperature is located, and the best and worst numerical predictions of the maximum temperature were respectively within 8°C and 15°C of the experimental measurements. The circumferential location of the measured maximum temperature is highlighted in figures 5.8(b-d), and the best and worst numerical predictions of the maximum temperature were respectively within 2°C and 8°C of the experimental measurements. For a given turbulence model, the choice of TFP/PHL model had little effect, on the average and maximum temperatures, with the exception of

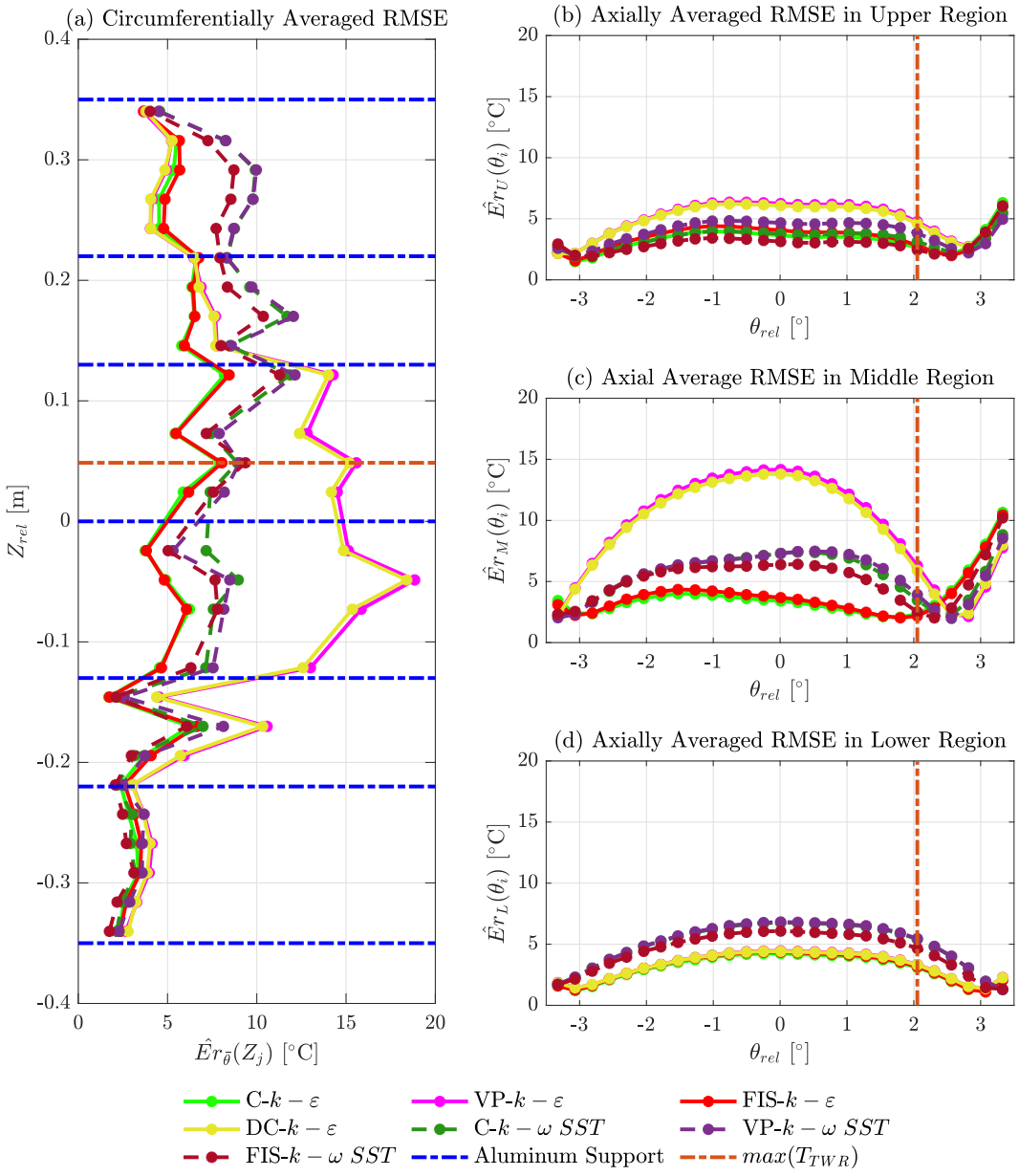

Figure 5.8: Circumferentially ($\hat{E}r_{\bar{\theta}}(Z_j)$) and axially ($\hat{E}r_U(\theta_i)$, $\hat{E}r_M(\theta_i)$, and $\hat{E}r_L(\theta_i)$) averaged RMSE profiles highlighting the location of the aluminum supports and maximum measured temperature ($max(T_{TWR})$). (a) Circumferentially averaged RMSE at each of the 26 axial (Z_{rel}) positions. (b) Axially averaged RMSE in the upper (U) region over 9 axial positions ($0.2 \leq Z_{rel} \leq 0.3$). (c) Axially averaged RMSE in the middle (M) region over 8 axial positions ($-0.1 \leq Z_{rel} \leq 0.1$). (d) Axially averaged RMSE in the lower (L) region over 9 axial positions ($-0.3 \leq Z_{rel} \leq -0.2$).

the cases VP and DC for the $k-\varepsilon$ model. The former discrepancy is believed to be associated with the turbulence model's inability to capture the flow in the center of the pole, as illustrated by the axial profiles of the circumferential average RMSE in figure 5.8(a), and the circumferential profiles averaged in the middle region shown in figure 5.8(c). A hypothesis for the latter is that the numerical simulations are rather sensitive to the imposed ("frozen") averaged flow when performing the computations for the heat transfer. Ultimately, even with these differences, the predictions of both the global and local quantities were comparable for all seven cases, and the less computationally intensive method (DC-$k-\varepsilon$) could arguably be implemented given that the results are consistent with the ones requiring more computational resources.

5.2.3 Results of the Mesh Independence Study

The simulations presented in the previous section employed 144M and 210M cells to meet the near-wall mesh criteria on all the (more than ten-thousand) surfaces of the calculation domain when using the $k-\varepsilon$ and $k-\omega$ SST turbulence models, respectively. Although the simulations were run on IREQ's high-performance computing cluster (taking approximately one month on 516 cores to converge), investigating the mesh-dependence of all models studied herein was unfeasible. Nevertheless, a mesh-independence test for a representative case (the constant property (C) simulation using the $k-\varepsilon$ model) was performed. In this test, three different calculation domains with 86M, 144M, and 310M cells were considered. Each refinement step was greater than the minimum successive refinement criterion of 1.3 (Baliga & Lokmanets, 2016). During the mesh refinement process, the windage losses, mass flow through the radiator, average pole temperature, and maximum pole temperature varied within 1% between the successive refinements, indicating asymptotic convergence. The variation in the windage losses over successive

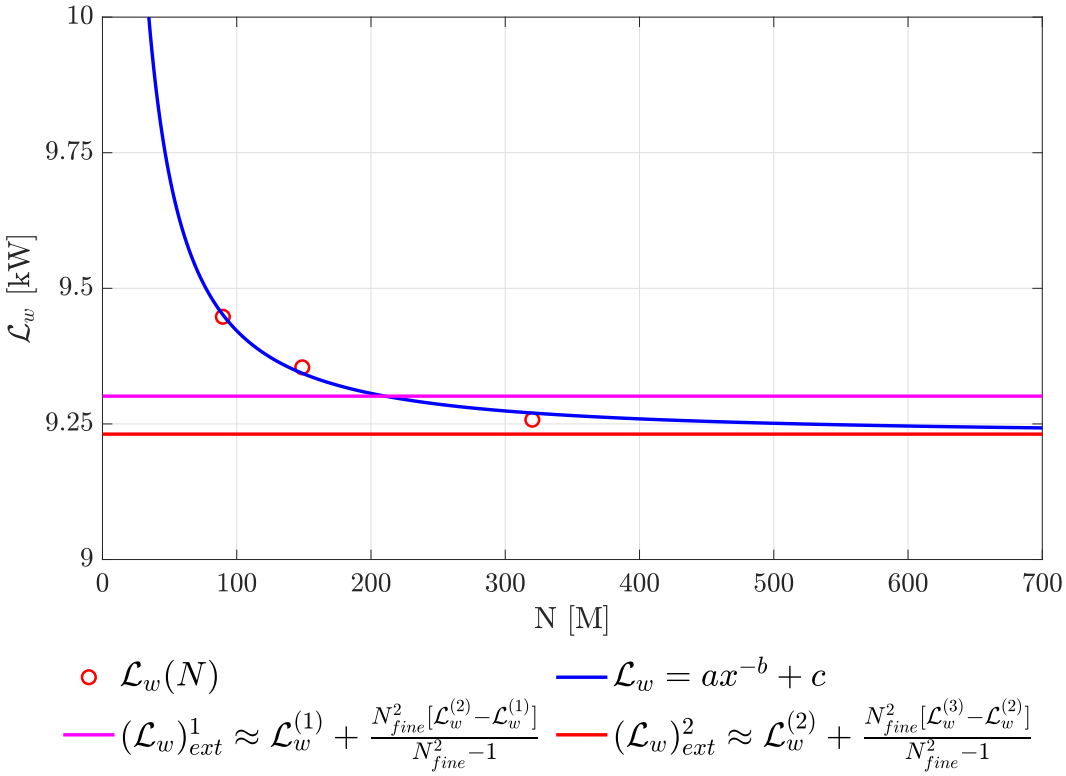

Figure 5.9: Mesh independent solution for the windage losses ($\mathcal{L}_w$) found using Richardson extrapolation. Red dots: prediction of the windage losses with increasing cell count (N) of 86M ($(\mathcal{L}_w)^{(1)}$), 144M ($(\mathcal{L}_w)^{(2)}$), and 310M ($(\mathcal{L}_w)^{(3)}$) cells. Blue line: a power function fit to highlight the convergence with increasing cell count. Pink line: the first extrapolated value ($(\mathcal{L}_w)^1_{ext}$) for the refinement step from first to second grid refinement ($N_{fine} = N_2/N_1$). Red line: second extrapolated value ($(\mathcal{L}_w)^2_{ext}$) for the refinement step from second to third grid refinement ($N_{fine} = N_3/N_2$).

Table 5.5: Mesh independent values for case: C-$k-\varepsilon$.

Quantity	$\mathcal{L}_w$	$\dot{m}_{rad}$	$\bar{T}_{sim}$	$max(T_{sim})$
Value	9.23 kW	5.30 kg/s	60.4°C	107.4°C
Error	+3.60%	-5.36%	+4.4°C	+2.1°C

refinements is illustrated in figure 5.9. The mesh-independent values (found via Richardson extrapolation) and their comparison with experimental results are presented in table 5.5. The mesh-independent values presented in table 5.5 lie within 1% of those presented in tables 5.3 and 5.4, which implies that the computational meshes used in the aforementioned cases were sufficiently refined. Thus, the constant property case with the $k-\varepsilon$ turbulence model was utilized as the baseline case for subsequent analyses.

5.3 Model-Based Design

An advantage offered by CFDHT software is the ability to perform model-based design (MBD) to investigate performance improvements of a given system by making adjustments to the design of the related equipment in the context of a numerical simulation, rather than making them on a physical model, which can be difficult, time-consuming, and expensive. In this context, in an effort to improve the performance of the ventilation circuit of the of IREQ's scale model, three design modifications were considered: i) increasing the surface area of the spider arms; ii) restricting the rotor inlet; and iii) modifying the pit openings (as described in section 3.2). The modifications considered were restricted to those that could be implemented on IREQ's scale model, and eventually extrapolated to an in-service hydroelectric generator. Furthermore, the mathematical models of the numerical simulations used were identical to those employed in the C-$k-\varepsilon$ case presented in the previous sections. This case and the previous simulations within it therefore served as the baseline in subsequent comparative analyses to quantify the impact of the aforementioned three modifications on the performance of the ventilation circuit. To this end, the comparative analyses consisted of quantifying the percentage change ($\mathcal{D}$):

$$\mathcal{D} = \left[(\mathcal{X} - \mathcal{X}_{\mathrm{C}-k-\varepsilon})/X_{C-k-\varepsilon}\right] \cdot 100, \tag{5.6}$$

and temperature change (ΔT^*):

$$\Delta T^* = \mathcal{X} - T_{C-k-\varepsilon}, \tag{5.7}$$

of multiple quantities of interest ($\mathcal{X}$) between the modified case and the baseline (C-$k-\varepsilon$) case.

5.3.1 Spider Arm Modifications

The experimental temperature measurements taken on the surface of the scale model's heated pole demonstrated that the lower portion of the pole is hotter than the upper portion (see the experimental results in figure 5.7). This finding is attributable to the fact that less air passes through the lower portion of the rotor. Furthermore, this finding may also be partially attributed to the nonuniform axial configuration of the spider arms within the rotor of the scale model. One way to overcome this issue is to modify the spider arms such that they occupy the full height of the rotor, as illustrated in figure 5.10. Thus, by removing the wedge below the spider arm and extending the larger portion of the arm downwards, to occupy the full-length of the rotor rim, the frontal area responsible for "pushing" the flow through the rotor rim is increased by 35%. To investigate the effect of this modification to the spider arms on the windage losses, the radiator mass flow rate and rotor rim mass flow rates, as well as the distribution of the mass flow rate through the rotor rim flow and surface temperature of the heated pole, a numerical simulation was performed in which this modification was implemented. This case will be referred to as the full-length spider arm (FLSA) case.

The effect of the modified spider arm on the global flow quantities are given in table 5.6. The results given in this table demonstrate that the modified spider arms resulted in a 4.3% increase in the windage losses and a 1.1% and 8.5% increase in the mass flow rates through the radiator and rotor rim,

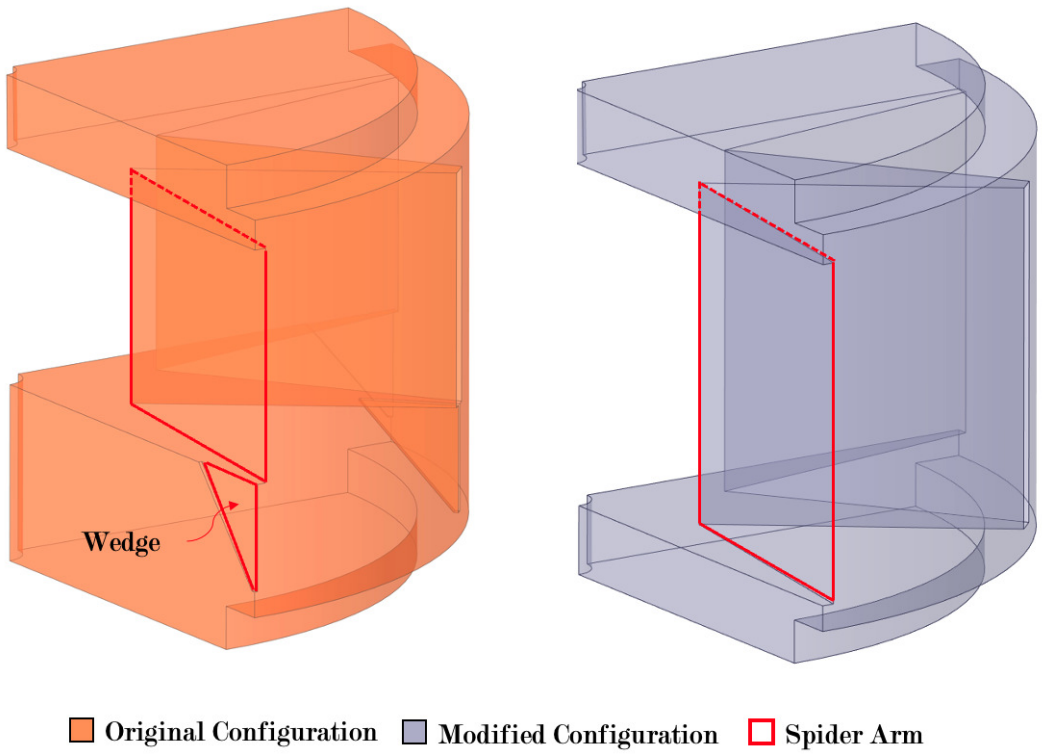

Figure 5.10: Difference between the original and modified configurations of the scale model spider arms.

Table 5.6: Comparison of the windage losses ($\mathcal{L}_w$), net/radiator mass flow rate ($\dot{m}_{rad}$), rotor rim mass flow rate ($\dot{m}_{RR}$) for the baseline (C-$k-\varepsilon$) and modified (FLSA) cases.

Case	$\mathcal{L}_w$ **[kW]**	$\dot{m}_{rad}$ **[kg/s]**	$\dot{m}_{RR}$ **[kg/s]**
C-$k-\varepsilon$	9.36	5.42	1.39
FLSA	9.77	5.48	1.51
$\mathcal{D}$	+4.2%	+1.1%	+8.6%

respectively. Although, the goal of increasing the flow rate through the rotor was achieved, it did so at the expense of increasing the windage losses in the system. However, these additional losses may be acceptable if the flow distributions through the rotor is more uniform, and the average and maximum operating temperatures of the heated pole are reduced.

To further investigate the effect of the modified spider arms, the distributions of the mass flow rate through four circumferential locations within the rotor rim were calculated, they are shown in figure 5.11. The flow in the lower portion ($Z_{rel} < -0.2$ m) of the rotor increased, leading to a more uniform axial distribution of the mass flow rates through the rotor rim for all four circumferential locations. However, figure 5.11 also demonstrates that even if the average mass flow rate passing through the rotor was increased when the spider arms were modified, the flow decreased in certain regions within the rotor rim at different axial heights when compared to the baseline case. Therefore, it is not evident *a priori* whether the increase in the frontal area of the spider arms serves to reduce local and global temperature values on the surface of the heated pole.

To address the question posed above, the temperature profiles for the baseline and modified cases at three different axial heights on the surface of the heated pole are plotted in figure 5.12. The figure demonstrates that the temperatures decreased in the upper and middle regions of the pole by a few degrees, as a result of this modification to the spider arms. However, the temperature profiles remained essentially the same in the lower portion of the pole, despite the changes in the mass flow rate through the lower rotor rim ducts. Table 5.7 quantifies the average and maximum temperatures over the entire surface of the heated pole for the baseline and modified cases, as well as the resultant temperature change (ΔT^*) caused by the modification. From

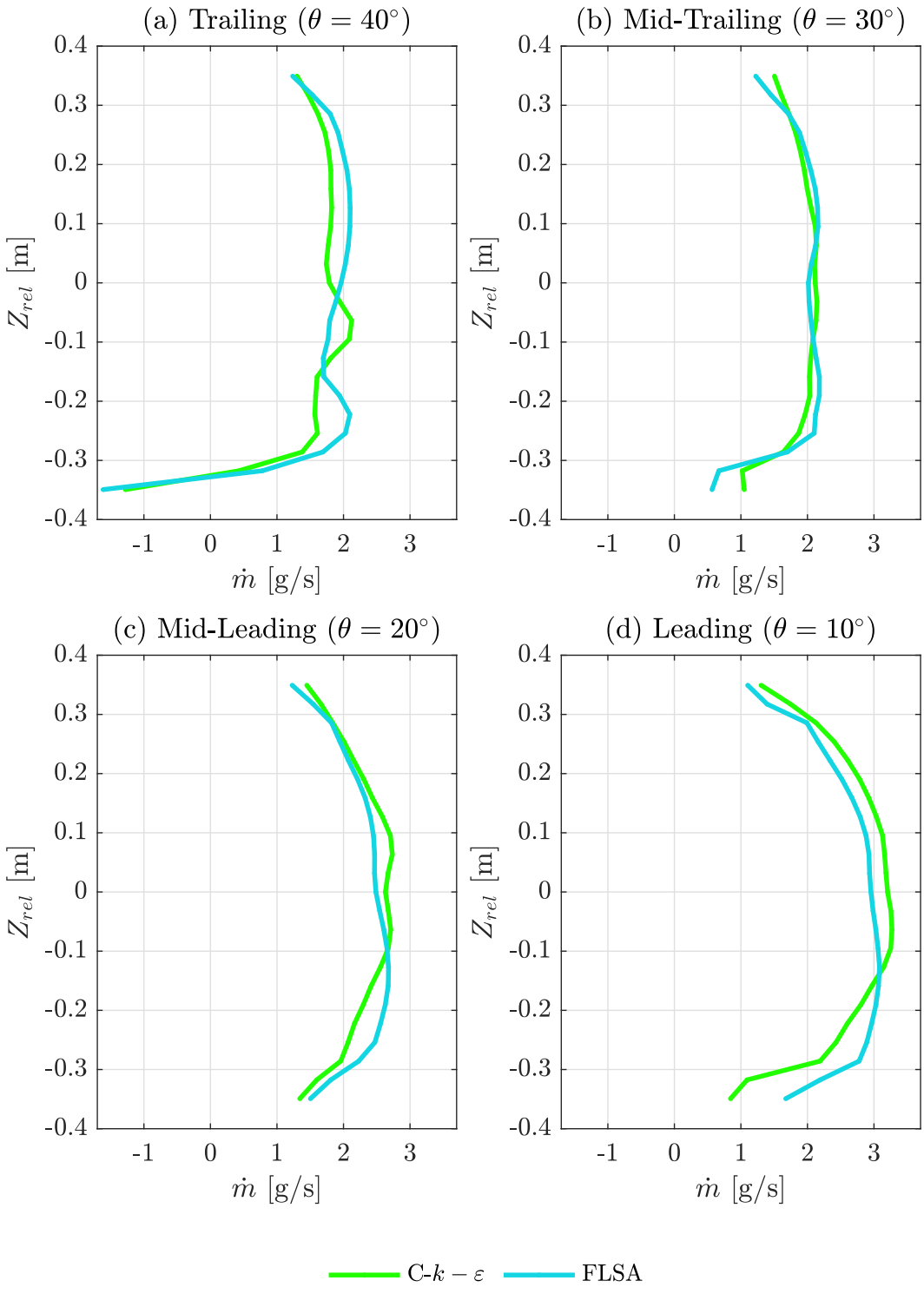

Figure 5.11: Comparison of the axial distribution of the radial mass flow rates passing through the rotor rim ducts of the scale model at four circumferential positions (trailing (a), mid-trailing (b), mid-leading (c), and leading (d)) for the baseline and modified (FLSA) cases. The lines shown are for clarity, as the results are discrete points for each rotor rim duct.

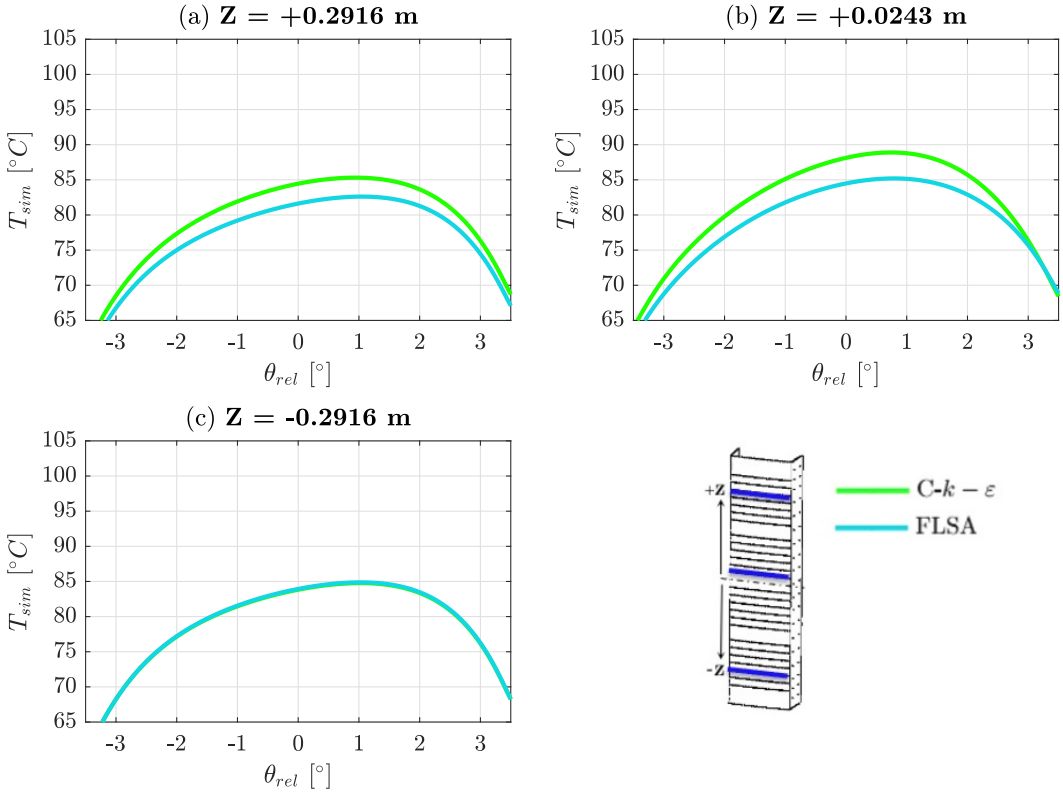

Figure 5.12: Predicted (T_{sim}) temperature profiles for the baseline and modified (FLSA) cases at three of the twenty-six relative axial positions along the height of the heated pole. Each height corresponds to the upper (a), middle (b), and lower (c) regions of the pole.

Table 5.7: Comparison of the average ($\overline{T}_{sim}$) and maximum ($max(T_{sim})$) surface temperatures between the baseline (C-$k-\varepsilon$) and modified (FLSA) cases.

Case	$\overline{T}_{sim}$ [°C]	$max(T_{sim})$ [°C]
C-$k-\varepsilon$	60.6	108.0
FLSA	60.3	105.4
ΔT^* [°C]	-0.3	-2.6

these results, it can be concluded that increasing the length of the spider arms did not significantly change (-0.3°C) the average temperature, but reduced the maximum temperature by 2.6°C. Since the heated pole is located between the mid-trailing and mid-leading zones on the rotor rim, the small temperature changes could be attributed to the fact that the increased length of the spider arm had a less significant impact on the flow through the rotor rim in these regions when compared to the trailing and leading edges (see figure 5.11).

5.3.2 Rotor Inlet Modifications

After consulting with experts at IREQ and considering many different proprietary ventilation configurations of hydroelectric generators, it was found that generators with open rotor configurations had more demonstrated cases of overheating than those with partially closed rotor inlets. Although the sample size was limited and the rotor inlet area varied between the cases, it was deemed worthwhile to investigate this observation by way of numerical simulations. To this end, a numerical simulation was performed in which horizontal plates were inserted at the radial end of the spider arms to reduce the rotor inlet area by 25%, as illustrated in figure 5.13. The effect of the restricted rotor inlet area on the windage losses, radiator mass flow rate, and rotor mass flow rate, distribution of the mass flow rates through the rotor rim, and temperature distribution of the surface of the heated pole were then investigated. This case will be referred to as the partially closed rotor inlet (PCRI) case.

The effects of the partially closed rotor inlet on the global flow quantities are given in table 5.8. The results in this table demonstrate that the PCRI case resulted in a 4.7% decrease in the windage losses and a 1.1% and 35.3% increase in the mass flow rates through the radiator and rotor rim, respectively. Even with a reduced inlet area, a similar amount of air passed through the

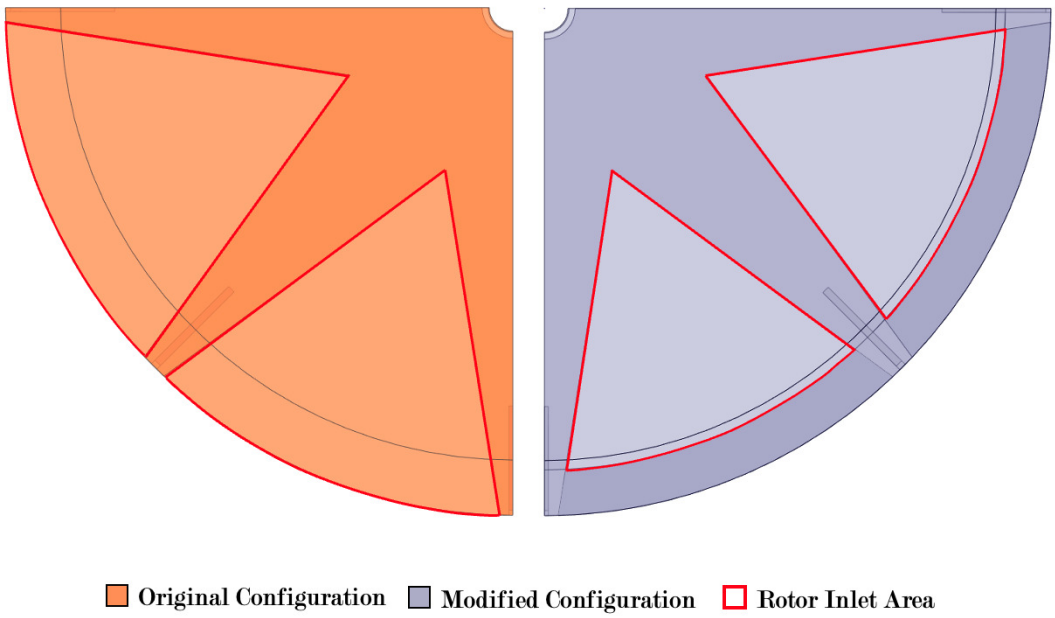

Figure 5.13: Difference between the original and modified configuration of the scale model rotor inlet.

Table 5.8: Comparison of the windage losses ($\mathcal{L}_w$), net/radiator mass flow rate ($\dot{m}_{rad}$), rotor rim mass flow rate ($\dot{m}_{RR}$), upper fan blade mass flow rate ($\dot{m}_{UF}$), lower fan blade mass flow rate ($\dot{m}_{LF}$) for the baseline (C-$k-\varepsilon$) and modified (PCRI) cases.

Case	$\mathcal{L}_w$ **[kW]**	$\dot{m}_{rad}$ **[kg/s]**	$\dot{m}_{RR}$ **[kg/s]**	$\dot{m}_{UF}$ **[kg/s]**	$\dot{m}_{LF}$ **[kg/s]**
C-$k-\varepsilon$	9.36	5.42	1.39	2.69	2.39
PCRI	8.91	5.48	1.88	2.21	2.40
$\mathcal{D}$	-4.7%	+1.1%	+35.3%	-17.8%	+0.4%

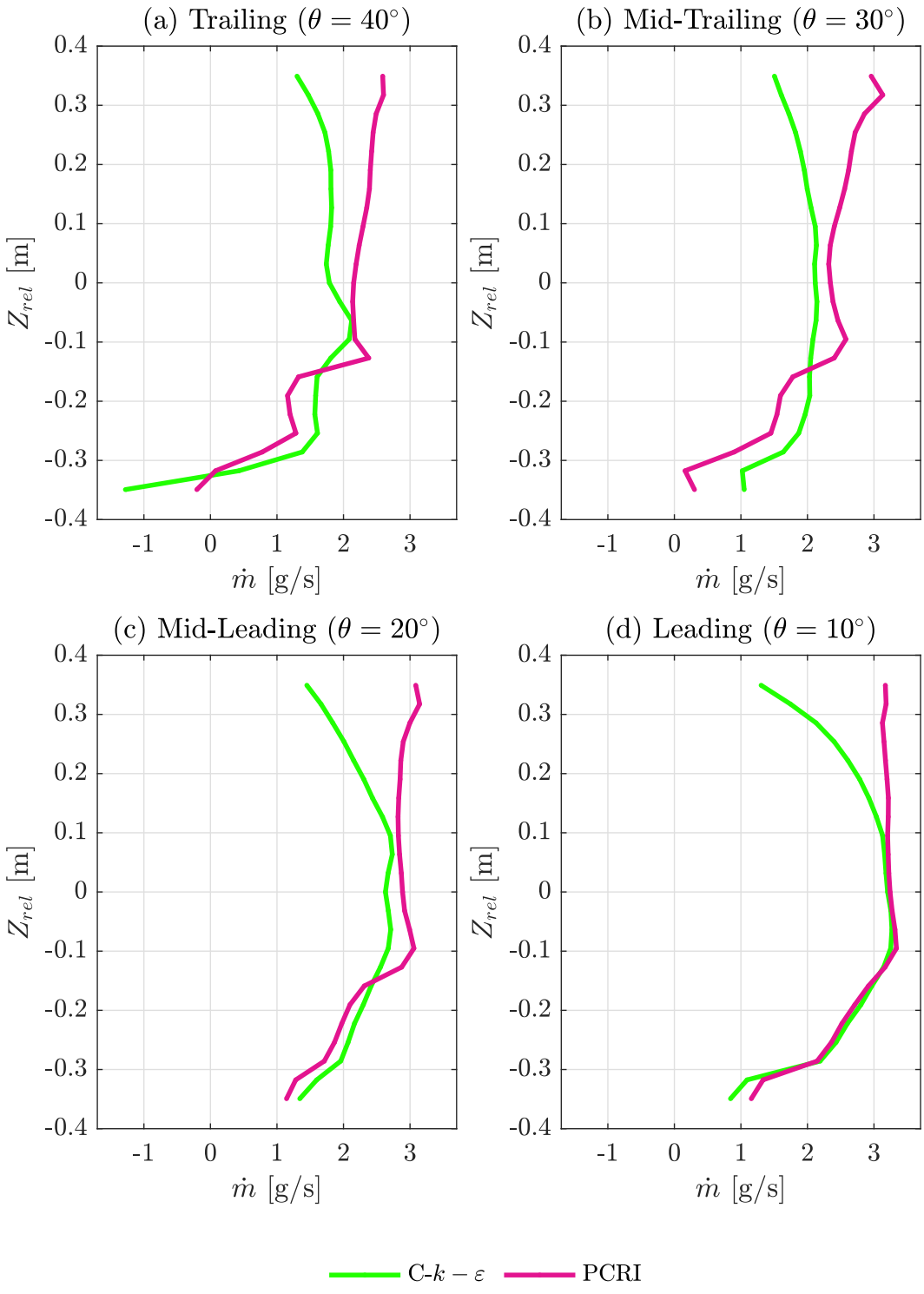

Figure 5.14: Comparison of the axial distribution of the radial mass flow rates passing through the rotor rim ducts of the scale model at four circumferential positions (trailing (a), mid-trailing (b), mid-leading (c), and leading (d)) for the baseline and modified (PCRI) cases. The lines shown are for clarity, as the results are discrete points for each rotor rim duct.

radiator and the windage losses were reduced. This is largely attributed to the reduction (17.8%) in the flow passing through the upper fan blades, which indicate that they are a large contributor to the windage losses and should be the object of future improvements. Moreover, the partial closing of the rotor inlet increased the flow passing through the rotor rim by 35.3%. Although the flow passing through the rotor rim is primarily responsible for cooling the poles on the outer rim, the fan blades also contribute to the cooling of the poles.

To further investigate the impact of the reduction in the rotor inlet area on the flow distribution through the rotor rim, the mass flow rates at four circumferential locations within the rotor rim were analyzed (figure 5.14). In all four regions, the flow passing through the rotor from the mid-plane to the upper portion ($Z_{rel} \geq -0.1$ m) increased, and *vice versa*, which led to a larger inhomogeneity of the flow rates between the lower and upper regions of the rotor. Thus, it is unclear if solely increasing the mass flow rate in the upper region of the rotor, while decreasing the flow in the lower portion of the rotor and in the upper fan blades, reduced the local and global temperatures on the surface of the heated pole.

To assess the impact of the reduced inlet area on the global and local temperatures of the heated pole, the circumferential temperature profiles at three different axial heights on the surface of the heated pole for the baseline and modified (PCRI) cases were investigated, and the results are presented in figure 5.15. These results demonstrates that the surface temperatures increased by almost 10°C in the upper region, and remained within 1°C in the middle/lower regions, respectively. Table 5.9 quantifies the average and maximum temperatures of the baseline and modified (PCRI) cases over the entire surface of the heated pole, as well as the temperature change between the cases.

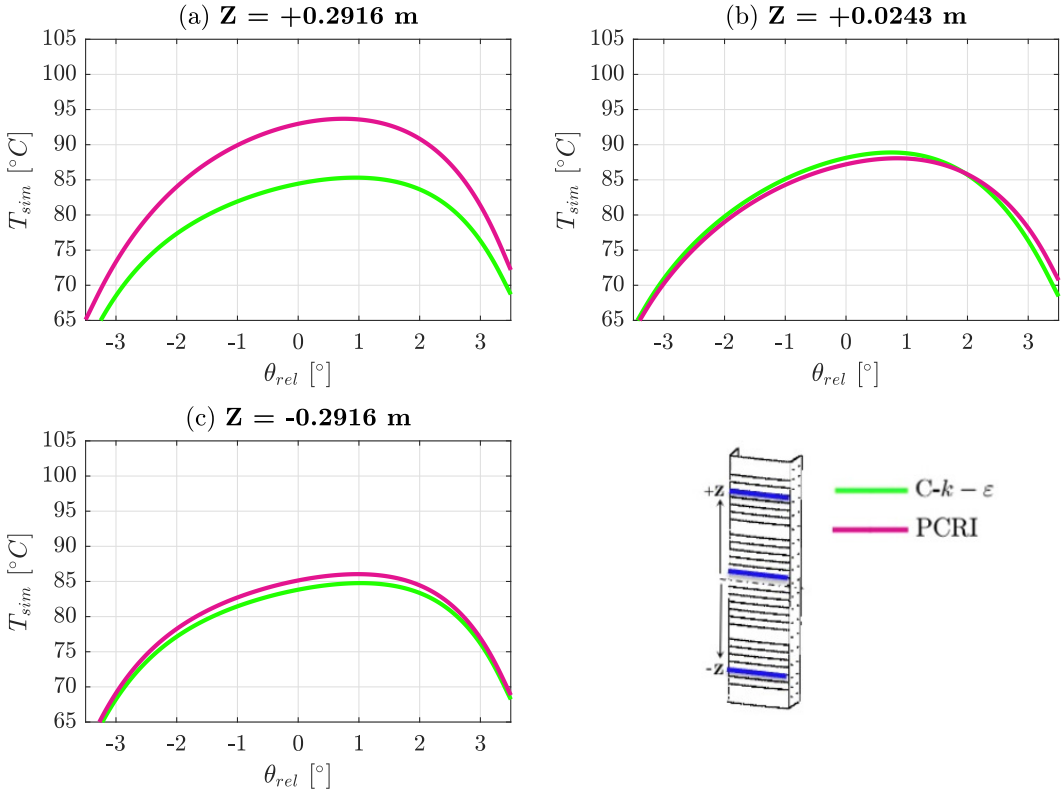

Figure 5.15: Predicted (T_{sim}) temperature profiles for the baseline and modified (PCRI) cases at three of the twenty-six relative axial positions along the height of the heated pole. Each height corresponds to the upper (a), middle (b), and lower (c) regions of the pole.

Table 5.9: Comparison of the average ($\overline{T}_{sim}$) and maximum ($max(T_{sim})$) surface temperatures between the baseline (C-$k-\varepsilon$) and modified (PCRI) cases.

Case	$\overline{T}_{sim}$ [°**C**]	$max(T_{sim})$ [°**C**]
C-$k-\varepsilon$	60.6	108.0
PCRI	61.5	106.5
ΔT^* [°**C**]	+0.9	-1.5

These results demonstrate that decreasing the rotor inlet area marginally increased (0.9°C) the average temperature and marginally reduced (-1.5°C) the maximum temperature. Therefore, decreasing the rotor inlet area had little effect on reducing the average and maximum operating temperatures of the heated pole. A possible explanation for this observation is that although the mass flow rate through the rotor rim was substantially increased, the flow in the upper fan blades was decreased by 17.8%. This indicated that the upper region of the pole's exterior face is predominately cooled by the flow from the upper fan blades. However, preventing the flow from entering the upper fan blade region also demonstrated its contribution to the windage losses, which decreased by 4.7%. Therefore, optimizing both the rotor inlet area and the profile of the fan blades may improve the scale model's ventilation.

5.3.3 Pit Opening Modifications

Section 1.3.4 highlighted the differences between the experimental results of Bach *et al.* (2015) and the numerical results of Toussaint *et al.* (2011) for the flow in the pit inlet. Bach *et al.* (2015) hypothesized that the differences were potentially associated with the alterations made to the pit outlet when meshing the computational domain of the scale model. It is common practice in CFD to simplify portions of complex geometries, to facilitate the meshing of the calculation domain, when it is believed that such simplifications will not substantially alter the flow field. In the case of the pit outlet of the scale model, the round (3 cm radius) corners of the pit outlet were omitted by Toussaint *et al.* (2011) for this very reason. However, in an attempt to corroborate the hypothesis of Bach *et al.* (2015), the scale model's pit outlet was modified, and a new computational domain was generated, as illustrated in figure 5.16. This case is referred to as the rounded pit outlet (RPO) case.

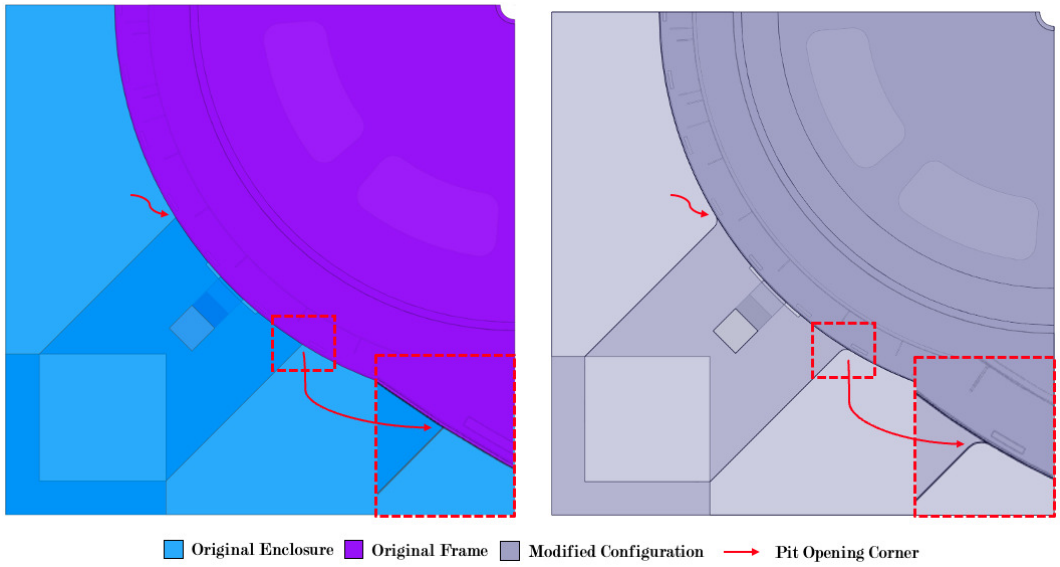

Figure 5.16: Bottom view of the scale model highlighting the difference between the original and modified configuration (RPO).

Table 5.10: Comparison of the windage losses ($\mathcal{L}_w$), net/radiator mass flow rate ($\dot{m}_{rad}$), and pit mass flow rate ($\dot{m}_{pit}$) between the baseline (C-$k-\varepsilon$) and modified (RPO) cases.

Case	$\mathcal{L}_w$ **[kW]**	$\dot{m}_{rad}$ **[kg/s]**	$\dot{m}_{pit}$ **[kg/s]**
C-$k-\varepsilon$	9.36	5.42	-1.0
RPO	9.34	5.39	-1.3
$\mathcal{D}$	-0.2%	-0.6%	+30.0%

Table 5.11: Comparison of the average ($\overline{T}_{sim}$) and maximum ($max(T_{sim})$) surface temperatures between the baseline (C-$k-\varepsilon$) and modified (RPO) cases.

Case	$\overline{T}_{sim}$ **[°C]**	$max(T_{sim})$ **[°C]**
C-$k-\varepsilon$	60.6	108.0
RPO	61.0	108.7
ΔT^* **[°C]**	+0.4	+0.7

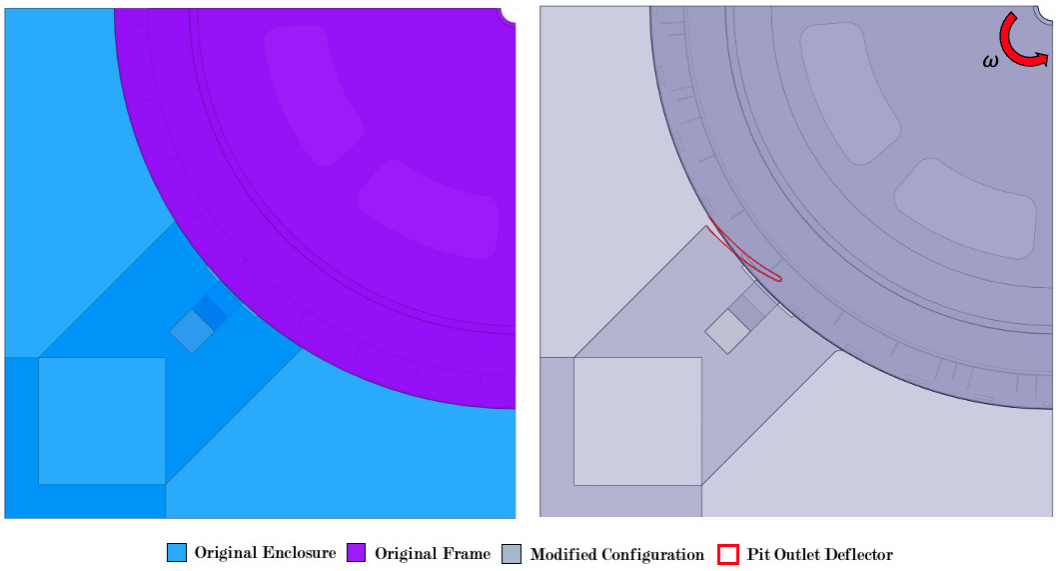

Figure 5.17: Bottom view of the scale model highlighting the differences between the original and modified configuration with an added deflector at the pit outlet (DFPO).

Table 5.12: Comparison of the windage losses ($\mathcal{L}_w$), net/radiator mass flow rate ($\dot{m}_{rad}$), and pit mass flow rate ($\dot{m}_{pit}$) between the baseline (C-$k-\varepsilon$) and modified (DFPO) cases.

Case	$\mathcal{L}_w$ **[kW]**	$\dot{m}_{rad}$ **[kg/s]**	$\dot{m}_{pit}$ **[kg/s]**
C-$k-\varepsilon$	9.36	5.42	-1.00
DFPO	8.60	5.80	-0.04
$\mathcal{D}$	-8.8%	+7.0%	-96.0%

The effects of the rounded pit outlet on the global flow quantities are summarized in table 5.10. The results in this table illustrate that the changes in windage losses and the net flow rate were within 1% of the baseline values, which presumably is due to the fact that the rotating components and (narrow) stator ducts are the main contributors to the windage losses. Furthermore, the mass flow rate exiting the pit inlet increased by 30% and continued to exit rather than enter the pit inlet, which indicated that the numerical simulations are quite sensitive to geometrical changes in this area. Table 5.11 illustrates that the modifications to the pit outlet had little to no impact on the average and maximum pole surface temperatures, which is a consequence of this modification having little effect on the overall behavior of the flow in the rotor. Further analyses of the flow field beneath the rotor and within the enclosure revealed that the flow is predominately exiting the pit inlet because a large portion of the high-velocity flow near the outer portion of the enclosure makes contact with the pit outlet wall and is redirected upwards. Therefore, in an attempt to prevent the high-velocity flow at the bottom of the enclosure from interfering with the low-velocity flow passing through the pit, a flow deflector was added to the computational domain, as illustrated in figure 5.17. To determine the impact of the flow deflector on the global and local flow and heat transfer quantities of interest, a simulation with the modified enclosure was performed and is referred to as the deflected flow at the pit outlet (DFPO) case.

The effects of adding the flow deflector at the pit outlet on the global flow quantities are given in table 5.12. These results demonstrate that the windage losses were reduced by 8.8% and that net mass flow through the scale model increased by 7%. Furthermore, the deflector reduced the flow exiting the pit inlet by 97%. Ultimately, the deflector effectively stopped the flow from

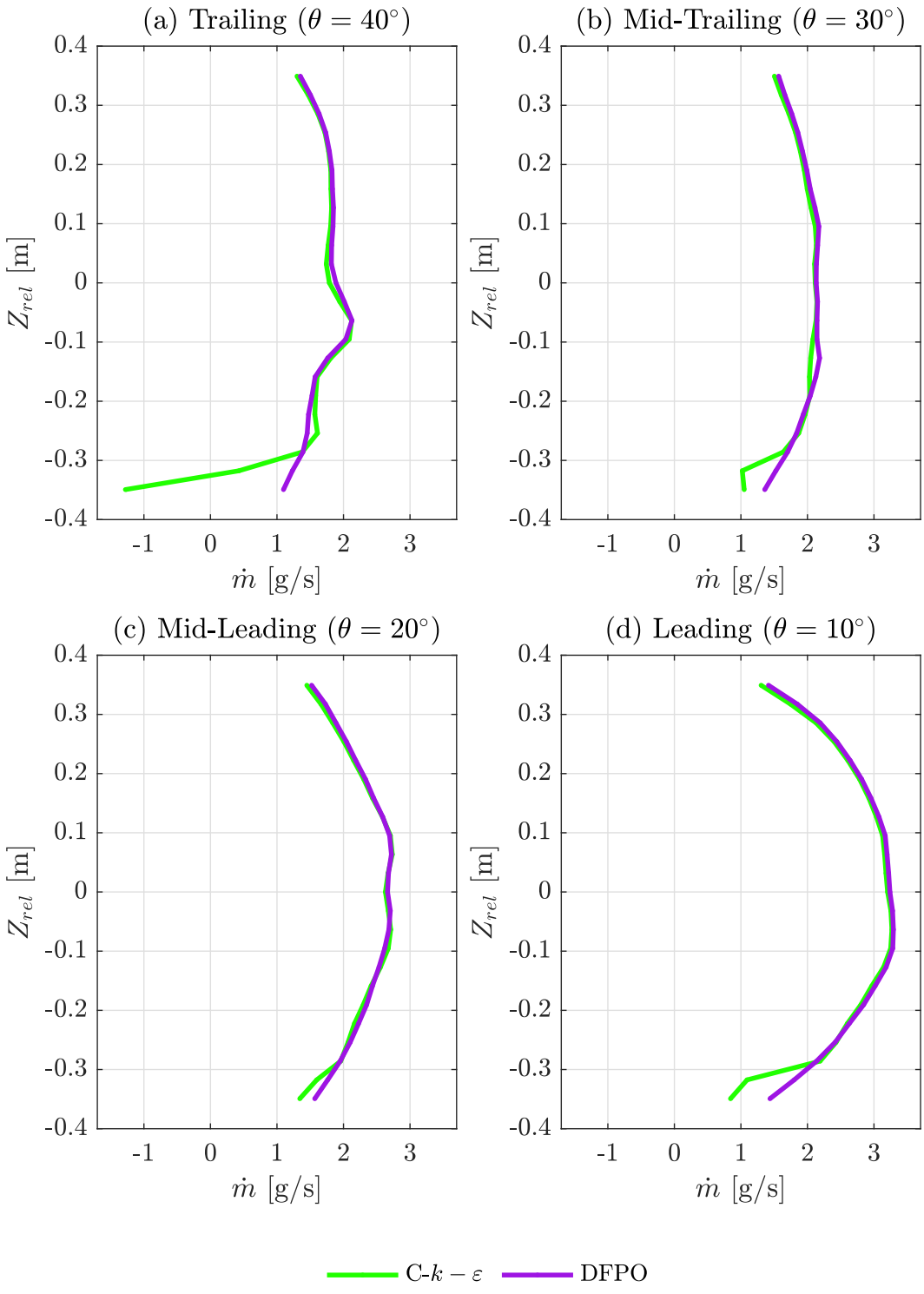

Figure 5.18: Comparison of the axial distribution of the radial mass flow rates passing through the rotor rim ducts of the scale model at four circumferential positions (trailing (a), mid-trailing (b), mid-leading (c), and leading (d)) for the baseline and modified (DFPO) cases. The lines shown are for clarity, as the results are discrete points for each rotor rim duct.

exiting the pit inlet (as intended), and it allowed more flow to enter the rotor and therefore pass through the radiator. Furthermore, the addition of the flow deflector revealed that the flow impingement occurring at the bottom of the enclosure and near the pit outlet was responsible for a considerable portion of the windage losses of the system.

The deflector also influenced the mass flow rate in the rotor rim, as illustrated by the axial distributions of the mass flow rates at the four circumferential locations within the rotor rim, as depicted in figure 5.18. In all four regions, the flow passing through the rotor in the lower region ($Z_{rel} < -0.3$) increased, which led to an overall increase in the amount of flow passing through the rotor. Although the results showed improvements in the global and local flow quantities of interest, it remained unclear whether these improvements reduced the local and global temperatures on the surface of the heated pole.

To address the issue mentioned above, temperature profiles at three different axial heights on the surface of the heated pole for the baseline and modified (DFPO) cases were analyzed and are presented in figure 5.19. These results demonstrate that the temperatures increased by approximately 5°C in the lower region but were similar in the middle and upper regions. Table 5.13 summarizes the average and maximum temperatures of the baseline and modified (DFPO) cases. These results demonstrate that adding the deflector marginally (0.8°C) increased the average temperature without changing the maximum temperature. Therefore, adding the deflector at the pit outlet had little effect on reducing the average and maximum operating temperatures of the heated pole. However, it demonstrated that the flow impingement at the pit outlet is a large contributor to the windage losses. Thus, it would be worthwhile to optimize the flow deflector to further facilitate the passing of the air through the pit openings and the rotor.

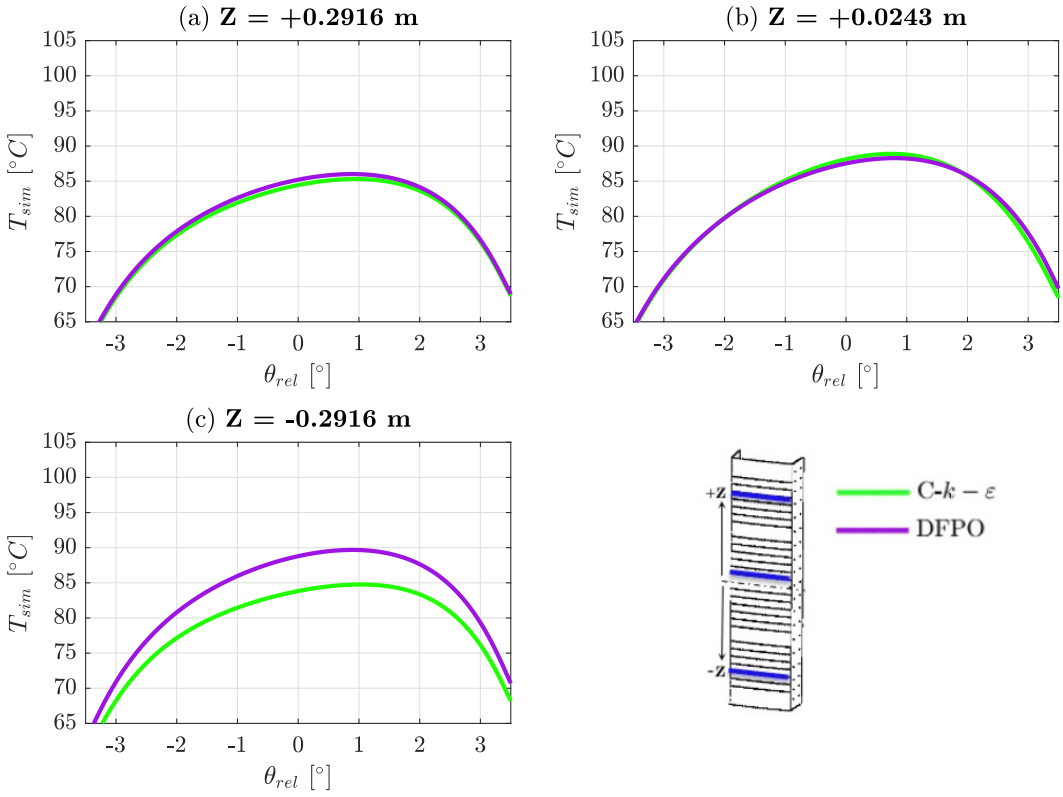

Figure 5.19: Predicted (T_{sim}) temperature profiles for the baseline and modified (DFPO) cases at three of the twenty-six relative axial positions along the height of the heated pole. Each height corresponds to the upper (a), middle (b), and lower (c) regions of the pole.

Table 5.13: Comparison of the average ($\overline{T}_{sim}$) and maximum ($max(T_{sim})$) surface temperatures between the baseline (C-$k-\varepsilon$) and modified (DFPO) cases.

Case	$\overline{T}_{sim}$ **[°C]**	$max(T_{sim})$ **[°C]**
C-$k-\varepsilon$	60.6	108.0
DFPO	61.4	108.0
ΔT^* **[°C]**	+0.8	0

CHAPTER 6
Conclusions and Future Work

This chapter presents the conclusions of the present research and recommendations for future work. It is divided into four sections. In the first and second sections, the insights gained from the experimental and computational investigations undertaken in this work are reviewed, respectively. The third section summarizes the findings of the efforts to improve the ventilation circuit of radially-cooled hydroelectric generators and related suggestions. The final section provides recommendations for the ways in which the present research may be extended in the future.

6.1 Insights Gained from the Experimental Investigations

The experimental investigations undertaken in this work provided several important insights. It was shown that the original design of the TMFM was capable of measuring the mass flow rate within the rotor rim ducts of an in-service hydroelectric generator. This measurement was a historic one for Hydro-Québec, as it was the first measurement of its kind in an in-service hydroelectric generator. However, the original design was in need of improvement due to its high cost (∼$1,000 CAD), low measurement repeatability (9%) and accuracy (above 10%) due to its artisanal fabrication and fragility. Thus, an improved design with a measurement accuracy within 8% and a measurement repeatability of 3.5% was developed and experimentally validated by way of PIV. These improvements were a result of i) a more repeatable laser welding fabrication process to affix the heating element wires to the PCBs; ii) installation of the heating element wires vertically such that their principal axes of

thermal expansion were at an angle of 90° to the RTD axes; and iii) embedding the fragile RTD wires within PCBs to shield them from the surrounding environment. Furthermore, the improved design used 50% fewer parts without the use of large metallic components, reduced the fabrication cost by 90%, and used embedded connectors to facilitate on-site installation. These improvements enabled the installation of eight newly designed TMFMs within the scale model to measure the mass flow rate passing through the rotor rim ducts. The measurements demonstrated that the mass flow rate within the rotor rim of the scale model is neither axially nor circumferentially uniform, which is a critical aspect that is generally not accounted for by manufacturers of hydroelectric generators in their design of such machines.

6.2 Insights Gained from the Computational Investigations

The computational investigations undertaken in this work provided several important insights. It was shown that when automated meshing algorithms (developed by *Numeca*) are used for discretizing the fluid flow and heat transfer calculations domain in radially-cooled hydroelectric generators, the mesh-generation time was reduced by several orders of magnitude when compared to manual meshing methods (*ANSYS ICEM*) and the numerical predictions were similar for the same CFDHT software (*CFX* in this case). An assessment of the results obtained with four TFP models demonstrated that the viscous dissipation term could be neglected in the energy equation for the fluid flow; and the predictions obtained with the fluid properties assumed constant at values corresponding to a steady-state global temperature (case-C), were almost as accurate as those obtained with temperature-dependent fluid properties (case-VP). Thus, case-C could be used in place of the computationally more expensive case-VP. The investigation of different PHL models demonstrated that modeling the heat losses due to natural convection using

empirically prescribed convective heat transfer coefficients (as done in case-C, case-VP, and case-DC) were sufficiently accurate when compared to more complex and computational expensive direct methods (case-FIS). It was also observed that no correlation exists between the imposed contact resistances (applied in between the heated pole and aluminum supports) and the error in the prediction of the temperatures on the surface of the heated pole. In addition, it was found that the predicted temperatures on the surface of the heated pole may be correlated with the predicted flow distribution in the central zone of the heated pole. The results presented in Chapter 5 also demonstrated that solving the equations of conservation of mass and momentum in a decoupled manner from the energy equations (case-DC) may be employed with reasonable accuracy when compared to the coupled case (case-C) if computational resources are limited. Lastly, both the $k-\varepsilon$ and $k-\omega$ SST turbulence models predicted the experimental results for the global flow and heat transfer quantities with similar accuracy, which warranted the use of the former over the latter given its reduced computational requirements. Ultimately, these key aspects favor the use of standard modeling approaches, corroborate the findings of previous researchers in the field, and demonstrated that the flow within the ventilation circuit of hydroelectric generators is i) highly complex, and ii) amenable to improvement that may ultimately enhance the performance and longevity of such machines.

6.3 Findings of Efforts to Improve the Ventilation Circuit

The efforts to improve the ventilation circuit of a radially cool hydroelectric generator yielded several useful findings. The attempted modifications (discussed in Section 5.3) demonstrated that both the fan blades and the flow impingement in the lower portion of the enclosure are large contributors to the windage losses. Moreover, the average and maximum operating temperatures

in the upper region of the rotor poles are predominantly impacted by the flow from the fan blades, and the flow through the rotor rim can be i) increased in the upper region by reducing the rotor inlet area, and ii) increased in the lower region by removing the wedge and extending the height of the spider arms. The present research also demonstrated that the addition of a flow deflector at the outlet of the pit openings was able to divert the high-velocity flow in the lower region of the enclosure and nearly prevent the flow from exiting the pit inlet. The largest reduction in windage losses resulted from the addition of a deflector at the pit outlet, and the largest reduction in the average and maximum temperatures was a result of increasing the length of the spider arms. Furthermore, the largest increase in net flow rate through the radiator and rotor rim were a result of the addition of the deflector at the pit outlet, and a reduction the rotor inlet, respectively. To reduce the windage losses and operating average and maximum temperatures, the radiator and rotor rim flow rates must be increased, and flow must pass through the pit openings in the intended direction, which can be achieved via further improvements to and/or using a combination of two or more of the presented modifications.

6.4 Recommendations for Future Work

Ample work is still needed to fully understand and improve the ventilation of hydroelectric generators. In this context, six different avenues are worth considering: undertaking additional measurements on in-service hydroelectric generators; acquisition of more data using scale models; continuing to validate and improve the performance of the TMFM; further streamlining the numerical modeling processes; investigating alternate ventilation configurations; and investigating the heat transfer in and from in-service rotor poles.

Undertaking additional measurements on in-service hydroelectric generators will provide quantitative insight into the thermal management of such

machines. Furthermore, such measurements are necessary to demonstrate the economic viability of both the experimental and computational investigations required to improve the ventilation of radially-cooled hydroelectric generators.

Further knowledge can be gained by performing measurements within the scale model's ventilation circuit. Measurements of the flows passing through the rotor rim ducts, ceiling openings, pit openings, and around the surface of the heated pole are still required to validate complementary numerical models. Such measurements will provide insights into the differences between the results obtained using the TMFM and the numerical simulations. Furthermore, the scale model offers the access and possibility to modify its ventilation circuit, to experimentally demonstrate the performance of proposed improvements.

Continuing to validate and improve the performance of the TMFM will lead to more confidence in quantitive measurements of the mass flow rates through the rotor rim of hydroelectric generators. Although qualitative measurements are beneficial in the identification of potential ventilation problems, accurate quantitative measurements are essential for validation of numerical models. For such, the effect of rotation on the blockage factor of the TMFM must be determined. This can be achieved by installing the TMFM in the scale model and measuring the flow passing through it by way of PIV. The latter is a challenging task as the visual accesses needed to perform such a measurement is limited but can be improved by modifying the scale model. Furthermore, since the incidence angle (both radial and axial) can be rather large at the inlet, measuring the flow at the outlet should be considered, as the more radially exiting tendency of the flow could facilitate its measurement using PIV.

Streamlining the numerical models of hydroelectric generators will facilitate the investigation of the different ventilation circuits found in hydroelectric

generators. Currently, too much time and effort is spent on the geometry and mesh generation. Furthermore, the required computational time and power is too large to be readily available to engineers designing such machines. Encouragement in this regard can be derived by noting that commercial CFDHT tools are continuously improving and becoming able to accommodate increasingly large and complex problems. This was seen throughout the years of this work and showed that even minor improvements can facilitate the modeling process substantially. It should also be noted that the results obtained in this work showed that simplifying the modeling of the pole heat losses by employing empirical convective heat transfer coefficients and solving the equations of mass and momentum decoupled from the energy equations reduced the required computational resources. However, further simplified approaches should also be investigated to reduce the computational effort and thus enable its widespread use in the design of such machines.

Investigating alternate ventilation configurations is key to improving the thermal management of hydroelectric generators. Short-term economically justifiable gains may be made by improving the ventilation of existing hydroelectric generators. However, long-term benefits can only be gained by using model-based design to simulate proposed improvements to the ventilation of hydroelectric generators, given that many ventilation improvements can only be implemented during the design phase (as opposed to retrofitting them after they have already been manufactured). For example, the size/shape of the spider arms and rotor rim ducts are almost impossible to change after the manufacturing and installment of such machines.

Improving the numerical models by accounting for the actual behavior of rotor poles is key to the detection of hot-spots for in-service hydroelectric

generators. From a diagnostics perspective, the heated pole used in the computational investigations conducted in this research is an idealization, with important differences from the actual pole design and construction. Rotor poles are comprised of many layers of insulating and conductive materials, making them difficult to model as the thermal contact resistance, and in some instances, the thermal conductivity of the insulating materials is unknown *a priori*. However, quantifying the latter aspects experimentally and including such information in numerical models could potentially provide key diagnostics information for such machines.

REFERENCES

Adrian, R.J. & Westerweel, J. 2011 *Particle Image Velocimetry*, 1^{st} edn. Cambridge University Press.

ANSYS-Inc. 2011 *ANSYS CFX—Solver Modeling Guide* **R14.0**, Canonsburg, PA, U.S.A.

Aoki, H., Nohira, H. & Arai, H. 1967 Convective Heat Transfer in an Annulus with an Inner Rotating Cylinder. *Bulletin of ASME* pp. 523–532.

Bach, E., Mydlarski, L., Torriano, F., Charest-Fournier, J., Sirois, H., Morissette, J. & Hudon, C. 2015 PIV Characterization of the Air Flow in a Scale Model of a Hydrogenerator. *Proceedings of the ASME 2015 Power Conference* San Diego, California, USA. June 28-July 2. V001T12A003.

Baliga, B. R. & Lokmanets, I. 2016 Generalized Richardson Extrapolation Procedures for Estimating Grid-Independent Numerical Solutions. *Int. J. Num. Methods for Heat & Fluid Flow* **vol. 26**, pp. 1121–1144.

Blevins, Robert D. 2001 *Flow-Induced Vibrations*, 2^{nd} edn. Krieger Publishing Company.

Bourdreault, E., Lavoie, E., Lavalée, E. & Lavoie, S. 2011 Maquette Tournante Alternateur: Rapport de Conception Mécanique. *Rapport Technique* IREQ-2011-0069, Institut de Recherche d'Hydro-Québec (IREQ), Varennes, Canada.

Churchill, S.W. & Chu, H.H.S 1975 Correlating Equations for Laminar and Turbulent Free Convection from a Vertical Plate. *International Journal of Heat and Mass Transfer* **vol. 18**, pp. 1323–1329.

Conner, P.H., Pickering, S.J., Gerada, C., Eastwick, C.N. & Micallef, C. 2013 CFD Modeling of an Entire Synchronous Generator for Improved Thermal Management. *Institution of Engineering and Technology (IET) Electric Power Applications* **vol. 7**, pp. 231–236.

Dagel, D.J., Grossetete, G.D. & Maccallum, D.O. 2016 Measurement of Laser Weld Temperatures for 3D Model Input. *Sandia Report* SAND2016-10703, Sandia National Laboratories, Albuquerque, New Mexico.

Dang, D.-D., Pham, X.-T., Labbe, P., Torriano, F., Morissette, J.-F. & Hudon, C. 2017 CFD Analysis of Turbulent Convective Heat Transfer in a Hydro-Generator Rotor-Stator System. *Applied Thermal Engineering* **vol. 130**, pp. 17–28.

Dastous, J.-B. & Lanteigne, J. 2010 Vérification de la Résistance à l'Impact de Composants de la Maquette Alternateur. *Rapport Technique* IREQ-2010-0073, Institut de Recherche d'Hydro-Québec (IREQ), Varennes, Canada.

Dimanchev, E., Hodge, J. & Parsons, M. 2020 Two-Way Trade in Green Electrons: Deep Decarbonization of the Northeastern U.S. and the Role of Canadian Hydropower. *MIT CEEPR Working Paper 2020-003* .

Esch, T. & Menter, F. 2001 Elements of Industrial Heat Transfer Predictions. 16^{th} Brazilian Congress of Mechanical Engineering (COBEM) Uberlandia, Canada.

Figliola, R.S. & Beasley, D.E. 2011 *Theory and Design for Mechanical Measurements*, 5^{th} edn. Wiley & Sons.

Giles, M.B. 1988 Non-Reflecting Boundary Conditions for the Euler Equations. *CFDL Report 88-1* MIT Dept. of Aero. and Astro.

Giles, M.B. 1991 UNSFLO: A Numerical Method for Unsteady Flow in

Turbomachinery. *Gas Turbine Laboratory Report GTL 205* MIT Dept. of Aero. and Astro.

Goldstein, R.J., Sparrow, E.M. & Jones, D.C. 1973 Natural Convection Mass Transfer Adjacent to Horizontal Plates. *International Journal of Heat and Mass Transfer* **vol. 16**, pp. 1025–1035.

Gunabushanam, N. & Suresh, J. 2006 Experimental and CFD Analysis of Hydrogenerator Ventilation Components. *International Council of Large Electric Systems (CIGRE)* .

Hartono, E., Golubev, M., Moradnia, P., Chernoray, V. & Nilsson, H. 2012*a* A PIV Study of the Cooling Air Flow in an Electric Generator Model. *Technical Report* Department of Applied Mechanics, Chalmers University of Technology, Göteborg, Sweden.

Hartono, E., Golubev, M., Moradnia, P., Chernoray, V. & Nilsson, H. 2012*b* PIV Measurement of Air Flow in a Hydro Power Generator Model. 16^{th} *International Symposium on Applications of Laser Techniques to Fluid Mechanics* Lisbon, Portugal.

Hijazi, A. & Madhaven, V. 2008 A Novel Ultra-High Speed Camera for Digital Image Processing Applications. *Measurement Science and Technology* pp. 1–11.

Hudon, C., Guddemi, C., Gingras, S., Leite, R.C. & Mydlarski, L. 2016 Rotor Temperature Monitoring using Fiber Bragg Gratings. *Proceedings of the Electrical Insulation Conference (EIC)* pp. 456–459, Montéal, Québec, Canada, 19 - 22 June.

Hudon, C., Leduc, J., Torriano, F., Bélanger, S., Soares, M., Dastous, J.-B., Marcoullier, L., Lévesques, J.-B., Lavoie, E., Lemire, R. & Jobidon, N. 2011 Rapport Global Maquette Tournante Alternateur. *Rapport Technique* IREQ-2011-0071, Institut de Recherche

d'Hydro-Québec (IREQ), Varennes, Canada.

Hudon, C., Merkhouf, A., Chaaban, M., Bélanger, S., Torriano, F., Leduc, J., Lafleur, F., Morissette, J.-F., Millet, C. & Gagne, M. 2010 Hydro-Generator Multi-Physics Modeling. *European Journal of Electrical Engineering* **vol. 13**, pp. 563–589.

Hydro-Québec 2019 Setting New Sights with our Clean Energy. *Strategic Plan* **vol. 2020-2024**, pp. 1–48.

Hydro-Québec 2020 Cross-section View of a Generating Unit. Online; accessed May 22, 2020.

Hydro-Québec 2021 Generating Stations. Online; accessed January 1, 2021.

Jackson, D. & Launder, B. 2007 Osborne Reynolds and the Publication of His Papers on Turbulent Flow. *Annu. Rev. Fluid Mech.* **vol. 39**, pp. 19–35.

Jamshidi, H., Nilsson, H. & Chernoray, V. 2015 CFD-Based Design and Analysis of the Ventilation of an Electric Generator Model Validated with Experiments. *International Journal of Fluid Machinery and Systems* **vol. 8**, pp. 113–123.

Jichao, H., Baojun, G., Dajun, T., Hongsen, Z., Fang, X. & Weili, L. 2017 Calculation and Analysis of Complex Fluid Flow and Thermal Fields in a Fully Air-Cooled Hydrogenerator. *International Journal of Thermal Sciences* **vol. 116**, pp. 278–286.

Kadar, B. 1981 Temperature and Concentration Profiles in Fully Turbulent Boundary Layers. *Int. J. Heat Mass Transfer* **vol. 24**, pp. 1541–1544.

Kastner, G., Fernleitner, E. & Brunner, M. 2010 Usage of Computational Fluid Dynamics in the Design Process for Prototype Hydro-Generators. *Proceedings of the* 16^{th} *International Seminar on Hydropower Plants* Vienna, Austria.

Kays, William M. 1994 Turbulent Prandtl Number - Where Are We? *J.*

Heat Transf. **vol. 116**, pp. 284–295.

Keane, R.D. & Adrian, R.J. 1990 Optimization of Particle Image Velocimeters. I. Double Pulsed System. *Measurement Science and Technology* pp. 1202–1215.

Keane, R.D. & Adrian, R.J. 1992 Theory of Cross-Correlation Analysis of PIV Images. *Applied Scientific Research* pp. 191–215.

Kirouac, M. 2017 Système Embarqué pour la Mesure de Débit massique dans les Jantes d'un Rotor d'Alternateur de Réseau. *Rapport Technique* Université de Sherbrooke, Québec, Canada.

Klomberg, S., Farnleitner, E., Kastner, G. & Bíró, O. 2014*a* Comparison of CFD Analyzing Strategies for Hydro Generators. *International Conference of Electrical Machines (ICEM)* pp. 1990–1995.

Klomberg, S., Farnleitner, E., Kastner, G. & Bíró, O. 2014*b* Implementation of a New Simulation Strategy for a Cooling Study of Large Hydro Generators. *International Conference of Power Electronics, Machines and Drives (PEMD)* pp. 1–6.

Kähler, C. J., Sammler, B. & Kompenhans, J. 2002 Generation and Control of Tracer Particles for Optical Flow Investigations in Air. *Experiments in Fluids* pp. 736–742.

Lancial, N., Torriano, F., Beaubert, F., Harmand, S. & Rolland, G. 2017 Taylor-Couette-Poiseuille Flow and Heat Transfer in an Annular Channel with a Slotted Rotor. *International Journal of Thermal Sciences* **vol. 112**, pp. 92–103.

Lang, H., Kral, C., Haumer, A., Haigis, M. & Schulz, R. 2006 Investigation of the Thermal Behavior of a Salient Pole Synchronous Machine. *Proceedings of the* 17^{th} *International Conference on Electrical Machines* Chania, Crete Island, Greece.

Laskin, S. 1948 Submerged Aerosol Unit. *AEC Project Quarterly Report UR-38.* University of Rochester.

Launder, B. & Sandham, N. 2002 *Closure Strategies for Turbulent and Transitional Flows*, 1^{st} edn. Cambridge University Press.

Launder, B.E. & Sharma, B.I. 1974 Application of the Energy Dissipation Model of Turbulence to the Calculation of Flow Near a Spinning Disc. *Letter in Heat and Mass Transfer* **vol. 1, no. 2**, pp. 131–138.

Launder, B.E. & Spalding, D.B. 1972 Mathematical Model of Turbulence. *Academic Press* New York.

Lienhard, V. & Helland, K. 1989 An Experimental Analysis of Fluctuating Temperature Measurements using Hot-Wires at Different Overheatse. *Experiments in Fluids* **vol .7**, pp. 265–270.

Lloyd, J.R. & Moran, W.R. 1974 Natural Convection Adjacent to Horizontal Surfaces of Various Planforms. *ASME J. Heat Transfer* pp. pp. 443–447.

Luo, J.Y., Issa, R.I. & Gosman, A.D. 1994 Prediction of Impeller-Induced Flows in Mixing Vessels Using Multiple Frames of Reference. *IChemE Symposium Series* pp. pp. 549–556.

Lévesque, J.-B. & Pichette, J. 2020 Mesure des Propriétés Mécaniques en Tension du Matériau de Fabrication additive ULTEM-9085. *Rapport Technique* IREQ-2020-0092, Institut de Recherche d'Hydro-Québec (IREQ), Varennes, Canada.

Lévesque, M., Hudon, C., Petit, A., Gingra, S., Guddemi, C., Picard, J., Sirois, H., Charest-Fournier, J.P., Morissette, J.F. & Torriano, F. 2013 Analyse des Mesures de Température par Sonde ThermaWatch Rotor. *Rapport Technique* IREQ-2013-0143, Institut de Recherche d'Hydro-Québec (IREQ), Varennes, Canada.

Meinhart, C.D., Wereley, S.T. & Santiago, J.G. 2000 A PIV Algorithm for Estimating Time-Averaged Velocity Fields. *Journal of Fluids Engineering* pp. 285–289.

Menter, F.R. 1994 Two-Equation Eddy-Viscosity Turbulence Modeling for Engineering Applications. *AIAA Journal* **vol. 32, no.8**, pp. 252–263.

Merkhouf, A., Bélec, M., Amyot, N., Provencher, H., Lévesque, M., Torriano, F., Hudon, C., Lafleur, F., Marcouiller, L. & Essalihi, M. 2017 Étude de lÉtat de l'Art des Outils de Diagnostic de Rotor des Alternateurs Hydrauliques. *Rapport Technique* IREQ-2017-0035, Institut de Recherche d'Hydro-Québec (IREQ), Varennes, Canada.

Moradnia, P., Chernoray, V. & Nilsson, H. 2014*a* Experimental Assessment of a Fully Predictive CFD Approach for Flow of Cooling Air in an Electric Generator. *Applied Energy* **vol. 124**, pp. 223–230.

Moradnia, P., Golubev, M., Chernoray, V. & Nilsson, H. 2014*b* Flow of Cooling Air in an Electric Generator Model – An Experimental and Numerical Study. *Applied Energy* **vol. 114**, pp. 644–653.

Niebles Atencio, B., Jamshidi, H., Lijemark,L., Nilsson, H. & Chernoray, V. 2020 Assessment of the Naphthalene Sublimation Technique for Determination of Convective Heat Transfer in Fundamental and Industrial Applications. *Heat and Mass Transfer* **vol. 56**, pp. 113–123.

Olsen, M.G. & Adrain, R.J. 2000 Out-of-Focus Effects on Particle Image Visibility and Correlation in Microscopic Particle Image Velocimetry. *Experiments in Fluids* pp. 166–174.

Pickering, S., Lampard, D. & Shanel, M. 2001 Modelling Ventilation and Cooling of the Rotors of Salient Pole Machines. *Electric Machines and Drives IEEE International Conference* pp. 806–808, cambridge, Massachusetts, U.S.A.

Pope, S. 2000 *Turbulent Flows*. Cambridge University Press.

Raffel, M., Willert, C. E., Wereley, S. T. & Kompenhans, J. 2007 *Particle Image Velocimetry: A Practical Guide*, 2^{nd} edn. Springer.

Saleban, N., P. Germano, C. Hudon & Y. Perriard 2013 Développement de Capteurs de Mesures de la vitesse de l'Air dans le Rotor des Alternateurs. *Master's Thesis* École Polytechnique Fédérale de Lausanne (EPFL).

Saxer, A.P. 1992 Numerical Analysis of Three-Dimensional Inviscid Rotor/Stator Interactions Using Non-Reflecting Boundary Conditions. *Ph.D. Thesis* MIT Dept. of Aero. and Astro.

Schrittwieser, M., Marn, A., Farnleitner, E. & Kastner, G. 2014 Numerical Analysis of Heat Transfer and Flow of Stator Duct Models. *IEEE Transactions on Industry Applications* **vol. 50**, pp. 226–233.

Sciacchitano, A., Wieneke, B. & Scarano, F. 2013 PIV Uncertainty Quantification by Image Matching. *Measurement Science and Technology* .

Shanel, M., Pickering, S. J. & Lampard, D. 2003 Conjugate Heat Transfer Analysis of a Salient Pole Rotor in an Air Cooled Synchronous Generator. *Electrical Machines and Drives IEEE International Conference* Madison, Wisconson, U.S.A.

Soloff, S. M., Adrian, R. J. & Liu, Z.-C. 1997 Distortion Compensation for Generalized Stereoscopic Particle Image Velocimetry. *Measurement Science and Technology* pp. 1441–1454.

Soo, S. L., Tien, C.L. & Kadambi, V. 1959 Determination of Turbulence Characteristics of Solid Particles in a Two-Phase Stream by Optical Autocorrelation. *Review of Scientific Instruments* pp. 821–824.

Tavoularis, S. 2009 *Measurement in Fluid Mechanics*, 1^{st} edn. Cambridge University Press.

Torriano, F., Lancial, N., Lévesque, M., Rolland, G., Hudon, C., Beaubert, F., Morissette, J.-F. & Harmand, S. 2014 Heat Transfer Coefficient Distribution on the Pole Face of a Hydrogenerator Scale Model. *Applied Thermal Engineering* **vol. 70**, pp. 153–162.

Torriano, F., Venne, K., Kirouac, M., Provencher, L. & Mydlarski, L. inventors; Hydro Québec, assignee 2021*a* Débitmetre Électronique à Bilan Thermique Canada Patent Application No. PCT/CA2021/051831.

Torriano, F., Venne, K., Provencher, L., Kirouac, M., Lévesque, J.-B. & Bissonnette, S. 2021*b* Développement d'un Capteur Anémométrique pour la Mesure de Débit d'Air dans les Évents de Jante d'un Alternateur. *Rapport Technique* IREQ-2021-0072, Institut de Recherche d'Hydro-Québec (IREQ), Varennes, Canada.

Toussaint, K., Torriano, F., Morissette, J.-F., Hudon, C. & Reggion, M. 2011 CFD Analysis of Ventilation Flow for a Scale Model Hydro-Generator. *ASME Power Conference* pp. 627–637, Denver, Colorado, U.S.A.

Venne, K. 2017 Design of an Anemometer to Characterize the Flow in the Rotor Rim ducts of a Hydroelectric Generator. *Master's Thesis* McGill University.

Venne, K., Mydlarski, L.B., Torriano, F., Kirouac, M., Charest-Fournier, J.-P. & Hudon, C. 2018 Design of a Thermal Mass Flow Meter for Measurements within the Rotor Rim Ducts of a Hydroelectric Generator. Proceedings of the ASME 2018 5^{th} Joint US-European Fluids Engineering Division Summer Conference Montréal, Québec, Canada.

Viazzo, S. & Poncet, S. 2014 Numerical Simulation of the Flow Stability in a High Aspect Ratio Taylor- Couette System Submitted to a Radial Temperature Gradient. *Computers & Fluids* pp. 15–26.

Vieser, Wolfgang., Esch, T. & Menter, F. 2002 Heat Transfer Predictions using Advanced Two-Equation Turbulence Models. *CFX Technical Memorandum* **CFX-VAL10/0602**.

Vogt, B. & Lahres, S. 2013 Calculation of Cooling and Ventilation of Large Hydro Generators with Advanced 3D Numerical Methods. *Proceedings of the International HYDRO Conference* Innsbruck, Austria.

Westerweel, J. 1994 Efficient Detection of Spurious Vectors in Particle Image Velocimetry Data. *Experiments in Fluids* pp. 236–247.

Westerweel, J. 1997 Fundamentals of Digital Particle Image Velocimetry. *Measurement Science and Technology* pp. 1379–1392.

Westerweel, J. & Scarano, F. 2005 Universal Outlier Detection for PIV Data. *Experiments in Fluids* pp. 1096–1100.

Wilcox, David C. 2006 *Turbulence Modeling for CFD*, 3^{rd} edn. DCW Industries.

Yakhot, V., Orszag, S.A., Thangam, S., Gatski, T.B. & Speziale, C.G. 1992 Development of Turbulence Models for Shear Flows by a Double Expansion Technique. *Physics of Fluids* **vol. 4**, pp. 1510–1520.

APPENDIX A
A Meshing Strategy for Hydroelectric Generators

The development of a suitable strategy for discretizing the computational domain of radially-cooled hydroelectric generators was an additional challenging aspect of the proposed research. In industrial CFDHT applications, often, mesh generation is one of the most complex and time-consuming aspects, but little information is available in the open literature on the intricate details required to generate a satisfactory mesh for complex geometries. Although meshing strategies may not be viewed by some as the most critical or scientifically significant aspect of CFDHT simulations, the improvements to the meshing of the complex geometry of the scale model of a hydroelectric generator, developed as part of this work, provided significant improvement that will have an impact on the ability to numerically model such sophisticated equipment. Thus, this appendix provides all the necessary details required (*i.e.* software used, functions, step-by-step processes, *etc.*) for the benefit of all, and in particular researchers at IREQ.

At the time of the development of the meshing strategy in this work, IREQ had access to three software packages to discretize the calculation domain: *ANSYS ICEM CFD* (ICEM), *Numeca HEXPRESS* (HEX), and *Numeca HEXPRESS/Hybrid* (HH). The first is a manual meshing software that creates hexahedral meshes with conformal interfaces. The second is an automatic meshing software that creates anisotropic hexahedral cells with non-conformal cell interfaces, which is advantageous for components of large aspect ratios. The third is also an automatic hexahedral mesh generator, but uses isotropic cells with conformal interfaces, and occasionally uses tetrahedral cells to better

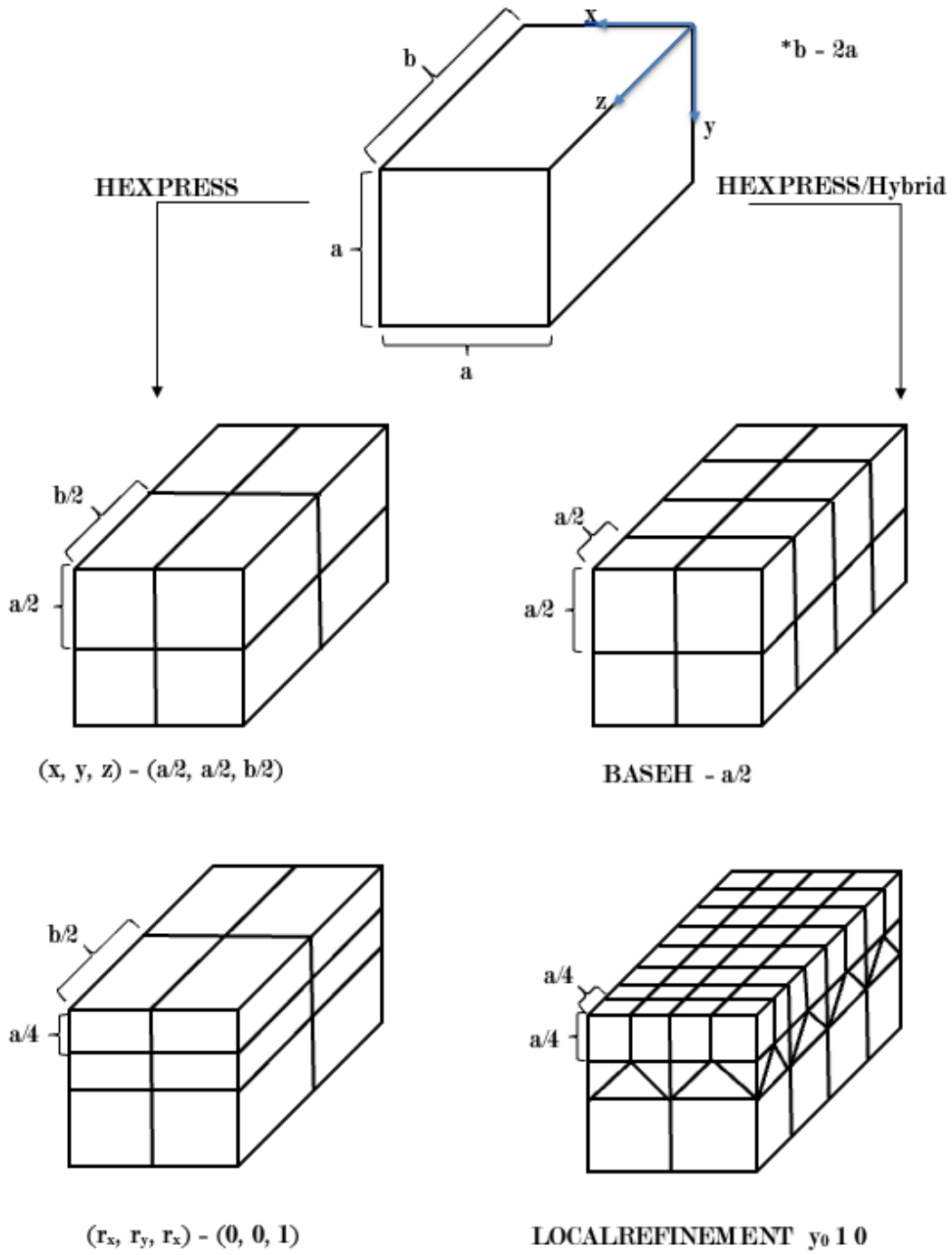

Figure A.1: Illustration of the mesh generation and refinement processes on a cuboid with HEXPRESS and HEXPRESS/Hybrid.

adapt to complex geometries. A sketch comparing the differences in the mesh adaptation techniques of the latter two software packages on a cuboid with wall size four times its height is illustrated in figure A.1. Since HH creates isotropic hexahedral/tetrahedral meshes, it tends to use more elements when compared to the other software packages. However, because it is parallelized, it tends to generate a given mesh more rapidly. Each software had its advantages and disadvantages. Ultimately, the meshing strategy employed in this work utilized all three meshing software packages to quickly create the mesh for a subsequent CFDHT analysis of a hydroelectric generator.

A.1 Strategy Employed for Hydroelectric Generators

After several attempts, a strategy employing a favorable mix of compromises between four metrics was chosen (*i.e.* i) mesh evaluation metrics, ii) mesh generation time, iii) number of computational nodes, and iv) practicality). The strategy ultimately used all three meshing software packages (i.e. ICEM, HEX, and HH) in two groups: i) meshing of geometries consisting entirely of simple rectangular or square shapes, and ii) meshing of all other geometries. If the component fell into the first group, then ICEM was used, as it was estimated that it would take an hour or less to generate its mesh, in addition to obtaining a superior mesh quality for the same amount of user input (time) when compared to other automatic meshing software packages. The strategy for components falling into the second group required the use of both HEX and HH. However, HEX was only used for its graphical user interface (GUI) to reduce the user input (time) required to create the HH mesh scripts (*i.e* .conf files) and then the mesh was generated using the HH algorithm. The strategy employed for the second group is illustrated in figure A.2 and comprised 8 parts: i) geometry manipulation, ii) refinement group creation, iii) mesh type decision (i.e. conforming or non-conforming), iv) specifying the

initial mesh, v) geometry adaptation, vi) geometry snapping, vii) mesh file creation, and viii) post-processing.

The geometry manipulation consisted of using any computer-aided design (CAD) tool to create the computational domain. For this work ANSYS Space Claim Design Modeler (SCDM) was used and the files were converted to CATIA (V5) files, which is compatible with HEX/HH. However, almost any CAD tool could be used if it can be converted to a HEX/HH compatible file. The first step of the geometry manipulation was to simplify the scale model geometry. This consisted of removing any fine details (e.g. rivets, screws, etc.) that would have minor effects on the numerical model, but large implications when generating the computational domain. As previously mentioned, the computational domain was then subdivided to further simplify the meshing process. Each division required the use of a GGI to conserve mass, momentum, and energy across the interface of two different sub-domains. Thus, the divisions were made based on the length scales of important features found in the scale model's computational domain to reduce the number of cells (or nodes) required to mesh that domain. For example, one of the smallest features in the scale model are the stator ducts. If these ducts are not isolated when using HH, the number of cells in the computational domain would drastically increase. Thus, GGIs allowed for interconnected sub-domains with a mismatched ratio of cells at the interfaces. However, along both the rotor-stator and fluid-solid interfaces, this ratio was kept as close to unity as possible to accelerate convergence and maintain conservation principles across the interface. Ultimately, two SCDM tools: split and imprint, were used to subdivide the computational domain. The former permitted the subdivision of the computational domain along predetermined regions (*i.e.* rotor, stator, *etc.*), and the latter permitted the creation of 2D faces on the subdivided domains, which allowed for an

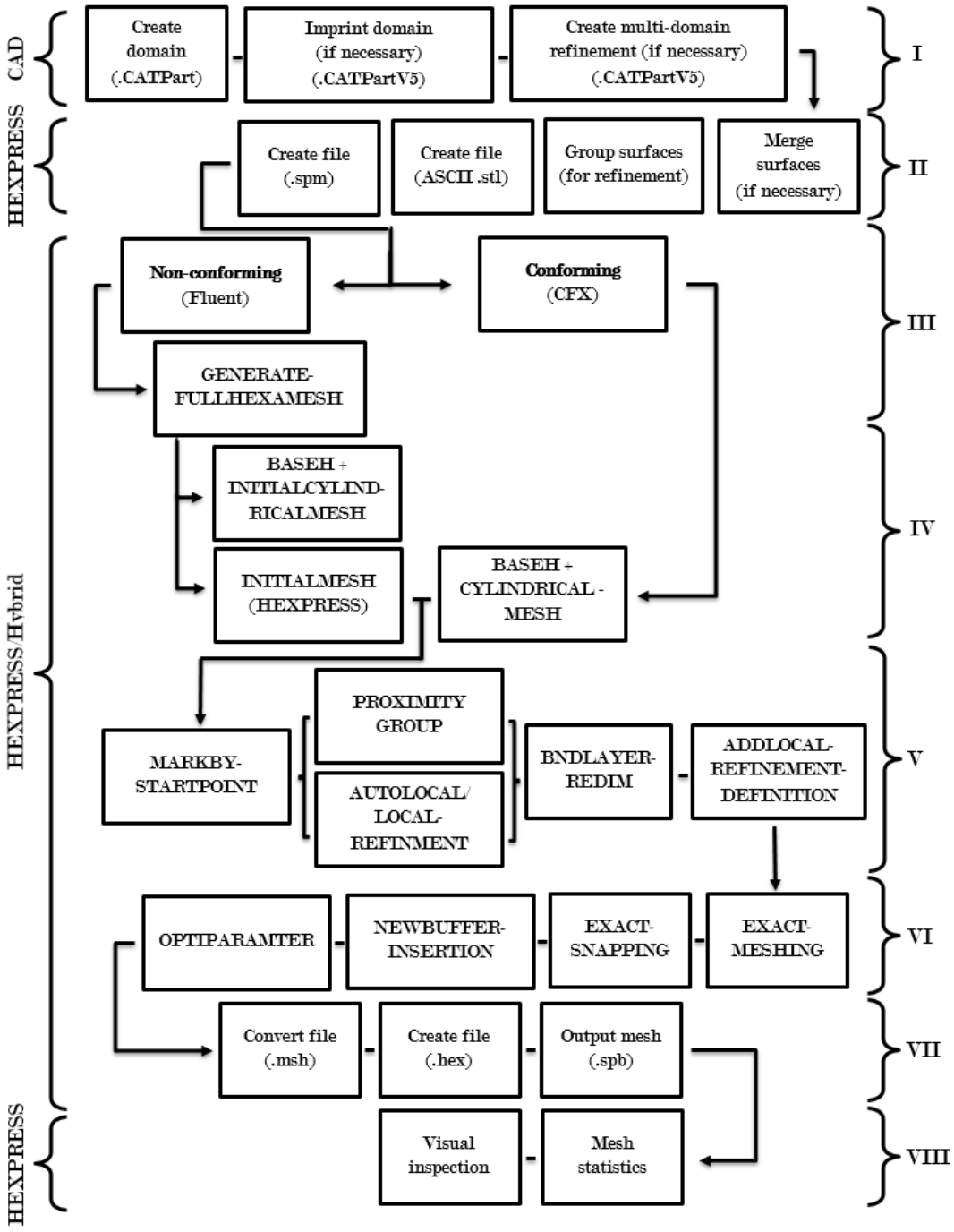

Figure A.2: Eight-step flow chart for the mesh strategy development of hydro-electric generators: i) geometry manipulation, ii) refinement group creation, iii) mesh type decision, iv) initial mesh specification, v) geometry adaptation, vi) geometry snapping, vii) mesh file creation, and viii) post-processing.

appropriate interface link in the CFDHT software. Therefore, using SCDM and GGIs, the scale model was subdivided into 11 components, as previously indicated in figure 3.1. This specification then permitted the allocation of the refinement groups.

To limit the number of cells in the computational domain, refinements were applied to capture small components and/or potential gradients in the flow (*i.e.* near walls), which were then gradually relaxed (or diffused) from these regions to reduce the cell count. Although the computational domain of the scale model was heavily subdivided, mesh refinement and diffusion were also employed to limit the node count. Since the features requiring refinement in the scale model's computational domain are repetitive, it was essential to create refinement groups. It was found that the creation of such groups for the scale model was best handled by HEX. This process required four major steps: i) merging faces, ii) grouping faces, iii) creation of the new CAD model with named groups in standard triangle language (.stl) American Standard Code of Information Interchange (ASCII) format, and iv) creation of the Salt Package Manager (.spm) file. The first step was required to further simplify the domain, because when the CAD file (*e.g.* .CATPart) was loaded into HEX, it was converted into a connection of faces (*e.g.* .dom file). However, this division might not be necessary, or it may create redundant refinement groups. Once the latter were eliminated, the faces were grouped in HEX using the boundary conditions settings. Once a given face was selected, the "Select all geometrically similar faces" algorithm was invoked such that the array of similar faces were grouped and renamed to a common name, which permitted the implementation of identical refinements on these regions in subsequent steps. Currently, Numeca only offers this algorithm in HEX, which is the only reason the software was preferred over the others for the refinement group

creation. (Due to persistent interactions with Numeca, it will be available in 2021 in Numeca's new software OMNIS). Each subdivision of the scale model had hundreds of geometrically similar faces. Because grouping them by hand would have taken days, a tool that automatically achieved this in seconds was essential. Once, the refinement groups were created, the file had to be strictly saved in .stl ASCII format so that the names of the faces in the refinement groups were preserved when opened in HH. The final step was to save the file in HH in .spm format. The completion of the aforementioned steps permitted the choice of the type of mesh and the creation of the HH configuration file (.conf).

Among the preliminary decisions that were made when writing the HH configuration file was the type of mesh (*i.e.* conforming or not). A conforming mesh is one that avoids the creation of hanging nodes after its refinement. A hanging-node is an edge or face node that is not connected to vertices of neighboring cells sharing those edges or faces. Thus, a non-conforming mesh would allow the creation of hanging nodes. The difference between conforming and non-conforming meshes, and the creation of hanging nodes during refinement, is illustrated in figure A.3. By default, HH generates a conforming mesh and the activation of a non-conforming mesh requires the use of the following command: GENERATEFULLHEXAMESH (as illustrated in figure A.2). Ultimately, the mesh choice was a compromise between: i) the CFDHT solver, ii) number of cells, and iii) mesh quality. When confined to ANSYS CFD solvers, only Fluent is compatible with a non-conforming mesh type. Generally, a non-conforming mesh will have fewer calculation nodes than a conforming one. Furthermore, a non-conforming mesh will better adapt to complex geometries and have more elements of better quality (high orthogonality and low skewness). However, the latter two points were overcome by

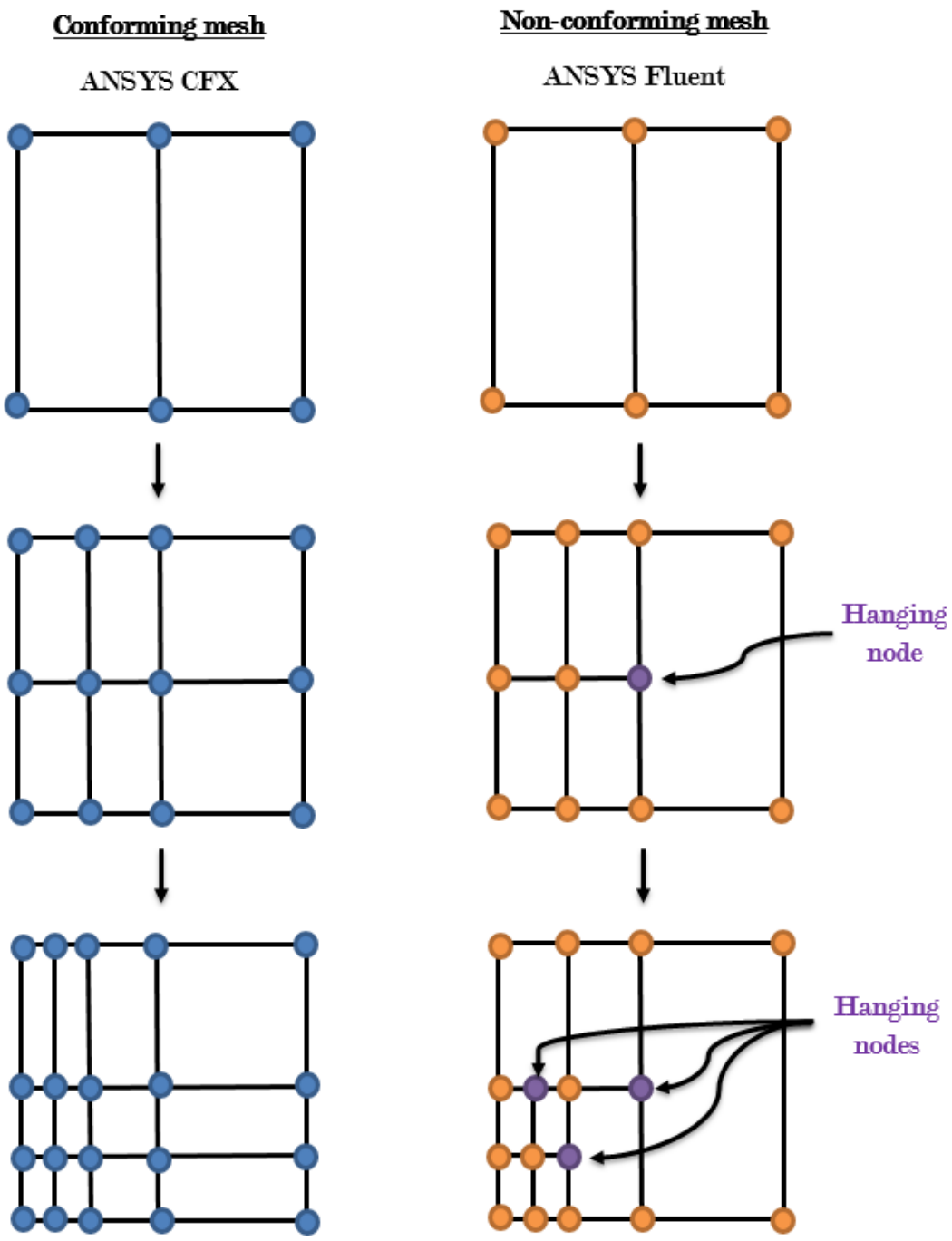

Figure A.3: Sketch illustrating the differences between a non-conforming and conforming mesh when face refinements are invoked.

use of a conforming mesh and increasing the refinement or node count due to the available computational resources. When developing the numerical model for the scale model, a conforming mesh was preferred as CFX was a more appropriate solver for turbomachines (*i.e.* rotating-stationary domains), based on the experience of experts at IREQ.

After determining the type of mesh in the configuration file, the initial mesh was specified. To set the initial mesh, both the coordinate system and the initial size was specified. The former is typically easier to determine than the latter. Since the scale model is essentially a rotating cylinder, the cylindrical coordinate system was employed. Different HH cylindrical mesh generation commands were tested, but the command CYLINDIRCALMESH was utilized. In HH, the initial size in all directions was specified by the command: BASEH. In this case, the domain was discretized in sectors from the minimum to maximum radius of the domain of interest with the isotropic cell definition at the average radius. Ultimately, iterative adjustments were made between the initial mesh size and the mesh surface adaptation to limit the cell count and the stretching ratio between the boundary layer and the outer flow (or Eulerian mesh).

Once the initial mesh size was determined, the functions that fall under geometry adaptation were specified as shown in the process flow chart in figure A.2. First, the command MARRKBYSTARTPOINT was used to aid the mesh algorithm in removing cells from the initial mesh that do not fall within the boundary of the computational domain. Next, a combination of PROXIMITYGROUP and AUTOLOCAL/LOCALREFINEMENT commands were used to capture small details of the geometry and control the surface mesh size based on angles between surfaces and user-controlled refinement definitions. In

HH, the mesh refinement follows the following expression:

$$\Delta R = BASEH * 0.5^{r}, \tag{A.1}$$

where the surface mesh size (ΔR) is a function of the initial mesh size (BASEH) and the refinement index (r). Thus, near a prescribed surface, the cells were halved until the refinement index was respected, as illustrated in figure A.1. Furthermore, if a zone or volume required refinement (*e.g.* the rotor rim ducts, interpole region, and stator ducts of the scale model), CAD files representing these zones were added to the configuration file and refined using the command ADDLOCALREFINEMENTDEFINITION. Lastly, a boundary layer was defined to better control near-wall effects. In the present study, the recommended three-layer boundary mesh (or equidistant layers grown from the surface of the geometry) were used, where the wall size in the first layer (Δs) was defined as:

$$\Delta s = 0.57\Delta R, \tag{A.2}$$

and the total size of the three layers was simply three times that value. To further control the first layer of the wall boundary mesh, the command BNDLAYERREDIM was used to re-dimension the first layer specifying the stretching ratio and the number of layers. The latter command aided the control of the minimum y^{+} value to adhere to the recommendations of the turbulence models used in the present study. Given that the actual flow field is seldom known *a priori*, estimates for the first wall size were difficult to prescribe. However, in cases where estimates of the velocity could be made, a local Reynolds number (Re_x) was calculated to allow for the estimates of the skin friction coefficient (C_f) over a flat plate by way of the following correlation:

$$C_f = \frac{0.026}{Re_x^{1/7}}, \tag{A.3}$$

which is designed for turbulent flow. Once the skin friction coefficient was evaluated, the wall shear stress (τ_w):

$$\tau_w = \frac{1}{2} C_f \rho U_\infty^2, \tag{A.4}$$

and the friction velocity (u^*):

$$u^* = \sqrt{\frac{\tau_w}{\rho}}, \tag{A.5}$$

(where U_∞ is the free stream velocity and ρ the fluid density) were also evaluated. Using the calculated values of the friction velocity, an estimate for the first layer wall size was determined from the following equation:

$$\Delta s = \frac{y_{des}^+ \mu}{u^* \rho}, \tag{A.6}$$

which is a function of the dynamic viscosity of the fluid (μ) and the desired dimensionless wall-normal position (y_{des}^+). These estimates were impossible to make for all the countless surfaces in the numerical domain of the scale model. Thus, an iterative approach was utilized, in which post-processed values were considered until the y^+ criterion was met on all surfaces. To limit the node count, all simulations employing the standard $k - \varepsilon$ turbulence model used a HRM approach with $y^+ \geq 30$, whereas the simulations that employed the $k-\omega$ SST turbulence model only respected the $y^+ \approx 1$ criterion on the surfaces of the heated pole, rotor, stator, such that the AWT was invoked.

After the geometry adaptation functions were specified in the configuration file, the geometry snapping functions were specified. As illustrated in figure A.2, four different functions were employed. Different parameters were used based on the sub-domain of interest, but their objective was to fix low quality cells and correctly adhere to the defined boundaries of the computational domain.

The last step of the meshing strategy was the creation of the mesh file and the analysis of the mesh quality. Each subdivision of the computational domain's mesh file was exported into three formats: i) HH spider file (.spb), ii) HEXPRESS grid point file (CGNS format), and iii) Fluent mesh format (.msh). It was regarded as a best practice to generate the natural spider file (.spb) from HH, and to then use the program DATAMAPPER to convert the spider file into an HEXPRESS grid point file (.hex). This was performed in such a manner because the HEX GUI was better equipped to provide mesh statistics and pin-point bad cells in a given mesh. Once this was completed, the HH spider file (.spb) was then converted using DATAMAPPER to the ANSYS Fluent native file (.msh), since HH is only able to convert to this ANSYS mesh format, and it is an allowable format for the CFX CFDHT solver.

A.2 Mesh Evaluation Metrics

Metrics to accelerate convergence, minimize numerical instabilities, and improve accuracy of a numerical simulation for a given mesh have been established for *ANSYS* commercial codes (ANSYS-Inc., 2011). Many different metrics can be considered to evaluate a given mesh. However, since HH was used in the present study, only two mesh metrics were considered: orthogonality and skewness, given that other metrics were inherently respected.

Mesh orthogonality for a given cell (Λ_i) is a measure of the perpendicularity of a face from a normal vector to its centroid defined as

$$\Lambda_i = min\left[\frac{\underline{A}_i \cdot \underline{f}_i}{|\underline{A}_i||\underline{f}_i|}, \frac{\underline{A}_i \cdot \underline{c}_i}{|\underline{A}_i||\underline{c}_i|}\right], \tag{A.7}$$

which is a function of the face area vector ($\underline{A}_i$), the vector from the centroid of the cell to the centroid of the face i ($\underline{f}_i$), and the vector from the centroid of the cell to the centroid of a shared face i of an adjacent cell ($\underline{c}_i$). Vectors are denoted with an underbar and are depicted in figure A.4(a). The orthogonality metric

is normalized, with values between 0 (bad) and 1 (excellent) that quantify the squareness of a given cell.

The mesh skewness for a given cell (Φ_i) is a measure of the deviation from an idealized (*e.g.* equilateral triangle or equiangular quadrilateral) face/cell, defined as:

$$\Phi_i = max\left[\frac{\theta_{max} - \theta_e}{180 - \theta_e}, \frac{\theta_e - \theta_{min}}{\theta_e}\right], \tag{A.8}$$

which is a function of the largest angle in the cell (θ_{max}), the smallest angle in the face (θ_{min}), the angle corresponding to the equiangular face (θ_e), as depicted in figure A.4(b). The latter is 60° for an equilateral triangle and 90° for an equiangular quadrilateral. The skewness is a normalized metric, with values between 0 (excellent) and 1 (bad) that quantify the deviation from an ideal triangle.

(a) Orthogonality (Λ_i)

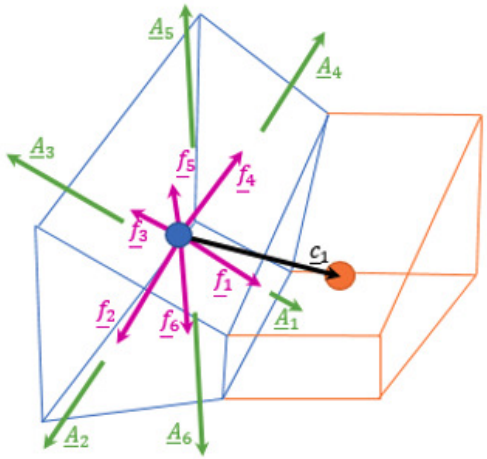

Bad	Poor	Fair	Good	Great	Excellent
0 - 0.001	0.001 – 0.14	0.15 – 0.20	0.20 – 0.69	0.70 – 0.95	0.95 – 1.00

(b) Skewness (Φ_i)

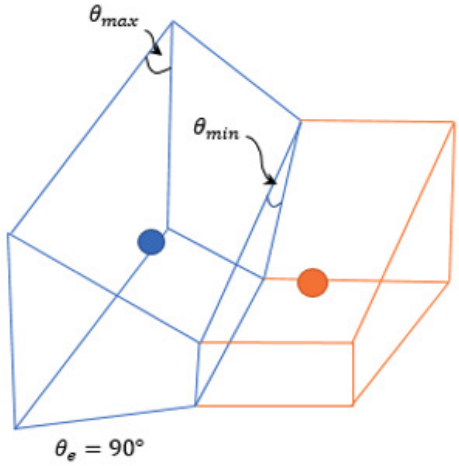

Excellent	Great	Good	Fair	Poor	Bad
0 – 0.25	0.25 – 0.50	0.50 - 0.80	0.80 - 0.94	0.95 - 0.97	0.98 – 1.00

Figure A.4: Mesh evaluation metrics and grading. (a) Orthogonality mesh evaluation metrics/grading. (b) Skewness mesh evaluation metrics/grading.

In the current study, two computational domains corresponding to each turbulence model investigated (*i.e.* $k-\varepsilon$ and $k-\omega\ SST$) were generated for the fluid flow within the scale model, and one computational domain for the solid components of the heated pole. For each computational domain, the percentage of the total cell count corresponding to the lowest acceptable grading bins were tabulated for the orthogonality (*i.e.* Λ_{poor} and Λ_{fair}) and skewness (*i.e.* Φ_{poor} and Φ_{fair}) in table A.1(a). To meet the near-wall mesh criteria for the $k-\varepsilon$ and $k-\omega\ SST$ turbulence models, 125M and 190.6M cells were respectively required in the fluid domain, as shown in tables A.1(b-c). Moreover, 19M cells were used in the solid portion of the computational domain, as shown in table A.1(d). Also shown in tables A.1(b-d), is the computer time (T) required to generate the fluid and solid computational domains. Generation of the fluid computational domain took approximately 5 and 6 hours of computer time using HH, for each respective turbulence model, which was a substantial reduction in the time required to generate a similar mesh using ICEM (which took 3 months). Generation of the solid computational domain took 10 hours to generate, with 8 hours attributed to the components of the heating pads, which were generated in ICEM due to the simplicity of the geometry. Even if one cell of the computational domain consisting of several million cells is in a lower category, the grade of the entire domain is placed in that category to respect the grading scheme established by ANSYS-Inc. (2011). Thus, marks of poor were given for both the fluid computational domains, although only fractions of a percent of the total amount of cells were in the poor ($0.13\cdot10^{-4}\%$ and $0.08\cdot10^{-4}\%$) and fair ($0.50\cdot10^{-4}\%$ and $0.30\cdot10^{-4}\%$) categories for the respective $k-\varepsilon$ and $k-\omega\ SST$ turbulence models. Thus, the mesh quality of the computational domains generated in HH were deemed practically equivalent to the mesh generated in ICEM.

In summary, the meshing strategy developed herein for radially-cooled hydroelectric generators reduced the mesh generation time from months to hours, with a minimal impact on the quality of the mesh, which will improve the effectiveness of engineers/researchers in simulating and improving hydroelectric generators. Before this work, considerable efforts were required to mesh radially-cooled hydroelectric generators, which consumed much of the time allotted to model the ventilation circuit of such machines. Now, with a day's work of user input, a mesh can be generated for a given hydroelectric generator, and implementing modifications to the computational domain to improve its ventilation can be achieved within a few hours. Thus, engineers/researchers (specifically at the IREQ) can employ this meshing strategy to improve their effectiveness by spending less time generating the mesh and more time improving the ventilation of hydroelectric generators.

Table A.1: Mesh evaluation metric/grade and computer time for the fluid and solid computational domains. (a) Orthogonality (Λ) and skewness (Φ) mesh evaluation metric/grade (G). Mesh evaluation metrics, total cells, and computer time (T) for the fluid computational domain for the $k-\varepsilon$ (b) and $k-\omega$ SST (c) turbulence models, as well as, for the solid computational domain (d).

(a) ANSYS mesh evaluation metric/grade (G)

Λ	0 - 0.001	0.001 - 0.14	0.15 - 0.2	0.2 - 0.7	0.7 - 0.95	0.95 - 1
Φ	1 - 0.98	0.97 - 0.95	0.94 - 0.8	0.8 - 0.5	0.5 - 0.25	0.25 - 0
G	Bad	Poor	Fair	Good	Great	Excellent

(b) Fluid computational domain - $k-\varepsilon$

Λ_{poor}	Λ_{fair}	Φ_{poor}	Φ_{fair}	**Total cells**	**T**
[%]	[%]	[%]	[%]	[M]	[hr:min]
$0.13 \cdot 10^{-4}$	$0.50 \cdot 10^{-4}$	$0.02 \cdot 10^{-4}$	$3.69 \cdot 10^{-4}$	125.0	5:07

(c) Fluid computational domain - $k-\omega$

Λ_{poor}	Λ_{fair}	Φ_{poor}	Φ_{fair}	**Total cells**	**T**
[%]	[%]	[%]	[%]	[M]	[hr:min]
$0.08 \cdot 10^{-4}$	$0.30 \cdot 10^{-4}$	0	$1.65 \cdot 10^{-4}$	190.6	6:17

(d) Solid computational domain

Λ_{poor}	Λ_{fair}	Φ_{poor}	Φ_{fair}	**Total Cells**	**T**
[%]	[%]	[%]	[%]	[M]	[hr:min]
0	0	0	0	19.4	10:00

APPENDIX B
Simulations & Experiments Required for Measurements at Paugan

The successful implementation of the original TMFM design at the Paugan hydropower plant required several numerical simulations and experiments to demonstrate that the TMFM could be safely installed on an in-service hydroelectric generator. The mechanical simulations of the original TMFM design, mechanical simulations of the first structural support, the mechanical integrity test of former two, and mechanical simulations of the second structural support are presented in the current chapter.

B.1 Mechanical Simulations of TMFM Prototype

For the first phase, FEM simulations of both the TMFM and structural mechanism were performed using ANSYS Mechanical and verified by qualified engineers at IREQ. The simulation approach used for the TMFM is illustrated in figure B.1 and consisted of modeling the prototype and a section of the rotor rim it comes into contact while rotating at 500 rpm at a radius (R) of 1.135 m. Furthermore, the boundary conditions consisted of a compression only support between the back of the arms/frame and the rotor rim, fixed support between the PCBs and the arms, and a bolt pretension of 1068 N for the eight, 4-40 socket head screws that sandwich the two sections of the faceplate and the arms. Moreover, the materials of the structural components are aluminum (for the frame and arms) and steel (for the screws) and their mechanical properties are summarized in table B.1. The principal force induced by the rotation (Ω) on the TMFM is the centrifugal force ($F_\Omega = m\Omega^2 R$), which is directly proportional to the mass (m) of the prototype. Thus, all the small components with relatively low mass (*e.g.* the wires of the heating element and the 0-80

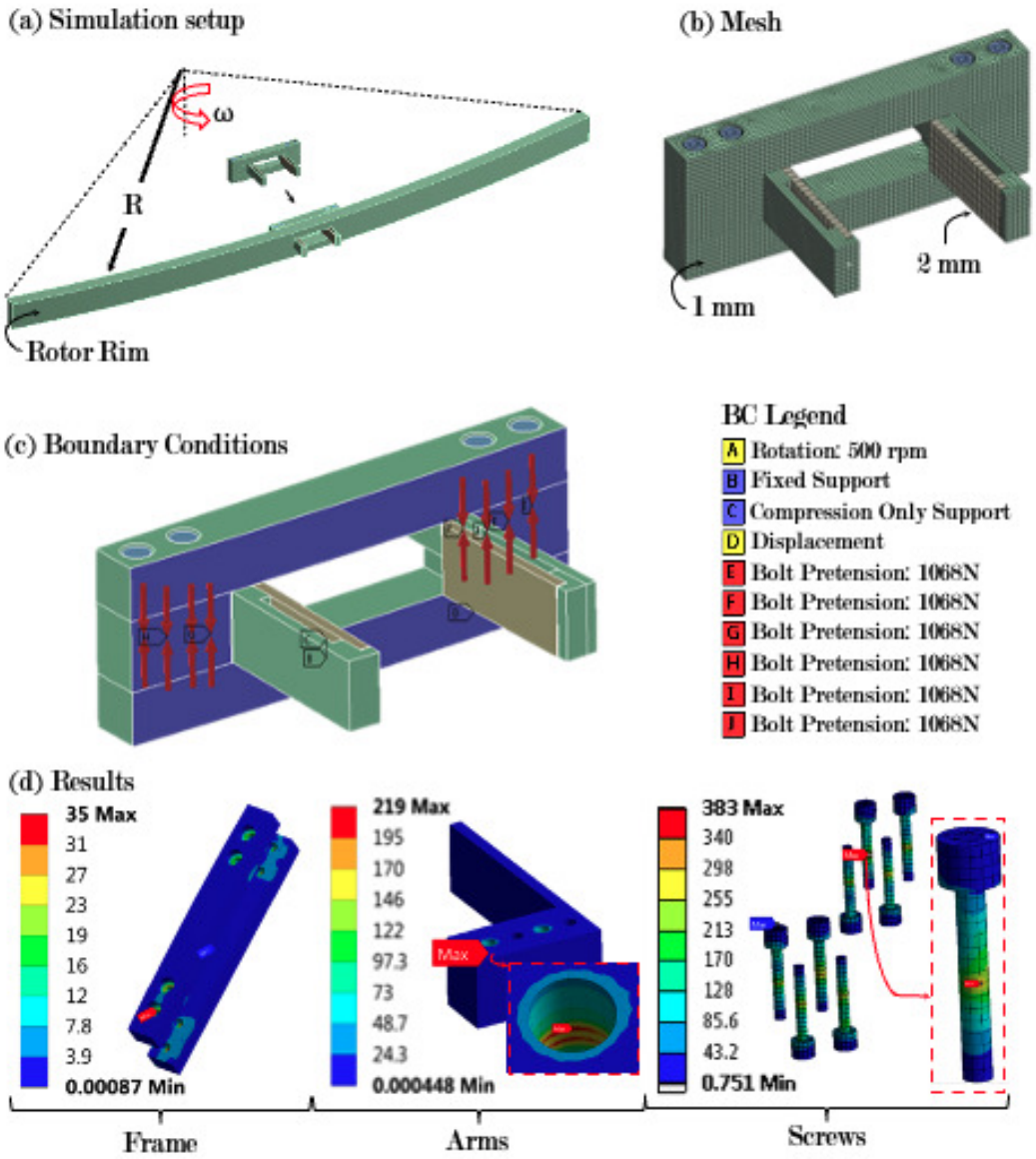

Figure B.1: (a) Simulation setup, (b) mesh, (c) boundary conditions, and (d) results of the von Mises stresses of the main components of the TMFM prototype.

Table B.1: Factor of safety (FS) of the TMFM's components.

Component	**Material**	σ_y **[MPa]**	FS
Faceplate	Al 6061	276	7.9
Arms	Al 6061	276	1.3
Screws	ASTM F835-G2	379	-
Screws	ASTM F835-G8	1,172	3

screws that fasten the PCBs to the arms) were omitted from the numerical simulations. Typically, the rotational speed of the scale model is 300 rpm, however for precautionary purposes all mechanical simulations preformed for equipment to be installed on rotating machinery must be performed at the maximum speed, which is 500 rpm for the scale model. Thus, at a rotational speed of 500 rpm, the maximum centrifugal acceleration per unit mass and gravity ($\breve{F}_\Omega = \Omega^2 R/g$) induced on the TMFM is approximately 318 g (*i.e.* 318 times the acceleration of gravity). In summary, the simulations results shown in figures B.1(a-d) and table B.1 demonstrate that the maximum stresses are well below the yield stress, or the factor of safety ($FS = \sigma_y/\sigma_{max}$) is sufficiently large in all the major components with exception to the screws. The maximum stresses in the screws exceeded the yield stress, but in a rather localized region resulting in a plastic deformation of 0.03 % (or 0.4 μm/mm). Thus, the initial steel grade (G2) for the screws was underestimated and replaced by G8 screws with a higher yield strength (170 ksi (1,172 MPa)), which translates into a factor of safety of 3.

B.2 Mechanical Simulations of First Structural Support

Once the process to validate the performance of the prototype was sufficiently refined, the development of complementary subsystems was required to allow for *in situ* measurement with the prototype in a hydroelectric generator. These subsystems were developed in close collaboration with Kirouac (2017) and included a data acquisition (DAQ) unit and a structural support that would secure the DAQ unit to the rotor of a hydroelectric generator. Due to the complexity of such a measurement, both subsystems required verification of their structural integrity and testing on the scale model prior to their installation in a hydropower plant.

To prevent rotational imbalances, limit the rotational forces on the system, and due to the limited access for the installation of the DAQ unit on the rotor shaft of the scale model, the DAQ unit was subdivided into two segments: the acquisition system and the power management/communication systems. Therefore, the structural mechanism was designed to mount each segment on opposite ends via two aluminum frames and a set of steel collars fastened by 20 bolts. One frame holds the metal plate of acquisition system while the other holds the metal plate of the power management and communication systems. The thickness of each plate was adjusted to compensate for the differences in weights between each segment and balance the overall system. Each frame was then fixed to a set of collars that are themselves mounted to the shaft of the scale model to limit the rotational forces on the system. Once the designs for the DAQ unit and the structural mechanism were finalized, the mechanical integrity of the overall system was verified in two phases. The first being via mechanical FEM simulations and the second being onsite testing.

The approach utilized to model the structural mechanism is illustrated in figure B.2 and consisted of modeling half of the symmetrical domain and performing two simulations to monitor the effect the bolt pretension (or tightening torque) boundary condition that binds the two pieces of the collars together has on the stresses of the overall system. The materials and their mechanical properties used for the four major components of the structural mechanism: the frame, collars, bolts, and weighted plate are summarized in table B.2. The mass of the frame and each segment of the DAQ unit (*i.e.* the acquisition system and the power management/communication system) were measured resulting in a mass of 1.9 kg, 4.08 kg, and 4.17 kg, respectively. If the mass of each segment is not balanced it will result in an additional centrifugal force of 70 N at 500 rpm and 25 N at 300 rpm. In the numerical simulations, both

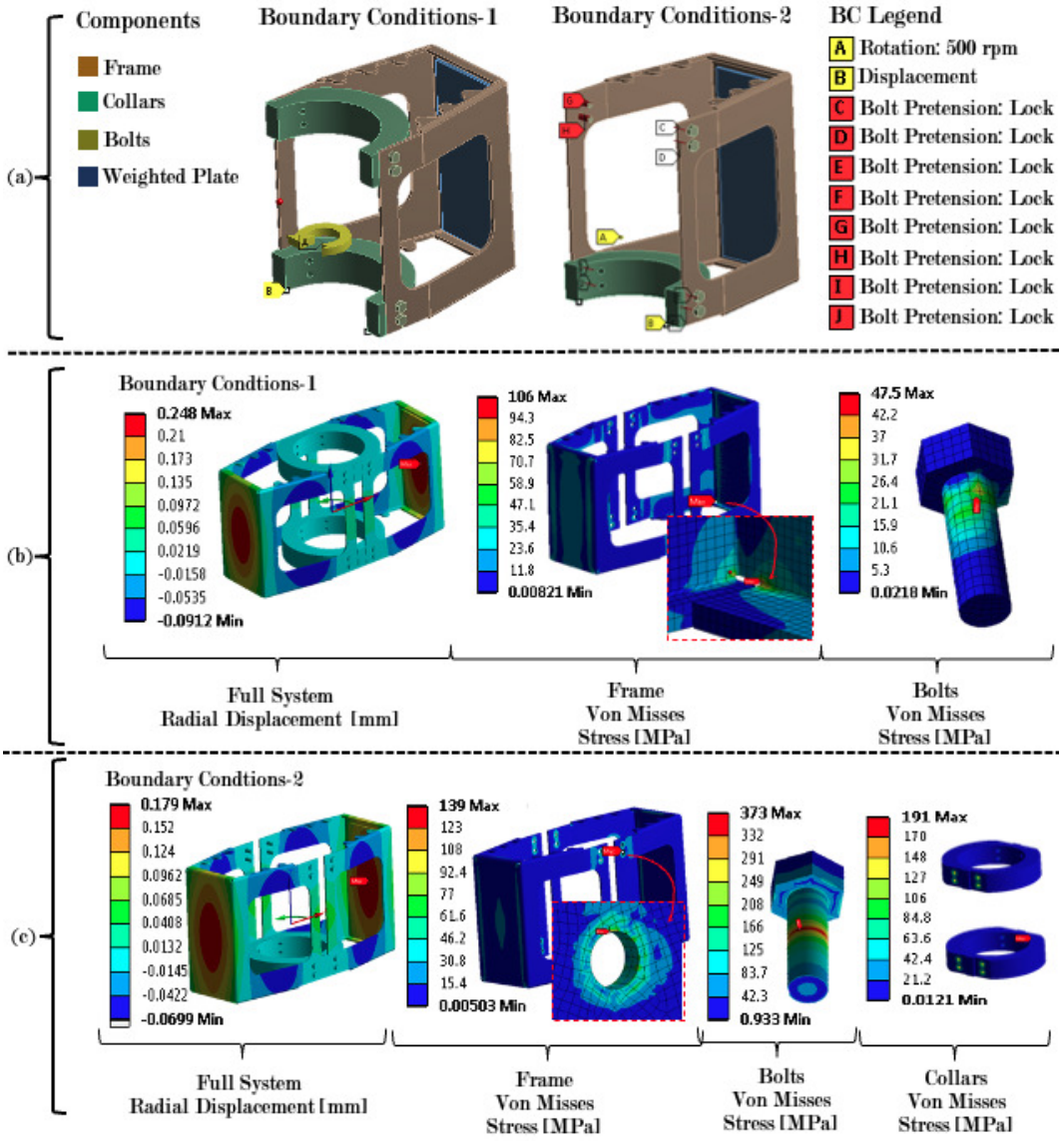

Figure B.2: (a) Boundary conditions. (b,c) Radial displacement/von Mises stress contours of the structural mechanism for two sets of boundary conditions. Performed in collaboration with Kirouac (2017).

Table B.2: Factor of safety (FS) of the structural support's components

Component	**Material**	σ_y **[MPa]**	FS_{BC-1}	FS_{BC-2}
Frame	Al 5052-H32	193	1.8	1.4
Collars	Steel 44W	300	8.6	1.6
Bolts	SAE J429-G2	379	7.9	1.0

segments of the DAQ unit were modeled as uniform plates with an equivalent mass of 6 kg each. Therefore, the intention was to use weighted plates to balance the system, and thus, the simulations assumed it to be balanced. In summary, figures B.2(a-c) and table B.2 illustrate that the maximum stresses are below the yield stress and the regions of maximum stress were very localized for both bolt pretension conditions, and thus, the design was judged satisfactory.

B.3 Mechanical Integrity Test

The second phase of the mechanical integrity tests consisted of installing all the equipment on the scale model, exposing the equipment to the g-forces mentioned above, and to visually inspect the equipment for mechanical degradation. The latter was overseen by licensed engineers at Hydro-Québec with experience in the installation of equipment on hydroelectric generators. Illustrated in figures B.3(a-b) are the installation of the systems mentioned herein and the results of the visual inspections. The TMFM was installed in the bottom row of rotor rim ducts to facilitate the inspection, and to prevent the sensor from vibrating within the ducts a light layer of silicone was applied to secure it in place. Furthermore, all wires powering the TMFM from the DAQ were also secured. The series of tests were performed in the following manner 50 rpm for 15 minutes, 300 rpm for 1 hour, and 300 rpm for 2 hours, all followed by visual inspection performed by licensed engineers. The duration of the tests were determined by the average time a given test would be performed onsite. All visual inspections concluded that no mechanical degradation was present, and the systems were safe to be installed in a hydropower plant.

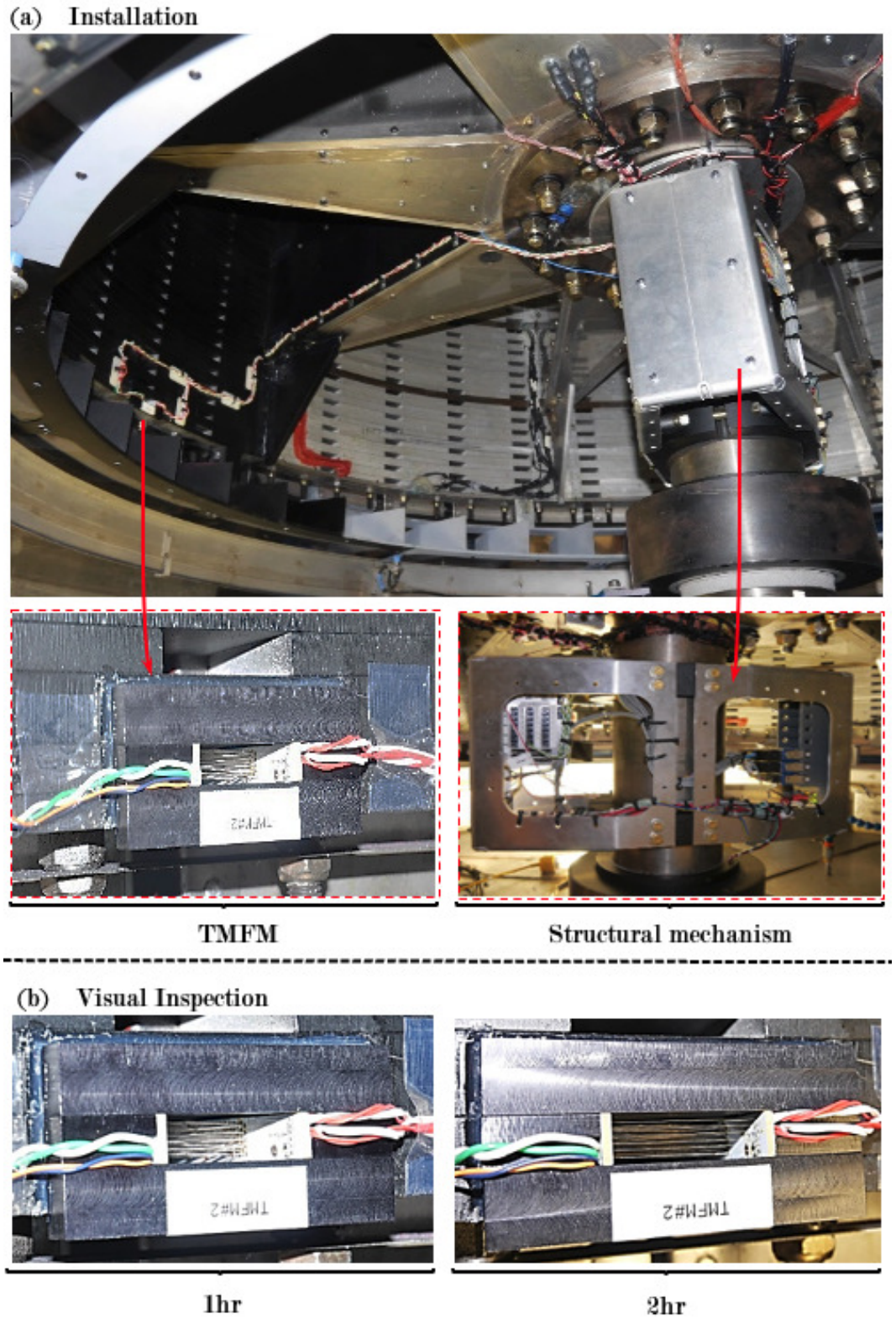

Figure B.3: (a) Installation of the TMFM and the structural mechanism in the scale model. (b) Images on the of the TMFM after one hour and two hours of continuous rotation at 300 rpm.

B.4 Mechanical Simulations of Second Structural Support

After testing the DAQ unit's structural support and verifying its mechanical integrity on the scale model, the system was tested at one of Hydro-Quebec's oldest (1928) hydropower plants named Paugan as part of this study. The generator for which the access was granted had a rotational speed of 128.5 rpm, a runaway speed of 260 rpm, and a rim radius of 5.6 m (219 in). This translated into a centrifugal acceleration of 51 g at nominal speed and 199 g at the runaway speed. Since the FEM simulations demonstrated that the TMFM was capable of withstanding accelerations that were 1.5 times higher than those experienced at runaway, and the visual inspection demonstrated that the TMFM was capable of withstanding accelerations that are twice those under normal operation, the TMFM was deemed safe to be installed in the hydroelectric generator at Paugan. However, onsite inspections of the hydroelectric generator indicated that the structural mechanism designed for the scale model would not be suitable for the hydroelectric generator at Paugan, because the space available along the shaft between the floor of the generator and the top of the rotor was approximately three times less than that of the scale model. Therefore, a different structural mechanism and fixation method was required.

As illustrated in figure B.4(a), the new structural mechanism designed for Paugan consisted of gauge-7 (4.55 mm) steel (ASTM A27) sheet metal bent with a radius of curvature of 0.5 mm (0.02 in) in a semi-enclosed box fastened to the undercarriage of the rotor via 9-3/8″ UNC SAE G-8 bolts to encapsulate the DAQ unit. The minimum distance between the center of gravity of the structural mechanism and the rotor's axis of rotation (R_2) was 80 cm (31.5 in), which was restricted by the locking mechanism of the rotor, as illustrated

in figure B.4(b). To verify the mechanical integrity of the structural mechanism, FEM simulation were performed and overseen by a licensed engineer at Hydro-Quebec. The simulation approach/boundary conditions illustrated in figure B.4(c) consisted of modeling the structural mechanism at a rotational speed of 260 rpm with distributed masses of 3 kg each on the surfaces where the DAQ unit is held, point masses of 50 g each to represent the cable connectors, as well as a gravitational force. All the specified boundary conditions had an influence on the forces induced on the bolts fastening the structural mechanism to the rotor, which is the weak point of the mechanism. To further simplify the model, the bolts were modeled indirectly rather than directly using nine fixed support discs with an inner diameter equal to the bolt diameter and an outer diameter that is 2.5 times the diameter of the bolt. Using this simplification, the membrane stress (or average stress across the thickness of the solid) was calculated to verify that it did not exceed the proof stress (σ_{proof}), such that no plastic deformation was present. The results of the simulation is illustrated in figure B.4(d), and demonstrate that the stresses in the structural mechanism are relatively low except in localized regions of secondary stresses. However, even in the localized areas, the stresses were well below the maximum allowable membrane stress (135 Mpa). For the bolts, a conservative (*i.e.* without friction) estimate indicated a maximum shear stress and tensile stress of 38 MPa and 80 MPa respectively, which are both considerably inferior to the allowable proof stress of the bolts. A summary of the results and the associated factors of safety illustrated in table B.3. The results demonstrated that the FS was 15 for the enclosure and 10 for the bolts. Thus, the simulation results demonstrated that the structural mechanism was sufficiently safe to be installed in the hydroelectric generator at Paugan.

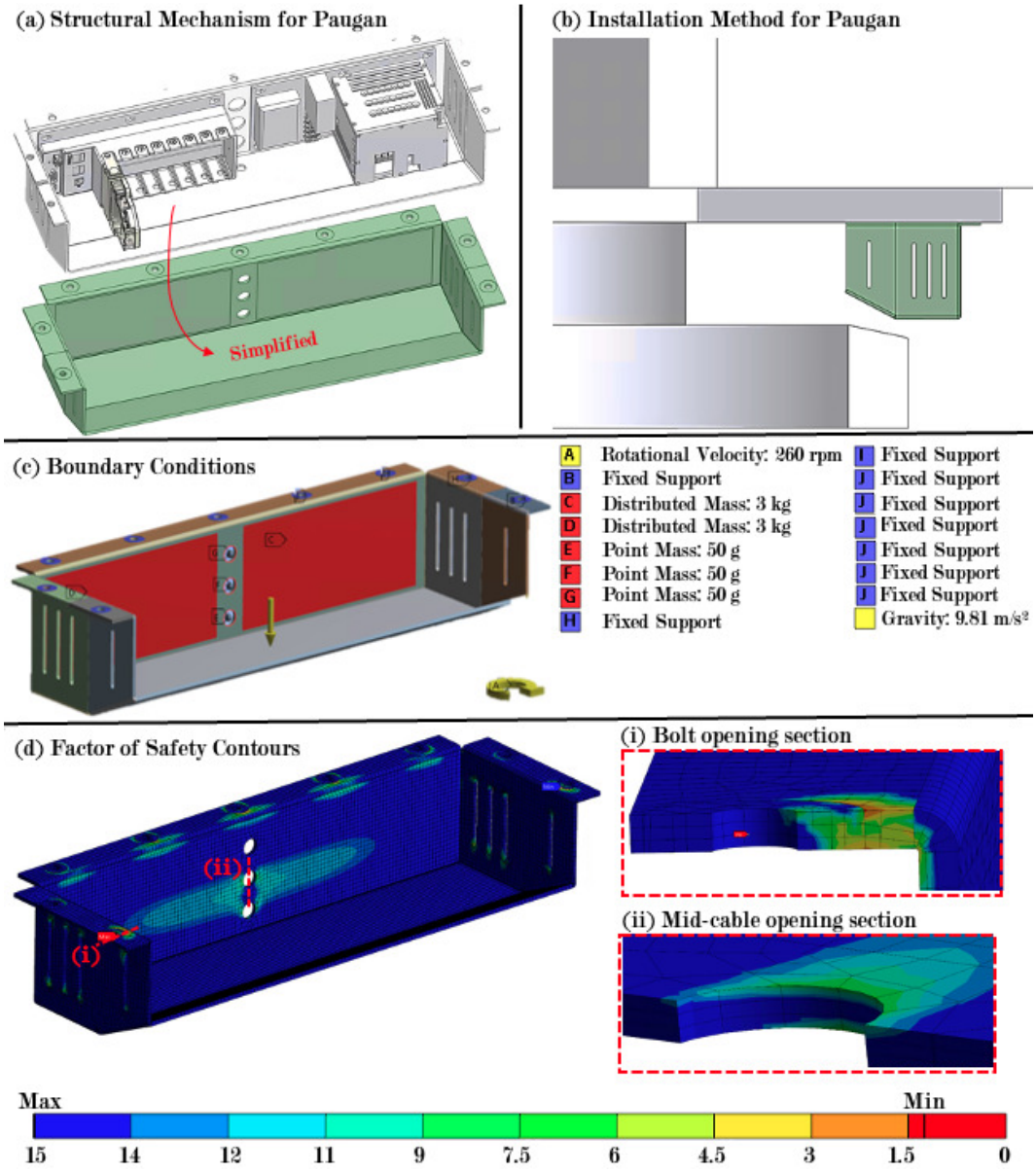

Figure B.4: (a) Structural support and the simplified simulation geometry. (b) Rotor Installation method. (c) Simulation boundary conditions. (d) FS contours highlighting sections of the bolt opening (i) and cable opening (ii).

Table B.3: Simulation specifications for the structural support.

Ω **[rpm]**: 260		**R [m]**: 0.8		$\breve{F}_{\omega}$ **[g]**: 61	
Component	**Material**	σ_y **[MPa]**	σ_U **[MPa]**	σ_{proof} **[MPa]**	FS
Enclosure	ASTM A27	205	415	-	15
3/8" UNC - Bolts	SAE G8	900	1030	830	10.4

APPENDIX C
Background on PIV

The present chapter provides the necessary background utilized in the present work to perform the PIV experiments in the static model. This information can be divided into two sections: the six main steps of PIV, and the PIV post-processing steps employed herein.

C.1 Six Main Steps of PIV

The process of obtaining the velocity of a given flow field using PIV was divided into six steps and is graphical represented in figure 2.20: i) seeding of the flow, ii) illumination of the seeding particles, iii) capturing the motion of the illuminated particles, iv) calibration, v) synchronization of the illumination and imaging process, and vi) post-processing of the data. These steps are described in the paragraph that follow.

Suitably seeding the flow was key, as a particle must be large enough to scatter a sufficient amount of light towards the camera, yet small enough to closely follow the motion of the fluid without perturbing it. Typically, this is attained by matching the particle density to the density of the fluid medium, which is easily achieved when the medium is water. However, when the medium is air, no particles of a similar density exist, and thus, the particle size must be chosen such that it tracks the flow despite the density difference. Alternatively stated, the Stokes number of the particles in a given medium must be much less than one. For air, this is satisfied with particles made of common household oils (*e.g.* canola oil, olive oil, *etc.*) with a diameter between 1-10 μm, as was demonstrated by Raffel *et al.* (2007). Particles of such size were generated using an aerosol generator, such as the one developed

by Laskin (1948), which uses an impactor plate to remove oversized particles leading to a polydisperse distributions with mean diameters of 1 μm when using cholesterol containing oils. Furthermore, Kähler *et al.* (2002) showed the size distribution of the droplets obtained using the oil generator was a good compromise between achieving the required light scattering intensity for the camera to capture and the inertial effects due to the density difference.

Once the seeding particles were distributed into the flow they were illuminated by a thin laser sheet, which was created by converting a 532 nm wavelength Nd:YAG laser beam with a cylindrical lens to expand the beam, and a spherical lens to adjust the thickness of the sheet (Adrian & Westerweel (2011)). A double pulsed Nd:YAG laser was used because it has: dual cavities that can emit two different pulses separated by microseconds, in addition to a pulse energy as high as 320 mJ, a pulse pair repetition rate as high as 10 Hz, and a near Gaussian beam profile – an important principle utilized by cross-correlation techniques to track the motion of the particles used to deduce the velocity of the flow. In the current study, two-dimension-two-component (2D2C) PIV was utilized, and thus, only the in-plane-velocity was inferred from a given measurement volume generated by a thin light sheet. Thus, the thickness of the light sheet was kept to a minimum (1 - 3 mm) to avoid mistaking cross-component particle motion as in-plane motion.

The motion of the illuminated particles was then captured using a charged coupled device (CCD) camera, which has an electronic sensor that converts light into an electric charge. Most modern digital cameras used for PIV are equipped with CCD sensors or a rectangular array of individual CCDs referred to as pixels, which are approximately 100 μm^2 in size. Adrian & Westerweel (2011) mention that since most PIV data analysis techniques use three-point fitting techniques to determine the particle location, it is important that the

rectangular CCD array has a sufficient amount of pixels, such that, a seeding particle (plus its diffraction) covers 2-3 pixels to reduce displacement bias or peak-locking errors. Furthermore, the camera's field of view must be large enough to focus on all the particles in the measurement area. Cameras used for PIV typically operate in dual-frame mode, which allows for the capturing of successive images within 50 ns (limited only by the frame-transfer time or disk buffer) with a 100 ms successive image pair delay limited by the read-out time of the two frames (Hijazi & Madhaven (2008)). All particle displacements captured by the camera were stored in pixels since the displacement in meters depends on the camera settings (magnification, focal length, and aperture) and its distance from the particles (*i.e.* distance between the lens and the object plane).

To convert the displacements measured by the CCD sensor from pixels to meters, a calibration procedure was performed. The procedure consisted of placing a calibration target of equally spaced dots in the camera's field-of-view and applying a post-processing image fit model to convert the target's image spacing to the known physical spacing. The model utilized was that proposed by Soloff *et al.* (1997) and is a third order polynomial with 19 vector coefficients that are evaluated using a series of inputs corresponding to the point distribution of the calibration. These inputs were used to generate a virtual grid, which was superimposed onto the calibration image, with the goal being for the intersection of the virtual grid to match the grid point on the calibration image. Due to sources of error (*e.g.* image contrast, background noise, *etc.*) the match is never perfect, and thus the accuracy of the fit is quantified by the average projection error (in pixels), which is defined as the standard deviation of the distance between the dots on the calibration image

and the corresponding virtual grid intersection. In the present study, it was always below 0.5 pixels.

One of the last steps is the synchronization of all the preceding steps. This was ensured using a timing box controlled via Dantec's *Dynamic Studios* software. The software graphically represents the functions of the timing box into a timing diagram composed of five lines corresponding to each of the electrical signals it receives: an external trigger signal, exposure frame one, exposure frame two, laser pulses, and the two saving frames. Peaks on each line of the diagram represents the activation of each signal in order from left-to-right. The activation of the signals in the timing box follows the following sequence:

1. An external signal commences the image capturing process.
2. The camera diaphragm opens (after a delay) for the first exposure frame.
3. The laser flashes (first pulse), at the end of the first exposure frame (corresponding to the camera diaphragm closing).
4. The captured image of the laser pulse is immediately transferred to the CCD's interline register as part of the first saving frame.
5. The diaphragm reopens for the second exposure frame.
6. The laser flashes (second pulse) after a preset delay (called the time between pulses) at the start of the second exposure frame to reduce the time interval between the images.
7. The first image is transferred to the frame grabber allowing the placement of the second image in the interline register as part of the second saving frame.
8. The camera diaphragm closes (corresponding to the end of the second exposure frame).
9. The second image is transferred to the frame grabber.

Lastly, this process was repeated until a sufficient amount of image pairs were obtained.

After a sufficient number of images were acquired, several post-processing procedures were required to obtain a vectorial representation of the flow.

C.2 Static Model PIV Post-Processing Steps

The procedure employed in *Dynamic Studios* for the present work is illustrated in figure 2.22 and included the following four steps: adaptive correlation, range and N-sigma validation, universal outlier detection, and vector dewarping and statistics.

Adaptive correlation is a function in *Dynamic Studios* that uses the statistical approach of Soo *et al.* (1959) applied to a series of interrogation windows, which calculates the cross-correlation of the particle displacement between two frames in a given window to obtain the vectorial displacement in that window. This process is mathematically defined by the following equation:

$$R(\Delta x) = \int I_1(x) I_2(x + \Delta x) dx, \tag{C.1}$$

where I_1 and I_2 represent the image intensity field in the first and second images at a given location (x) and at one slightly shifted $(x + \Delta x)$. This will only correctly detect the displacement of the particles if a few conditions are met. First, because only one displacement vector is obtained for a given interrogation window, the displacement of all the particles must be the same, and thus, the interrogation window must be small. Second, Keane & Adrian (1990) state that at least ten particles must reside within the window. Third, in combination with the minimum particle requirement, the particle density must be low enough to avoid overlap. Keane & Adrian (1992) expressed this overlap as:

$$SD = N_L \Delta z \Big(\frac{d_e}{M_{ag}} \Big)^2, \tag{C.2}$$

which is a function of the mean number of particles per unit volume that are sufficiently large to be seen by the camera (N_L), the laser light sheet thickness (Δz), the diameter of the particle as seen by the camera (d_e), and the camera magnification (M_{mag}). The particle diameter as seen by the camera, is the only parameter not intuitively known, because it depends on three main factors, defined by Olsen & Adrain (2000) as:

$$d_e = \sqrt{(M_{ag} \cdot d_p)^2 + (2.44 f_{\#}(M_{ag} + 1)\lambda)^2 + \left(\frac{M_{ag} \cdot Z \cdot D_a}{s_0 \cdot Z}\right)^2}. \qquad \text{(C.3)}$$

The first term is the geometric enlargement effect, which states that the image of the particle diameter is directly related to the particle size itself (d_p) via the optical magnification (M_{ag}). The second term is the diffraction enlargement effect, which is related to the the ratio between objective lens diameter and the aperture's diameter ($f_{\#}$), and the wavelength of the scattered light (λ). The last term is the defocusing enlargement effect, which is a function of the magnification (M_{ag}), the object's distance from the focal plane (Z), the lens aperture diameter (D_a), and the object distance (s_0). Therefore, a high-quality image for the statistical analysis requires that $SD << 1$, a condition that was always satisfied in the present work. Even if these three conditions were met, the correlation was never perfect due to particles exiting the interrogation window between the two pulses or the effects of background noise. This makes the detection of the tallest peak increasingly difficult, and ultimately, the tallest peak may not represent the actual displacement. To remedy this, the ratio between the amplitude of the tallest correlation peak to the amplitude of the second tallest peak – coined the peak detectability – is monitored. Keane & Adrian (1992) advise that any window with a peak detectability less than or equal to 1.2 is to be rejected. Although the cross-correlation was mathematically defined as a continuous integral, in reality the data obtained is discrete

because the CCD sensor is not continuous. Thus, the discrete form of the cross-correlation is:

$$R(p,q) = \frac{1}{M_{win} \cdot N_{win}} \sum_{m=1}^{M_{win}} \sum_{n=1}^{N_{win}} I_1(m,n) I_2(m+p, n+q), \tag{C.4}$$

where the cross-correlation is applied to an interrogation window of length (M_{win}) and width (N_{win}) in pixels and shifted along the length (p) or width (q) by a specified pixel amount. This expression is never directly computed as an alternative and faster approach of calculating its fast Fourier transform (FFT) is used in practice:

$$R(\mu,\nu) = \bar{F}_1(\mu,\nu) F_2(\mu,\nu), \tag{C.5}$$

where the overbar indicates the complex conjugate, and $F_1(\mu,\nu)$ and $F_2(\mu,\nu)$ are the discrete Fourier transforms (DFT) of the image intensity field defined by Adrian & Westerweel (2011) as:

$$F(\mu,\nu) = \frac{1}{M \cdot N} \sum_{m \in M} \sum_{n \in N} I(m,n) e^{-2\pi i \left(\frac{m\mu}{M} + \frac{n\nu}{N} \right)}. \tag{C.6}$$

Ultimately, the precision in the estimation of the particle image displacements using this technique was principally determined by the pixel resolution. Westerweel (1994) recommend a 1 mm^2 resolution for 64 by 64 pixels for most PIV applications. The camera used in the current study was a FlowSense 4M Mk2 containing a CCD sensor that is approximately 3 by 3 cm^2 containing 2048 by 2048 pixels, such that the recommendations of Westerweel (1994) was respected. However, the importance of this effect was subsequently reduced by Westerweel (1997) using a subpixel refinement technique, where two-dimensional Gaussian profiles corresponding to the intensity of the tallest peak and its neighbors instead of simply detecting the tallest peak. Thus, the displacement estimated in this manner increased the precision from 0.5 pixels

to 0.05 pixels. Another method that further increased the resolution and help achieve the minimum particle requirement in an interrogation window was window adaptation. This technique offsets the interrogation window around a given point between two images by first calculating a rough displacement with a larger window and then reducing its size and translating it by the calculated rough displacement to obtain a more precise displacement. Therefore, this technique captured more particles per window and reduced the size of the interrogation windows, which increased the spatial resolution. In the current study, this technique was applied with two successive window size reductions and two iterations for each size.

Finally, after the displacement vector was obtained, it was divided by the time interval between pulses to obtain the velocity vector in pixels per second. All these intricate details were employed in *Dynamic Studios* adaptive correlation function, which, as shown in figure 2.22(b), resulted in an initial vectorial representation of the flow. However, subsequent steps were required to remove spurious vectors.

Among the steps used to remove the spurious vectors in the post-processing workflow presented in the present study were range and N-sigma validation. The former is based on the notion that any measured velocity field should have a certain coherence. However, it is not uncommon that the velocity field obtained using the adaptive correlation technique may draw the naked eye to a few erroneous vectors. One approach employed to remove these vectors was range validation, which is a method that employs user-specified minimum and maximum thresholds for the vectors:

$$\epsilon_{i,j}^{min} < u_{i,j} < \epsilon_{i,j}^{max}, \tag{C.7}$$

where the threshold (ϵ) is specified for each component individually for a two-dimensional velocity vector ($u_{i,j}$). This process is demonstrated by comparing the images of figure 2.22(b) and 2.22(c), in which all abnormally large vectors from the adaptive correlation were rejected (shown in red). However, not all invalid vectors were removed using this rudimentary process. Another approach used in concert with the former method was N-sigma validation, which is a statistical approach that takes advantage of the intrinsic nature of steady flow fields that are of interest in the present study. Moreover, measurements of steady flow at subsequent times are essentially the repetition of the same measurement, and thus, the flows should result in a probability distribution. Therefore, assuming that the data is normally distributed, the probability distribution function of interest was the following:

$$f_n(u) = \frac{1}{\sigma\sqrt{2\pi}} e^{-0.2\left(\frac{U-\mu_{stat}}{\sigma}\right)}, \tag{C.8}$$

which is a function of the mean (μ_{stat}), standard deviation (σ), and the number of samples (M) of the measured flow field. Thus, N-sigma validation compares each vector between the pairs of images taken and assumes that a vector should fall within a specified radius (r):

$$\left(\frac{U-\mu_{stat}}{\sigma}\right) = r^2 \leq N^2, \tag{C.9}$$

where the acceptance limit/threshold (ϵ) was set to be the following range:

$$4 \leq \epsilon \leq 6, \tag{C.10}$$

such that all the outliers were removed even if the data did not follow a normal distribution. If the flow does contain important transient effects, the acceptance limit can be adjusted so that these effects are not considered spurious.

The last step used to remove spurious vectors was the universal outlier detection method. This method was proposed by Westerweel (1994) and takes advantage of the certain smoothness that flows in nature exhibit, and thus, the displacement of neighboring points at a given time should be considered when removing spurious vectors. Ultimately, after comparing the global mean, local mean, and local median, the author concluded that the normalized vector residual (r_0) with respect to the local median, defined as:

$$r_0 = \frac{|\Delta x_0 - \Delta x_m|}{\sigma_m}, \tag{C.11}$$

is the best quantity to consider, where the absolute value of the difference between the displacement vector at a specified point (Δx_0) and the median displacement in the region near that point (Δx_m) normalized by a constant value (σ_m). Thus, when the normalized vector residual is larger than a given threshold, the displacement vector is considered spurious and is replaced by the median displacement. The inherent limitation of this technique lies in the choice of the normalization constant and the threshold value. At the time of the paper, Westerweel (1994) proposed that the normalization constant be set to unity and adapted the threshold to the local properties of the flow. It was not until eleven years later when, Westerweel & Scarano (2005) proposed the widely used universal method. This method replaced the normalization factor with the median of the neighbors' residuals (r_m) and a small offset (σ_ϵ) to improve the performance and avoid divergence when very low fluctuation levels are present. Since the precision of PIV displacement is of the order of 0.1 pixels, the authors chose this value for the offset. This led to the adoption of the universal outlier method:

$$r_0 = \frac{|\Delta x_0 - \Delta x_m|}{r_m + \sigma_\epsilon} \leq r_c = 2, \tag{C.12}$$

where Westerweel & Scarano (2005) set the the threshold value (r_c) to 2, as it was the optimal value for typical flows in their wide range of PIV data. This value can be adjusted but was respected in the current study.

Once all spurious vectors were removed, the vector field was converted into SI units and statistics of the flow field were calculated. In PIV it is assumed that the camera is oriented normal to the light-sheet, however, rarely is this perfectly achieved. Thus, these imperfections were taken care by overlapping a calibration image of dot with a known physical spacing. The image was then converted into SI units as mentioned previously by using third-order polynomial proposed by Soloff *et al.* (1997). In the current study, only the average flow quantities including the mass flow rate or average velocity were of interest. These quantities could have been obtained either by averaging the correlation, the displacement, or the images. All three methods were compared by Meinhart *et al.* (2000) and the authors' findings are illustrated in figure 2.22(e). The results indicate that the three methods are almost identical for good quality images, however since correlation averaging was the most commonly used and better results were achieved when the minimum particle per interrogation window requirement was not met, this approach was used in the current study. The result of such an average over 2,700 frames is illustrated in figure 2.22(f), where the green vectors represent the vectors replaced the average value.

APPENDIX D
Background on Rotor-Stator Interface Models

Hydroelectric generators, like most turbomachinery, have adjacent rotating and non-rotating components, and the flows in both these regions are of interest. The link between the rotating and stationary components is called the rotor-stator interface (RSI). Commercial CFDHT codes generally have three approaches to model the RSI: i) the multiple reference frames (MRF) or frozen rotor (FR) approach, ii) the stage or mixing-plane (MP) approach, and iii) and unsteady RANS (URANS) approach, also called the transient-rotor or sliding mesh (SM) approach. Each one transfers the flow information from upstream to downstream in a different manner, as illustrated in figure D.1, and as briefly described below.

D.1 Frozen Rotor Approach

The frozen rotor (FR) approach is the least computationally expensive model because the RANS equations are solved in the relative frame of reference with the rotor fixed in space, and thus a steady-state version of an intrinsically unsteady phenomenon is solved (Luo *et al.*, 1994). Most rotors of turbomachines at steady-sate operate at a constant angular velocity (ω), which is the case for hydroelectric generators. The flow in the rotor can be analyzed in two different frames: i) a rotating frame (i.e. a frame of reference fixed to the rotor), and ii) a stationary frame (i.e. a frame of reference fixed to the stator). In the former frame of reference, the rotor appears to be stationary. Mathematically, the velocity of a particle in the stationary frame (^{S}) relative to the rotating frame (^{R}) is expressed as the velocity at a fixed reference point plus the swirl velocity or the orbital angular velocity at a reference

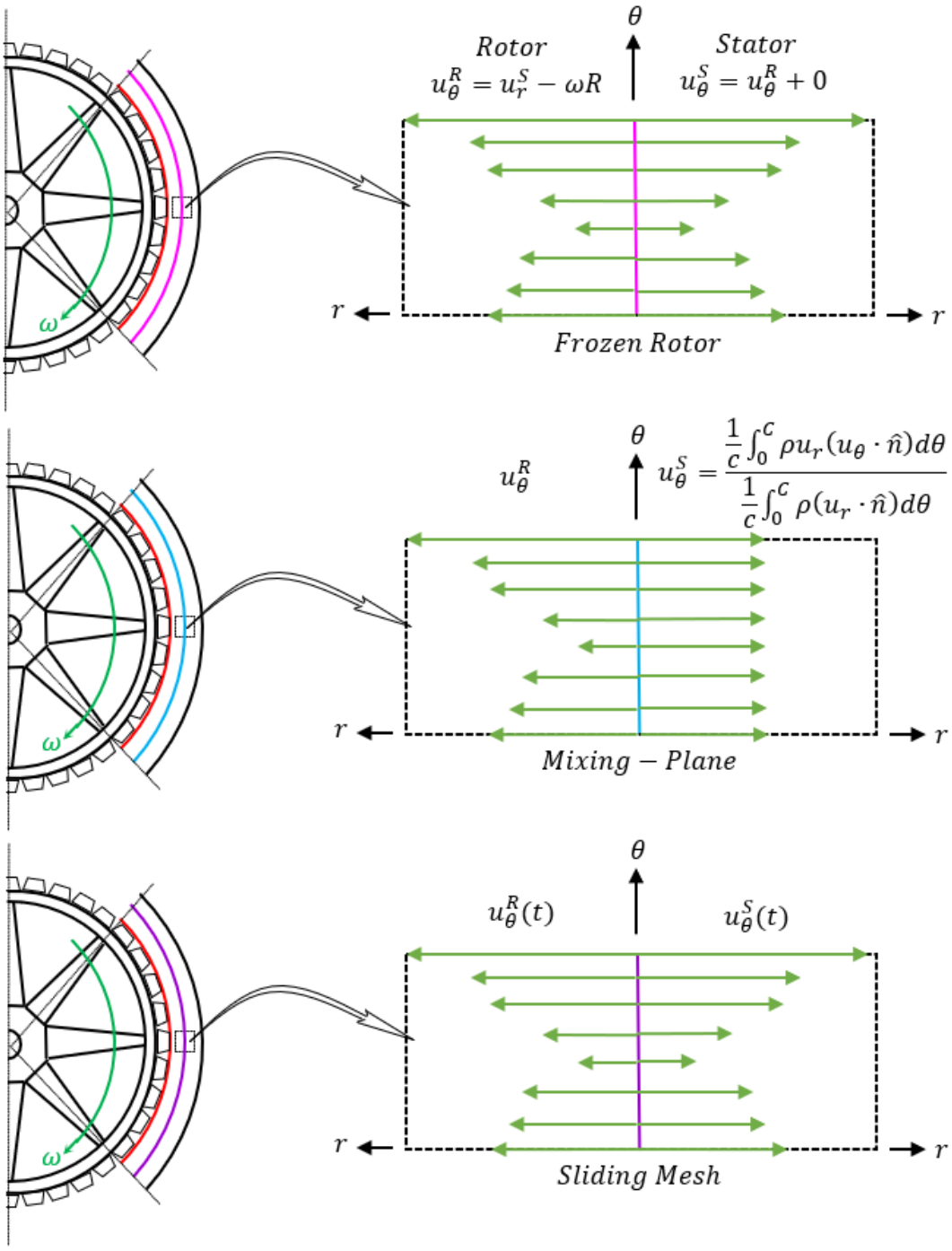

Figure D.1: Sketches of the velocity profile downstream of the rotor-stator interface (RSI) of a hydroelectric generator based on the: i) frozen rotor (FR), ii) mixing-plane (MP, and iii) sliding mesh (SM) approaches.

point, which is at a given distance from the origin of rotation ($\underline{r}$):

$$\underline{u}^S = \underline{u}^R + \underbrace{\underline{\omega} \times \underline{r}}_{\text{Swirl Velocity}}.$$

Taking the derivative with respect to time, the acceleration in the stationary frame is obtained as:

$$\underline{a}^S = \underline{a}^R + \underbrace{(d\omega/dt)^S \times \underline{r}}_{\text{Relative Angular Acceleration}} + \underbrace{2\underline{\omega} \times \underline{u}^R}_{\text{Coriolis Acceleration}} + \underbrace{\underline{\omega} \times (\underline{\omega} \times \underline{r})}_{\text{Centripetal Acceleration}},$$

where two fictious acceleration terms arise: i) the Coriolis acceleration, which always points towards the axis of rotation, and ii) the centripetal acceleration, which always points perpendicular to the axis of rotation. Thus, for a rotor in the rotating frame relative to a truly stationary frame and spinning at a constant angular velocity the following equation applies:

$$\underline{a}^R = - \underbrace{2\underline{\omega} \times \underline{u}^R}_{\text{Coriolis Acceleration}} - \underbrace{\underline{\omega} \times (\underline{\omega} \times \underline{r})}_{\text{Centripetal Acceleration}}.$$

The FR approach uses advantage of this by solving the RANS equations in the rotating frame for the rotor by: i) using the velocity in the rotating frame:

$$\underline{u}^R = \underline{u}^S - \underbrace{\underline{\omega} \times \underline{r}}_{\text{Swirl Velocity}},$$

and ii) adding the coordinate transform source term (S_{FR}):

$$S_{FR} = - \underbrace{2\varepsilon_{ijk}\omega_k u_j}_{\text{Coriolis Force}} - \underbrace{\varepsilon_{mni}\omega_n(\varepsilon_{ijk}\omega_j r_k)}_{\text{Centrifugal Force}},$$

which takes into account the two fictitious forces that arise in the coordinate transformation. When using commercial CFD codes, the user is asked to specify in their model a rotating fluid region with a constant angular velocity, and thus, in this region, the coordinate transform source term is non-zero until

is crosses the RSI to the stationary fluid region where it is zero. Furthermore, special treatment is required at the RSI because the diffusion and advection terms in the RANS equations for the stationary domain require values in the adjacent rotating domain. To circumvent this issue, the FR approach enforces the continuity of the absolute velocity ($\underline{u}^S$) to provide constant values of the velocity across the RSI by converting the RANS equations in the cells adjacent to the RSI to the stationary frame (Luo *et al.*, 1994):

$$\frac{\partial u_i^S}{\partial x_j} = \frac{\partial u_i^R}{\partial x_j} + \varepsilon_{mni}\frac{\partial}{\partial x_n}(\varepsilon_{ijk}\omega_j r_k).$$

The main disadvantage of this model is that the solution is dependent on the relative position of the rotor to the stator. Thus, different relative positions of the rotor will result in different numerical solutions. Consequently, effects of inherently unsteady flow due to the change in rotor position are neglected. Moreover, this approach takes an image of an instantaneous flow field of the rotor at a particular location at a given time as shown in figure D.1 – hence the name frozen rotor. In reality, in the stationary frame (or stationary side of the RSI) one would observe variations in velocity that are dependent on the unsteadiness of the rotor's rotation. Thus, good judgment as to whether this effect is important in a given model is required.

D.2 Mixing Plane Approach

The mixing-plane (MP) model was developed to bridge the gap between rotor-location-dependent solutions and fully unsteady transient-rotor simulations by modeling the unsteady rotor behavior. The approach is based on the work of Giles (1988, 1991) and Saxer (1992). By using a Fourier analysis of the linearized Euler equations and assuming that the solution at the rotor-stator interface (RSI) can be decomposed circumferentially in 3-D space into Fourier modes with non-reflecting boundaries, the authors maintained a

smooth transition of the flow quantities through the RSI. This approach differentiates itself from the FR approach by decomposing the intrinsically unsteady phenomenon into a steady one by time-averaging the rotor flow and spatially averaging the stator flow using a mixed-out flow approach. As shown in figure D.1, mixed-out flow assumes that adequately downstream of the RSI, the flow is circumferentially uniform and thus, the downstream flux ($\mathcal{F}$) must be equal to the average flux at the RSI ($\breve{\mathcal{F}}$) (Giles, 1988, 1991):

$$\breve{\mathcal{F}}_n(u_i) = \mathcal{F}_n(\tilde{u}_i) = \frac{1}{\mathcal{C}} \int_0^{\mathcal{C}} \mathcal{F}_n(u_i) \; d\theta \quad \text{for} \quad n = 1, 2, ..., N,$$

where the flux of the mixed-out flow variables ($\mathcal{F}(\tilde{u}_i)$) is expressed as the zeroth Fourier mode. To appropriately resolve the axial distribution of the flow, the integral is performed over a sufficient number (N) of uniformly distributed axial bands of a given circumference ($\mathcal{C}$). This approximation is consistent with what an observer would see from a rotating surface emitting a constant stream of air. The approach becomes more accurate with increasing: i) rotational speed, ii) stream-wise rotating surfaces, and ii) observation distance from the rotor. However, Saxer (1992) mentions that such an approach will generate viscous losses and artificially increase entropy. To conserve mass, momentum, and energy at the RSI, the flux-averaged quantities must be matched, which is relatively straightforward for all variables except the circumferential velocity:

$$\tilde{u}_{\theta,S} = \tilde{u}_{\theta,R} + \omega R,$$

because the rotor's angular speed (ωR) must be introduced on the rotor side due to the use of relative flow variables. Thus, the MP approach has the advantage of removing the sensitivity of the rotor's relative position to the stator. However, it fails to model the wake effects of the rotor due to the averaging process.

D.3 Sliding Mesh Approach

When unsteady wake effects at the RSI are too important to neglect, the sliding mesh (SM) approach is required. This RSI model, unlike the previous two approaches, is unsteady and requires the solution of the unsteady RANS equations (URANS). Thus, at each time step, the flow quantities are passed through the RSI. This method often requires very fine time steps and very small grid spacings at the RSI to ensure numerical stability, making this model the most computationally expensive of the three. Once the RSI model is chosen, the RSI must be placed at a particular distance in the air gap (δ), which is defined at the space between the rotor and the stator.

D.4 RSI Model Investigated

In the present study, only the MP RSI model was investigated. This was chosen for two main reasons. First, to follow the recommendations of Toussaint *et al.* (2011), who utilized the MP model at a 3 $\delta/4$ placement, and found good agreement with experimental values for the radiator mass flow rate and windage losses. Furthermore, preliminary tests (not shown here) utilizing: i) the new meshing strategy proposed herein, and ii) the FR model, agreed with the findings of Toussaint *et al.* (2011), as the windage losses were not accurately predicted. Second, the SM model would have to be employed to improve the predictions obtained using the MP model, which would be too computationally expensive and time consuming for the scope of the proposed research. The current study required 144M and 210M cells to meet the near-wall mesh criteria for the $k-\varepsilon$ and $k-\omega$ turbulence models, respectively. However, to obtain converged numerical results when employing the SM model, the cell count would increase significantly. This conclusion can be arrived at by maintaining a near one-to-one cell size (Δx) match at the RSI, and a CFL

(Courant-Fridrichs-Lewy) number of one:

$$CFL = \frac{u\Delta t}{\Delta x} \approx 1,$$

which is a function of the velocity of the flow (u), the time step of the unsteady simulation (Δt), and the grid spacing (Δx). It was initially estimated that for a grid spacing of 0.5 mm at the RSI, a time step in the range of 10^{-4}-10^{-5} s would be required. Unsteady simulations with much simpler computational domains have been run on CASIR (IREQ's HPC cluster), using 512 cores with around 10M elements, and have taken approximately 2 months to converge with a similar time step. Thus, a simulation with nearly 250M cells (to account for the increased cell count at the RSI) on 512 cores could take over a year to converge. This estimated timeframe was too large, and increasing the number of cores to obtain the necessary converged numerical results was out of the scope of the current project.

APPENDIX E
Uncertainty Analysis

The present chapter presents both the methods and the mathematical expression utilized to quantify the uncertainty in the experimental measurements performed as part of the present research. This information can be divided into three sections providing: i) the background for the uncertainty analysis employed, and ii) the calculations of the uncertainty in the PIV measurements, and iii) the calculations of the uncertainty in the TMFM measurements.

E.1 Background on First-Order Uncertainty Propagation

The present uncertainty analysis follows that established by Venne (2017). A measured value (x) can be separated into its average component ($\bar{x}$) and its deviation ($\mathcal{U}_x$) as:

$$x = \bar{x} + \mathcal{U}_x. \tag{E.1}$$

The deviation is often referred to as the measurement uncertainty or error. There are two main types of errors i) bias errors and ii) precision errors. Bias errors remain constant during a given series of measurements and can be comparatively estimated, or quantified by calibration and experience. Precision errors are the scatter in the measured data and are affected by: i) the measurement system (*i.e.*, repeatability and resolution), ii) the measurand, (*i.e.*, temporal and spatial variations (*e.g.* turbulence)), iii) the process (*i.e.*, variations in operating and environmental conditions), and iv) the measurement procedure/technique (*i.e.* repeatability). As a rule of thumb, an error is a precision error if it can be statistically estimated otherwise it is a bias error. It is common to encounter precision errors without available statistical data.

This is overcome by performing an error propagation analysis to quantify the error. Typically, a measurement requires several operations and each operation introduces a source of error. Figliola & Beasley (2011) showed that the root-sum-squares (RSS) method can be used to determine the uncertainty in a measured value (x), with a defined number (N) of sources of error (e_i), as follows:

$$\mathcal{U}_x = \pm\sqrt{\sum_{i=1}^{N} e_i^2}, \quad for \quad i = 1, 2, \ldots, N. \tag{E.2}$$

This is considered a very conservative estimate which assumes: i) the quantity behaves in a Gaussian manner, and ii) the error will occur on a worst-case basis. However, the error of the measured value of interest is often based on a functional relationship (y), as shown:

$$y = \bar{y} + \Delta y = f(x + \Delta x). \tag{E.3}$$

Therefore, a Taylor series expansion is performed to quantify the error:

$$\bar{y} + \Delta y = f(\bar{x}) + \pm\left\{ \left(\frac{dy}{dx}\right)_{x=\bar{x}} \cdot \Delta x + \left(\frac{d^2y}{dx^2}\right)_{x=\bar{x}} \cdot (\Delta x)^2 + \cdots \right\}. \tag{E.4}$$

From the above equation, it can be determined that the mean value for the functional relationship ($\bar{y}$) must be the function evaluated at the average measured value ($f(\bar{x})$), and the uncertainty must be the value within the curly brackets. Assuming a linear approximation for the change in the functional relationship (Δy), which is valid if the change in the measure value (Δx) is small, the higher order terms of the Taylor series expansion may be neglected to obtain a first-order approximation:

$$\Delta y \approx \left(\frac{dy}{dx}\right)_{x=\bar{x}} \cdot \Delta x, \tag{E.5}$$

where the derivative defines the slope of the line passing through the mean value. Therefore, it may be assumed that for small deviations from the mean,

the slope predicts the approximate relationship between the change in the measured value (Δx) and the change in the functional relationship (Δy). Consequently it has been shown by Figliola & Beasley (2011), that the uncertainty in the measured value ($\mathcal{U}_x$) is related to the uncertainty in the functional relationship ($\mathcal{U}_y$) by:

$$\mathcal{U}_y = \left(\frac{dy}{dx}\right)_{x=\bar{x}} \cdot \mathcal{U}_x. \tag{E.6}$$

This can be extended to a multivariable relationships of any number (N) of variables ($x_1, x_2, \ldots, x_L$) for a result ($\mathcal{R}$):

$$\mathcal{R} = f_1(x_1, x_2, \ldots, x_N), \tag{E.7}$$

and each variable (x) holds some measurable uncertainty that could affect the result. As for the measured value itself, the result can be similarly divided into its sample mean ($\bar{\mathcal{R}}$) and uncertainty ($\mathcal{U}_\mathcal{R}$):

$$\mathcal{R} = \bar{\mathcal{R}} + \mathcal{U}_\mathcal{R}, \tag{E.8}$$

where the sample mean is expressed as:

$$\bar{\mathcal{R}} = f_1(\bar{x}_1, \bar{x}_2, \cdots, \bar{x}_L), \tag{E.9}$$

and its uncertainty may be expressed by the following relationship:

$$\mathcal{U}_\mathcal{R} = f_1\Big(\mathcal{U}_{\bar{x}_1}, \mathcal{U}_{\bar{x}_2}, \cdots, \mathcal{U}_{\bar{x}_N}\Big). \tag{E.10}$$

Each uncertainty ($\mathcal{U}_{\bar{x}_i}$) in the range ($i = 1, 2, \ldots, N$) is the best estimate for the uncertainty of each independent variable of the result, which in turn reflects the propagation of uncertainty through the result. Figliola & Beasley (2011) also demonstrated that the general sensitivity index ($\mathcal{Q}_i$) of the result on a

given measured value can be expressed as:

$$\mathcal{Q}_i = \frac{\partial R}{\partial x}_{x=\bar{x}}, \quad for \quad i = 1, 2, \ldots, N. \tag{E.11}$$

The contribution of the uncertainty in the independent variable and the result is estimated by the multiplication of the sensitivity index and the uncertainty for the given measured value of interest ($\mathcal{Q}_i \mathcal{U}_{\bar{x}_i}$), and Figliola & Beasley (2011) state that the most probable estimate of the uncertainty of the result is:

$$\mathcal{U}_{\mathcal{R}} = \pm \sqrt{\sum_{i=1}^{N} \left(\mathcal{Q}_i \mathcal{U}_{\bar{i}} \right)^2}. \tag{E.12}$$

Thus, the value of the variable to be measured is generally affected by the instrument resolution, and as a rule of thumb, a numerical value called the zeroth-order uncertainty ($\mathcal{U}_0$) is assigned. The latter is expressed as of one half of the instrument resolution (R_{inst}) at a probability of 95%:

$$\mathcal{U}_0 = \pm 0.5 \cdot R_{inst}. \tag{E.13}$$

In most cases, this type of error is provided by the manufacturer.

E.2 Uncertainty in the PIV Measurements

The inferred velocity field (u) obtained from a PIV measurement is calculated using the estimated particle displacement (Δx) and the specified time between pulses (Δt) as follows:

$$u = \frac{\Delta x}{\Delta t}. \tag{E.14}$$

Using a first order uncertainty propagation analysis, the uncertainty in the inferred velocity field ($\mathcal{U}_u$) can be expressed as:

$$\mathcal{U}_u = \sqrt{\left[\left(\frac{\partial u}{\partial \Delta x} \right) \cdot \mathcal{U}_{\Delta x} \right]^2 + \left[\left(\frac{\partial u}{\partial \Delta t} \right) \cdot \mathcal{U}_{\Delta t} \right]^2}, \tag{E.15}$$

which is a function of the uncertainty in the particle displacement ($\mathcal{U}_{\Delta x}$) and the uncertainty in the time between pulses ($\mathcal{U}_{\Delta t}$). The sources of error that contribute to the former are: i) position of the equipment (*e.g.* laser, camera, and calibration target), and ii) error in the calculation of the cross-correlation in the particle displacement. The latter is associated with the minimum precision in the time delay between the laser pulses.

Every piece of equipment required to ensure the perpendicularity between the laser sheet and the camera's field of view, was fastened to traversing mechanisms to limit the rectangular position errors to within 1 mm and angular position errors to within 0.5°. With such precisions, the normal (out of plane) velocity errors are assumed negligible. The Errors in the calculation of the cross-correlation are the most difficult to quantify as they depend on multiple parameters (i.e. tracer dynamics, image mapping, interrogation computation, spatial resolution, vector placements with the interrogation windows, flow kinematics, sampling error, and calculation of the velocity derivatives), which are given by Adrian & Westerweel (2011). However, Sciacchitano *et al.* (2013) demonstrated that all other sources of error are negligible with respect to the camera resolution, which using subpixel refinement techniques (Westerweel, 1997) can be estimated to be 0.1 pixels. In the current study, the latter corresponded to a 6.25 μm error in the displacement, as interrogation windows of 16×16 pixels corresponded to 1×1 mm were utilized.

The precision in the time between pulses is limited by the electronics used (timing box) and given by the manufacturer to be 12.5 ns. For the experiments, time between pulses of 115, 50, and 40 μs were utilized for the three average flow speeds of interest (2.15, 4.91, and 6.88 m/s), and therefore corresponds to fractions of a percentage in error for each time delay.

Table E.1: Uncertainties in the inferred velocities ($\mathcal{U}_{u_1}$, $\mathcal{U}_{u_2}$, and $\mathcal{U}_{u_3}$) for the PIV measurements validating the performance of the improved TMFM.

Flow Speeds		
u_1	u_2	u_3
2.15 m/s	4.91 m/s	6.88 m/s
Time Between Pulses		
Δt_1	Δt_2	Δt_3
115 μs	50 μs	40 μs
Specified Zeroth-Order Uncertainties		
$\mathcal{U}_{\Delta x}$		$\mathcal{U}_{\Delta t}$
3.13 μm		6.25 ns
Calculated First-Order Uncertainties		
$\mathcal{U}_{u_1}$	$\mathcal{U}_{u_2}$	$\mathcal{U}_{u_3}$
0.03 m/s	0.06 m/s	0.08 m/s

In summary, the calculated values for the zeroth-order and first-order uncertainties are listed in table E.1 for the six flow speeds and corresponding time between pulses.

E.3 Uncertainty in the TMFM measurements

The mass flow rates obtained using the TMFM ($\dot{m}_{TMFM}$) were inferred from the following equation:

$$\dot{m}_{TMFM} = \frac{\mathcal{P}_{inj}}{c_p}\left(\frac{1}{\Delta T_b}\right) = \left(\frac{c_p^{-1} EI}{T_{b_{out}} - T_{b_{in}}}\right), \tag{E.16}$$

where the power injected ($\mathcal{P}_{inj}$) into the flow through the heating element is controlled by a power supply (which controls the voltage (E) and current (I)), the specific heat at constant pressure (c_p) of the air is evaluated at the outlet bulk temperature using a second-order polynomial curve-fit:

$$c_p(T_{b_{out}}) = aT_{b_{out}}^2 + bT_{b_{out}} + c, \tag{E.17}$$

and the outlet ($T_{b_{out}}$)/inlet($T_{b_{in}}$) bulk temperatures are obtained using a linear calibration equation:

$$T_b = \frac{R - R_0}{\alpha}, \tag{E.18}$$

which is a function of the measured resistance (R), base resistance (R_0), and coefficient of thermal expansion of the RTDs.

The uncertainty in the mass flow rate inferred by the TMFM ($\mathcal{U}_{\dot{m}_{TMFM}}$)can be expressed by utilizing a first-order propagation of uncertainty, as follows:

$$\begin{aligned}\mathcal{U}_{\dot{m}_{TMFM}} = \pm\Bigg\{ &\left[\left(\frac{\partial \dot{m}_{TMFM}}{\partial c_p}\right)\cdot \mathcal{U}_{c_p}\right]^2 + \left[\left(\frac{\partial \dot{m}_{TMFM}}{\partial E}\right)\cdot \mathcal{U}_{E}\right]^2 \\ &+ \left[\left(\frac{\partial \dot{m}_{TMFM}}{\partial I}\right)\cdot \mathcal{U}_{I}\right]^2 + \left[\left(\frac{\partial \dot{m}_{TMFM}}{\partial_{T_{b_{out}}}}\right)\cdot \mathcal{U}_{T_{b_{out}}}\right]^2 \\ &+ \left[\left(\frac{\partial \dot{m}_{TMFM}}{\partial_{T_{b_{in}}}}\right)\cdot \mathcal{U}_{T_{b_{in}}}\right]^2\Bigg\}^{1/2}, \end{aligned} \tag{E.19}$$

which is a function of the partial derivative of each variable and their uncertainties. In the above equation, both the uncertainty for the current and voltage are zeroth-order uncertainties, whereas the uncertainty in the specific heat at constant pressure ($\mathcal{U}_{c_p}$) is defined as:

$$\mathcal{U}_{c_p} = \pm\sqrt{\left[\left(\frac{\partial c_p}{\partial T_{b_{out}}}\right)\cdot\mathcal{U}_{T_{b_{out}}}\right]^2} = \pm(2aT_{b_{out}} + b)\cdot\mathcal{U}_{T_{b_{out}}}, \tag{E.20}$$

and the uncertainty in the inlet/outlet bulk temperatures ($\mathcal{U}_{T_b}$) are:

$$\mathcal{U}_{T_b} = \pm\sqrt{\left[\left(\frac{\partial T_b}{\partial R}\right)\cdot\mathcal{U}_{T_b}\right]^2} = \pm\left(\frac{\mathcal{U}_R}{\alpha}\right), \tag{E.21}$$

which are a function of the zeroth-order uncertainty in the resistance measurements ($\mathcal{U}_R$), and is written without the inlet/outlet subscripts for brevity (but must be performed for each).

In summary, the calculated values for the zeroth-order and first-order uncertainties are listed in table E.2 for a representative set of thermal and electrical values. It is important to note that the uncertainties presented for mass flow rates inferred using the TMFM do not account for every possible source of error, including the heat losses in the system.

Table E.2: Uncertainties ($\mathcal{U}$) of the variables in the calculation for the mass flow rate using the TMFM for a representative set of thermal and electrical values.

Representative Thermal Values			
$T_{b_{in}}$	$T_{b_{out}}$	c_p	
46.2°C	66.2°C	1007 J/kg°C	
Representative Electrical Values			
E	I	$\mathcal{P}_{inj}$	
31 V	2.7 A	84 W	
Specified Zeroth-Order Uncertainties			
$\mathcal{U}_E$	$\mathcal{U}_I$	$\mathcal{U}_R$	
$5 \cdot 10^{-3}$ V	$5 \cdot 10^{-3}$ A	$5 \cdot 10^{-3}$ Ω	
Calculated First-Order Uncertainties			
$\mathcal{U}_{c_p}$	$\mathcal{U}_{T_{b_{in}}}$	$\mathcal{U}_{T_{b_{out}}}$	$\mathcal{U}_{\dot{m}_{TMFM}}$
$1.4 \cdot 10^{-3}$ $J/kg°C$	$45 \cdot 10^{-3}$ °C	$23 \cdot 10^{-3}$ °C	$13 \cdot 10^{-3}$ g/s